
Cancer
Cell
Volume 24
Number 3
September 9, 2013
www.cellpress.com
Xbp1s− Progenitors Survive
Proteasome Inhibitors in Multiple Myeloma

Tony Pawson (1952–2013)

Tony Pawson, a world-renowned scientist and a pioneer who made groundbreaking contributions that shaped our current understanding of how cellular signal transduction pathways are regulated in normal tissues and in cancer cells, sadly passed away on August 7, 2013 at the age of 60.

Anthony James Pawson was born on October 18, 1952 in Maidstone in the County of Kent in England. His mother was a high school biology teacher with a special interest in botany. His father was a well-known soccer player who played for the Oxford University team and for the English soccer team at the 1952 Olympiad in Helsinki. His father was also a successful cricket player, a member of the English fly-fishing team for the 1989 world championship, and, later in life, an author and correspondent for the Observer. Tony mentioned that he obtained his interest in science and the natural world from his mother, but his passion for writing, his competitiveness, his determination, and his own love of fly fishing from his father.

After spending his school years at Winchester College, Tony received his undergraduate education as a member of Clare College at Cambridge University. In Cambridge, he became interested in biochemistry and had the opportunity to spend time in the laboratory performing experiments in the field of protein synthesis. In 1973, Tony moved to London for his Ph.D. degree at ICRF (Imperial Cancer Research Fund, which is now called Cancer Research UK) with Alan Smith. During Tony's Ph.D. studies, the focus of his research was the mode of action and mechanism of oncogenesis mediated by retroviruses and how retroviruses propagate themselves. After obtaining his Ph.D. in 1976, Tony crossed the Atlantic and worked at the laboratory of Steven Martin at the University of California, Berkeley. Martin focused on investigating the mechanism of action of Rous Sarcoma virus, a retrovirus that causes tumors in chickens and transforms cultured cells by expressing its oncogenic protein, v-Src. During his postdoctoral training, Tony started to explore the structure and mechanism of action of the Fujinami avian sarcoma virus and the role played by its oncogenic protein, v-Fps, in cell transformation. In 1981, Tony took an independent faculty position at the University of British Columbia in Vancouver, where he continued to investigate the oncogenic v-Fps protein, increasingly focused on the role of its tyrosine kinase activity in cell transformation. A few years later, in 1985, Tony moved to the Samuel Lunenfeld Research Institute at Toronto's Mount Sinai Hospital, where he became Distinguished Investigator and Director of Research, and was also Professor of Molecular Genetics at the University of Toronto. Tony remained in Toronto for the rest of his career.

Tony was very much at the center of an exceptional convergence of several different areas of basic biomedical research during the last three decades of the 20th century, which revolutionized our understanding of the molecular basis of cell signaling and malignant transformation. These important discoveries contributed to new approaches for the development of many new cancer drugs.

Tony Pawson

The molecular basis of cancer was revealed through a stunning explosion of discoveries. These advances include: the genetic origins of malignancies; the mode of action of retroviral oncogenes; the discoveries of new growth factors and cytokines that stimulate cell proliferation, differentiation, and other vital cellular processes; the methodology to identify and track genetic changes in cancer cells; the identification of evolutionary conserved critical components of cellular signaling pathways in nematodes and *Drosophila*; and biochemical determination of how signals that are initiated at the cell surface and are propagated intracellularly by growth factor receptor activation stimulate cell proliferation and other basic processes that are required for cellular homeostasis. Subsequent application of this new knowledge led to the development of what is now defined as cancer-targeted therapies, which have changed the way in which many deadly cancers are now being treated.

Tony is perhaps best known for his identification of the Src homology 2, or SH2, domain and the resulting concept of modular interaction domains as key elements of the molecular infrastructure of signaling. While inspecting the primary structure of v-Fps early in his career, Tony and his colleagues made an important observation. They realized that, in addition to the catalytic tyrosine kinase domain of v-Fps that is also seen in the oncogenic Src and Abl tyrosine kinases, these oncogenic proteins contain a conserved noncatalytic region of ~100 amino acids, which they termed the SH2 domain (the tyrosine kinase is the SH1 domain). Through biochemical analyses of the tyrosine kinase activities of a variety of v-Fps mutants and comparison of their cellular transformation properties, Tony's laboratory demonstrated that the v-Fps SH2 domain plays an important role in controlling both the tyrosine kinase activity and cell transformation. Members of the Src and Abl tyrosine kinase families contain an additional conserved noncatalytic region of ~60 amino acids, designated the Src homology 3 (SH3) domain,

Reprinted from Cell *154*, Published online September 5, 2013. http://dx.doi.org/10.1016/j.cell.2013.08.038.

located N terminal to the SH2 domain of Src and Abl. Tony proposed that SH2 and SH3 domains function as independent protein modules that maintain their unique functions in different host proteins and that they play important regulatory roles in controlling the activity and localization of Src and other cytoplasmic tyrosine kinases. This concept of modularity gained significant traction when the laboratory of Hidesaburo Hanafusa found that the transforming gene of the CT10 retrovirus, v-Crk, encodes a viral gag protein fused to only SH2 and SH3 domains, demonstrating that SH2 and SH3 domains can function alone as oncogenes. The SH2 domain of Crk was shown to bind directly to phosphotyrosine (P-Tyr)-containing proteins, indicating that SH2 domains may recognize specific tyrosine-containing regions in a phosphorylation-dependent manner. Because many signaling molecules with different enzymatic activities, such as phospholipase Cγ (PLCγ), Ras GTPase-activating protein (GAP), and the Src family kinases, contain SH2 domains, this realization provided a link between activation of cytoplasmic and receptor tyrosine kinases (RTKs). Indeed, experiments performed in Tony's and other laboratories demonstrated that, following their stimulation with ligands, the EGF receptor (EGFR), PDGF receptor (PDGFR), and other activated RTKs form physical complexes with signaling molecules such as PLCγ, GAP, or adaptor proteins such as Grb2 or Nck by binding to the SH2 domains of these signaling proteins. For example, in 1992, Tony's laboratory demonstrated that complex formation between the scaffold protein Shc and phosphotyrosines on activated EGFR leads to tyrosine phosphorylation of Shc, which in turn forms a complex with the SH2 domain of the adaptor protein Grb2. Grb2 uses its two SH3 domains to bind the guanine nucleotide exchange factor Sos so that Shc effectively recruits Sos to the cell membrane (and thus activates Ras) through SH2 and SH3 domain-mediated interactions. The resulting activated (GTP-bound) Ras molecules stimulate a cascade of three protein kinases, resulting in activation and nuclear translocation of MAP kinase. This highly conserved signaling pathway relays information from the cell membrane to the nucleus and other intracellular compartments to regulate a variety of EGF-induced cellular processes.

More than 20 years later, in one of his last and most elegant articles that was published in July 2013—only three weeks before he passed away—Tony's laboratory described a comprehensive analysis of the cellular functions of Shc at different time points following EGF stimulation. His laboratory used mass spectrometry and other state-of-the-art technologies to demonstrate that Shc responds to EGF stimulation in "multiple waves of distinct phosphorylation events and protein interactions." In other words, at different time points following EGF stimulation, Shc forms distinct complexes with different positive or negative regulators to control many of the pleiotropic cellular responses induced by EGF stimulation. These two publications, spanning more than two decades of scientific effort, provide a clear testament to the originality, brilliance, and focus that have been a hallmark of Tony's entire scientific career.

In addition to his main interest in elucidating the biological roles and mechanisms underlying the actions of SH2, SH3, and other small protein modules in mediating protein-protein and other interactions during signal transduction, Tony's laboratory made important contributions to other fields of biomedical research, including analysis of molecular mechanisms that govern cellular polarity and molecular mechanisms that control axon guidance, as well as systems biology with an emphasis on elucidation of the dynamic nature of molecular events during cellular signaling. In all of these studies, he showed an uncanny ability to marry advances in technology with the most important biological questions to view the entire cell in terms of its molecular infrastructure.

The death of Tony Pawson shocked and saddened his many colleagues, former students, postdoctoral fellows, and friends all over the world. We will miss Tony's thoughtful and eloquent lectures. We will miss Tony's inspiring publications and the elegance and clarity of his scientific mind. We will miss our informal discussions at scientific meetings that were filled with good humor, Tony's characteristic chuckle, and his sharp insights. Tony's legacy will be remembered and will be an inspiration for future generations of scientists.

Joseph Schlessinger[1,*]
[1]Department of Pharmacology, Yale University School of Medicine, New Haven, CT 06520, USA
*Correspondence: joseph.schlessinger@yale.edu
http://dx.doi.org/10.1016/j.ccr.2013.08.026

Why Proteasome Inhibitors Cannot ERADicate Multiple Myeloma

Robert Z. Orlowski[1,2,*]
[1]Department of Lymphoma/Myeloma
[2]Department of Experimental Therapeutics
The University of Texas MD Anderson Cancer Center, Houston, TX 77030, USA
*Correspondence: rorlowsk@mdanderson.org
http://dx.doi.org/10.1016/j.ccr.2013.08.014

Proteasome inhibitors are key parts of our armamentarium against multiple myeloma, but the disease can become resistant through poorly defined mechanisms. In this issue of *Cancer Cell*, Leung-Hagesteijn and colleagues describe XBP1s^{-} subpopulations of tumor cells that are resistant to bortezomib and may account for therapeutic failures in the clinic.

Multiple myeloma is a clonal proliferation of neoplastic plasma cells that can present clinically with hypercalcemia, renal insufficiency, anemia, bony lesions, bacterial infections, hyperviscosity, and amyloidosis. Worldwide, approximately 86,000 patients will be diagnosed each year with myeloma, which, in many areas, makes it the second most common hematologic malignancy, while about 63,000 patients die every year from disease-related complications (Becker, 2011). In the United States, due to an aging populace, it is anticipated that the number of cases of myeloma will grow by 57% between 2010 and 2030 (Smith et al., 2009), ranking myeloma behind only stomach and liver cancer in the rate of growth of new cases. These facts indicate that multiple myeloma is, and will continue to be, a significant source of morbidity and mortality. Fortunately, a number of advances over the past decade have dramatically improved patient outcomes. Among these are the advent of novel chemotherapeutics, including the immunomodulatory agents thalidomide, lenalidomide, and pomalidomide, and the proteasome inhibitors (Moreau et al., 2012) bortezomib and carfilzomib. All of these drugs have garnered regulatory approvals and are used in patients with newly diagnosed, relapsed, or relapsed/refractory disease and have contributed to a doubling of the median overall survival in many populations. This has been fueled by a greater understanding of the pathobiology of myeloma and by the development of more physiologically relevant preclinical models, allowing for greater success in translating laboratory concepts into patient-focused therapies. Indeed, a number of the most potent combination regimens in use have been rationally developed based on studies of the mechanisms of action of these drug classes (Mahindra et al., 2012).

Despite these significant advances, patients are currently treated on an empiric basis, typically with the regimens that have the highest response rates to which they have access, rather than based on the principles of precision medicine (Mendelsohn, 2013). The proteasome inhibitors bortezomib and carfilzomib as single agents in the relapsed and refractory settings both have response rates of approximately 25%, indicating a role for innate or primary resistance in modulating their activity. Response rates and, even more importantly, response durability can be improved by using them earlier in the disease process and incorporating them into combination regimens. However, no clinically relevant biomarkers have been validated that would allow practitioners to prospectively identify patients with disease that is most likely to respond to proteasome inhibition, and the same is true for the immunomodulatory drugs. In addition, even in patients whose disease initially responds, resistance to proteasome inhibitor-based therapy emerges in many, indicating a role for acquired or secondary resistance through incompletely understood mechanisms. As a result, some patients are exposed to the toxicities of these agents without a benefit, delaying their access to more effective options, and wasting precious healthcare resources. Clinically, these factors contribute to the natural history of the disease, which follows a course characterized by multiple relapses and decreasing durations of benefit with each subsequent line of therapy.

The work of Leung-Hagesteijn et al. (2013) in this issue of *Cancer Cell* may, however, begin to change the current status quo. Early attempts to identify mechanisms of innate bortezomib resistance implicated a role for overexpression of proteasome genes and especially of *PSMD4* (Shaughnessy et al., 2011). Later, studies of acquired resistance models suggested mutations of the β5 proteasome subunit targeted by bortezomib were involved. However, these β5 mutations were subsequently not detected in patient samples, as indicated in the introduction by Leung-Hagesteijn et al. (2013). More recently, induction of signaling through the insulin-like growth factor (IGF)/IGF-1 receptor pathway has been implicated in acquired resistance (Kuhn et al., 2012), and clinical trials to test this possibility are planned. Finally, upregulation of a cluster of *NRF2* oxidative stress response genes, including *CHOP* (*DDIT3*), was identified as a possible resistance signature in studies of murine myeloma models and clinically annotated gene expression profiling data sets (Stessman et al., 2013).

In contrast, Leung-Hagesteijn et al. (2013) provide a different perspective starting from kinome-wide RNA interference studies intended to identify modulators of proteasome inhibitor sensitivity. They report that suppression of inositol-requiring enzyme 1 (IRE1) and its downstream effector, X-box binding protein 1 (XBP1), was associated with bortezomib

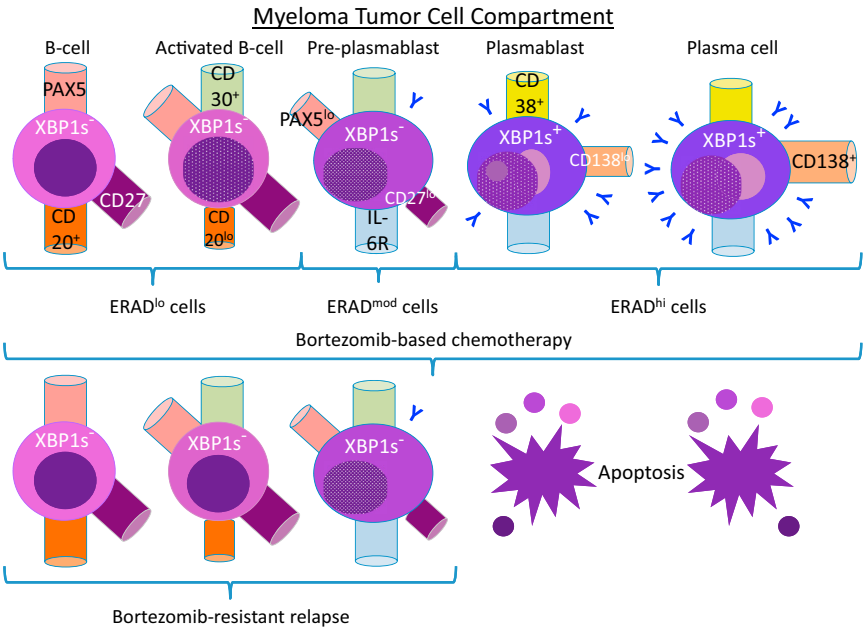

Figure 1. Model of Proteasome Inhibitor Resistance

Patients with multiple myeloma may have a number of neoplastic subpopulations, including B cells, activated B cells, pre-plasmablasts, plasmablasts, and plasma cells. B cells are typically cluster differentiation antigen 20$^+$ (CD20$^+$)/CD27$^+$/paired box 5$^+$ (PAX5$^+$) and do not have spliced X-box binding protein 1 message (XBP-1 s$^-$), whereas activated B cells are similar but express lower levels of CD20 and can be CD30$^+$. Neither B cells nor activated B cells are involved in substantial immunoglobulin synthesis, and both therefore have relatively low levels of proteasome-assisted, endoplasmic reticulum-associated protein degradation (ERAD^{lo}). Pre-plasmablasts are probably CD27^{lo}/PAX5^{lo}/CD30$^+$/XBP-1 s$^-$, express the interleukin 6 receptor (IL-6R$^+$), produce low levels of monoclonal protein (Y), and therefore have modest levels of ERAD activity (ERAD^{mod}). Plasmablasts are CD38$^+$/CD138^{lo}/IL-6R$^+$/XBP-1 s$^+$, secrete increased levels of monoclonal protein, and therefore have higher ERAD activity (ERAD^{hi}). Finally, terminally differentiated plasma cells are CD38$^+$/CD138$^+$/IL-6R$^+$/XBP-1 s$^+$, produce high levels of monoclonal protein, and have the highest levels of ERAD activity. These phenotypic characteristics are taken from the work of Leung-Hagesteijn et al. (2013) and from other literature sources. Plasmablasts and plasma cells are sensitive to proteasome inhibitors such as bortezomib because of their high level of immunoglobulin synthesis, leading to high levels of ERAD-related stress, which triggers dependence on the unfolded protein response (UPR). B cells, activated B cells, and pre-plasmablasts, in part because they are XBP-1 s$^-$, produce less immunoglobulin and are therefore less susceptible. Treatment with bortezomib eradicates plasmablasts and plasma cells, which initially may make up the bulk of the tumor compartment and results in elimination of the monoclonal protein marker. However, B cells, activated B cells, and pre-plasmablasts, which initially are a minor component of the tumor compartment, survive. After expansion of these cells, patients may then develop clinical relapses that are bortezomib-resistant with disease that is hypo- or nonsecretory and may require a different treatment approach.

resistance. This, to some extent, challenges a current dogma, because IRE1 and XBP1 make up one arm of the unfolded protein response (UPR). Indeed, UPR activation was felt to represent an adaptation to proteasome-assisted endoplasmic reticulum-associated degradation (ERAD), which causes ER stress in plasma cells due to their large loads of misfolded proteins. These IRE1^{lo} and XBP1^{lo} cells showed lower expression of plasma cell maturation markers, lower immunoglobulin synthesis, and lower levels of UPR activation, consistent with a lower stress level and proteasome load, which would make them resistant to proteasome inhibitors. Moreover, plasma cell maturation markers were enriched in samples from patients who responded to bortezomib-based therapy and reduced in those with no response to bortezomib. Finally, analysis of patient samples revealed the presence of up to five tumor cell subpopulations, including B cells, activated B cells, pre-plasmablasts, plasmablasts, and plasma cells, which would be expected to have different sensitivities to bortezomib (Figure 1). Consistent with this possibility, myeloma B cell and pre-plasmablast progenitors were found to survive proteasome inhibition and be enriched in samples that were refractory to bortezomib.

These findings have a number of key implications for innate and acquired proteasome inhibitor resistance. First, they suggest that the seeds for bortezomib resistance, and cross-resistance with other proteasome inhibitors, are already present in perhaps all patients and that this phenotype will inevitably emerge through the attrition of bortezomib-sensitive plasmablasts and plasma cells (Figure 1). Second, they support the possibility that gene expression profiling or whole genome sequencing to identify the baseline proportion of these progenitor cells present in patients prior to initiation of therapy may predict the extent of benefit to be expected from bortezomib. Finally, they imply that potentially curative strategies will need to target both the committed plasma cells and the progenitor, or stem cell-like cells.

While these hypotheses are being tested, the current findings will also need to be validated in a wider array of primary samples and additional gene expression profiling data sets. One question that needs to be answered is whether the same proteasome inhibitor-resistant progenitor cells survive therapy with bortezomib in combination with other agents. This would be especially of interest for the combination of bortezomib and lenalidomide, because the latter may target clonogenic side-population cells (Jakubikova et al., 2011), and this regimen is one of our current standards of care against myeloma. Another important question is whether it would be possible to induce differentiation of progenitor cells to more committed plasma cells, such as through epigenetic therapies, to enhance or restore proteasome inhibitor sensitivity. Finally, it is likely that multiple mechanisms contribute to the development of the proteasome inhibitor-resistant phenotype. For example, while the current studies indicate that cells with a decreased proteasome load are resistant, it is also possible that changes that enhance plasma cell proteasome capacity would antagonize the beneficial effects of bortezomib and carfilzomib. Taken together, however, these findings do provide an important direction for future preclinical and clinical

studies that will hopefully bring us to the point that we can apply precision medicine to the therapy of multiple myeloma.

ACKNOWLEDGMENTS

R.Z.O. would like to acknowledge support from the National Cancer Institute in the form of The MD Anderson Cancer Center SPORE in Multiple Myeloma (P50 CA142509) and the Southwest Oncology Group (U10 CA032102). R.Z.O. has received research funding from Bristol-Myers Squibb, Celgene Corporation, Millennium: The Takeda Oncology Company, and Onyx Pharmaceuticals. Also, R.Z.O. has served on advisory boards for Array Biopharma, Bristol-Myers Squibb, Celgene Corporation, Genentech, Merck, Millennium: The Takeda Oncology Company, and Onyx Pharmaceuticals.

REFERENCES

Becker, N. (2011). Recent Results Cancer Res. *183*, 25–35.

Jakubikova, J., Adamia, S., Kost-Alimova, M., Klippel, S., Cervi, D., Daley, J.F., Cholujova, D., Kong, S.Y., Leiba, M., Blotta, S., et al. (2011). Blood *117*, 4409–4419.

Kuhn, D.J., Berkova, Z., Jones, R.J., Woessner, R., Bjorklund, C.C., Ma, W., Davis, R.E., Lin, P., Wang, H., Madden, T.L., et al. (2012). Blood *120*, 3260–3270.

Leung-Hagesteijn, C., Erdmann, N., Cheung, G., Keats, J.J., Stewart, A.K., Reece, D., Chung, K.C., and Tiedemann, R.E. (2013). Cancer Cell *24*, this issue, 289–304.

Mahindra, A., Laubach, J., Raje, N., Munshi, N., Richardson, P.G., and Anderson, K. (2012). Nat Rev Clin Oncol *9*, 135–143.

Mendelsohn, J. (2013). J. Clin. Oncol. *31*, 1904–1911.

Moreau, P., Richardson, P.G., Cavo, M., Orlowski, R.Z., San Miguel, J.F., Palumbo, A., and Harousseau, J.L. (2012). Blood *120*, 947–959.

Shaughnessy, J.D., Jr., Qu, P., Usmani, S., Heuck, C.J., Zhang, Q., Zhou, Y., Tian, E., Hanamura, I., van Rhee, F., Anaissie, E., et al. (2011). Blood *118*, 3512–3524.

Smith, B.D., Smith, G.L., Hurria, A., Hortobagyi, G.N., and Buchholz, T.A. (2009). J. Clin. Oncol. *27*, 2758–2765.

Stessman, H.A., Baughn, L.B., Sarver, A., Xia, T., Deshpande, R., Mansoor, A., Walsh, S.A., Sunderland, J.J., Dolloff, N.G., Linden, M.A., et al. (2013). Mol. Cancer Ther. *12*, 1140–1150.

RASAL2: Wrestling in the Combat of Ras Activation

Jia Shen,[1,2] Yan Wang,[1] and Mien-Chie Hung[1,2,3,*]
[1]Department of Molecular and Cellular Oncology, The University of Texas MD Anderson Cancer Center, 1515 Holcombe Boulevard, Houston, TX 77030, USA
[2]The University of Texas Graduate School of Biomedical Sciences at Houston, Houston, TX 77030, USA
[3]Center for Molecular Medicine and Graduate Institute of Cancer Biology, China Medical University, Taichung 402, Taiwan
*Correspondence: mhung@mdanderson.org
http://dx.doi.org/10.1016/j.ccr.2013.08.024

Oncogenic activation of Ras proteins due to missense mutations is frequently detected in human cancers but rarely in breast cancer. In this issue of *Cancer Cell*, McLaughlin and colleagues report that ablation of the GasGAP gene, *RASAL2*, is an alternative mechanism by which Ras becomes activated in breast cancer.

Ras GTPases are essential components of signaling pathways that emanate cues from cell surface receptors to regulate diverse cellular processes, including cell cycle progression, cell survival, actin cytoskeletal organization, cell polarity and movement, as well as vesicular and nuclear transport (Vigil et al., 2010). Ras proteins (H-Ras, N-Ras, and K-Ras), together with their two key regulators (guanine nucleotide exchange factors/GEFs and GTPase-activating proteins/GAPs), constitute cellular binary switches that cycle between "on" and "off" conformations conferred by the loading of GTP or GDP, respectively. The transition between the active GTP-bound and inactive GDP-bound states of Ras GTPases is controlled by GEFs, which promote the activation of Ras proteins by stimulating GDP for GTP exchange, and GAPs, which terminate the activation status by accelerating Ras-mediated GTP hydrolysis (Bos et al., 2007; Tcherkezian and Lamarche-Vane, 2007). Ras GTPases and cancer are tightly associated, as high frequency of mutational activation of Ras proteins is observed in ~33% of human cancers. The intrinsic GTP hydrolysis activity of Ras is the predominant target of the most common somatic mutations that are found in the oncogenic variants of *RAS* alleles (Pylayeva-Gupta et al., 2011). Specifically, oncogenic substitution in residue G12 or G13 results in pronounced attenuation of intrinsic GTP hydrolysis, which leads to the persistence of the GTP-bound state of Ras and subsequently activates a multitude of Ras-dependent downstream effector pathways. Beyond Ras, hyperactivation of GEFs and functional deregulation, including suppression and loss-of-function mutations of GAPs, have also been suggested to play important roles in cancer progression (Vigil et al., 2010).

Despite the prevalence of oncogenic RAS mutations in human cancers, *K-RAS*, *H-RAS*, and *N-RAS* are rarely mutated in breast cancer (Karnoub and Weinberg, 2008). Nonetheless, the Ras/ERK pathway is hyperactivated in more than half of breast cancers and has been implicated in tumor progression and recurrence (von Lintig et al., 2000), suggesting that Ras proteins may be more frequently activated by alternative mechanisms in this type of tumors. A new study by McLaughlin et al. (2013) in this issue of *Cancer Cell* uncovers the role of RASAL2,

studies that will hopefully bring us to the point that we can apply precision medicine to the therapy of multiple myeloma.

ACKNOWLEDGMENTS

R.Z.O. would like to acknowledge support from the National Cancer Institute in the form of The MD Anderson Cancer Center SPORE in Multiple Myeloma (P50 CA142509) and the Southwest Oncology Group (U10 CA032102). R.Z.O. has received research funding from Bristol-Myers Squibb, Celgene Corporation, Millennium: The Takeda Oncology Company, and Onyx Pharmaceuticals. Also, R.Z.O. has served on advisory boards for Array Biopharma, Bristol-Myers Squibb, Celgene Corporation, Genentech, Merck, Millennium: The Takeda Oncology Company, and Onyx Pharmaceuticals.

REFERENCES

Becker, N. (2011). Recent Results Cancer Res. *183*, 25–35.

Jakubikova, J., Adamia, S., Kost-Alimova, M., Klippel, S., Cervi, D., Daley, J.F., Cholujova, D., Kong, S.Y., Leiba, M., Blotta, S., et al. (2011). Blood *117*, 4409–4419.

Kuhn, D.J., Berkova, Z., Jones, R.J., Woessner, R., Bjorklund, C.C., Ma, W., Davis, R.E., Lin, P., Wang, H., Madden, T.L., et al. (2012). Blood *120*, 3260–3270.

Leung-Hagesteijn, C., Erdmann, N., Cheung, G., Keats, J.J., Stewart, A.K., Reece, D., Chung, K.C., and Tiedemann, R.E. (2013). Cancer Cell *24*, this issue, 289–304.

Mahindra, A., Laubach, J., Raje, N., Munshi, N., Richardson, P.G., and Anderson, K. (2012). Nat Rev Clin Oncol *9*, 135–143.

Mendelsohn, J. (2013). J. Clin. Oncol. *31*, 1904–1911.

Moreau, P., Richardson, P.G., Cavo, M., Orlowski, R.Z., San Miguel, J.F., Palumbo, A., and Harousseau, J.L. (2012). Blood *120*, 947–959.

Shaughnessy, J.D., Jr., Qu, P., Usmani, S., Heuck, C.J., Zhang, Q., Zhou, Y., Tian, E., Hanamura, I., van Rhee, F., Anaissie, E., et al. (2011). Blood *118*, 3512–3524.

Smith, B.D., Smith, G.L., Hurria, A., Hortobagyi, G.N., and Buchholz, T.A. (2009). J. Clin. Oncol. *27*, 2758–2765.

Stessman, H.A., Baughn, L.B., Sarver, A., Xia, T., Deshpande, R., Mansoor, A., Walsh, S.A., Sunderland, J.J., Dolloff, N.G., Linden, M.A., et al. (2013). Mol. Cancer Ther. *12*, 1140–1150.

RASAL2: Wrestling in the Combat of Ras Activation

Jia Shen,[1,2] Yan Wang,[1] and Mien-Chie Hung[1,2,3,*]
[1]Department of Molecular and Cellular Oncology, The University of Texas MD Anderson Cancer Center, 1515 Holcombe Boulevard, Houston, TX 77030, USA
[2]The University of Texas Graduate School of Biomedical Sciences at Houston, Houston, TX 77030, USA
[3]Center for Molecular Medicine and Graduate Institute of Cancer Biology, China Medical University, Taichung 402, Taiwan
*Correspondence: mhung@mdanderson.org
http://dx.doi.org/10.1016/j.ccr.2013.08.024

Oncogenic activation of Ras proteins due to missense mutations is frequently detected in human cancers but rarely in breast cancer. In this issue of *Cancer Cell*, McLaughlin and colleagues report that ablation of the GasGAP gene, *RASAL2*, is an alternative mechanism by which Ras becomes activated in breast cancer.

Ras GTPases are essential components of signaling pathways that emanate cues from cell surface receptors to regulate diverse cellular processes, including cell cycle progression, cell survival, actin cytoskeletal organization, cell polarity and movement, as well as vesicular and nuclear transport (Vigil et al., 2010). Ras proteins (H-Ras, N-Ras, and K-Ras), together with their two key regulators (guanine nucleotide exchange factors/GEFs and GTPase-activating proteins/GAPs), constitute cellular binary switches that cycle between "on" and "off" conformations conferred by the loading of GTP or GDP, respectively. The transition between the active GTP-bound and inactive GDP-bound states of Ras GTPases is controlled by GEFs, which promote the activation of Ras proteins by stimulating GDP for GTP exchange, and GAPs, which terminate the activation status by accelerating Ras-mediated GTP hydrolysis (Bos et al., 2007; Tcherkezian and Lamarche-Vane, 2007). Ras GTPases and cancer are tightly associated, as high frequency of mutational activation of Ras proteins is observed in ~33% of human cancers. The intrinsic GTP hydrolysis activity of Ras is the predominant target of the most common somatic mutations that are found in the oncogenic variants of *RAS* alleles (Pylayeva-Gupta et al., 2011). Specifically, oncogenic substitution in residue G12 or G13 results in pronounced attenuation of intrinsic GTP hydrolysis, which leads to the persistence of the GTP-bound state of Ras and subsequently activates a multitude of Ras-dependent downstream effector pathways. Beyond Ras, hyperactivation of GEFs and functional deregulation, including suppression and loss-of-function mutations of GAPs, have also been suggested to play important roles in cancer progression (Vigil et al., 2010).

Despite the prevalence of oncogenic RAS mutations in human cancers, *K-RAS*, *H-RAS*, and *N-RAS* are rarely mutated in breast cancer (Karnoub and Weinberg, 2008). Nonetheless, the Ras/ERK pathway is hyperactivated in more than half of breast cancers and has been implicated in tumor progression and recurrence (von Lintig et al., 2000), suggesting that Ras proteins may be more frequently activated by alternative mechanisms in this type of tumors. A new study by McLaughlin et al. (2013) in this issue of *Cancer Cell* uncovers the role of RASAL2,

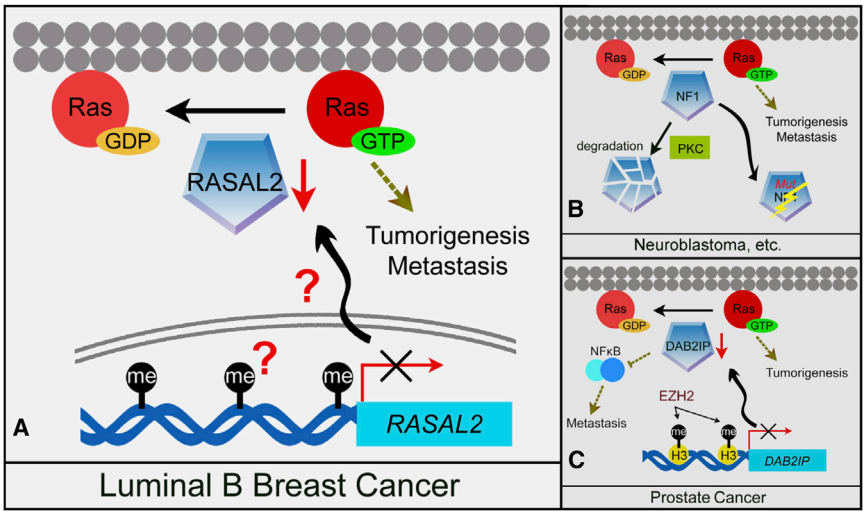

Figure 1. Alternative Activation of Wild-Type Ras via Deregulation of RasGAPs in Human Cancers

(A) Suppression of *RASAL2* is specifically found in human luminal B breast cancer and correlates with the hypermethylation status of *RASAL2* promoter CpG sites. Loss of *RASAL2* activates wild-type Ras and promotes cancer progression and metastasis in the breast cancer xenograft model and genetically engineered mouse models (McLaughlin et al., 2013).

(B) Germline mutational loss of the NF1 tumor suppressor is found in familial cancer syndrome neurofibromatosis type 1 and is mutated or suppressed via PKC-dependent proteasome degradation in several sporadic cancers, including glioblastoma, non-small cell lung cancer, neuroblastoma, and melanoma (McGillicuddy et al., 2009; Vigil et al., 2010).

(C) DAB2IP, another RasGAP, is also epigenetically silenced by EZH2 and functions as a tumor and metastasis suppressor via activation of both Ras and NF-kB pathways in prostate cancer (Min et al., 2010).

a RasGAP that is less well characterized, as a tumor suppressor in breast cancer through direct blockage of Ras activation. They found that *RASAL2* is frequently absent or minimally expressed in cells derived from luminal breast cancer. Reconstitution of RASAL2 in cells with low endogenous expression suppressed Ras-GTP and the activation of downstream ERK. Conversely, knockdown of RASAL2 in normal immortalized mammary epithelial cells enhanced Ras-GTP and increased the level of phospho-ERK. These results demonstrate that RASAL2 is a functional RasGAP and that its loss activates the Ras/ERK signaling pathway.

Whereas reconstitution of RASAL2 in *RASAL2*-deficient breast cancer cells inhibited anchorage-independent colony growth and potently suppressed tumor growth in vivo, it had almost no significant effect on RAS mutant tumors. The dependency of Ras mutation status suggests that the RasGAP domain in RASAL2 plays an important role. Indeed, two RasGAP domain mutants (K417E and K567X) that are defective in blocking the activation of Ras/ERK pathway failed to suppress anchorage-independent cell growth, indicating that the RasGAP domain is essential for the tumor suppressor function of RASAL2. Elevated levels of K-Ras-GTP and H-Ras-GTP significantly contributed to the pathogenesis promoted by RASAL2 inactivation. In contrast, ablation of RASAL2 enhanced cell migration and invasion in vitro and promoted cancer progression from ductal carcinoma in situ (DCIS) to invasive carcinoma in a breast cancer xenograft model using MCF10A-DCIS cells.

The functional role of RASAL2 was further examined by the authors in genetically engineered mice lacking *Rasal2*. *Rasal2*$^{-/-}$ mice exhibit shorter overall survival as compared to control animals. However, *Rasal2*$^{-/-}$ mice did not develop tumors, suggesting that the loss of *Rasal2* itself is not sufficient to drive tumorigenesis in mice. Interestingly, *Rasal2*$^{-/-}$ mice that crossed with *MMTVneu* developed substantially more metastases than the *MMTVneu* mice, with higher frequency and larger size of metastases, as well as an additional spectrum of distant metastases, including brain, kidney, ovary, and gastrointestinal tract, which are not observed in *MMTVneu* mice. Correspondingly, the activation of Ras/ERK and AKT were substantially elevated in the compound mice, suggesting that the loss of *Rasal2* promotes metastasis via activation of Ras. In addition, the authors also propose that RASAL2 may play a broader tumor-suppressive role in other cancer types as the loss of *Rasal2* potently promotes metastasis in *Trp53* mutant mice.

To understand the suppression mechanism of RASAL2 in human breast cancers, McLaughlin et al. (2013) examined the DNA methylation status of *RASAL2* promoter and identified two CpG sites that are specifically methylated in luminal B breast tumors, revealing an alternative mechanism of Ras activation through epigenetic ablation of *RASAL2* (Figure 1A). Notably, the DNA methylation patterns are significantly different between luminal B and basal-like breast tumors (Holm et al., 2010), with one being the most and the other least frequently methylated, respectively. As little is known about the molecular mechanisms that are responsible for the suppression of *RASAL2* via promoter methylation, particularly in luminal B breast cancer, more questions remain, such as whether methylation of *RASAL2* promoter CpG sites is a consequence of generally elevated DNA methylation due to enhanced activity of DNA methyltransferases in luminal B subtype or whether *RASAL2* is specifically targeted for silencing to activate Ras/ERK signaling in these tumors. The detailed contribution of promoter methylation to the suppression of *RASAL2* in breast cancer will be interesting to further pursue. The evidence shown by the authors provides an interesting correlation between enhanced promoter methylation and reduced *RASAL2* mRNA levels, but it is still not clear if other mechanisms for *RASAL2* inactivation coexist in breast cancers. Indeed, RasGAPs, exemplified by NF1 and DAB2IP tumor suppressors, are susceptible to multiple ways of deregulation (Figures 1B and 1C), including epigenetic silencing, proteasome-mediated degradation, and loss-of-function mutations (Bos et al., 2007; McGillicuddy et al., 2009; Min et al., 2010). Understanding the exact regulations of *RASAL2*

suppression could shed light on new anticancer strategies that inhibit the activation of wild-type Ras by restoring expression of the corresponding RasGAP.

Intriguingly, despite the fact that each of the RasGAP members harbors a conserved RasGAP domain, not all exhibit tumor suppressor functions (Min et al., 2010). Accordingly, the existence of non-Ras-associated functions of RasGAPs has been proposed and further demonstrated in the case of DAB2IP (Min et al., 2010), which acts as a signaling scaffold that coordinately regulates Ras and NF-kB activation to promote tumor growth and metastasis (Figure 1C), respectively. Whether other conserved domain(s) besides the RasGAP domain of RASAL2 also exert a Ras-independent tumor-suppressive signaling cascade remains to be investigated. Additionally, how the RasGAPs coordinate with each other to regulate the activation of Ras in different human cancers is not clear. Epigenetic suppression of DAB2IP (Dote et al., 2004) and the mutation of NF1 (The Cancer Genome Atlas Database) are also observed in breast cancers, raising the question of whether the deregulation events of RasGAPs are mutually exclusive or whether they coexist for sufficient addiction to wild-type Ras activation in breast cancer.

REFERENCES

Bos, J.L., Rehmann, H., and Wittinghofer, A. (2007). Cell *129*, 865–877.

Dote, H., Toyooka, S., Tsukuda, K., Yano, M., Ouchida, M., Doihara, H., Suzuki, M., Chen, H., Hsieh, J.T., Gazdar, A.F., and Shimizu, N. (2004). Clin. Cancer Res. *10*, 2082–2089.

Holm, K., Hegardt, C., Staaf, J., Vallon-Christersson, J., Jönsson, G., Olsson, H., Borg, A., and Ringnér, M. (2010). Breast Cancer Res. *12*, R36.

Karnoub, A.E., and Weinberg, R.A. (2008). Nat. Rev. Mol. Cell Biol. *9*, 517–531.

McGillicuddy, L.T., Fromm, J.A., Hollstein, P.E., Kubek, S., Beroukhim, R., De Raedt, T., Johnson, B.W., Williams, S.M., Nghiemphu, P., Liau, L.M., et al. (2009). Cancer Cell *16*, 44–54.

McLaughlin, S.K., Olsen, N.O., Dake, B., De Raedt, T., Lim, E., Bronson, R.T., Beroukhim, R., Polyak, K., Brown, M., Kuperwasser, C., and Cichowski, K. (2013). Cancer Cell *24*, this issue, 365–378.

Min, J., Zaslavsky, A., Fedele, G., McLaughlin, S.K., Reczek, E.E., De Raedt, T., Guney, I., Strochlic, D.E., Macconaill, L.E., Beroukhim, R., et al. (2010). Nat. Med. *16*, 286–294.

Pylayeva-Gupta, Y., Grabocka, E., and Bar-Sagi, D. (2011). Nat. Rev. Cancer *11*, 761–774.

Tcherkezian, J., and Lamarche-Vane, N. (2007). Biol. Cell *99*, 67–86.

Vigil, D., Cherfils, J., Rossman, K.L., and Der, C.J. (2010). Nat. Rev. Cancer *10*, 842–857.

von Lintig, F.C., Dreilinger, A.D., Varki, N.M., Wallace, A.M., Casteel, D.E., and Boss, G.R. (2000). Breast Cancer Res. Treat. *62*, 51–62.

It Takes a CAD to Kill a Tumor Cell with a LMP

Erich Gulbins[1] and Richard N. Kolesnick[2,*]
[1]Department of Molecular Biology, University of Duisburg-Essen, Hufelandstrasse 55, 45122 Essen, Germany
[2]Laboratory of Signal Transduction, Memorial Sloan-Kettering Cancer Center, 415 East 68th Street, New York, NY 10065, USA
*Correspondence: r-kolesnick@ski.mskcc.org
http://dx.doi.org/10.1016/j.ccr.2013.08.025

Cancer cells display lysosome hypertrophy, secreting lysosomal hydrolases for tumor progression. Hypertrophy renders lysosomes fragile, increasing lysosomal membrane permeabilization (LMP) tendency. In this issue of *Cancer Cell*, Petersen and colleagues show that lysosomal sphingomyelin content determines LMP and cationic drugs displace acid sphingomyelinase from lysosomal membranes, increasing tumor LMP and death.

Early on after the discovery of lysosomes by Christian de Duve as a separate compartment that confines highly destructive hydrolases for the demolition and reutilization of cellular substituents, the concept that these structures might alternatively represent "suicide bags" was proposed (de Duve, 1983). This led to an intense search for lysosomatrophic agents that might access this biology for therapeutic purpose. Although a set of lysosomal detergents with long hydrophobic tails and medium pK were defined as capable of inducing lysosomal membrane permeabilization (LMP) and thereby releasing the destructive power of hydrolases into the cytoplasm, this concept was rapidly retired, because it was not possible to assign lethal causality to these compounds based on LMP as opposed to postmortal lysosomal destruction (Miller et al., 1983).

In the interim, the field of cathepsin protease biology developed. Cathepsins represent a class of cysteine, serine, and aspartate proteases that segregate into lysosomes and, under homeostatic conditions, serve to reutilize polypeptides for ongoing cellular metabolic requirements. Lysosomes contain more than 50 cathepsins, and, as a class, they have been associated with various human pathologies, including cancer. Numerous cathepsins and other lysosomal enzymes, e.g., heparanase, have been strongly associated with cancer cell proliferation, angiogenesis, and metastasis (Kallunki et al., 2013). Evidence indicates that, upon secretion, these tumor-promoting lysosomal enzymes act extracellularly. To accommodate this burgeoning need, tumor cells in general display enlargement

suppression could shed light on new anticancer strategies that inhibit the activation of wild-type Ras by restoring expression of the corresponding RasGAP.

Intriguingly, despite the fact that each of the RasGAP members harbors a conserved RasGAP domain, not all exhibit tumor suppressor functions (Min et al., 2010). Accordingly, the existence of non-Ras-associated functions of RasGAPs has been proposed and further demonstrated in the case of DAB2IP (Min et al., 2010), which acts as a signaling scaffold that coordinately regulates Ras and NF-kB activation to promote tumor growth and metastasis (Figure 1C), respectively. Whether other conserved domain(s) besides the RasGAP domain of RASAL2 also exert a Ras-independent tumor-suppressive signaling cascade remains to be investigated. Additionally, how the RasGAPs coordinate with each other to regulate the activation of Ras in different human cancers is not clear. Epigenetic suppression of DAB2IP (Dote et al., 2004) and the mutation of NF1 (The Cancer Genome Atlas Database) are also observed in breast cancers, raising the question of whether the deregulation events of RasGAPs are mutually exclusive or whether they coexist for sufficient addiction to wild-type Ras activation in breast cancer.

REFERENCES

Bos, J.L., Rehmann, H., and Wittinghofer, A. (2007). Cell *129*, 865–877.

Dote, H., Toyooka, S., Tsukuda, K., Yano, M., Ouchida, M., Doihara, H., Suzuki, M., Chen, H., Hsieh, J.T., Gazdar, A.F., and Shimizu, N. (2004). Clin. Cancer Res. *10*, 2082–2089.

Holm, K., Hegardt, C., Staaf, J., Vallon-Christersson, J., Jönsson, G., Olsson, H., Borg, A., and Ringnér, M. (2010). Breast Cancer Res. *12*, R36.

Karnoub, A.E., and Weinberg, R.A. (2008). Nat. Rev. Mol. Cell Biol. *9*, 517–531.

McGillicuddy, L.T., Fromm, J.A., Hollstein, P.E., Kubek, S., Beroukhim, R., De Raedt, T., Johnson, B.W., Williams, S.M., Nghiemphu, P., Liau, L.M., et al. (2009). Cancer Cell *16*, 44–54.

McLaughlin, S.K., Olsen, N.O., Dake, B., De Raedt, T., Lim, E., Bronson, R.T., Beroukhim, R., Polyak, K., Brown, M., Kuperwasser, C., and Cichowski, K. (2013). Cancer Cell *24*, this issue, 365–378.

Min, J., Zaslavsky, A., Fedele, G., McLaughlin, S.K., Reczek, E.E., De Raedt, T., Guney, I., Strochlic, D.E., Macconaill, L.E., Beroukhim, R., et al. (2010). Nat. Med. *16*, 286–294.

Pylayeva-Gupta, Y., Grabocka, E., and Bar-Sagi, D. (2011). Nat. Rev. Cancer *11*, 761–774.

Tcherkezian, J., and Lamarche-Vane, N. (2007). Biol. Cell *99*, 67–86.

Vigil, D., Cherfils, J., Rossman, K.L., and Der, C.J. (2010). Nat. Rev. Cancer *10*, 842–857.

von Lintig, F.C., Dreilinger, A.D., Varki, N.M., Wallace, A.M., Casteel, D.E., and Boss, G.R. (2000). Breast Cancer Res. Treat. *62*, 51–62.

It Takes a CAD to Kill a Tumor Cell with a LMP

Erich Gulbins[1] and Richard N. Kolesnick[2,*]
[1]Department of Molecular Biology, University of Duisburg-Essen, Hufelandstrasse 55, 45122 Essen, Germany
[2]Laboratory of Signal Transduction, Memorial Sloan-Kettering Cancer Center, 415 East 68th Street, New York, NY 10065, USA
*Correspondence: r-kolesnick@ski.mskcc.org
http://dx.doi.org/10.1016/j.ccr.2013.08.025

Cancer cells display lysosome hypertrophy, secreting lysosomal hydrolases for tumor progression. Hypertrophy renders lysosomes fragile, increasing lysosomal membrane permeabilization (LMP) tendency. In this issue of *Cancer Cell*, Petersen and colleagues show that lysosomal sphingomyelin content determines LMP and cationic drugs displace acid sphingomyelinase from lysosomal membranes, increasing tumor LMP and death.

Early on after the discovery of lysosomes by Christian de Duve as a separate compartment that confines highly destructive hydrolases for the demolition and reutilization of cellular substituents, the concept that these structures might alternatively represent "suicide bags" was proposed (de Duve, 1983). This led to an intense search for lysosomatrophic agents that might access this biology for therapeutic purpose. Although a set of lysosomal detergents with long hydrophobic tails and medium pK were defined as capable of inducing lysosomal membrane permeabilization (LMP) and thereby releasing the destructive power of hydrolases into the cytoplasm, this concept was rapidly retired, because it was not possible to assign lethal causality to these compounds based on LMP as opposed to postmortal lysosomal destruction (Miller et al., 1983).

In the interim, the field of cathepsin protease biology developed. Cathepsins represent a class of cysteine, serine, and aspartate proteases that segregate into lysosomes and, under homeostatic conditions, serve to reutilize polypeptides for ongoing cellular metabolic requirements. Lysosomes contain more than 50 cathepsins, and, as a class, they have been associated with various human pathologies, including cancer. Numerous cathepsins and other lysosomal enzymes, e.g., heparanase, have been strongly associated with cancer cell proliferation, angiogenesis, and metastasis (Kallunki et al., 2013). Evidence indicates that, upon secretion, these tumor-promoting lysosomal enzymes act extracellularly. To accommodate this burgeoning need, tumor cells in general display enlargement

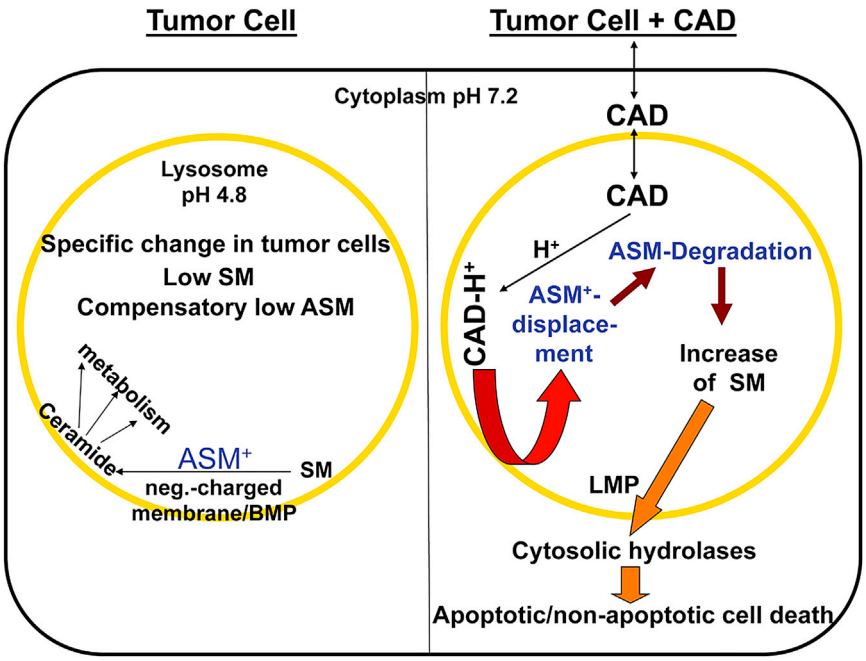

Figure 1. Mechanism of CAD Effect on LMP

Left: tumor cell lysosomes contain lower SM levels than normal cell lysosomes and a compensatory lower ASM activity.

Right: CADs functionally inhibit ASM by physico-chemical mechanisms. CADs are weak bases with a cationic center and a lipophilic portion. The unprotonated form of the drug crosses membranes. Within the highly acidic lysosomal compartment, the cationic part of the drug is protonated, trapped, and concentrated. The lipophilic part of CADs folds into the lysosomal membrane, while the protonated part of the molecule displaces positively-charged ASM from the negatively-charged inner lysosomal membrane surface, resulting in proteolytic degradation of ASM within the lysosomal lumen (Hurwitz et al., 1994). In ASM-reduced tumor cells, further reduction in ASM by CADs increases lysosomal SM concentration, which destabilizes the already fragile tumor cell lysosomal membrane, contributing to LMP and cell death. Normal cells do not undergo CAD-induced LMP. ASM also localizes to secretory lysosomes, the cell surface, and is secreted (Henry et al., 2013). Surface forms of ASM are often pro-apoptotic for various anticancer treatments. Surface ASM resides in acidic plasma membrane subdomains and is inhibited by CADs. Thus, use of CADs to antagonize lysosomal ASM will have to assess the potential negative impact of this class of drugs on this therapeutic biology.

of the lysosomal compartment. Mounting evidence for a role of lysosomal constituents in tumor progression has spawned numerous preclinical and clinical efforts to abort lysosomal enzyme action (Kallunki et al., 2013).

More recently, the focus has been on the notion that this expanded lysosomal compartment might represent a tumor vulnerability (Kallunki et al., 2013). Substantive data indicate that tumor cell lysosomes are more fragile than normal lysosomes, i.e., they are more susceptible to LMP, leading to tumor demise by apoptotic and nonapoptotic death mechanisms. This lysosome fragility is posited (at least in part) to result from the extra burden of destructive enzymes contained within tumor cell lysosomes. Petersen et al. (2013; in this issue of *Cancer Cell*) have been major proponents of this latter concept over the past decade. Work by Petersen et al. (2013) and Kirkegaard et al. (2010; in a recent publication in *Nature*), have made the novel observation that the sphingomyelin (SM) content of lysosomal membranes regulates membrane fragility and thus tendency toward LMP. Initial studies focused on the mechanism for the lysosome protective effect of HSP70. Kirkegaard et al. (2010) first tracked the trafficking of recombinant fluorescent HSP70 into lysosomal membranes. They determined that HSP70 bound preferentially to the endolysosomal membrane-specific anionic lipid, bis(monoacylglycer)phosphate (BMP). Because Konrad Sandhoff had previously shown that BMP binds acid sphingomyelinase (ASM) with high affinity (Linke et al., 2001), thereby stimulating the enzymatic hydrolysis of SM to ceramide, Petersen et al. (2013) made the conceptual leap that SM metabolism might regulate LMP. In a tour de force set of investigations, they showed that HSP70 binding to BMP stabilized the BMP-ASMase interaction, thereby lowering lysosomal membrane SM levels, which reduced membrane fragility (Kirkegaard et al., 2010). An argument was thereafter made that HSP70 might be used therapeutically to stabilize point-mutated ASM in Niemann-Pick disease, an inherited disorder characterized by SM accumulation in lysosomes, lysosomal fragility, and either a progressive neurodegenerative course (type A) or progressive visceral organ abnormalities (type B).

With these observations in hand and the emerging data suggesting that cancer cells manifest lysosomal traits analogous to those of NPD patients, Petersen et al. (2013) began to explore the potential of attacking tumor cells by engaging SM metabolism. This group had been investigating the capability of the cationic drug (CAD) siramesine to induce LMP and cell death of tumor cells (Ostenfeld et al., 2005) and applied the lessons learned from HSP70 lysosomal biology to tumors (Figure 1). Using vector- and *c-src*^{Y527F}-transduced NIH 3T3 murine embryonic fibroblasts (MEFs), evidence was provided that the hypersensitivity of the *c-src*-transduced MEFs to siramesine was distinct from that of sphingosine and Leu-LeuOMe, lysosomotropic detergents that also induce LMP, and was not due to neutralization of lysosomal pH per se. Rather, it appeared that siramesine acted like some other CADs that had been recently shown to displace ASM from the inner lysosomal membrane, resulting in hydrolytic cleavage of ASM. In fact, siramesine treatment leads to decreased ASM activity and increased SM content in *c-src*-transduced, but not vector-transduced, NIH 3T3 MEFs, rendering these SM-replete lysosomes susceptible to LMP and cell death. This susceptibility to siramesine appeared generic to tumor cells as compared to detransformed variants or isogenic normal cell lines. In a large set of in vitro and in vivo models, CADs, as a class, reproducibly antagonized tumor formation, growth, and/or metastases.

From these data, it might have been predicted that tumor cells would ubiquitously display low levels of lysosomal

ASM accompanied by high levels of lysosomal SM, thereby rendering their lysosomal membranes exceptionally fragile. Counterintuitively, studies in cell culture and published data indicated that diverse tumors actually display reduced SM content. Sequencing three pairs of vector- and *c-src*-transduced NIH 3T3 MEFs revealed the reduction of both ASM and neutral sphingomyelinase (NSM). Consistent with this observation, a search of public microarray databases revealed that human tumor tissues generically display reduced ASM and NSM. The authors conclude from these data that the primary event must be reduction in SM levels by an unknown mechanism, followed by secondary reduction in sphingomyelinases. It was proposed that this generic SM reduction compensated for the fragility of the expanded tumor lysosomal compartment chronically exposed to excess destructive hydrolases. This speculation must eventually be addressed experimentally. As a consequence of this unique biology, Petersen et al. (2013) hypothesized that the low levels of lysosomal ASM might render tumor cells particularly sensitive to stoichiometric inactivation by CADs and subsequent LMP-induced tumor cell death.

Studies using cells with multi-drug resistance (MDR) due to ABCB1 overexpression support the hypothesis that targeting lysosomal SM levels might represent a novel therapeutic strategy. Published data showed MDR improved by CADs, and, in 1995, Levade noted that this correlated with ASM inhibition (Jaffrézou et al., 1995). Because ABCB1 is a physiologic transporter of sphingolipids, it was not entirely surprising that MDR variants of the PC3 and DU145 prostate cancer lines displayed higher ASM levels and activity than the parental lines. What is exciting about the current publication is the observation that, in addition to siramesine antagonizing MDR, siRNA to *SMPD1*, the ASM gene, was as effective as siRNA to *ABCB1* in reverting the MDR phenotype.

The question of how to approach these new concepts clinically remains. Because CADs are well represented in the pharmacologic armamentarium, with millions of patients being prescribed tricyclic antidepressant, calcium channel blocker, and antihistamine CADs, it seems unlikely that a potent antitumor effect would have gone unnoticed. Perhaps a retrospective analysis will be revealing. Alternatively, perhaps the range of doses required for the diverse clinical applications of these drugs are insufficient for LMP, which would represent a toxicity of this drug class. Thus, it may be important to select CADs with potent LMP-inducing capabilities to take forward into the clinic. Ultimately, CAD drug scheduling, dosing, and combination with chemotherapeutics will have to be addressed if these concepts of SM-based LMP therapy are to be effectively tested clinically.

REFERENCES

de Duve, C. (1983). Eur. J. Biochem. *137*, 391–397.

Henry, B., Ziobro, R., Becker, K.A., Kolesnick, R., and Gulbins, E. (2013). Handb Exp Pharmacol. *215*, 77–88.

Hurwitz, R., Ferlinz, K., and Sandhoff, K. (1994). Biol. Chem. Hoppe Seyler *375*, 447–450.

Jaffrézou, J.P., Chen, G., Durán, G.E., Muller, C., Bordier, C., Laurent, G., Sikic, B.I., and Levade, T. (1995). Biochim. Biophys. Acta *1266*, 1–8.

Kallunki, T., Olsen, O.D., and Jäättelä, M. (2013). Oncogene *32*, 1995–2004.

Kirkegaard, T., Roth, A.G., Petersen, N.H., Mahalka, A.K., Olsen, O.D., Moilanen, I., Zylicz, A., Knudsen, J., Sandhoff, K., Arenz, C., et al. (2010). Nature *463*, 549–553.

Linke, T., Wilkening, G., Lansmann, S., Moczall, H., Bartelsen, O., Weisgerber, J., and Sandhoff, K. (2001). Biol. Chem. *382*, 283–290.

Miller, D.K., Griffiths, E., Lenard, J., and Firestone, R.A. (1983). J. Cell Biol. *97*, 1841–1851.

Ostenfeld, M.S., Fehrenbacher, N., Høyer-Hansen, M., Thomsen, C., Farkas, T., and Jäättelä, M. (2005). Cancer Res. *65*, 8975–8983.

Petersen, N.H.T., Olsen, O.D., Groth-Pedersen, L., Ellegard, A.-M., Bilgin, M., Redmer, S., Ostenfeld, M.S., Ulanet, D., Dovmark, T.H., Lønborg, A., et al. (2013). Cancer Cell *24*, this issue, 379–393.

Cancer Cell
Previews

A Bach2 Link between Pre-B Cell Receptor Checkpoint and Pre-B Cell ALL

B. Hilda Ye[1,*] and Yun Mai[1]
[1]Department of Cell Biology, Albert Einstein College of Medicine, Bronx, NY 10461, USA
*Correspondence: hilda.ye@einstein.yu.edu
http://dx.doi.org/10.1016/j.ccr.2013.08.017

Bach2 is a transcription factor required for affinity maturation of B cells. A recent study reveals, quite unexpectedly, that Bach2 also plays a key role in the pre-B cell receptor checkpoint and functions as a tumor suppressor in pre-B cell acute lymphocytic leukemia.

From lineage specification to the ultimate production of plasma cells, the B cell development program is not only marked by distinct phases of Ig rearrangement and diversification, but cell fate decisions are also often closely coordinated with the functional status of the surface B cell receptor (BCR). It is now generally accepted that B cell development is programmed with a series of checkpoints that control the initiation of key downstream events. The first major checkpoint, the pre-B cell receptor (pre-BCR) checkpoint, governs the transition from the pre-BI (completion of V_H-DJ_H rearrangement) to the pre-BII stage (onset of immunoglobulin [Ig] light chain rearrangement) (Herzog and Jumaa, 2012). Structurally resembling a mature BCR, the pre-BCR signaling complex is formed between a productively rearranged Ig heavy chain (IgH), the invariant, surrogate light chain, and two accessory signaling molecules, Igα and Igβ. Because V_H-DJ_H joining carries a great risk of disrupting the V segment open reading frame, the pre-BCR checkpoint is believed to function as a quality control step to monitor the structural integrity of the newly synthesized IgH chain on a pre-BI cell. Consequently, cells expressing nonfunctional pre-BCRs are either eliminated (negative selection) or allowed to rearrange the second IgH allele if still available. Cells equipped with a signaling competent pre-BCR are allowed to expand and proceed to the pre-BII stage, where Ig light chain rearrangement is initiated (positive selection).

Despite its importance in B cell development, regulation of the pre-BCR checkpoint remains incompletely understood. First, the transcription factor network operating at this checkpoint has yet to be defined. Second, it is not clear how signals from the pre-BCR are integrated into the cell fate decision in a manner that enables negative selection prior to positive selection. In a recent *Nature Medicine* article, Swaminathan et al. (2013) made exciting discoveries that shed light on both fronts. In searching for novel regulators of the pre-BCR checkpoint, the investigators honed in on Bach2 after analyzing relevant gene expression changes in both humans and mice.

Bach2 is a transcription factor previously implicated in Ig class switch recombination and efficient germinal center formation in mature B cells (Muto et al., 2004). Two attractive features about Bach2 were noted. Bach2 was significantly upregulated by Pax5 at the onset of V_H-DJ_H rearrangement. In addition, the dramatic cell death that results from Pax5-triggered V_H-DJ_H joining and subsequent negative section was greatly diminished in *Bach2*$^{-/-}$ pro-B/pre-BI cells. This was accompanied by reduced expression of p53 and Arf. Subsequent chromatin immuneprecipitation (ChIP) and gene expression analysis revealed that both *Cdkn2a* (which encodes Arf) and *Tp53* loci are under reciprocal regulation by Bach2 and Bcl6, a transcriptional repressor previously shown by the same group to facilitate positive selection by suppressing *Tp53* (Duy et al., 2011). The fact that additional genes involved in checkpoint function were also regulated by Bach2 and Bcl6 in opposite directions adds further support to the notion that the interplay between Bach2 and Bcl6 coordinates the orderly transition from negative to positive selection.

Two types of experiments provided the most definitive proof for a Bach2 requirement in negative selection. First, in a pre-B differentiation system based on tyrosine kinase inhibition (TKI) of BCR-ABL-transformed pre-B cells, Bach2 deficiency reduced the V(D)J rearrangement efficiency by ~20-fold, a defect concurrent with a similar reduction in the mRNA of *Rag1/2*. The notion that Bach2 can directly regulate *Rag1/2* transcription is supported by several assays including a Bach2 ChIP of the *Rag1* and *Rag2* promoters. The second set of experiments, which included an elegant test of V_H-DJ_H junction length distribution, showed that >50% of the *Bach2*$^{-/-}$ precursor B cells contain nonfunctional V_H-DJ_H joining, compared to only ~10% in wild-type controls. Most importantly, reexpression of Bach2 eliminated nonfunctional IgH rearrangements almost completely. Collectively, the results presented by Swaminathan et al. (2013) have clearly established Bach2 as a key regulator in the pre-BCR checkpoint. Mechanistically, these data are consistent with a model where Bach2, operating downstream of Pax5, promotes V_H-DJ_H rearrangement by sustaining Rag1/2 expression on the one hand, and, on the other hand, purges cells carrying nonfunctional IgH rearrangements through p53-dependent cell death (Figure 1A).

The second major and novel conclusion from this study carries significant clinical implications. Swaminathan et al. (2013) proposed that BACH2 is a novel tumor suppressor in pre-B cell acute lymphocytic leukemia (pre-B ALL), a notion that enforces the general concept that pre-B cell checkpoint regulators often also play roles in pre-B ALLs. PAX5, BCL6, and another pre-B cell checkpoint regulator, SLP-65, have all been previously implicated in pre-B ALLs (Duy et al., 2011;

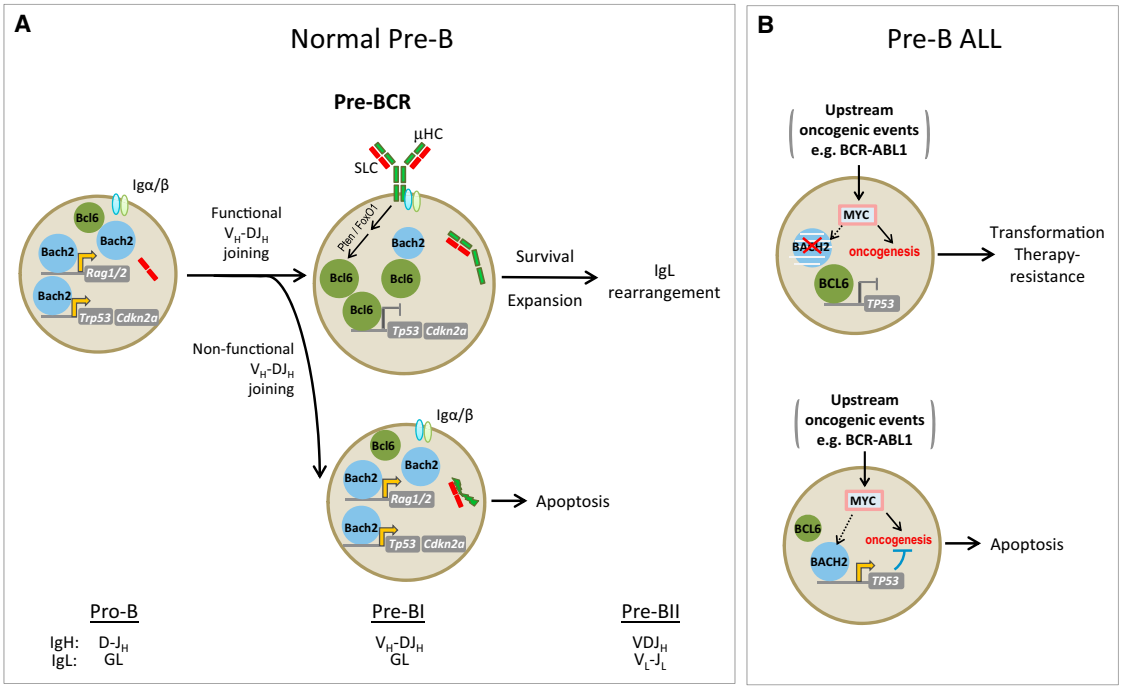

Figure 1. Model Illustrating the Cell Fate Outcome Influenced by the Interplay between Bach2 and Bcl6 at the Pre-Bcr Checkpoint and in Pre-B All

(A) In pre-BI cells, the absence of a functional pre-BCR leaves Bach2 expression at a relatively high level, which eventually triggers p53-dependent apoptosis when V_H-DJ_H joining has failed on both IgH alleles. This is the proposed mechanism for purging nonfunctional IgH rearrangement from the pre-B cell pool (bottom). During positive selection, signals transduced from a signaling competent pre-BCR lead to a shift in the Bach2-Bcl6 balance and the subsequent suppression of *Cdkn2a*/*Tp53* by Bcl6, which is a prerequisite condition for cell survival, expansion, and onset of the Ig light chain rearrangement at the pre-BII stage (top).

(B) In progenitor B cells, BACH2 expression favors p53 activation, which then imposes a barrier against transformation by aberrantly activated oncogenes (bottom). In cells where BACH2 expression or activity is reduced by either genetic or epigenetic changes, BCL6 overrides BACH2 influence and suppresses p53. This shift in the BACH2-BCL6 balance thus impairs the anti-cancer barrier, leading to de novo transformation of pre-B cells or acquisition of therapy resistance in established pre-B ALLs (top). Dashed arrows indicate it is currently unclear how aberrantly activated oncogenes might activate the BACH2-p53-apoptosis axis.

Herzog et al., 2006; Mullighan et al., 2007). The tumor suppressor function of BACH2 is supported by a large volume of results from cell culture-based experiments and genetic analysis of mouse and human pre-B ALLs, as well as clinical response data of pediatric B-ALL patients (Swaminathan et al., 2013). The most striking experiment among many is a Myc transformation assay performed in a bone marrow transplantation setting, a test well-known to evoke the ARF/p53-enforced tumor suppressive barrier (Lowe et al., 2004). Consistent with the ability of Bach2 to antagonize Myc-induced transformation, Myc-transduced *Bach2*$^{-/-}$ pre-B cells gave rise to lethal leukemia within 3 weeks, while recipients of Myc-transduced, Bach2-proficient cells remained leukemia-free for up to 10 weeks.

Clinical data from pediatric ALL patients demonstrated the ability of BACH2 expression to predict survival outcome (Swaminathan et al., 2013). Specifically, at the time of diagnosis, loss of BACH2 expression strongly correlated with predicted minimal residual disease and lower relapse-free survival. Comparing matched sample pairs collected at initial diagnosis and subsequent relapse, the authors found loss of BACH2 expression to be a common feature of disease relapse. How could BACH2 expression or function be lost during pre-B ALL development? The authors presented four possible scenarios, each supported by evidence from primary human ALL samples. These include a hot spot mutation in the BTB domain of BACH2 (found in five of ten Ph$^+$ ALL cases), promoter hypermethylation, PAX5 inactivation, and deletion of 6q15, where the human *BACH2* gene resides. Of note, in three out of four 6q15 deletion cases examined, the deletion was an acquired event at relapse. Combined with a general reduction of *BACH2* mRNA in all relapsed cases, this observation raises the distinct possibility that leukemia subclones with low BACH2 were more resistant than subclones with higher BACH2 expression to standard ALL treatment. This notion is in line with the differential toxicity of TKI in BCR-ABL-transformed wild-type and *Bach2*$^{-/-}$ pre-B cells. Because BACH2 and BCL6 play opposing roles in p53 regulation, checkpoint control, and patient outcome (Figure 1B), the authors propose to pharmacologically inhibit BCL6 using the BCL6 peptide inhibitor RI-BPI (Duy et al., 2011; Polo et al., 2004) in order to restore p53 expression and hence therapeutic response.

The study by Swaminathan et al. (2013) raises a number of tantalizing questions. Is the positive role of Bach2 on p53

expression exerted directly at the level of p53 transcription? Because Bach2 and Bcl6 recognize distinct DNA binding sequences, what is the mechanism underlying their competitive binding behavior in shared target promoters? In addition, at least under certain circumstances, Bach2 can shuttle between the cytoplasm and nucleus in a redox sensitive fashion (Chen et al., 2013; Muto et al., 2002). Therefore, is Bach2 subcellular localization modulated during the pre-BCR checkpoint? Since Bach2 has emerged as a key regulator of the pre-BCR checkpoint, these issues merit future studies.

REFERENCES

Chen, Z., Pittman, E.F., Romaguera, J., Fayad, L., Wang, M., Neelapu, S.S., McLaughlin, P., Kwak, L., and McCarty, N. (2013). PLoS ONE *8*, e69126.

Duy, C., Hurtz, C., Shojaee, S., Cerchietti, L., Geng, H., Swaminathan, S., Klemm, L., Kweon, S.M., Nahar, R., Braig, M., et al. (2011). Nature *473*, 384–388.

Herzog, S., and Jumaa, H. (2012). Curr. Opin. Immunol. *24*, 166–172.

Herzog, S., Storch, B., and Jumaa, H. (2006). Immunol. Res. *34*, 143–155.

Lowe, S.W., Cepero, E., and Evan, G. (2004). Nature *432*, 307–315.

Mullighan, C.G., Goorha, S., Radtke, I., Miller, C.B., Coustan-Smith, E., Dalton, J.D., Girtman, K., Mathew, S., Ma, J., Pounds, S.B., et al. (2007). Nature *446*, 758–764.

Muto, A., Tashiro, S., Tsuchiya, H., Kume, A., Kanno, M., Ito, E., Yamamoto, M., and Igarashi, K. (2002). J. Biol. Chem. *277*, 20724–20733.

Muto, A., Tashiro, S., Nakajima, O., Hoshino, H., Takahashi, S., Sakoda, E., Ikebe, D., Yamamoto, M., and Igarashi, K. (2004). Nature *429*, 566–571.

Polo, J.M., Dell'Oso, T., Ranuncolo, S.M., Cerchietti, L., Beck, D., Da Silva, G.F., Prive, G.G., Licht, J.D., and Melnick, A. (2004). Nat. Med. *10*, 1329–1335.

Swaminathan, S., Huang, C., Geng, H., Chen, Z., Harvey, R., Kang, H., Ng, C., Titz, B., Hurtz, C., Sadiyah, M.F., et al. (2013). Nat. Med. *19*, 1014–1022.

Mechanisms of Targeted Therapy Resistance Take a De-TOR

Leanna R. Gentry,[1] Timothy D. Martin,[1] and Channing J. Der[1,2,*]
[1]Department of Pharmacology
[2]Lineberger Comprehensive Cancer Center
University of North Carolina at Chapel Hill, Chapel Hill, NC 27599, USA
*Correspondence: cjder@med.unc.edu
http://dx.doi.org/10.1016/j.ccr.2013.08.021

The effectiveness of cancer therapeutics targeting signal transduction pathways is comprised of a diversity of mechanisms that drive de novo or acquired resistance. Two recent studies identify mTOR activation as a point of convergence of mechanisms that cause resistance to inhibitors of the Raf-MEK-ERK and PI3K signaling.

A critical turning point in the fight against advanced and metastatic melanomas occurred just over a decade ago with the discovery and characterization of the *BRAF* activating mutation V600E in about 60% of melanomas (Davies et al., 2002). This mutation causes constitutive activation of the B-Raf serine/threonine kinase, resulting in aberrant and persistent activation of the Raf-MEK-ERK mitogen-activated protein kinase cascade. Importantly, *BRAF* V600E correlated with poor prognosis in patients with metastatic melanoma. This prompted the development and clinical evaluation of Raf and MEK inhibitors for the treatment of *BRAF* mutant metastatic melanoma (Salama and Flaherty, 2013). The dramatic antitumor activities of these inhibitors led to Food and Drug Administration approval of two Raf (vemurafenib and dabrafenib) and one MEK (trametinib) inhibitor for the treatment of *BRAF* mutant melanoma (Chapman et al., 2011; Flaherty et al., 2012; Hauschild et al., 2012). Despite the clinical success of these inhibitors, resistance has limited their long-term clinical impact. Although patient selection based on *BRAF* mutation status defines the patient population that would benefit from Raf or MEK inhibition, 20%–50% of patients showed no initial response, suggesting de novo resistance in a significant subset of melanoma patients (Chapman et al., 2011; Hauschild et al., 2012). Furthermore, even for patients who do respond initially, within three months, essentially all suffer from relapsed tumors that have acquired drug resistance. This has led to numerous studies that have identified multiple mechanisms of de novo and/or acquired resistance to Raf, inhibition with mechanisms that cause ERK reactivation downstream of the inhibitor block, as well as ERK-independent mechanisms (Sullivan and Flaherty, 2013).

Corcoran et al. (2013) have recently identified a mechanism that may provide a more unifying model for the diverse mechanisms already identified. Although decreased phosphorylation of ERK (pERK) has thus far been the standard used to gauge tumor sensitivity in both clinical and preclinical studies, Corcoran et al. (2013) found that robust inhibition of pERK was still observed in melanoma

expression exerted directly at the level of p53 transcription? Because Bach2 and Bcl6 recognize distinct DNA binding sequences, what is the mechanism underlying their competitive binding behavior in shared target promoters? In addition, at least under certain circumstances, Bach2 can shuttle between the cytoplasm and nucleus in a redox sensitive fashion (Chen et al., 2013; Muto et al., 2002). Therefore, is Bach2 subcellular localization modulated during the pre-BCR checkpoint? Since Bach2 has emerged as a key regulator of the pre-BCR checkpoint, these issues merit future studies.

REFERENCES

Chen, Z., Pittman, E.F., Romaguera, J., Fayad, L., Wang, M., Neelapu, S.S., McLaughlin, P., Kwak, L., and McCarty, N. (2013). PLoS ONE *8*, e69126.

Duy, C., Hurtz, C., Shojaee, S., Cerchietti, L., Geng, H., Swaminathan, S., Klemm, L., Kweon, S.M., Nahar, R., Braig, M., et al. (2011). Nature *473*, 384–388.

Herzog, S., and Jumaa, H. (2012). Curr. Opin. Immunol. *24*, 166–172.

Herzog, S., Storch, B., and Jumaa, H. (2006). Immunol. Res. *34*, 143–155.

Lowe, S.W., Cepero, E., and Evan, G. (2004). Nature *432*, 307–315.

Mullighan, C.G., Goorha, S., Radtke, I., Miller, C.B., Coustan-Smith, E., Dalton, J.D., Girtman, K., Mathew, S., Ma, J., Pounds, S.B., et al. (2007). Nature *446*, 758–764.

Muto, A., Tashiro, S., Tsuchiya, H., Kume, A., Kanno, M., Ito, E., Yamamoto, M., and Igarashi, K. (2002). J. Biol. Chem. *277*, 20724–20733.

Muto, A., Tashiro, S., Nakajima, O., Hoshino, H., Takahashi, S., Sakoda, E., Ikebe, D., Yamamoto, M., and Igarashi, K. (2004). Nature *429*, 566–571.

Polo, J.M., Dell'Oso, T., Ranuncolo, S.M., Cerchietti, L., Beck, D., Da Silva, G.F., Prive, G.G., Licht, J.D., and Melnick, A. (2004). Nat. Med. *10*, 1329–1335.

Swaminathan, S., Huang, C., Geng, H., Chen, Z., Harvey, R., Kang, H., Ng, C., Titz, B., Hurtz, C., Sadiyah, M.F., et al. (2013). Nat. Med. *19*, 1014–1022.

Mechanisms of Targeted Therapy Resistance Take a De-TOR

Leanna R. Gentry,[1] Timothy D. Martin,[1] and Channing J. Der[1,2,*]
[1]Department of Pharmacology
[2]Lineberger Comprehensive Cancer Center
University of North Carolina at Chapel Hill, Chapel Hill, NC 27599, USA
*Correspondence: cjder@med.unc.edu
http://dx.doi.org/10.1016/j.ccr.2013.08.021

The effectiveness of cancer therapeutics targeting signal transduction pathways is comprised of a diversity of mechanisms that drive de novo or acquired resistance. Two recent studies identify mTOR activation as a point of convergence of mechanisms that cause resistance to inhibitors of the Raf-MEK-ERK and PI3K signaling.

A critical turning point in the fight against advanced and metastatic melanomas occurred just over a decade ago with the discovery and characterization of the *BRAF* activating mutation V600E in about 60% of melanomas (Davies et al., 2002). This mutation causes constitutive activation of the B-Raf serine/threonine kinase, resulting in aberrant and persistent activation of the Raf-MEK-ERK mitogen-activated protein kinase cascade. Importantly, *BRAF* V600E correlated with poor prognosis in patients with metastatic melanoma. This prompted the development and clinical evaluation of Raf and MEK inhibitors for the treatment of *BRAF* mutant metastatic melanoma (Salama and Flaherty, 2013). The dramatic antitumor activities of these inhibitors led to Food and Drug Administration approval of two Raf (vemurafenib and dabrafenib) and one MEK (trametinib) inhibitor for the treatment of *BRAF* mutant melanoma (Chapman et al., 2011; Flaherty et al., 2012; Hauschild et al., 2012). Despite the clinical success of these inhibitors, resistance has limited their long-term clinical impact. Although patient selection based on *BRAF* mutation status defines the patient population that would benefit from Raf or MEK inhibition, 20%–50% of patients showed no initial response, suggesting de novo resistance in a significant subset of melanoma patients (Chapman et al., 2011; Hauschild et al., 2012). Furthermore, even for patients who do respond initially, within three months, essentially all suffer from relapsed tumors that have acquired drug resistance. This has led to numerous studies that have identified multiple mechanisms of de novo and/or acquired resistance to Raf, inhibition with mechanisms that cause ERK reactivation downstream of the inhibitor block, as well as ERK-independent mechanisms (Sullivan and Flaherty, 2013).

Corcoran et al. (2013) have recently identified a mechanism that may provide a more unifying model for the diverse mechanisms already identified. Although decreased phosphorylation of ERK (pERK) has thus far been the standard used to gauge tumor sensitivity in both clinical and preclinical studies, Corcoran et al. (2013) found that robust inhibition of pERK was still observed in melanoma

cell lines resistant to Raf or MEK inhibitors, assayed by measuring growth inhibition and apoptosis induction. Instead, Corcoran et al. (2013) made the intriguing discovery that levels of ribosomal protein S6 (pS6) phosphorylation, a key component downstream of mTORC1, can be used as a marker of ERK-independent resistance to Raf and MEK inhibitor treatment (Figure 1). Analysis of melanoma cell lines with different sensitivities to vemurafenib indicated that while the common biomarkers pERK and pAKT responded similarly, pS6 decreased in sensitive lines but was sustained in insensitive lines even upon increasing doses of vemurafenib. To determine if MEK inhibition also required downregulation of pS6 for sensitivity, cells were treated with the MEK1/2 inhibitor selumetinib in the presence of activated mTOR, achieved by knockdown of Tsc2, a major negative regulator of mTORC1. This resulted in fewer apoptotic cells, signifying that mTOR activity protected cells against apoptosis induced by MEK inhibition. Combination of an mTOR catalytic inhibitor with vemurafenib increased cell death, further suggesting that a combinatorial approach of Raf and mTOR inhibition may prove efficacious in vemurafenib-resistant melanomas. Preclinical modeling using mouse xenografts mirrored the cell line findings, with pERK downregulation seen in both sensitive and insensitive tumors, whereas pS6 downregulation was only observed in sensitive tumors.

The authors then addressed a critical issue of whether these cell culture and mouse model results could be translated to cancer patients. Most intriguingly, fine-needle aspiration (FNA) biopsies from the mouse xenograft tumors demonstrated real-time decreases in pS6 upon treatment. This approach was then advanced to be successfully applied to melanoma patients. In a time-sensitive setting where treatment choices and changes must be made quickly for the health of the patient, using FNAs to assess biomarker status is ideal, because it is minimally invasive and can be performed multiple times. FNAs were then used to probe pS6 and pERK response to vemurafenib in metastatic melanoma patients. This led to the promising result of an almost 5-fold increase in progression-free survival seen in patients with decreased pS6 in their tumors compared to patients whose tumors did not. Although these combined mTOR and Raf inhibition studies have shown efficacy in tumor cells and xenograft models, this approach still must be assessed in human patients. There is a trial currently recruiting for advanced cancers that will assess the combination of vemurafenib with the mTOR inhibitor everolimus. Hopefully the results from this clinical trial will support the data reported by Corcoran et al. (2013), showing improved patient outcome once both Raf and mTORC1 are blocked.

Notably, another study in the same issue of *Science Translational Medicine* by Elkabets et al. (2013) reveals mTOR-mediated resistance to p110α inhibition in *PIK3CA* mutant breast cancers. Preclinical and clinical evaluation indicated that *PIK3CA* mutation status provided an incomplete genetic marker for response to PI3K inhibition (Bendell et al., 2012; Maira et al., 2012). In these breast cancer cells, inhibition of mTOR by everolimus sensitized tumor cells to the p110α-specific inhibitor BYL719. Similar to the results reported by Corcoran et al. (2013), mTORC1 activity and pS6 were identified as important biomarkers to p110α inhibitor response. Interestingly, breast cancer cell lines with acquired resistance to BYL719 were established, and these also displayed enhanced mTORC1 activity compared to their matching control cells, indicating kinome reprogramming to p110α inhibitor treatment. Depletion of mTOR via shRNA from the acquired p110α inhibitor-resistant cells was sufficient to prevent proliferation, and a combination of BYL719 and mTORC1 inhibitor therapy prevented the tumorigenic growth of BYL719 resistant cells in mouse xenografts. Elkabets et al. (2013) also examined breast cancer patient biopsies from an ongoing phase I clinical trial of BYL719 treatment for *PIK3CA* mutant solid tumors. Strikingly, those patients that responded to BYL719 treatment showed a loss of pS6 staining intensity in their tumors as compared to biopsies before treatment began, whereas those patients whose tumors did not respond to BYL719 treatment maintained high levels of pS6 during treatment. Interestingly, biopsies from two patients that initially responded to BYL719 therapy, but later showed tumor progression, displayed a return of pS6 to levels similar to that seen prior to any BYL719 treatment, further implicating mTORC1 activation in the acquired resistance to BYL719/p110α therapy.

In summary, the findings from these two studies support mTOR activation as a key driver of resistance to PI3K inhibition in *PIK3CA* mutant breast cancer and resistance to Raf or MEK inhibition in *BRAF* mutant melanoma. It will be

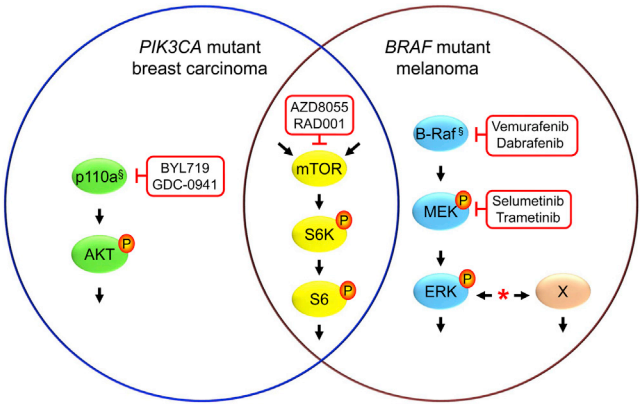

Figure 1. mTOR-Driven Mechanisms of Cancer Cell Resistance to Raf, MEK, and PI3K Inhibitors

A subset of *BRAF* mutant melanomas possesses de novo resistances to Raf or MEK inhibitor therapy, and essentially all cancers that are responsive initially develop acquired resistance. A diversity of mechanisms of resistance has been described (*) that most commonly cause ERK reactivation downstream of the inhibitor block or activation of ERK-independent (X) mechanisms. Similarly, only a subset of *PIK3CA* (encodes p110α) mutant cancers is responsive to p110α isoform selective (BYL719) or pan-class I (GDC-0941) PI3K inhibitors. In *BRAF* mutant ([§]) melanomas or *PIK3CA* ([§]) mutant breast carcinomas, activation of mTOR correlates with inhibitor resistance, and concurrent treatment with an allosteric (RAD001/Everolimus) or catalytic (AZD8055) mTOR inhibitor overcomes resistance. The phosphorylated state of S6, a substrate of mTORC1-activated S6 kinase, provides a marker for resistance and response. mTORC1 activation can be activated downstream of both PI3K and ERK as well as by other mechanisms, possibly providing a point of convergence for multiple mechanisms of resistance.

important to explore whether mTOR activation will act as a resistance mechanism to inhibitors of other signaling components in other cancer types. Additional patient analyses and combination inhibitor clinical trials will be needed to validate the importance of mTORC1 activation as a biomarker to predict patient response and mTOR inhibitor combination treatment to overcome resistance. mTOR is regulated downstream of both Raf and PI3K signaling and consequently may define a key point of convergence of the divergent resistance mechanisms that have been identified. Finally, the signaling mechanisms that cause mTOR activation to drive resistance as well as the downstream consequences of mTOR signaling that promote resistance are issues that remain to be fully elucidated.

REFERENCES

Bendell, J.C., Rodon, J., Burris, H.A., de Jonge, M., Verweij, J., Birle, D., Demanse, D., De Buck, S.S., Ru, Q.C., Peters, M., et al. (2012). J Clin Oncol. *30*, 282–290.

Chapman, P.B., Hauschild, A., Robert, C., Haanen, J.B., Ascierto, P., Larkin, J., Dummer, R., Garbe, C., Testori, A., Maio, M., et al.; BRIM-3 Study Group. (2011). N. Engl. J. Med. *364*, 2507–2516.

Corcoran, R.B., Rothenberg, S.M., Hata, A.N., Faber, A.C., Piris, A., Nazarian, R.M., Brown, R.D., Godfrey, J.T., Winokur, D., Walsh, J., et al. (2013). Sci Transl Med. *5*, 196ra198.

Davies, H., Bignell, G.R., Cox, C., Stephens, P., Edkins, S., Clegg, S., Teague, J., Woffendin, H., Garnett, M.J., Bottomley, W., et al. (2002). Nature *417*, 949–954.

Elkabets, M., Vora, S., Juric, D., Morse, N., Mino-Kenudson, M., Muranen, T., Tao, J., Campos, A.B., Rodon, J., Ibrahim, Y.H., et al. (2013). Sci Transl Med. *5*, 196ra199.

Flaherty, K.T., Robert, C., Hersey, P., Nathan, P., Garbe, C., Milhem, M., Demidov, L.V., Hassel, J.C., Rutkowski, P., Mohr, P., et al.; METRIC Study Group. (2012). N. Engl. J. Med. *367*, 107–114.

Hauschild, A., Grob, J.J., Demidov, L.V., Jouary, T., Gutzmer, R., Millward, M., Rutkowski, P., Blank, C.U., Miller, W.H., Jr., Kaempgen, E., et al. (2012). Lancet *380*, 358–365.

Maira, S.M., Pecchi, S., Huang, A., Burger, M., Knapp, M., Sterker, D., Schnell, C., Guthy, D., Nagel, T., Wiesmann, M., et al. (2012). Mol. Cancer Ther. *11*, 317–328.

Salama, A.K., and Flaherty, K.T. (2013). Clin Cancer Res. *19*, 4326–4334.

Sullivan, R.J., and Flaherty, K.T. (2013). Eur. J. Cancer *49*, 1297–1304.

Comment on "Platelet-Derived Nucleotides Promote Tumor Cell Transendothelial Migration and Metastasis via $P2Y_2$ Receptor" by Schumacher et al.

Matthew T. Harper,[1,*] Joshua S. Savage,[1,2] and Alastair W. Poole[1,*]
[1]School of Physiology and Pharmacology, Bristol Heart Institute, Medical Sciences Building, University of Bristol, Bristol BS8 1TD, UK
[2]Present address: Cancer Research UK Clinical Trials Unit (CRCTU), School of Cancer Sciences, University of Birmingham, Edgbaston, Birmingham B15 2TT, UK
*Correspondence: m.harper@bris.ac.uk (M.T.H.), a.poole@bris.ac.uk (A.W.P.)
http://dx.doi.org/10.1016/j.ccr.2013.08.016

We were very interested to read in *Cancer Cell* the recent paper by Schumacher et al., "Platelet-Derived Nucleotides Promote Tumor Cell Transendothelial Migration and Metastasis via $P2Y_2$ Receptor" (Schumacher et al., 2013). In this paper, the authors show the importance of platelet secretion in promoting tumor metastasis and convincingly demonstrate an important role for ATP from platelet dense granules acting on endothelial $P2Y_2$. Part of the evidence for this depends on Munc13-4-deficient mice (*Unc13d*^{Jinx}), whose platelets cannot secrete their dense granules. However, Schumacher et al. also report that there was no difference in secretion of platelet α-granules or in integrin activation (Figures 2A–2D, S2C, and S2D in Schumacher et al., 2013). These findings are in contrast to published findings from our lab and others (Ren et al., 2010; Savage et al., 2013; Stegner et al., 2013).

Unc13d^{Jinx} platelets show reduced aggregation, integrin $\alpha_{IIb}\beta_3$ activation, and thrombus formation in vitro and in vivo (Ren et al., 2010; Savage et al., 2013). Integrin activation and subsequent platelet aggregation and thrombus formation are dependent on ADP secretion from platelet dense granules and stimulation of platelet $P2Y_{12}$. The aggregation defects we have seen in *Unc13d*^{Jinx} mice are therefore perhaps not surprising since the platelets of these mice cannot secrete their dense granules. Ren et al. also showed that thrombin-stimulated α-granule secretion was reduced by approximately 70% in *Unc13d*^{Jinx} platelets compared to wild-type controls. Stegner et al. (2013) stated that they saw a similar effect, and we also observe substantially reduced α-granule secretion in *Unc13d*^{Jinx} platelets (data not shown). We have also found that platelet α-granule secretion is also partly regulated by autocrine ADP secretion from dense granules, acting through $P2Y_{12}$. This partly accounts for the defect we see in α-granule secretion in *Unc13d*^{Jinx} platelets.

Platelet aggregation has been suggested to promote tumor metastasis, and platelet α-granules may also promote tumor metastasis since they are a source of a wide range of growth factors and cytokines. For example, as reported in another recent *Cancer Cell* paper, platelet-derived TGF-β plays a key role in tumor metastasis (Labelle et al., 2011). We suggest therefore that, in addition to activation of endothelial $P2Y_2$, another way in which platelet-released nucleotides might enhance tumor metastasis is through autocrine activation of platelet $P2Y_{12}$ and enhancement of aggregation and α-granule secretion.

REFERENCES

Labelle, M., Begum, S., and Hynes, R.O. (2011). Cancer Cell *20*, 576–590.

Ren, Q., Wimmer, C., Chicka, M.C., Ye, S., Ren, Y., Hughson, F.M., and Whiteheart, S.W. (2010). Blood *116*, 869–877.

Savage, J.S., Williams, C.M., Konopatskaya, O., Hers, I., Harper, M.T., and Poole, A.W. (2013). J. Thromb. Haemost. *11*, 771–775.

Schumacher, D., Strilic, B., Sivaraj, K.K., Wettschureck, N., and Offermanns, S. (2013). Cancer Cell *24*, 130–137.

Stegner, D., Deppermann, C., Kraft, P., Morowski, M., Kleinschnitz, C., Stoll, G., and Nieswandt, B. (2013). J. Thromb. Haemost. *11*, 1430–1433.

Response to Harper et al.

Dagmar Schumacher,[1] Boris Strilic,[1] Kishor Kumar Sivaraj,[1] Nina Wettschureck,[1,2] and Stefan Offermanns[1,2,*]
[1]Department of Pharmacology, Max Planck Institute for Heart and Lung Research, Ludwigstrasse 43, 61231 Bad Nauheim, Germany
[2]Medical Faculty, Johann Wolfgang Goethe University Frankfurt, Theodor-Stern-Kai 7, 60590 Frankfurt, Germany
*Correspondence: stefan.offermanns@mpi-bn.mpg.de
http://dx.doi.org/10.1016/j.ccr.2013.08.015

We thank Harper et al. for their comments on our publication. The authors of this correspondence point to some differences between our publication (Schumacher et al., 2013) and others with regard to the in vitro phenotype of Munc13-4-deficient platelets. Based on our experimental data, we think that Munc13-4 deficiency primarily blocks the release from dense granules, but not from α-granules of platelets. It is, however, well known that platelet activation involves multiple positive feedback loops and that the release of ATP/ADP from dense granules can promote platelet aggregation and α-granule release via the autocrine and paracrine activation of $P2Y_1$ and $P2Y_{12}$ receptors (Gachet, 2006; Kahner et al., 2006). Based on this concept, it is indeed expected that loss of ATP/ADP release from platelet dense granules also affects, under certain experimental conditions, the release of α-granules from activated platelets, as well as the aggregation of platelets. Whether these secondary effects of a blocked dense-granule release are seen in vitro depends on the experimental conditions used to study platelet function, such as platelet concentration or the concentration and type of applied stimuli. At intermediate thrombin concentrations, we actually saw a tendency of reduced PF4 release and integrin αIIbβ3 activation which, however, was not significant (Figures 2A and S2C in Schumacher et al., 2013). In the experiments mentioned by Harper et al., we used relatively low platelet concentrations, reducing the likelihood that sufficient amounts of ATP/ADP are released to induce secondary effects. Finally, at least in the case of tumor-cell-induced platelet activation, it is also possible that the small amount of ATP released from tumor cells (see Figure 1D in Schumacher et al., 2013) obscured a somewhat reduced α-granule release.

Whether the secondary effects of dense-granule release are of relevance for platelet-dependent tumor cell metastasis is not known. Nevertheless, we agree that solely on the basis of our experiments performed with Munc13-4-deficient platelets and animals, we would not be able to exclude that defects other than reduced dense granule secretion also contribute to the observed defects in transendothelial tumor cell migration and in vivo metastasis. We therefore mentioned in the discussion of this publication the possibility that "in addition to ATP, other platelet-derived factors, such as transforming growth factor β, promote, in particular, later stages of tumor cell extravasation (Labelle et al., 2011)."

However, our study goes beyond the description of the role of dense-granule secretion in platelet-dependent tumor cell transendothelial migration and metastasis. We also identified a downstream mechanism by demonstrating that the endothelial ATP receptor $P2Y_2$ mediates platelet-dependent tumor cell transmigration and that loss of $P2Y_2$, which is not present on platelets, strongly reduces tumor cell metastasis from primary tumors, as well as after intravenous injection of tumor cells. If the above described secondary effects played a major role in platelet dense-granule secretion-dependent tumor cell transendothelial migration and metastasis, we would expect the phenotype of Munc13-4 deficiency to be more severe than the phenotype of $P2Y_2$ deficiency. However, both platelet Munc13-4 deficiency and endothelial knockdown of $P2Y_2$ abolished platelet-dependent transendothelial tumor cell migration. More importantly, tumor cell metastasis in vivo, when studied in bone-marrow chimeras, was reduced both in $P2Y_2$-deficient mice transplanted with wild-type bone-marrow and in $P2Y_2$-deficient mice transplanted with Munc13-4-deficient bone marrow to the same degree, and no additive effect could be seen.

Thus, while we acknowledge that loss of dense-granule secretion in Munc13-4-deficient platelets can lead under certain experimental conditions to a secondary impairment of α-granule release, we think that our data show that dense-granule-derived ATP acting on $P2Y_2$ receptors is the primary mechanism through which blockade of ATP release from Munc13-4-deficient platelets affects tumor cell transendothelial migration and metastasis.

REFERENCES

Gachet, C. (2006). Annu. Rev. Pharmacol. Toxicol. *46*, 277–300.

Kahner, B.N., Shankar, H., Murugappan, S., Prasad, G.L., and Kunapuli, S.P. (2006). J. Thromb. Haemost. *4*, 2317–2326.

Labelle, M., Begum, S., and Hynes, R.O. (2011). Cancer Cell *20*, 576–590.

Schumacher, D., Strilic, B., Sivaraj, K.K., Wettschureck, N., and Offermanns, S. (2013). Cancer Cell *24*, 130–137.

Cancer Cell
Article

Xbp1s-Negative Tumor B Cells and Pre-Plasmablasts Mediate Therapeutic Proteasome Inhibitor Resistance in Multiple Myeloma

Chungyee Leung-Hagesteijn,[1] Natalie Erdmann,[1] Grace Cheung,[1] Jonathan J. Keats,[2] A. Keith Stewart,[3] Donna E. Reece,[1,4] Kim Chan Chung,[1] and Rodger E. Tiedemann[1,4,*]
[1]Princess Margaret Cancer Centre, Toronto, ON M5G 2M9, Canada
[2]Translational Genomics Research Institute, Phoenix, AZ 85004, USA
[3]Division of Hematology-Oncology, Mayo Clinic, Scottsdale, AZ 85259, USA
[4]University of Toronto, Toronto, ON M5S 1A8, Canada
*Correspondence: rodger.tiedemann@uhn.ca
http://dx.doi.org/10.1016/j.ccr.2013.08.009

SUMMARY

Proteasome inhibitor (PI) resistance mechanisms in multiple myeloma (MM) remain controversial. We report the existence of a progenitor organization in primary MM that recapitulates maturation stages between B cells and plasma cells and that contributes to clinical PI resistance. Xbp1s^{-} tumor B cells and pre-plasmablasts survive therapeutic PI, preventing cure, while maturation arrest of MM before the plasmablast stage enables progressive disease on PI treatment. Mechanistically, suppression of Xbp1s in MM is shown to induce bortezomib resistance via de-commitment to plasma cell maturation and immunoglobulin production, diminishing endoplasmic reticulum (ER) front-loading and cytotoxic susceptibility to PI-induced inhibition of ER-associated degradation. These results reveal the tumor progenitor structure in MM and highlight its role in therapeutic failure.

INTRODUCTION

Multiple myeloma (MM) is a late-stage lymphoid malignancy characterized by the accumulation of immunoglobulin (Ig)-secreting plasma cells within the bone marrow. Existing therapies for MM, including the proteasome inhibitors (PIs) bortezomib (BTZ) and carfilzomib, can extend survival but are not curative (Alexanian et al., 2012; Richardson et al., 2005). To understand the failure to cure, drug resistance mechanisms must be characterized. Although the binding target of PIs has been recognized since their inception, the mechanisms of PI cytotoxicity and resistance in MM remain controversial. While some studies have linked PI cytotoxicity to stabilization of tumor suppressors (such as p53), pro-apoptotic proteins (such as Noxa, Bim, and Bik), or inhibitors of anti-apoptotic proteins (such as NF-κB; Chen et al., 2010; McConkey and Zhu, 2008), others have identified induction of endoplasmic reticulum (ER) stress as the critical mediator of antitumor activity (Lee et al., 2003; Obeng et al., 2006).

Whereas each of the pleiotropic effects of PIs may cause cellular cytotoxicity in a specific context, induction of ER stress likely accounts for the unique sensitivity of MM to PIs in the clinic (Kim et al., 2008; Lee et al., 2003; Obeng et al., 2006). In plasma cells, the ER is expanded to accommodate the synthesis of secretory Ig. Physiologic ER stress, which can be very heavy in professional secretory cells, is counteracted via adaptations known collectively as the unfolded protein response (UPR). Three ER resident transmembrane proteins (Ire1, Perk, and Atf6) activate overlapping components of the UPR, which counters unfolded protein stress by suppressing global mRNA translation while selectively upregulating pathways that promote protein folding or degradation (Ron and Walter, 2007). PIs impede ER homeostasis by inhibiting proteasome-assisted ER-associated degradation (ERAD; Kim et al., 2008), causing

Significance

PIs, including bortezomib, are a mainstay of treatment for MM but fail to cure. Previously reported in vitro resistance mechanisms have not been validated in the clinic and reflect an artifact of cell culture. An alternative PI resistance mechanism is described here that occurs in patients with MM; because this differs from in vitro resistance reports, the need for clinical confirmation of in vitro drug resistance models is highlighted. Our results reveal that MM cells tolerate *XBP1* inactivation, which contributes to therapeutic resistance, suggesting that *IRE1* inhibitors may prove ineffectual in MM. Furthermore, an extensive progenitor organization is revealed in primary MM. Our results suggest that to achieve cure, treatment strategies must better address early MM progenitors.

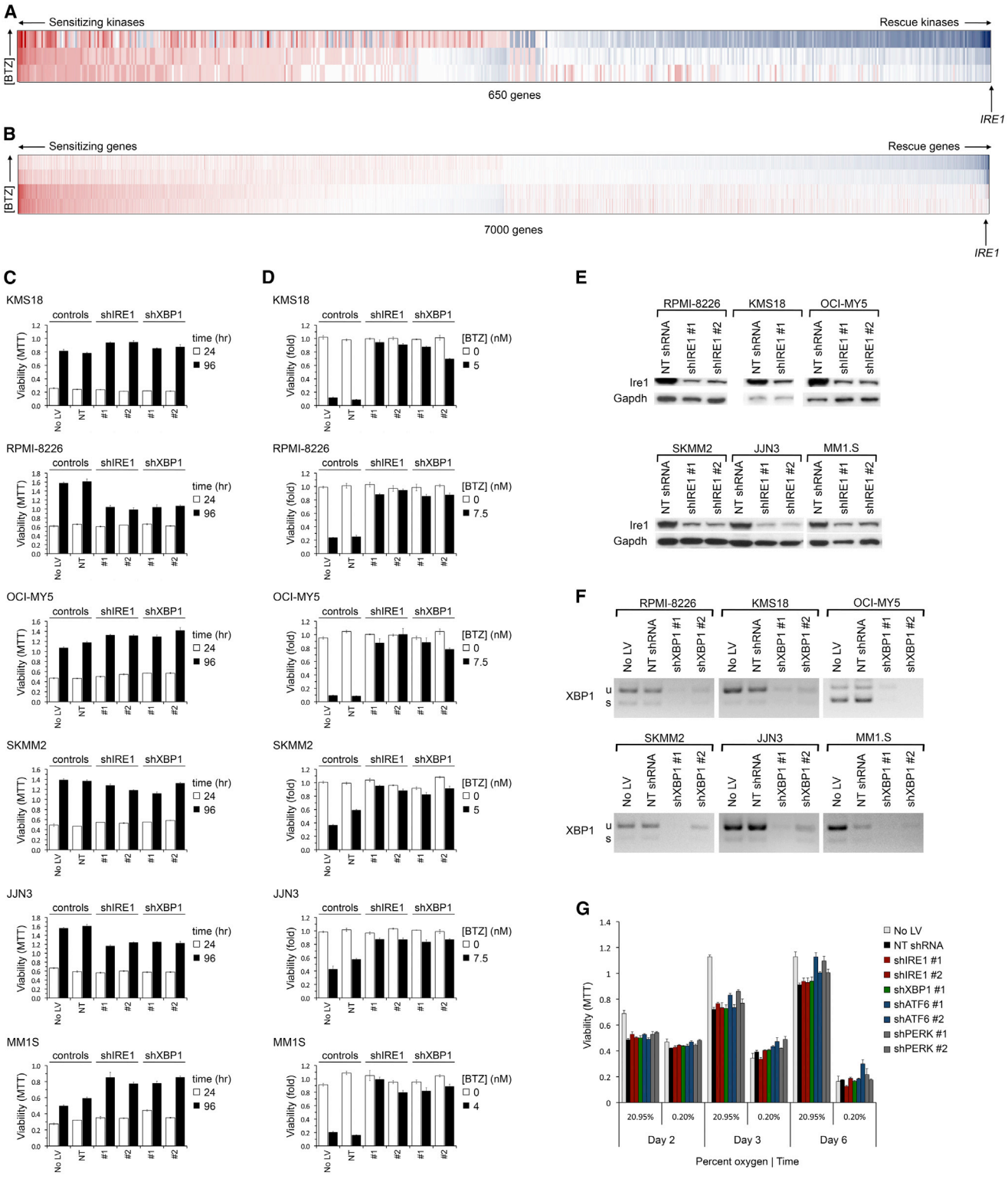

Figure 1. Loss of Ire1 or Xbp1 Reduces the Cytotoxic Activity of BTZ in MM

(A and B) Synthetic lethal BTZ-siRNA screens of the kinome (A) and "druggable" genome (B), conducted in KMS11 MM cells, showing genes ranked by the mean Bliss independence score of siRNA at BTZ IC90. Synthetic lethal genes whose RNAi caused greater than additive cytoxicity (in red) with BTZ are to the left; rescue genes whose RNAi reduced BTZ cytotoxcity (in blue) are to the right. *IRE1* ranking is shown.

(C) Viability (MTT assay) of MM cell lines expressing shIRE1 or shXBP1 for the indicated time following lentiviral (LV) infection. Controls included uninfected cells and cells expressing nontargeted (NT) shRNA.

(legend continued on next page)

ER stress. As a consequence, PI-treated tumor cells characteristically inactivate Eif2α, increase Atf4, and upregulate the expression of UPR genes such as *CHOP* (*DDIT3*) and *HSPA5* (Chen et al., 2010; Lee et al., 2003; Obeng et al., 2006; Zhu et al., 2010).

The mechanisms by which tumor cells escape the multiple cytotoxic effects of PIs are not implicit. One compelling possibility is that proteasome inhibition is prevented by mutation of the PI-binding site. Indeed, mutations of the BTZ-binding site on proteasome subunit β5 (*PSMB5*) or overexpression of *PSMB5* have been observed in various tumor cell lines and have been asserted to be the mechanism of PI resistance in both MM and leukemia (Balsas et al., 2012; de Wilt et al., 2012; Franke et al., 2011; Oerlemans et al., 2008; Rückrich et al., 2009). Notably, however, BTZ resistance in these studies was developed in vitro, using cell lines adapted to PI exposure, and the legitimacy of these models for the representation of drug resistance in patients remains unverified. To the contrary, multiple sequencing studies of primary MM tumors have failed to identify any proteasome mutations to account for PI resistance (Chapman et al., 2011; Lichter et al., 2012; Politou et al., 2006; Wang et al., 2008), suggesting that such mutations, although capable of mediating PI resistance in vitro, are infrequent in the clinic. In this study, we sought to define mechanisms of PI resistance in patients with MM.

RESULTS

Ire1-Xbp1 Signaling Is Dispensable for MM Tumor Cell Viability but Required for BTZ-Induced Cytotoxicity In Vitro

We have previously conducted kinome- and genome-scale siRNA studies in the KMS11 MM cell line treated with BTZ to functionally identify synthetic lethal chemosensitizing targets (Tiedemann et al., 2010, 2012; Zhu et al., 2011). We re-analyzed these results to identify genes whose silencing protected MM cells from BTZ-induced cytotoxicity (Figures 1A and 1B). While relatively few BTZ-rescue genes were detected, "endoplasmic reticulum to nucleus signalling 1" (*ERN1*), better known as *IRE1*, appeared critical for BTZ response in both studies. On kinome screening, *IRE1* was the kinase whose loss was most associated with BTZ resistance, whereas in genome-scale siRNA studies, *IRE1* ranked at the top 1% of genes required for BTZ-induced cell death.

Identification of *IRE1* in this context was surprising because Ire1 knockdown prevents activation of one branch of the homeostatic UPR pathway, and accordingly its loss might be predicted to diminish a cell's ability to respond to ER stress—rendering it more sensitive to BTZ—contrary to our observation. Therefore, to verify this result and to explore whether Ire1 suppression induces BTZ resistance in other MM subtypes, Ire1 was silenced in six other MM cell lines (Figures 1C and 1E); cells were then grown in the presence or absence of BTZ. In the absence of drug, loss of Ire1 was well tolerated (Figure 1C), albeit that mild reductions in proliferation were observed for RPMI-8226 and JJN3 cells. Conspicuously, however, suppression of Ire1 (Figure 1E) induced relative BTZ resistance in all MM lines tested (Figure 1D; Figures S1A–S1D available online), confirming our initial observation.

Ire1 activates the UPR via the bZIP transcription factor, Xbp1. When stimulated by ER stress, Ire1 splices 25 nucleotides from the unspliced *XBP1* mRNA (XBP1u) to yield a frame-shifted mRNA (XBP1s) that encodes the active transcription factor (Calfon et al., 2002). Because *XBP1* was not tested in our original siRNA studies, its effect on BTZ response was assessed next. Surprisingly, silencing of *XBP1* (Figure 1F), like *IRE1*, was well tolerated in MM cells (Figure 1C) even under conditions of extreme hypoxia (Figure 1G), contrary to previous reports that *XBP1* is required for myeloma pathogenesis (Carrasco et al., 2007). Strikingly, however, loss of Xbp1 induced BTZ resistance in all six MM cell lines tested, mirroring Ire1 suppression (Figure 1D). Similar results were obtained with four distinct shRNA. Therefore, the Ire1-Xbp1 pathway is dispensable for MM cell viability but promotes BTZ cytotoxicity, at least in MM cell lines grown in vitro.

Ire1-Xbp1 Signaling Is Suppressed in BTZ-Refractory Primary MM

To determine if attenuation of Ire1-Xbp1 signaling occurs in primary MM and plays a role in BTZ resistance, we next examined the gene expression of pretreatment tumor samples from patients with MM in whom either a complete response (CR) or progressive disease (PD) developed with single-agent BTZ treatment (Mulligan et al., 2007; Richardson et al., 2005). Conspicuously, almost all Xbp1 target genes (Shaffer et al., 2006) were expressed at lower levels in PD tumors (Figure 2A), concordant with our observation that Ire1-Xbp1 signaling modulates BTZ sensitivity in MM cell lines. However, the difference in Xbp1-target gene expression between BTZ CR and PD primary MM tumors was modest, suggesting that, pretreatment, Xbp1s activity may be suppressed in only a subpopulation of cells in BTZ-refractory tumors.

Notably, from a library of lymphoid transcription factor signatures, only Xbp1 correlated closely with clinical BTZ response. In comparison, no association was observed between BTZ response and tumor expression of p53, NF-κB, or Stat3 (Figure 2B). Similarly, no positive association was observed between BTZ resistance and proteasome expression in primary MM; instead, most proteasome subunits including *PSMB5* are downregulated in BTZ-resistant MM (Figure S2), contrary to in vitro resistance models.

The preferential expression of Xbp1 target genes in BTZ-sensitive MM tumors, relative to BTZ-resistant tumors, was

(D) Viability (MTT) of MM cell lines infected with LV to express shIRE1 or shXBP1 for 1 day and then treated with vehicle or BTZ at an approximate 75% inhibitory concentration (4–7.5 nM) for 3 days.
(E) Western blot of Ire1 levels in shIRE1-treated and control NT shRNA-treated MM cells.
(F) RT-PCR analysis of XBP1 mRNA in shXBP1-treated and control MM cells. u, unspliced; s, spliced.
(G) Viability of OCI-MY5 MM cells treated with UPR gene shRNA, following culture in normoxia (20.95% O_2) or extreme hypoxia (0.2% O_2).
Error bars represent ± SEM (n = 3).
See also Figure S1.

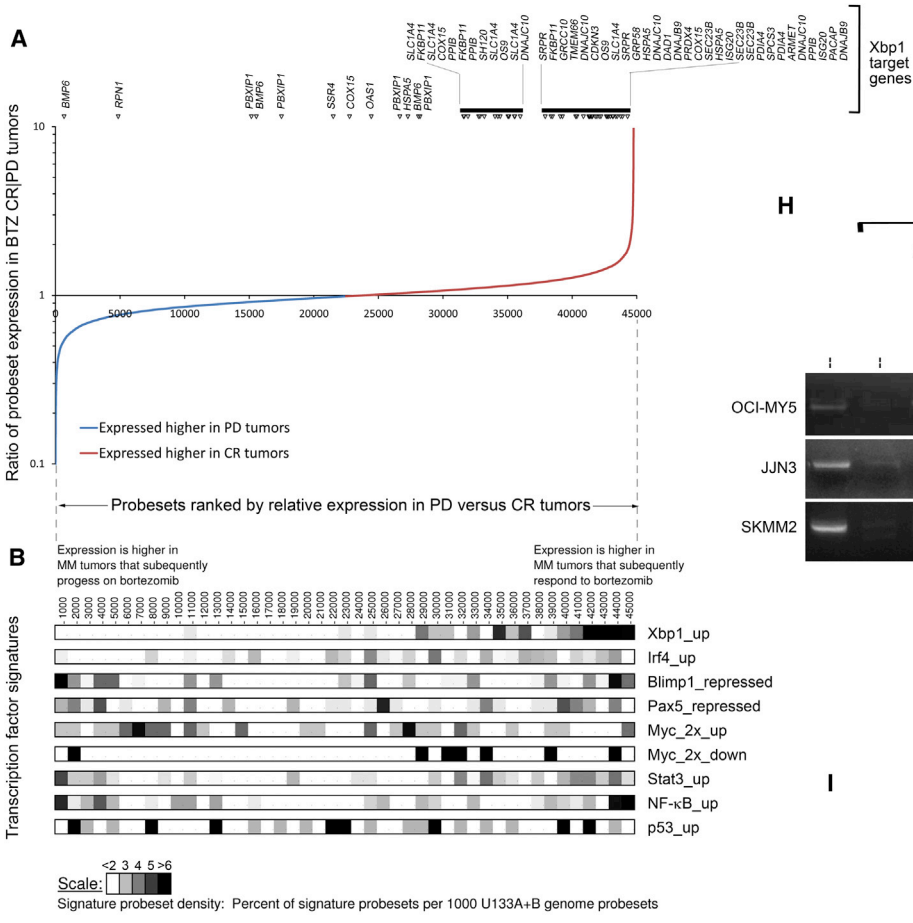

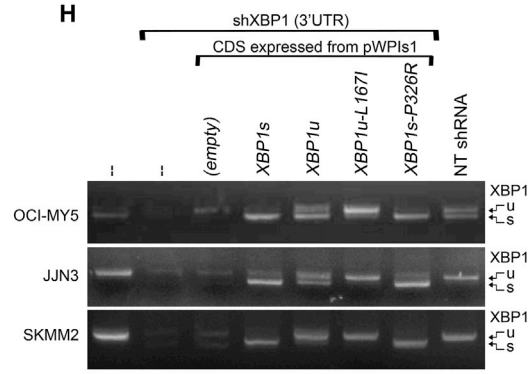

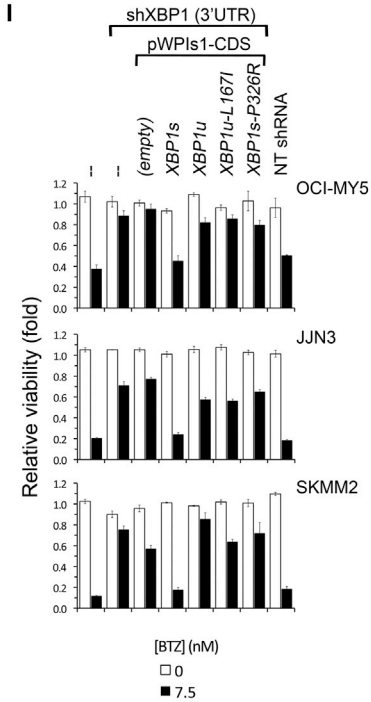

C

Gene set	Total genes	Genes found	p-value	q-value	NES
XBP1_Staudt_SigDB	76	67	0.073	0.073	1.49

D

Gene set	Total genes	Genes found	p-value	q-value	NES
V$XBP1_01 c3	108	77	0.026	0.026	1.47

E

Gene set	Total genes	Genes found	p-value	q-value	NES
XBP1_MM	803	605	0.024	0.024	1.39
IRE1_MM	982	728	0.024	0.048	1.42

F

Patient status pre BM biopsy	Mutation	Mutation location	nucelotide	Treatment post BM biopsy	Treatment response
Treated	XBP1-P326R	27521317	cCa/cGa	CyBorD	PD, died
Treated	XBP1-L167I	27522135	Ctc/Atc	none	died

G

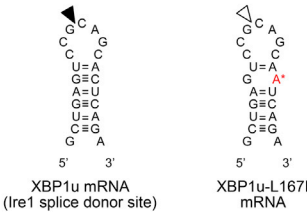

(legend on next page)

confirmed by gene set enrichment analysis (GSEA) using three independent Xbp1 gene signatures, derived by distinct methods. Whereas an Xbp1 signature derived from overexpression of Xbp1 in B cells (Shaffer et al., 2004) was moderately enriched in BTZ-sensitive primary MM tumors (q = 0.07; Figure 2C), a second Xbp1 signature representing genes with Xbp1-binding promoters, was significantly enriched (q = 0.026; Figure 2D). A third Xbp1 signature, derived from profiling of MM cells following Xbp1 knockdown, most closely matched the biological context in which Xbp1 activity was being assessed and showed the most significant enrichment in BTZ-sensitive MM (q = 0.024; Figure 2E). In addition, a fourth related Ire1 gene signature, derived from MM cells with Ire1 knockdown, was also enriched in BTZ-sensitive primary MM (q = 0.048; Figure 2E), consistent with the requirement for Ire1 activation of Xbp1. Thus, GSEA of primary MM tumors from patients treated with single-agent BTZ confirm that downregulation of the Ire1-Xbp1 pathway occurs in primary myeloma and correlates with therapeutic PI resistance.

XBP1 Mutations in MM

Suppression of Xbp1 signaling may occur through a variety of mechanisms, including *XBP1* gene mutation. Notably, while genome sequencing of 20 treated MM tumors did not identify any proteasome *PSMB5* mutations, this initial genomic analysis of MM did identify two mutations in *XBP1* (Chapman et al., 2011), both in treatment-refractory tumors (Figure 2F). Conspicuously, the first mutation, *XBP1-L167I*, maps to the Ire1 splice site on XBP1u and, we predicted, might prevent splice activation to XBP1s (Figure 2G). The second mutation, *XBP1s-P326R*, involves a nonconservative missense mutation within the trans-activation domain of Xbp1s, where loss of proline's conformational rigidity may affect tertiary structure and influence transcriptional activity.

To confirm if either or both of these mutations are inactivating, identical *XBP1* mutants were generated and expressed in MM cell lines (Figures 2H and 2I); simultaneously endogenous *XBP1* was silenced using a 3′UTR-targeted shXBP1. As predicted, the mutation, *XBP1-L167I*, consistently prevented splicing of XBP1u mRNA to XBP1s, whereas unmutated XBP1u mRNA, expressed in parallel, could be processed. While both XBP1u and XBP1s are translated, only Xbp1s protein is transcriptionally active; Xbp1u, which has a functional N-terminal leucine zipper motif, instead acts as an inhibitor of Xbp1s (Lee et al., 2003). *L167I* therefore inhibits *XBP1* both by decreasing Xbp1s and by increasing Xbp1u.

We next assessed whether these *XBP1* mutations have effects on drug response by testing the mutant *XBP1* cell lines for BTZ sensitivity (Figure 2I). Consistent with our earlier observations, knockdown of endogenous Xbp1 in OCI-MY5, JJN3, or SKMM2 control cells, using an *XBP1* 3′UTR-directed shRNA, attenuated BTZ cytotoxicity. Constitutive expression of an shRNA-resistant *XBP1s* CDS, however, re-established sensitivity to BTZ, despite endogenous *XBP1* silencing, verifying that BTZ sensitivity in MM cells is modulated specifically by Xbp1s. In contrast, constitutive expression of the mutant *XBP1s-P326R* or *XBP1u-L167I* CDS in MM cells failed to resensitize shXBP1-treated MM cells to BTZ, indicating that both mutations are functionally inactivating and promote BTZ resistance. These studies indicate that primary MM tumors tolerate inactivating mutations in *XBP1* and that PI therapy may exert a selective pressure for the emergence of cells with suppression of this pathway.

Of UPR Stress Transducers, Only Ire1-Xbp1, and Not Atf6 or Perk, Regulates BTZ Sensitivity

Ire1 is one of three ER transmembrane proteins that transduce stress signals to the nucleus to induce the UPR. To determine if loss of either of the other ER stress transducers, Perk or Atf6, induced BTZ resistance, each transducer was knocked down separately using two shRNA in RPMI-8226 and SKMM2 MM cells (Figure 3A). However, suppression of Atf6 or Perk, unlike suppression of Ire1-Xbp1, had no effect on BTZ sensitivity (Figures 3B, 3C, and S3), indicating that among the ER stress pathways, BTZ sensitivity maps specifically to Ire1-Xbp1.

BTZ Resistance Is Not Due to Increases in Perk or Atf6 or Loss of an Xbp1s Death Signal

Whereas BTZ cytotoxicity in MM has been linked to the induction of overwhelming ER stress, we show here that loss of the Ire1-Xbp1 branch of the ER homeostasis apparatus reduces BTZ lethality, contrary to expectation. To address this dilemma, and

Figure 2. Ire1-Xbp1 Signaling Is Suppressed or Mutated in BTZ-Refractory Primary Tumors from MM Patients

(A) Comparative gene expression of BTZ-responsive and -resistant primary MM from patients enrolled on the APEX 039 clinical study. Affymetrix probe sets are plotted by rank-order of differential mean expression in tumors that responded completely (CR) or that showed progressive disease (PD) following BTZ therapy. The vertical axis shows the log ratio of mean tumor expression intensity in the two response groups. Xbp1s target genes are identified above the plot.

(B) Heatmaps comparing the relative expression of an Xbp1 gene signature with that of other B cell transcription factor signatures in BTZ-sensitive (CR) versus BTZ-resistant (PD) primary MM tumors, using the same probe set rank-order as in (A). To normalize for signature sizes, results are plotted as the percentage of signature probe sets per 1,000 rank-ordered probe sets. The suffixes up, down, repressed, and 2× reflect the selection criteria used to define genes in the transcription factor signatures.

(C–E) Gene set enrichment analysis (GSEA) for Xbp1 target genes in primary MM, among genes preferentially expressed pretreatment in BTZ-responsive versus BTZ-refractory tumors. Four distinct Xbp1 signatures were used, derived either by overexpression of Xbp1 in B cells (C), by identification of genes with Xbp1-binding motifs within their promoters (D), or by shRNA knockdown of either Xbp1 or Ire1 in MM cells (E). NES, normalized enrichment score.

(F) *XBP1* mutations identified on initial genome sequencing of 38 patient MM, and subsequent patient treatment response. CyBorD, cyclophosphamide; BTZ, dexamethasone.

(G) The wild-type (left) and L167I mutation (right, indicated by the red letter) XBP1u mRNA sequences at the Ire1 splice site (indicated by the black arrow on the left) hairpin.

(H) RT-PCR analysis of XBP1u and XBP1s mRNA in three MM cell lines engineered to express mutant *XBP1* CDSs recapitulating mutations identified in primary tumors. Endogenous XBP1 mRNA was suppressed using a 3′UTR-targeted shXBP1.

(I) Relative viability (MTT) of the MM cell lines in (H) following treatment with BTZ or vehicle for 3 days (mean ± SEM).

See also Figure S2.

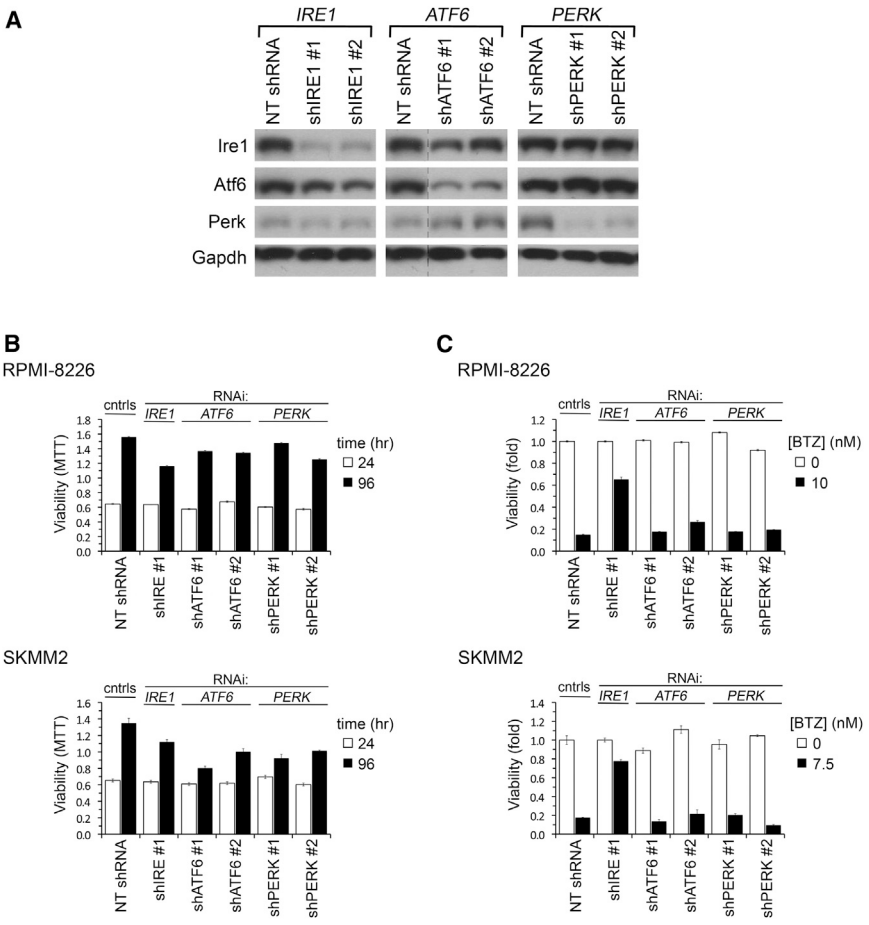

Figure 3. Only Ire1 among ER Stress Transducers Regulates BTZ Sensitivity in MM

(A) Immunoblot of indicated proteins in RPMI-8226 MM cells 1.5 days after LV infection to express shIRE1, shATF6, shPERK, or control NT shRNA. In the *ATF6* panel, irrelevant lanes were removed between NT shRNA and shATF6 lanes for all four blots; all samples were run on the same gel.

(B) Growth of MM cell lines expressing shIRE1, shATF6, shPERK, or control NT shRNA measured by sequential MTT assays 24 and 96 hr after LV infection.

(C) Viability (MTT assay) of MM cell lines infected with LV for 24 hr to express shIRE, shATF6, or shPERK and then treated with BTZ at IC90 or vehicle for 3 days.

Error bars show ± SEM. See also Figure S3.

to clarify the mechanism of PI resistance, we hypothesized that loss of Ire1-Xbp1 signaling in MM cells might cause a compensatory increase in Atf6 or Perk signaling (and in downstream UPR gene expression) that might "pre-adapt" MM cells to better withstand proteasome inhibition. To investigate this possibility, we generated MM cells in which both Ire1 and Atf6, or both Ire1 and Perk, were concurrently suppressed (Figures 4A and 4B). Notably, double knockdown of Ire1 and Perk, or of Ire1 and Atf6 together, in MM cells, failed to diminish the induction of BTZ resistance by Ire1 silencing (Figures 4C and 4D), indicating that neither of these parallel pathways individually mediates the BTZ resistance seen on Ire1 suppression. Conceivably, however, Ire1-Xbp1 suppression might cause compensatory increases in both Atf6 and Perk, either of which might then redundantly prime cells to survive proteasome inhibition. Therefore, to test this hypothesis, we also generated triple knockdown MM cells in which Ire1, Atf6, and Perk were all concurrently suppressed (Figure 4E). Surprisingly, these cells proved viable in tissue culture, although they demonstrated a growth disadvantage (Figure 4F). Notably, however, simultaneous silencing of both Atf6 and Perk failed to diminish BTZ resistance induced on Ire1 silencing (Figure 4G). Therefore, BTZ resistance arising from Ire1-Xbp1 loss is not mediated via parallel UPR pathways.

We next speculated that the overwhelming ER stress generated by PI therapy might induce a lethal signal transmitted via Ire1-Xbp1 and that loss of this death signal might underlie BTZ resistance. However, MM cells forced to constitutively overexpress Xbp1s protein, the final common effector of Ire1-Xbp1 signaling, remain viable in vitro (Figures 4H, 4I, and S4) and in vivo (Carrasco et al., 2007), providing no evidence for the existence of an Xbp1s death signal in these cells.

Ire1-Xbp1 Suppression in MM Blocks Commitment to Plasma Cell Differentiation and Lowers ER Stress

XBP1 is essential for differentiation of B lymphocytes to plasma cells, particularly for the terminal maturation of proliferating plasmablasts to plasma cells, for induction of Ig secretion, and for bone marrow colonization (Carrasco et al., 2007; Hu et al., 2009; Reimold et al., 2001). Because the role of Ire1-Xbp1 signaling in BTZ resistance remained unaccounted for, we next surmised that loss of Ire1-Xbp1 signaling might cause decommitment of MM cells to terminal plasma cell differentiation and that tumor cell immaturity might account for cellular BTZ resistance.

To investigate this possibility, we first assessed MM cell lines for evidence of reversion of plasma cell commitment following RNAi-induced silencing of *IRE1* or *XBP1*. Following knockdown of Ire1 or Xbp1, OCI-MY5 cells appeared smaller and rounder with less cytoplasm and perinuclear hof (Figure 5A), resembling pre-plasmablasts (Jourdan et al., 2011). Profiling of gene expression in *IRE1*- or *XBP1*-silenced MM cell lines demonstrated partial repression of markers of plasma cell maturation such as *SDC1 (CD138), CD38, IL6R*, and *IL6ST* in these cells and simultaneous weak mRNA expression of B cell markers such as *CD20* and *PAX5* (Figure 5B). Diminished expression of CD138 ± CD38 surface antigens on *XBP1*-silenced RPMI-8226 and JJN3 MM cells was confirmed by flow cytometry (Figure 5C), while upregulation of Pax5 protein in Ire1-Xbp1 inactivated MM cells was confirmed by immunoblot (Figure 5D). Because Pax5 is expressed in B cells but is suppressed in plasma cells (Nutt et al., 2011), these findings are consistent with the hypothesis

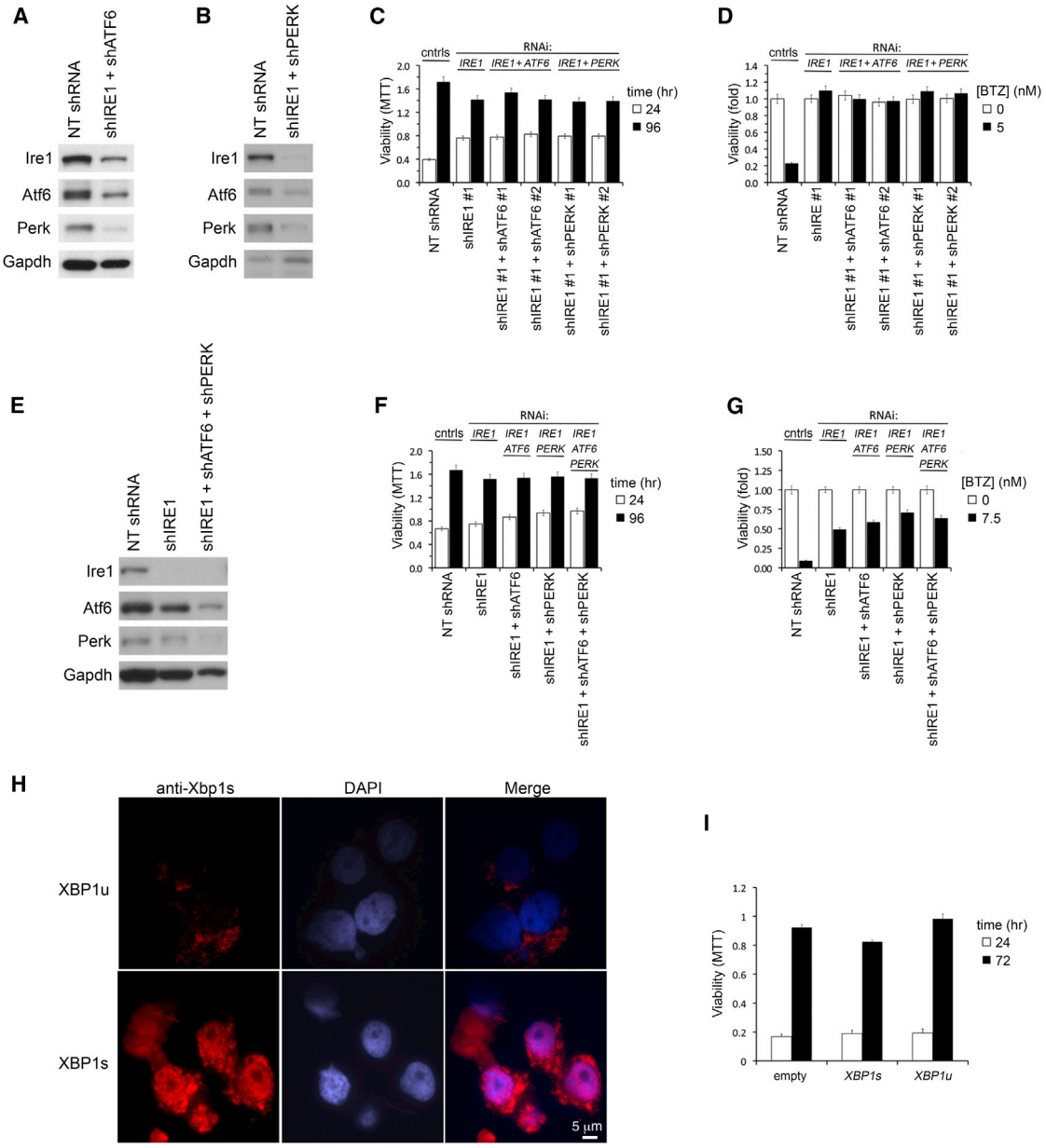

Figure 4. BTZ Resistance Induced by Ire1-Xbp1 Suppression Is Not Due to Adaptive Increases in Perk or Atf6

(A) Immunoblot of Ire1, Atf6, and Perk in JJN3 MM cells expressing concurrently shIRE1 and shATF6, 2 days postinfection. Control cells expressed NT shRNA.

(B) Same as (A) except that MM cells concurrently expressed shIRE1 and shPERK.

(C) Growth of JJN3 MM cells following knockdown of Ire1, or dual knockdowns of Ire1+Atf6 or Ire1+Perk, measured by sequential MTT assays 1 and 4 days after infection.

(D) Viability (MTT) of JJN3 MM cells infected with indicated LV shRNA combinations for 1 day and then treated with BTZ or vehicle for 3 days.

(E) Immunoblot of indicated proteins in JJN3 MM cells infected with LV to concurrently express shRNA targeting all three ER UPR transducers Ire1, Atf6, and Perk. Control cells expressed NT shRNA.

(F) Growth of JJN3 MM cells following triple knockdown of Ire1+Atf6+Perk, compared with single or dual gene knockdowns, measured by MTT assays 1 and 4 days after LV infection.

(G) Same as (D) but includes JJN3 MM cells with simultaneous triple knockdown of Ire1, Atf6, and Perk.

(H) Immunofluorescence staining for Xbp1s in OCI-MY5 MM stably overexpressing XBP1u or XBP1s CDS. Nuclei are stained with DAPI. Scale is identical for all micrographs.

(I) Growth of OCI-MY5 cells overexpressing XBP1u or XBP1s, compared with control cells infected with empty expression vector, measured by repeat MTT assays at 0 and 3 days.

Error bars represent ± SEM. See also Figure S4.

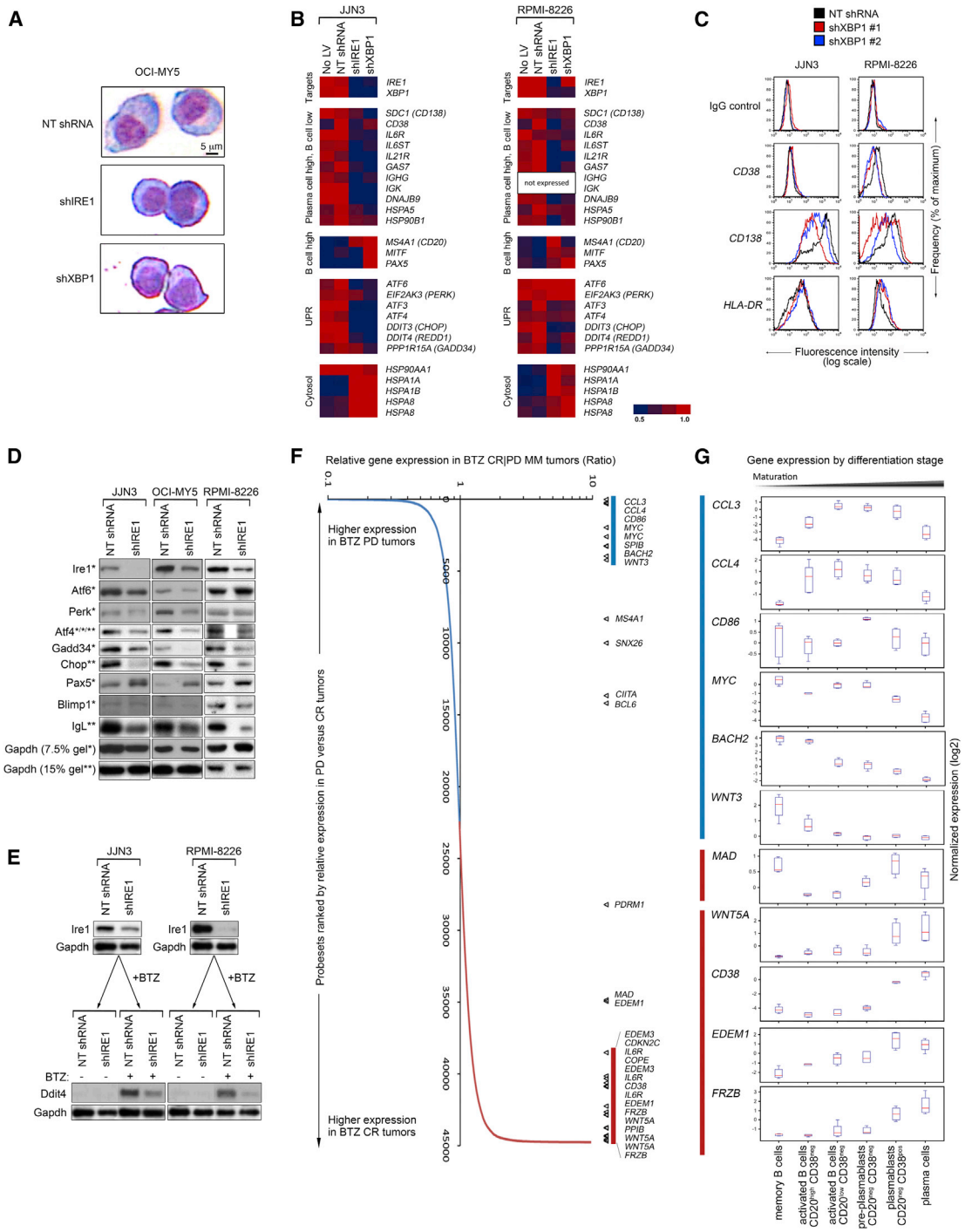

Figure 5. Ire1-Xbp1 Suppression and BTZ Resistance in MM Are Associated with De-Commitment to Plasma Cell Differentiation

(A) Giemsa stain of OCI-MY5 cells following expression of NT shRNA, shIRE1, or shXBP1. Scale is identical for all micrographs.

(B) Relative mRNA abundance of indicated genes in JJN3 and RPMI-8226 MM cell lines expressing shIRE1, shXBP1, or control NT shRNA.

(C) Flow cytometric analysis of surface CD38 and CD138 on JJN3 and RPMI-8226 MM cell lines expressing shXBP1 or control NT shRNA.

(D) Immunoblot analysis of indicated proteins in JJN3, OCI-MY5, and RPMI-8226 MM cell lines 3 days after LV infection to express shIRE1. Proteins were separated on either 7.5% (*) or 15% (**) polyacrylamide gels. IgL reflects κ for JJN3 and λ for RPMI-8226 and OCI-MY5.

(E) Immunoblot of Ddit4 induction by BTZ (100 nM, 6 hr) in JJN3 and RPMI-8226 MM cells expressing either shIRE1 or control shRNA.

(F) Relative expression of indicated B cell and plasma cell maturation genes among primary MM that respond (with CR) or fail to respond (with PD) to clinical BTZ treatment. Data are from pre-BTZ samples from patients treated on the APEX 039 study.

(G) Box-whisker plots of relative expression of indicated genes from (E) during physiological B cell to plasma cell maturation, with median shown in red.

See also Figure S5 and Table S1.

that Ire1-Xbp1 loss in MM cells causes a modest reversal of plasma cell maturation.

We next assessed Ig production in Xbp1s-silenced MM cells. By gene expression profiling, loss of Xbp1 or Ire1 was associated with decreased expression of both IgG heavy chain *(IGHG)* and Igκ-light chain (*IGK*), in IgGκ-secreting JJN3 cells, as well as decreased expression of *IL21R*, a regulator of IgG production (Ozaki et al., 2002; Figure 5B). A marked decline in Ig light chain protein production in Ire1-Xbp1s silenced MM cells was also observed by immunoblot (Figure 5D). *XBP1* is a known prerequisite for establishing Ig production by B cells (Reimold et al., 2001), and our data indicate that MM plasma cells remain dependent on Xbp1s for ongoing Ig synthesis.

We next hypothesized that by arresting or reversing their secretory plasma cell maturation, MM tumor cells may lessen their ER front loading by secretory Ig and thereby diminish both their basal ER stress and their risk of lethal ER stress arising from PI-induced ERAD inhibition, providing a mechanism by which Xbp1s loss (and other forms of maturation arrest) might cause PI resistance. Consistent with this, MM cell lines in which *IRE1* or *XBP1* were silenced showed reduced expression of UPR genes such as *ATF4*, *DDIT3* (*CHOP*), *DDIT4* (*REDD1*), *PPP1R15A* (*GADD34*), and *HSPA5* (*BiP*); and of downstream chaperones *HSP90B1* and *DNAJB9* (Figure 5B). Notably, this diminished expression of UPR genes in Ire1-Xbp1s inactivated MM cells reflected reduced ER stress rather than simple loss of Xbp1s-driven gene transcription because Ire1-Xbp1s silencing was accompanied by reduced or stable expression of genes in parallel ER stress pathways such as *EIF2AK3* (*PERK*), *ATF4*, and *PPP1R15A* (*GADD34*; Figures 5B and 5D). If loss of Xbp1s-driven gene expression alone accounted for the decline in *CHOP* and chaperones, without a concurrent decrease in ER stress, these parallel UPR homeostasis pathways would instead be activated as they assumed the burden of ER homeostasis. A significant decline in basal expression of Perk-responsive UPR elements Atf4, Gadd34, and Chop in shIRE1-treated MM cells was confirmed by immunoblot (Figures 5D, S5A, and S5B). Furthermore, suppression of Ire1 caused diminished induction of the Atf4 response gene *DDIT4* (*REDD1*) following either BTZ- or thapsigargin-induced ER stress (Figures 5E and S5C). Because Ire1-Xbp1s suppression causes de-commitment to Ig production and a decline in ER stress, whereas PI cytotoxicity in MM has been linked to exacerbation of ER stress, which in plasma cells is driven by Ig production (Obeng et al., 2006), these data provide a mechanistic link between Ire1-Xbp1 silencing in MM cells and PI insensitivity.

To determine if BTZ-refractory MM tumors in the clinic show evidence of plasma cell de-commitment or maturation arrest, we next examined the gene expression of tumor samples from patients with MM in whom either a CR or PD developed following treatment with BTZ (Figure 5F). We compared the differential gene expression of the two tumor groups with programmed changes in gene expression seen during the differentiation of B cells to plasma cells (Figure 5G; Table S1; Jourdan et al., 2011). Gene sets defining expression differences between $CD20^+$ memory B cells, activated $CD20^{low}$ $CD38^-$ B cells, $CD20^-$ $CD38^-$ pre-plasmablasts, $CD20^-$ $CD38^+$ $CD138^-$ plasmablasts, and plasma cells were derived using the expression profile of mature plasma cells as a common denominator. Notably, by GSEA, expression of plasma cell maturation genes was significantly enriched in BTZ-responsive tumors ($q = 0.03$, NES +1.5) and reduced in BTZ-resistant tumors ($q < 0.01$, NES −1.5), suggesting that while BTZ-responsive tumors contain a high proportion of mature plasma cells, BTZ-resistant MM tumors may contain greater proportions of less differentiated cells.

Included in the leading edge of differentiation genes whose expression was diminished in BTZ-resistant primary MM were *FRZB*, *WNT5A*, *IL6R*, *CD38*, *EDEM1*, and *EDEM3* (Figure 5F; red bar), which are all expressed at higher levels in plasma cells than in activated B cells or pre-plasmablasts (Figure 5G); their relative underexpression in BTZ-refractory MM therefore supports the presence of maturation arrest in PI-resistant primary tumors. Conversely, genes that appeared to be upregulated in BTZ-resistant MM tumors included the chemokine ligands *CCL3* and *CCL4, CD86*, *MYC*, *BACH2*, and *WNT3*, which are expressed at higher levels in activated B cells and pre-plasmablasts than in plasma cells (Figure 5F), suggesting that BTZ-refractory primary MM may be associated with increases in these progenitor subpopulations. Additional gene expression analyses of B cell maturation support the presence of a "sweet spot" maturation stage intermediate between B cells and plasma cells that may be intrinsically less susceptible to PI-induced cytotoxic ER stress (Figures S5D and S5E).

$Xbp1s^-$ B Cell Progenitors in MM

Our observations that Ire1-Xbp1 suppression correlates with BTZ resistance in MM and that B cell and pre-plasmablast gene set expression is increased in BTZ-refractory MM, lead us to examine primary MM tumors for the existence of $Xbp1s^-$ progenitor populations. Using FACS, viable plasma cells and B-lineage cells were isolated from patient bone marrows and then segregated according to CD38/CD138 status (Figures 6A and 6B). Tumor cells within these subpopulations were identified by the presence of tumor clone FISH abnormalities, and were further characterized for Xbp1s and CD20 expression by immunoflourescence-flourescent in situ hybridization (IF-FISH) (Figures 6C and S6). Using this technique we isolated five subpopulations of MM tumor cells from primary MM samples, including $CD20^+$ $CD38^-$ $CD138^-$ $Xbp1s^-$ B cells, $CD20^{low}$ $CD38^-$ $CD138^-$ $Xbp1s^-$ activated B cells, $CD20^-$ $CD38^-$ $CD138^-$ $Xbp1s^-$ pre-plasmablasts, $CD38^+$ $CD138^{low}$ $Xbp1s^+$ plasmablasts, and $CD38^+$ $CD138^+$ $Xbp1s^+$ plasma cells. The existence of these tumor progenitor cells was observed directly with IF-FISH and was confirmed by the greater-than background rate of cells positive for the tumor FISH abnormality within sorted subpopulations. Virtually all $CD38^-$ $CD138^-$ tumor cells were $Xbp1s^-$, while the majority of tumor B cells were $CD27^+$ (Figure 6C), consistent with a post-germinal center memory phenotype. In some samples, tumor B cells accounted for the majority of bone marrow memory B cells (not shown). $Xbp1s^-$ tumor B cells and pre-plasmablasts express lower levels of Chop than $Xbp1s^+$ tumor plasma cells and plasmablasts (Figure 6D), suggesting that $Xbp1s^-$ tumor progenitors, like Xbp1s-silenced MM cell lines,

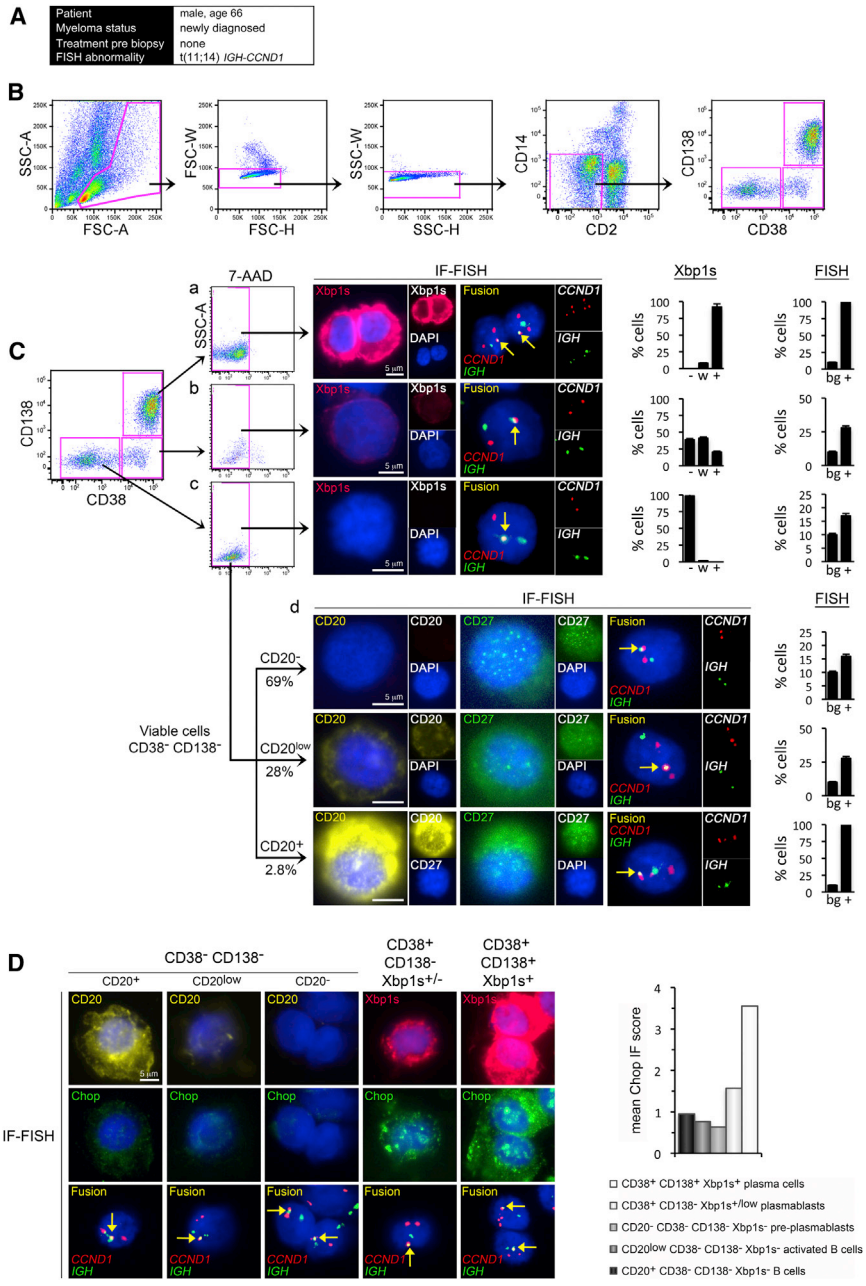

Figure 6. Tumor Progenitor Subpopulations in a Patient with Newly Diagnosed MM

(A) The clinical information of the patient whose bone marrow was examined.

(B) Bone marrow MM cells were enriched by sequential FACS for lymphoid FSC/SSC (left panel), by removal of aggregates (second and third panels) and by negative selection for CD2 (T and NK cells) and CD14 (monocytes). Gates are shown in pink.

(C) Tumor cells gated into subpopulations by CD38 and CD138 status. Single viable CD38$^+$ CD138$^+$ plasma cells (a), CD38$^+$ CD138$^-$ plasmablasts and B cells (b), and CD38$^-$ CD138$^-$ B cells (c) were examined for concurrent Xbp1s protein expression and for *IGH-CCND1* gene fusion (arrows) by IF-FISH on single cells. Viable CD38$^-$ CD138$^-$ B cells from (Cc) were further examined for concurrent CD20 and CD27 expression and for *IGH-CCND1* by IF-FISH (d). Each row illustrates a single cell. Scale bars (5 μm) are identical for IF and FISH; monochrome insets are shown at 0.5× scale. The overall proportion of cells in each subpopulation with strong (+), weak (w), or no (–) expression of Xbp1s and the proportion of cells positive (+) for *IGH-CCND1*, compared with the background rate (bg), are quantified and shown in the bar graphs. Error bars represent SEM (n > 100).

(D) Ddit3 (Chop) protein expression in primary MM tumor progenitors. Progenitor stages (left to right) were characterized by CD20, Xbp1s, and Chop IF-FISH. Each column illustrates single cells. Scale is consistent across micrographs. The mean Chop IF score by MM progenitor stage is quantified and shown in the bar graph.

See also Figure S6.

have lower basal ER stress than tumor cells that have undergone plasma cell maturation.

Xbp1s$^-$ MM B Cell and Pre-Plasmablast Progenitors Survive Therapeutic BTZ and Are Enriched in BTZ-Refractory MM

In newly diagnosed MM and in patients relapsing following treatment discontinuation, the predominating tumor cells are Xbp1s$^+$ plasma cells or plasmablasts (Figures 6, 7A, and 7D), although progenitor subpopulations including CD20$^-$ CD38$^-$ CD138$^-$ Xbp1s$^-$ pre-plasmablasts and CD20^{low} CD38$^-$CD138$^-$ Xbp1s$^-$ activated B cells were consistently identified (Figures 6Cd and 7Af). Progenitor CD20$^+$ CD38$^-$ CD138$^-$ Xbp1s$^-$ B cells with strong CD20 staining were identified in nearly all samples but were comparatively rare.

Supporting our conclusion that MM tumor cells with arrested secretory maturation are BTZ resistant, in some primary MM tumors with PD on BTZ therapy (Figure 7B), substantial expansion of tumor CD20^{low} CD38$^-$ CD138$^-$ Xbp1s$^-$ activated B cell and CD20$^-$ Xbp1s$^-$ pre-plasmablast subpopulations was observed, causing activated CD20^{low} B cells or CD20$^-$ pre-plasmablasts to become the predominant subpopulations in these tumors (Figures 7Be, 7Bf, and 7D). The marked expansion of these subpopulations in patients progressing on PI therapy is consistent both with a partial tumor maturation arrest and with relative invulnerability of these progenitor stages to BTZ. CD20$^+$ B cell progenitors were also detectable in these tumors and appeared viable and enriched despite BTZ-therapy (Figures 7Bf lower panels and 7D). In contrast, plasmablasts and plasma cells were reduced; their numbers, 7-AAD staining, and appearance (Figures 7Bb–d and 7D) suggested continued susceptibility of these more mature subpopulations to BTZ therapy.

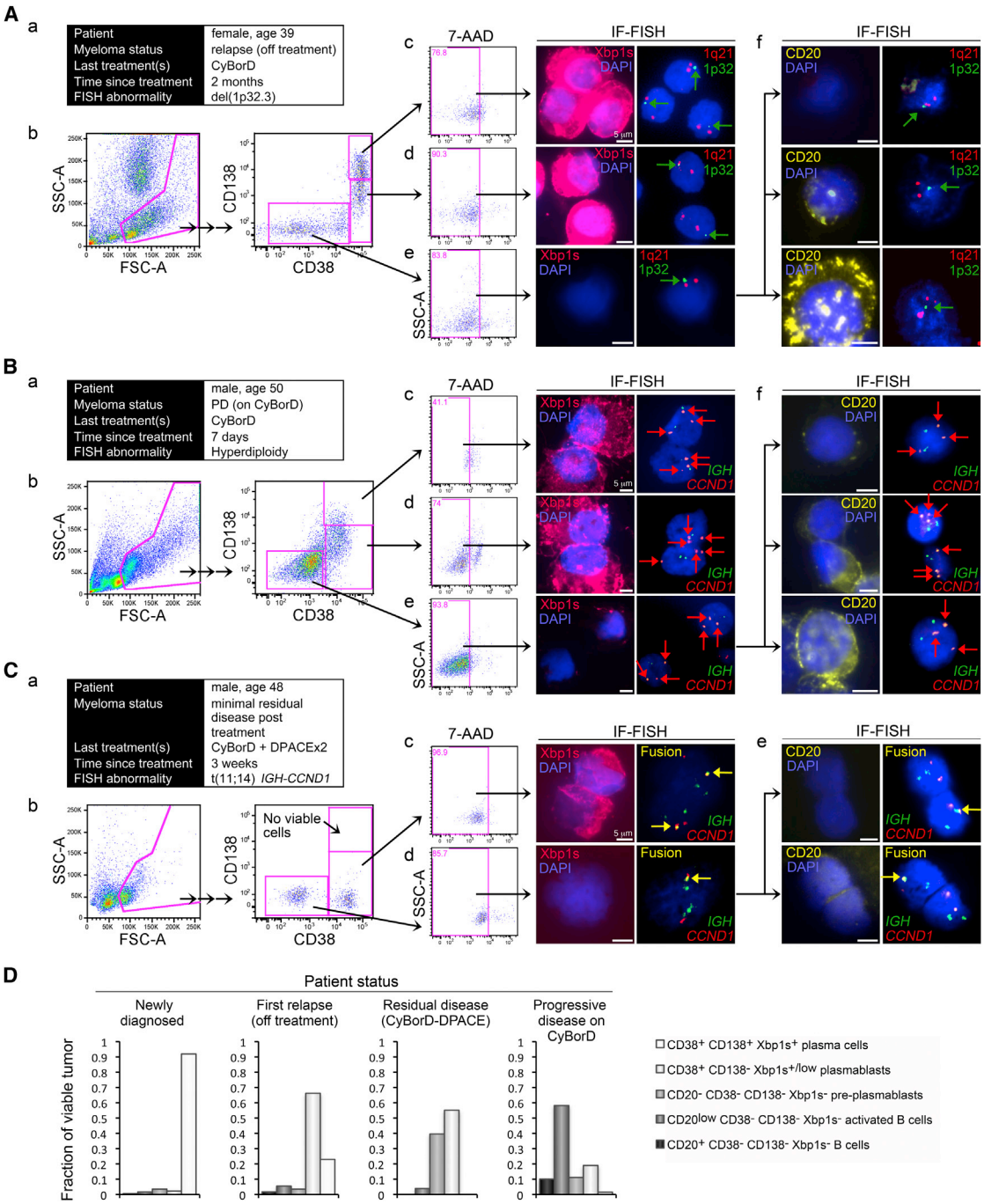

Figure 7. Tumor Progenitor Subpopulations in Relapsed or Refractory MM

(A) Findings from a patient with relapsed MM following BTZ discontinuation. (a) The clinical information of the patient whose bone marrow was examined. (b) Patient bone marrow was FACS sorted as in Figure 6. Viable CD38$^+$ CD138$^+$ plasma cells (c), CD38$^+$ CD138$^{-/low}$ plasmablasts (d), and CD38$^-$ CD138$^-$ cells (e) were examined for the presence of Xbp1s by IF and for the loss of chromosome 1p32 (arrows), which contains the *CDKN2C* locus, by FISH. (f) Viable CD38$^-$ CD138$^-$ B cells were also examined for CD20 expression and for chromosome 1p32 loss by IF-FISH.

(B) Findings from a patient with MM with progression on BTZ therapy. (a) The clinical information of the patient. (b) The patient's bone marrow was FACS sorted as in Figure 6. Viable CD38$^+$ CD138$^+$ plasma cells (c), CD38$^+$ CD138$^{-/low}$ plasmablasts (d), and CD38$^-$ CD138$^-$ cells (e) were examined for the presence of Xbp1s by IF and for trisomy of chromosome 11, which contains the *CCND1* locus (arrows), by FISH. (f) Viable CD38$^-$ CD138$^-$ B cells were also examined for CD20 expression and for gain of *CCND1* by IF-FISH.

(C) Findings from a patient with MM following intensive BTZ and DPACE chemotherapy with clinical response. (a) The clinical information of the patient. (b) The patient's bone marrow was FACS sorted as in Figure 6. Viable CD38$^+$ CD138$^+$ plasma cells were not identified. Viable CD38$^+$ CD138$^{-/low}$ plasmablasts (c), and

(legend continued on next page)

Because MM is incurable in the vast majority of patients even with intensive multiagent therapy, we evaluated the minimal residual disease in patients treated with BTZ-based therapy. Figure 7C shows a representative marrow sample obtained 3 weeks after sequential BTZ-based treatment (CyBorD) and DPACE chemotherapy. This sample shows an almost empty marrow with delayed recovery of normal marrow elements post-chemotherapy. At this sampling, no viable MM plasma cells could be detected by flow. However, small residual populations of tumor cells were identified, with phenotypes compatible with activated $CD20^{low}$ B cells, pre-plasmablasts and early $CD138^{-}$ $Xbp1s^{low}$ plasmablasts. Because $Xbp1s^{-}$ cells preferentially survive BTZ (Figure 1), the presence of $CD138^{-}$ $Xbp1s^{low}$ tumor plasmablasts in this marrow may reflect differentiation from earlier progenitors in the post treatment interval.

In each of the MM patient bone marrow samples examined in Figure 7, the proportion of $CD38^{-}$ $CD138^{-}$ $CD20^{+}$ B cells, $CD38^{-}$ $CD138^{-}$ $CD20^{low}$ activated B cells, and $CD38^{-}$ $CD138^{-}$ $CD20^{-}$ pre-plasmablasts that showed tumor-specific clonal FISH abnormalities, such as loss of chromosome 1p32, gain of *CCND1* or fusion of *IGH-CCND1* genes, consistently exceeded the background FISH positive rate, confirming the presence of tumor progenitor cells within these isolated subpopulations, as in Figure 6. Similar tumor progenitor subpopulations were also identified in hyperdiploid MM and in MM tumors bearing t(4;14) *IGH-FGFR3* gene rearrangement (Figure 8A), demonstrating that MM B cell and pre-plasmablast progenitors exist across a broad spectrum of MM genetic subtypes. Overall, our examination of primary MM tumors at various treatment stages suggests that persistence of tumor progenitor subpopulations accounts for the failure to cure MM with PI-based treatment strategies, even when complete response may be attained within the plasma cell compartment.

DISCUSSION

Although PIs can substantially debulk MM, these drugs fail to cure patients. We show here that primary MM tumors consist not only of $Xbp1s^{+}$ plasma cells and plasmablasts, but also of subpopulations of $Xbp1s^{-}$ pre-plasmablasts and of earlier $CD20^{+}$ B cell progenitors (Figure 8A) that are intrinsically PI insensitive. Whereas BTZ is potently cytotoxic to the predominating MM plasma cell and plasmablast compartments, tumor progenitor subpopulations including $Xbp1s^{-}$ pre-plasmablasts and B cells persist in BTZ-treated patients (Figure 8B). We propose that the inability of PIs such as BTZ to address these nonsecretory tumor cell progenitors substantially accounts for the failure of PI therapy to cure MM.

The malignant plasma cells encountered in MM are professional secretory cells typified by massive protein synthesis, an expanded ER network, and elevated basal ER stress. This likely explains the unique sensitivity of MM to PIs, which exacerbate ER stress by inhibiting ERAD (Elkabetz et al., 2004; Lee et al., 2003; Obeng et al., 2006). $Xbp1s^{-}$ progenitors however lack full secretory status and produce less Ig (Jourdan et al., 2011; Reimold et al., 2001). *XBP1*-silenced MM plasma cells similarly produce less Ig. Because the foremost activity of the ER in plasma cells is Ig synthesis, pre-plasmablasts and earlier progenitors, which produce less Ig, have a lower ER pre-load than plasma cells, rendering them predictably less vulnerable to lethal ER stress when ERAD is inhibited.

The finding that suppression of a branch of the ER homeostatic UPR mediates PI resistance, when PIs induce cytotoxicity in MM via the induction of ER stress, is notably contrary to any expectation from consideration of the UPR alone. However, whereas PIs cause activation of Atf6 and Perk in response to ER stress, Xbp1s activity is only minimally enhanced, perhaps because PIs stabilize ubiquitinated Xbp1u, which can act as a dominant negative (Davenport et al., 2007; Lee et al., 2003; Obeng et al., 2006). Because Xbp1 fails to contribute to ER homeostasis following PI treatment, its loss likely has no negative effect on the survival of PI-treated cells. Instead, the overriding effect for MM cells of Xbp1 suppression is a de-commitment to secretory Ig production, which reduces ER loading and ultimately enables the cell to better withstand ERAD inhibition.

Notably the existence of PI-insensitive $Xbp1s^{-}$ tumor progenitors within primary MM tumors likely produces class-effect PI resistance that is independent of drug identity, in contrast to resistance produced by PI-binding site *PSMB5* mutations. Therefore, primary MM tumors that are resistant to BTZ via $Xbp1s^{-}$ tumor progenitors may also prove to be cross-resistant to proteasome inhibition induced by carfilzomib, the second-in-class PI recently approved by the US Food and Drug Administration, consistent with early clinical findings (Siegel et al., 2012).

Xbp1 has been reported to be essential for MM pathogenesis (Carrasco et al., 2007). Because Ire1 directly regulates Xbp1, Ire1 inhibitors are currently under development for the treatment of MM (Koong et al., 2006; Kotz, 2011; Papandreou et al., 2011). However, we find that Xbp1 is not required for MM tumor cell survival, only for secretory maturation, and that its absence promotes PI resistance. This suggests that Ire1 inhibitors used outside of carefully construed combination strategies could prove ineffectual for the treatment of MM and may be deleterious if combined with PIs.

Maturation arrest likely represents a final common pathway that unifies a spectrum of genetic or epigenetic changes within MM tumors that escape therapeutic pressures or the limitations of the microenvironment. Notably, *PRDM1*, like *XBP1*, is essential for plasma cell maturation and for Ig production (Shapiro-Shelef et al., 2003) and is also recurrently mutated in MM tumors (Chapman et al., 2011), suggesting that mutation of genes other than *IRE1* or *XBP1* may drive maturation arrest in MM. Furthermore, mutations of *IRE1* and *XBP1* can be identified in MM cell lines that have not been exposed to BTZ (data not shown), suggesting that such mutations can serve purposes other than BTZ resistance. Expression profiling of BTZ-resistant MM tumors

$CD38^{-}$ $CD138^{-}$ B cells (d) were examined for concurrent Xbp1s protein expression by IF and for *IGH-CCND1* gene fusion (arrows), by FISH. (e) Viable $CD38^{-}$ $CD138^{-}$ B cells were also examined for CD20 expression and for *IGH-CCND1* by IF-FISH.
(D) MM tumor progenitor frequency summarized by patient status for the bone marrow examples presented.
Scale bar: 5 μM. See also Figure S7.

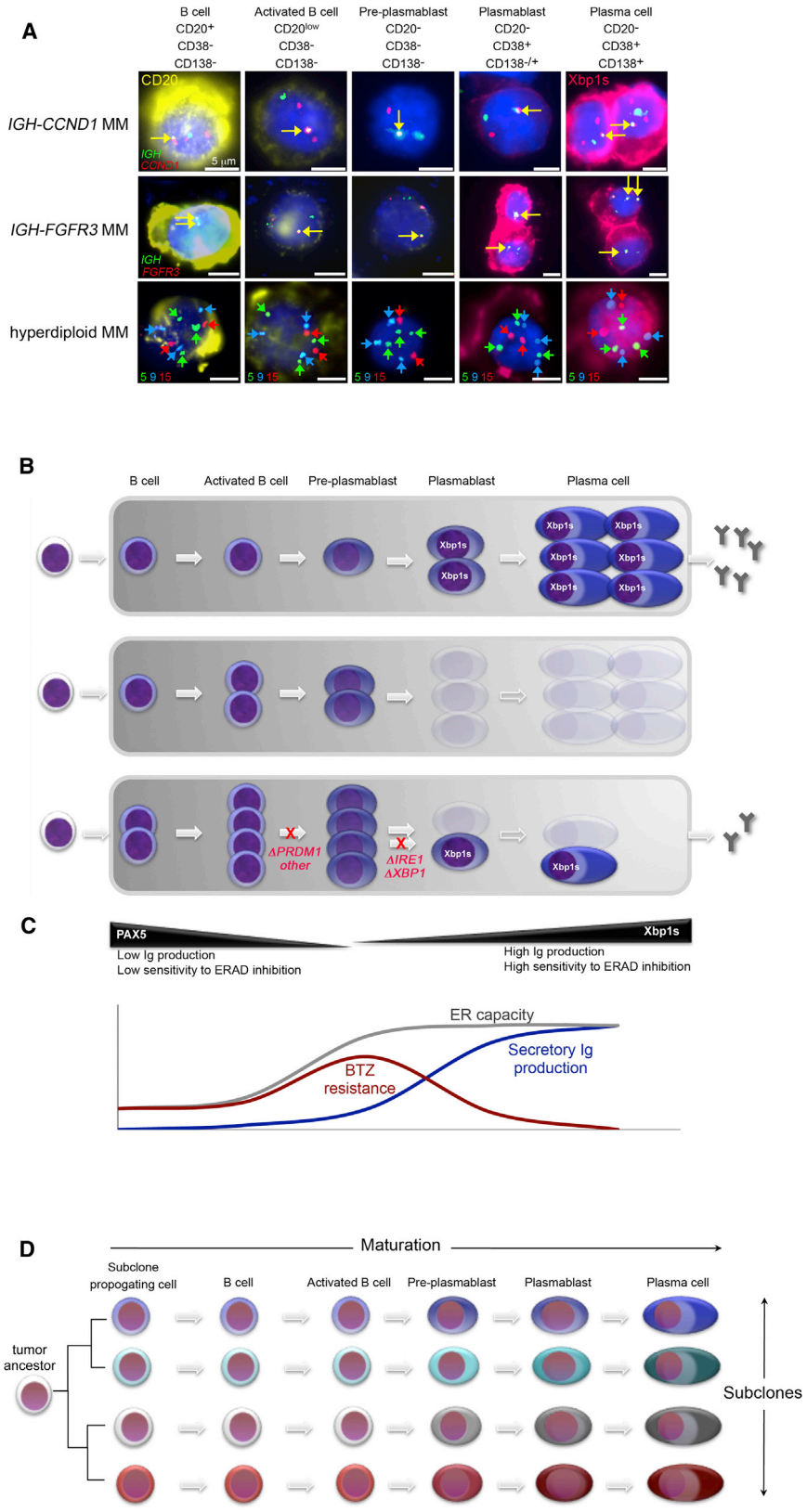

Figure 8. Tumor Progenitor Cells in Multiple Myeloma and Their Role in Therapeutic Resistance

(A) Summary of primary MM progenitor stages, which correspond to physiological stages of B cell to plasma cell maturation (from left to right), as observed in MM genetic subtypes with t(11;14) *IGH-CCND1* (top), t(4;14) *IGH-FGFR3/MMSET* (middle), or hyperdiploid karyotype (bottom). Progenitors were characterized by IF-FISH as in Figure 6. CD20 protein expression is shown in yellow; Xbp1s protein is shown in pink. Gene fusions between *IGH* (top and middle, green) and *CCND1* (top, red) or *FGFR3* loci (middle, red) are indicated by a yellow arrow. In the bottom row, trisomies of chromosomes 5 (green) and 9 (blue) and diploidy of chromosome 15 (red) are indicated by arrows. Scale bars: 5 μm.

(B) Schema showing tumor progenitor organization in newly diagnosed MM (top). Tumor B cell and pre-plasmablast progenitors are intrinsically resistant to PI, preventing cure, even in patients who achieve plasma cell complete response (CR; middle). MM progression on PI treatment is achieved in some MM tumors by maturation arrest at the pre-plasmablast or earlier B cell stages, preventing secretory commitment. Mutations identified in MM that may mediate maturation arrest are shown in red (bottom). Cells eliminated by PI therapy are shown as ghosts.

(C) Schema comparing the relative ER capacity and ER burden of plasma cell precursors. A "sweet spot" appears to exist at the activated B cell and pre-plasmablast stage, where ER maturation precedes secretory Ig production, contributing to the reduced susceptibility of these cells to lethal ER stress following PI-induced ERAD inhibition. Whereas some MM tumors develop PI resistance by maturation arrest at the pre-plasmablast stage, mantle cell lymphoma is instead reported to achieve PI resistance by promoting maturation toward this state.

(D) A model of intratumor cellular diversity, which likely contributes to the failure to cure MM. A plethora of tumor cell phenotypes arise from the presence of multiple genetic subclones and from multiple maturation stages within each subclone.

suggests that these tumors have reduced IL-6 sensitivity (with reduced *IL6R* and *IL6ST*), which can be directly attributed to suppression of Xbp1s. This suggests that MM maturation arrest not only enables PI resistance, but may also facilitate cytokine independence and extra-medullary growth. In addition, maturation arrest in MM likely contributes to the emergence of oligosecretory disease. Therefore, PIs appear to exert a selective pressure on MM tumors that may alter the clinical picture of relapsed MM encountered by modern physicians, contributing to a higher incidence of extra-medullary oligosecretory disease.

While we demonstrate that MM cells achieve BTZ resistance via de-commitment to terminal plasma cell maturation, others have instead found that MCL tumor cells attain BTZ resistance by plasmacytic differentiation (Pérez-Galán et al., 2011). However, BTZ-resistant MCLs fail to acquire Xbp1s or Ig secretion, indicating that such cells are not full-fledged plasma cells and suggesting that their differentiation state resembles that of BTZ-resistant MM cells, namely activated B cells or pre-plasmablasts. We propose that a maturation "sweet spot" exists between pre-germinal center B cells and plasma cells, exemplified by cells with low ER burden that are intrinsically less susceptible to the lethal effects of PI, because such cells express the machinery of the adaptive UPR, but have not yet committed to Ig production (Figure 8C).

The role of tumor progenitors and maturation arrest in therapeutic resistance described here may be illustrative for other drugs and cancers, particularly for therapies targeted toward distinctive characteristics of well-differentiated tissues such as secretion, hormone responsiveness, or antigen expression. Such treatments, like PIs, may fail to address less distinctive progenitor populations and may thereby fail to provide cure.

The biology of MM is shown to be related to that of other B cell non-Hodgkin lymphomas in demonstrating a discernible trail of tumor cell maturation from B cells. Whereas most MM contain multiple genetic subclones that respond to treatment in "clonal tides" (Keats et al., 2012), we propose that within each subclone there exists a spectrum of progenitors that markedly contribute to intratumor diversity and to the ability of MM tumors to endure treatment (Figure 8D). Because tumor progenitors contribute to treatment failure in MM, these subpopulations must be addressed by future therapeutic strategies to produce a pervasive cure for patients.

EXPERIMENTAL PROCEDURES

RNAi Screens

High-throughput siRNA studies in MM cells were conducted as described (Tiedemann et al., 2010, 2012; Zhu et al., 2011). To identify BTZ resistance mechanisms, genes were ranked by mean siRNA Bliss independence scores at BTZ IC90.

Gene Expression Data

MM tumor profiles from patients enrolled on the APEX Study 039 of BTZ were obtained from NCBI Gene Expression Omnibus (GEO; GSE9782; Mulligan et al., 2007). Three Xbp1 signature gene sets were used: XBP1_Staudt_SigDB reflects Xbp1 overexpression in B cells (Shaffer et al., 2006) and together with other lymphoid transcription factor signatures was obtained from http://lymphochip.nih.gov/signaturedb/; V$XBP1_01 represents genes with promoters containing a conserved Xbp1 motif and is from the Broad MSigDB at http://www.broadinstitute.org/gsea/msigdb/index.jsp; XBP1_MM and the related Ire1 signature, IRE1_MM, were generated by shRNA knockdown of Xbp1 or Ire1 in MM cells. Plasma cell progenitor profiles were obtained from ArrayExpress (http://www.ebi.ac.uk/microarray-as/ae/; E-MEXP-3034 and E-MEXP-2360; Jourdan et al., 2011).

Lentiviral Transductions

Viruses were prepared in 293T cells. MM cells were transduced using 293T supernatant diluted to 30%–50% in media and 8 μg/ml polybrene.

XBP1 Constructs

Human XBP1u and XBP1s cDNA (OriGene) were cloned into pWPIs1. Mutations were generated with PCR.

Gene Expression Profiling

Samples were hybridized on Affymetrix HG-U133 Plus 2.0 GeneChip microarrays (Affymetrix) and analyzed using GeneSpring GX 12.1 (Agilent Technologies).

MM Samples

All patient samples were obtained following informed consent in compliance with the Declaration of Helsinki and a protocol approved by the University Health Network Research Ethics Board.

IF-FISH

Slides were fixed in 4% paraformaldehyde, permeabilized with 0.5% Triton X-100, incubated with primary and secondary antibodies and then mounted in Vectashield (Vector Laboratories). IF images were acquired. Coverslips were removed and cells were treated with 0.005% pepsin in 0.01N HCl, 1% formaldehyde, and with ethanol and were then hybridized with Vysis LSI or Cytocell Aquarius DNA Probes. FISH images were acquired at IF image coordinates.

ACCESSION NUMBERS

The NCBI GEO accession number for the microarray results reported in this paper is GSE44968.

SUPPLEMENTAL INFORMATION

Supplemental Information includes Supplemental Experimental Procedures, seven figures, and one table and can be found with this article online at http://dx.doi.org/10.1016/j.ccr.2013.08.009.

ACKNOWLEDGMENTS

This research was supported by the Canadian Cancer Society (grant no. 701464), the Molly and David Bloom Chair in Multiple Myeloma Research, the Arthur Macaulay Cushing Estate, and The Princess Margaret Cancer Foundation. We thank the patients, Dr. Chris Chen, Dr. Ade Olujohungbe, and the Manitoba Tumor Bank for providing samples and Dr. Brad Wouters and Dr. Leif Bergsagel for expert comments.

Received: March 8, 2013
Revised: June 13, 2013
Accepted: August 13, 2013
Published: September 9, 2013

REFERENCES

Alexanian, R., Delasalle, K., Wang, M., Thomas, S., and Weber, D. (2012). Curability of multiple myeloma. Bone Marrow Res. *2012*, 916479.

Balsas, P., Galán-Malo, P., Marzo, I., and Naval, J. (2012). Bortezomib resistance in a myeloma cell line is associated to PSMβ5 overexpression and polyploidy. Leuk. Res. *36*, 212–218.

Calfon, M., Zeng, H., Urano, F., Till, J.H., Hubbard, S.R., Harding, H.P., Clark, S.G., and Ron, D. (2002). IRE1 couples endoplasmic reticulum load to secretory capacity by processing the XBP-1 mRNA. Nature *415*, 92–96.

Carrasco, D.R., Sukhdeo, K., Protopopova, M., Sinha, R., Enos, M., Carrasco, D.E., Zheng, M., Mani, M., Henderson, J., Pinkus, G.S., et al. (2007). The differentiation and stress response factor XBP-1 drives multiple myeloma pathogenesis. Cancer Cell *11*, 349–360.

Chapman, M.A., Lawrence, M.S., Keats, J.J., Cibulskis, K., Sougnez, C., Schinzel, A.C., Harview, C.L., Brunet, J.P., Ahmann, G.J., Adli, M., et al. (2011). Initial genome sequencing and analysis of multiple myeloma. Nature *471*, 467–472.

Chen, S., Blank, J.L., Peters, T., Liu, X.J., Rappoli, D.M., Pickard, M.D., Menon, S., Yu, J., Driscoll, D.L., Lingaraj, T., et al. (2010). Genome-wide siRNA screen for modulators of cell death induced by proteasome inhibitor bortezomib. Cancer Res. *70*, 4318–4326.

Davenport, E.L., Moore, H.E., Dunlop, A.S., Sharp, S.Y., Workman, P., Morgan, G.J., and Davies, F.E. (2007). Heat shock protein inhibition is associated with activation of the unfolded protein response pathway in myeloma plasma cells. Blood *110*, 2641–2649.

de Wilt, L.H., Jansen, G., Assaraf, Y.G., van Meerloo, J., Cloos, J., Schimmer, A.D., Chan, E.T., Kirk, C.J., Peters, G.J., and Kruyt, F.A. (2012). Proteasome-based mechanisms of intrinsic and acquired bortezomib resistance in non-small cell lung cancer. Biochem. Pharmacol. *83*, 207–217.

Elkabetz, Y., Shapira, I., Rabinovich, E., and Bar-Nun, S. (2004). Distinct steps in dislocation of luminal endoplasmic reticulum-associated degradation substrates: roles of endoplamic reticulum-bound p97/Cdc48p and proteasome. J. Biol. Chem. *279*, 3980–3989.

Franke, N.E., Niewerth, D., Assaraf, Y.G., van Meerloo, J., Vojtekova, K., van Zantwijk, C.H., Zweegman, S., Chan, E.T., Kirk, C.J., Geerke, D.P., et al. (2011). Impaired bortezomib binding to mutant beta5 subunit of the proteasome is the underlying basis for bortezomib resistance in leukemia cells. Leukemia.

Hu, C.C., Dougan, S.K., McGehee, A.M., Love, J.C., and Ploegh, H.L. (2009). XBP-1 regulates signal transduction, transcription factors and bone marrow colonization in B cells. EMBO J. *28*, 1624–1636.

Jourdan, M., Caraux, A., Caron, G., Robert, N., Fiol, G., Rème, T., Bolloré, K., Vendrell, J.P., Le Gallou, S., Mourcin, F., et al. (2011). Characterization of a transitional preplasmablast population in the process of human B cell to plasma cell differentiation. J. Immunol. *187*, 3931–3941.

Keats, J.J., Chesi, M., Egan, J.B., Garbitt, V.M., Palmer, S.E., Braggio, E., Van Wier, S., Blackburn, P.R., Baker, A.S., Dispenzieri, A., et al. (2012). Clonal competition with alternating dominance in multiple myeloma. Blood *120*, 1067–1076.

Kim, I., Xu, W., and Reed, J.C. (2008). Cell death and endoplasmic reticulum stress: disease relevance and therapeutic opportunities. Nat. Rev. Drug Discov. *7*, 1013–1030.

Koong, A.C., Chauhan, V., and Romero-Ramirez, L. (2006). Targeting XBP-1 as a novel anti-cancer strategy. Cancer Biol. Ther. *5*, 756–759.

Kotz, J. (2011). Cancer stress tests. SciBX *4*, 1–2.

Lee, A.H., Iwakoshi, N.N., Anderson, K.C., and Glimcher, L.H. (2003). Proteasome inhibitors disrupt the unfolded protein response in myeloma cells. Proc. Natl. Acad. Sci. USA *100*, 9946–9951.

Lichter, D.I., Danaee, H., Pickard, M.D., Tayber, O., Sintchak, M., Shi, H., Richardson, P.G., Cavenagh, J., Bladé, J., Façon, T., et al. (2012). Sequence analysis of β-subunit genes of the 20S proteasome in patients with relapsed multiple myeloma treated with bortezomib or dexamethasone. Blood *120*, 4513–4516.

McConkey, D.J., and Zhu, K. (2008). Mechanisms of proteasome inhibitor action and resistance in cancer. Drug Resist. Updat. *11*, 164–179.

Mulligan, G., Mitsiades, C., Bryant, B., Zhan, F., Chng, W.J., Roels, S., Koenig, E., Fergus, A., Huang, Y., Richardson, P., et al. (2007). Gene expression profiling and correlation with outcome in clinical trials of the proteasome inhibitor bortezomib. Blood *109*, 3177–3188.

Nutt, S.L., Taubenheim, N., Hasbold, J., Corcoran, L.M., and Hodgkin, P.D. (2011). The genetic network controlling plasma cell differentiation. Semin. Immunol. *23*, 341–349.

Obeng, E.A., Carlson, L.M., Gutman, D.M., Harrington, W.J., Jr., Lee, K.P., and Boise, L.H. (2006). Proteasome inhibitors induce a terminal unfolded protein response in multiple myeloma cells. Blood *107*, 4907–4916.

Oerlemans, R., Franke, N.E., Assaraf, Y.G., Cloos, J., van Zantwijk, I., Berkers, C.R., Scheffer, G.L., Debipersad, K., Vojtekova, K., Lemos, C., et al. (2008). Molecular basis of bortezomib resistance: proteasome subunit beta5 (PSMB5) gene mutation and overexpression of PSMB5 protein. Blood *112*, 2489–2499.

Ozaki, K., Spolski, R., Feng, C.G., Qi, C.F., Cheng, J., Sher, A., Morse, H.C., 3rd, Liu, C., Schwartzberg, P.L., and Leonard, W.J. (2002). A critical role for IL-21 in regulating immunoglobulin production. Science *298*, 1630–1634.

Papandreou, I., Denko, N.C., Olson, M., Van Melckebeke, H., Lust, S., Tam, A., Solow-Cordero, D.E., Bouley, D.M., Offner, F., Niwa, M., and Koong, A.C. (2011). Identification of an Ire1alpha endonuclease specific inhibitor with cytotoxic activity against human multiple myeloma. Blood *117*, 1311–1314.

Pérez-Galán, P., Mora-Jensen, H., Weniger, M.A., Shaffer, A.L., 3rd, Rizzatti, E.G., Chapman, C.M., Mo, C.C., Stennett, L.S., Rader, C., Liu, P., et al. (2011). Bortezomib resistance in mantle cell lymphoma is associated with plasmacytic differentiation. Blood *117*, 542–552.

Politou, M., Karadimitris, A., Terpos, E., Kotsianidis, I., Apperley, J.F., and Rahemtulla, A. (2006). No evidence of mutations of the PSMB5 (beta-5 subunit of proteasome) in a case of myeloma with clinical resistance to Bortezomib. Leuk. Res. *30*, 240–241.

Reimold, A.M., Iwakoshi, N.N., Manis, J., Vallabhajosyula, P., Szomolanyi-Tsuda, E., Gravallese, E.M., Friend, D., Grusby, M.J., Alt, F., and Glimcher, L.H. (2001). Plasma cell differentiation requires the transcription factor XBP-1. Nature *412*, 300–307.

Richardson, P.G., Sonneveld, P., Schuster, M.W., Irwin, D., Stadtmauer, E.A., Facon, T., Harousseau, J.L., Ben-Yehuda, D., Lonial, S., Goldschmidt, H., et al.; Assessment of Proteasome Inhibition for Extending Remissions (APEX) Investigators. (2005). Bortezomib or high-dose dexamethasone for relapsed multiple myeloma. N. Engl. J. Med. *352*, 2487–2498.

Ron, D., and Walter, P. (2007). Signal integration in the endoplasmic reticulum unfolded protein response. Nat. Rev. Mol. Cell Biol. *8*, 519–529.

Rückrich, T., Kraus, M., Gogel, J., Beck, A., Ovaa, H., Verdoes, M., Overkleeft, H.S., Kalbacher, H., and Driessen, C. (2009). Characterization of the ubiquitin-proteasome system in bortezomib-adapted cells. Leukemia *23*, 1098–1105.

Shaffer, A.L., Shapiro-Shelef, M., Iwakoshi, N.N., Lee, A.H., Qian, S.B., Zhao, H., Yu, X., Yang, L., Tan, B.K., Rosenwald, A., et al. (2004). XBP1, downstream of Blimp-1, expands the secretory apparatus and other organelles, and increases protein synthesis in plasma cell differentiation. Immunity *21*, 81–93.

Shaffer, A.L., Wright, G., Yang, L., Powell, J., Ngo, V., Lamy, L., Lam, L.T., Davis, R.E., and Staudt, L.M. (2006). A library of gene expression signatures to illuminate normal and pathological lymphoid biology. Immunol. Rev. *210*, 67–85.

Shapiro-Shelef, M., Lin, K.I., McHeyzer-Williams, L.J., Liao, J., McHeyzer-Williams, M.G., and Calame, K. (2003). Blimp-1 is required for the formation of immunoglobulin secreting plasma cells and pre-plasma memory B cells. Immunity *19*, 607–620.

Siegel, D.S., Martin, T., Wang, M., Vij, R., Jakubowiak, A.J., Lonial, S., Trudel, S., Kukreti, V., Bahlis, N., Alsina, M., et al. (2012). A phase 2 study of single-agent carfilzomib (PX-171-003-A1) in patients with relapsed and refractory multiple myeloma. Blood *120*, 2817–2825.

Tiedemann, R.E., Zhu, Y.X., Schmidt, J., Yin, H., Shi, C.X., Que, Q., Basu, G., Azorsa, D., Perkins, L.M., Braggio, E., et al. (2010). Kinome-wide RNAi studies in human multiple myeloma identify vulnerable kinase targets, including a lymphoid-restricted kinase, GRK6. Blood *115*, 1594–1604.

Tiedemann, R.E., Zhu, Y.X., Schmidt, J., Shi, C.X., Sereduk, C., Yin, H., Mousses, S., and Stewart, A.K. (2012). Identification of molecular vulnerabilities in human multiple myeloma cells by RNA interference lethality screening of the druggable genome. Cancer Res. *72*, 757–768.

Wang, L., Kumar, S., Fridley, B.L., Kalari, K.R., Moon, I., Pelleymounter, L.L., Hildebrandt, M.A., Batzler, A., Eckloff, B.W., Wieben, E.D., and Greipp, P.R. (2008). Proteasome beta subunit pharmacogenomics: gene resequencing and functional genomics. Clin. Cancer Res. *14*, 3503–3513.

Zhu, K., Dunner, K., Jr., and McConkey, D.J. (2010). Proteasome inhibitors activate autophagy as a cytoprotective response in human prostate cancer cells. Oncogene *29*, 451–462.

Zhu, Y.X., Tiedemann, R., Shi, C.X., Yin, H., Schmidt, J.E., Bruins, L.A., Keats, J.J., Braggio, E., Sereduk, C., Mousses, S., and Stewart, A.K. (2011). RNAi screen of the druggable genome identifies modulators of proteasome inhibitor sensitivity in myeloma including CDK5. Blood *117*, 3847–3857.

Cancer Cell
Article

Haploinsufficiency of *SAMD9L*, an Endosome Fusion Facilitator, Causes Myeloid Malignancies in Mice Mimicking Human Diseases with Monosomy 7

Akiko Nagamachi,[1,6] Hirotaka Matsui,[1,6] Hiroya Asou,[1] Yuko Ozaki,[1] Daisuke Aki,[1] Akinori Kanai,[1] Keiyo Takubo,[3] Toshio Suda,[3] Takuro Nakamura,[4] Linda Wolff,[5] Hiroaki Honda,[2,*] and Toshiya Inaba[1,*]
[1]Department of Molecular Oncology and Leukemia Program Project
[2]Department of Disease Model, Research Institute for Radiation Biology and Medicine
Hiroshima University, 1-2-3 Kasumi, Minami-ku, Hiroshima 734-8553, Japan
[3]Department of Cell Differentiation, The Sakaguchi Laboratory of Developmental Biology, Keio University School of Medicine, Shinjuku-ku, Tokyo 160-8582, Japan
[4]Division of Carcinogenesis, Cancer Institute, Japanese Foundation for Cancer Research, Tokyo 135-0063, Japan
[5]Leukemogenosis Section, Laboratory of Cellular Oncology, National Cancer Institute, NIH, Bethesda, MD 20892-4255, USA
[6]These authors contributed equally to this work
*Correspondence: hhonda@hiroshima-u.ac.jp (H.H.), tinaba@hiroshima-u.ac.jp (T.I.)
http://dx.doi.org/10.1016/j.ccr.2013.08.011

SUMMARY

Monosomy 7 and interstitial deletion of 7q (−7/7q−) are well-recognized nonrandom chromosomal abnormalities frequently found among patients with myelodysplastic syndromes (MDSs) and myeloid leukemias. We previously identified candidate myeloid tumor suppressor genes (*SAMD9*, *SAMD9-like* = *SAMD9L*, and *Miki*) in the 7q21.3 subband. We established *SAMD9L*-deficient mice and found that *SAMD9L*$^{+/-}$ mice as well as *SAMD9L*$^{-/-}$ mice develop myeloid diseases resembling human diseases associated with −7/7q−. *SAMD9L*-deficient hematopoietic stem cells showed enhanced colony formation potential and in vivo reconstitution ability. SAMD9L localizes in early endosomes. *SAMD9L*-deficient cells showed delays in homotypic endosome fusion, resulting in persistence of ligand-bound cytokine receptors. These findings suggest that haploinsufficiency of *SAMD9L* and/or *SAMD9* gene(s) contributes to myeloid transformation.

INTRODUCTION

The first report of monosomy 7 in patients with myeloid malignancies was published in 1964, soon after the discovery of the Philadelphia chromosome in 1960, that described the deletion of a C group chromosome in three patients with refractory anemia (myelodysplastic syndrome [MDS] by current criteria) that subsequently developed acute myelogenous leukemia (AML) (E.J. Freireich et al., 1964, Clin. Res., abstract). Since then, −7/7q− has been established as the most representative chromosomal abnormality in a wide variety of myeloid malignancies (10%–20%), including sporadic MDS in the elderly as the sole anomaly, secondary AML in young patients, and AML carrying leukemogenic chimeras as an additional chromosome abnormality (Brunning et al., 2008; Johnson and Cotter, 1997). Tremendous efforts have been made for decades to isolate the responsible genes in 7q. Recent studies indicate that the most frequent deletions among patients with MDS/AML occur within two broad regions with ambiguous borders near bands 7q22 and 7q34 (Jerez et al., 2012).

We recently identified a common microdeletion cluster in subband 7q21.3 in patients with juvenile myelomonocytic leukemia using microarray comparative genomic hybridization (mCGH) (Asou et al., 2009). This cluster contains three poorly

Significance

Chromosome loss may contribute to oncogenesis through mechanisms different from those caused by small deletions, which typically eliminate the function of one tumor suppressor gene by the deletion of one allele and a mutation in the other. In this report, we investigate two related genes, *SAMD9* and *SAMD9L*, as candidate-responsible genes for monosomy 7. Taking advantage that mouse lacks *SAMD9* gene, we established *SAMD9L*-deficient mice and found that *SAMD9L*$^{+/-}$ mice develop myeloid diseases strikingly resembling human diseases associated with −7/7q−. Because haploinsufficiency of an adjacent gene *Miki* contributes to the development of MDS through mitotic/nuclear abnormalities, our studies exemplify a mechanism for how large chromosome deletion can contribute to oncogenesis via haploinsufficiency of multiple responsible genes.

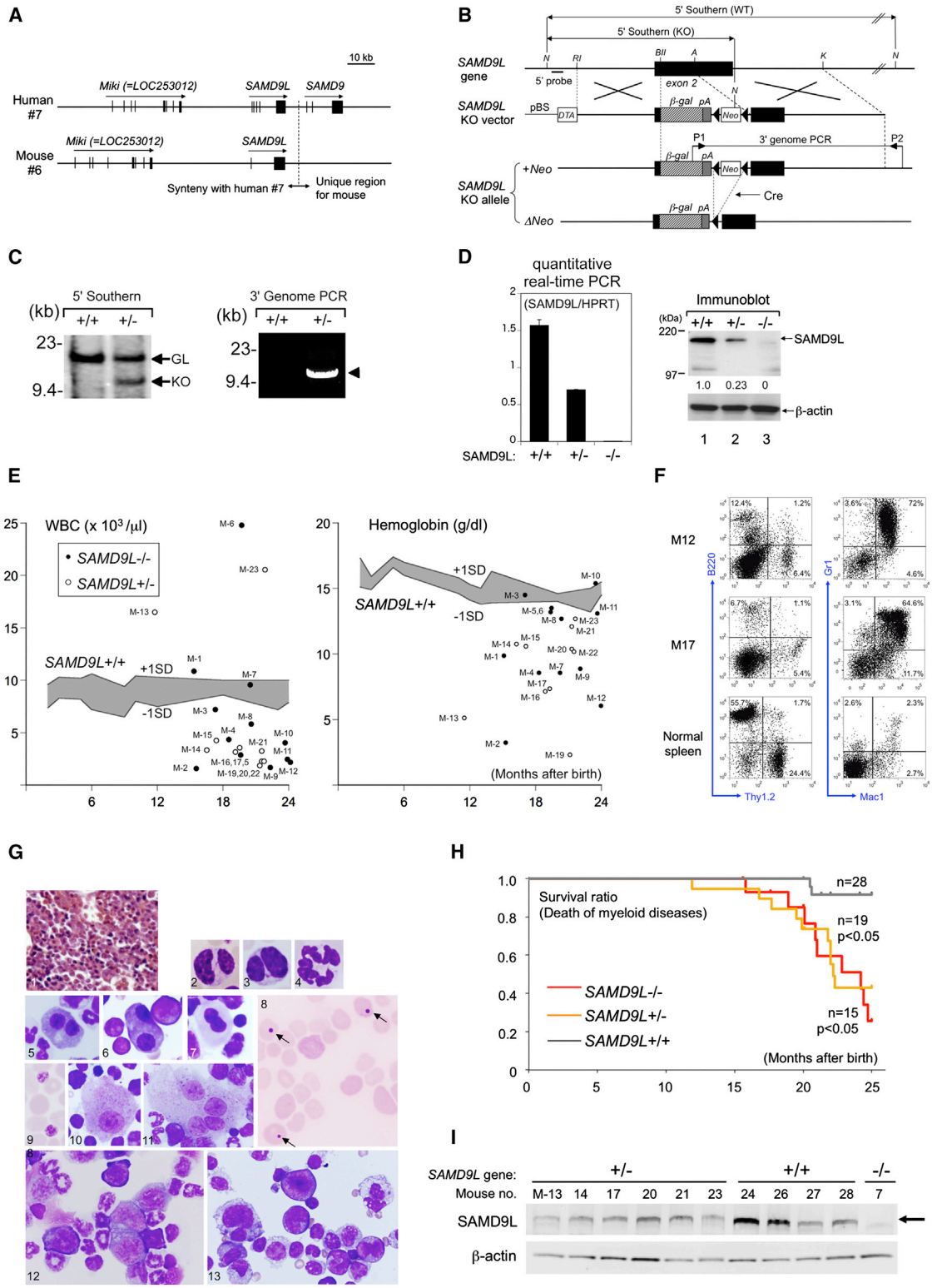

Figure 1. Development of Myeloid Dysplasia in *SAMD9L*-Deficient Mice

(A) Syntenic homology of the *SAMD9L* gene between humans and mice is presented. In humans, two related genes, *SAMD9* and *SAMD9L*, exist in tandem, whereas mice have only *SAMD9L*.

(B) Targeting strategy is illustrated. Part of the coding region of exon 2 is deleted and replaced by the *β-galactosidase* (*β-gal*) gene with the *polyA* (*pA*) and *floxed Neo*-resistance genes for removal of the *Neo*-resistance cassette by Cre recombinase. The positions of the 5′ probe for Southern blot and P1 and P2 primers for genomic PCR are shown. Restriction sites are *N* (NcoI), *RI* (EcoRI), *BII* (BglII), *A* (ApaI), and *K* (KpnI).

(legend continued on next page)

characterized genes: *sterile α motif* (*SAM*) *domain*-9 (*SAMD9*), *SAMD9L*, and *Miki* (*LOC253012*). Although mutations have rarely been seen in these genes, the genes reside proximal to the 7q22 band that is deleted in single copy in nearly 25% of patients with AML and MDS (Asou et al., 2009). We also found that Miki, a centrosomal protein that promotes alignment of chromosomes at metaphase, is a candidate gene responsible for mitotic/nuclear abnormalities routinely observed in patients with MDS (Ozaki et al., 2012).

The human *SAMD9* (*hSAMD9*) and *hSAMD9L* genes share a common gene structure and encode proteins with 60% amino acid identity. A common ancestral gene of *SAMD9/SAMD9L* is found in fish, frogs, and birds and shares roughly equal amino acid identity with both genes. Most mammals including rats have both *SAMD9* and *SAMD9L*. However, mice have only *SAMD9L*, and cows encode only an *SAMD9* homolog (Li et al., 2007), suggesting that SAMD9 and SAMD9L at least partially complement each other's functions. In humans, deleterious mutations in the *SAMD9* gene are known to cause normophosphatemic familial tumoral carcinosis (NFTC) (Topaz et al., 2006), a rare autosomal recessive disease. Because NFTC is characterized by abnormal inflammation of the skin and gingiva that is induced by excessive signaling via tumor necrosis factor α and/or interferon-γ pathways, it has been suggested that SAMD9 suppresses these inflammatory pathways (Chefetz et al., 2008). In this study, we establish *SAMD9L*-deficient mice to study possible roles of SAMD9L in the development of myeloid malignancies and elucidate its biological function.

RESULTS

SAMD9L-Deficient Mice Developed Myeloid Disorders

Mouse synteny for human chromosome subband 7q21.3 ends at the *SAMD9L* gene, and no *SAMD9* gene is present in the mouse genome (Figure 1A). We designed an *SAMD9L* knockout (KO) vector in which the central portion of exon 2 (encoding the entire SAMD9L protein) was removed and replaced with the β-*galactosidase* cDNA and an SV40 *polyA* signal, followed by a *floxed neomycin*-resistance cassette (Figure 1B). Recombinant embryonic stem cell clones (Figure 1C) were used to create $SAMD9L^{+/-}$ and $SAMD9L^{-/-}$ mice.

SAMD9L mRNA was expressed ubiquitously in mice with the highest expression in the kidney (Jiang et al., 2011). Quantitative real-time PCR revealed that the level of SAMD9L mRNA expression in the kidney of $SAMD9L^{+/-}$ mice was 45% of that in WT mice, whereas the protein expression level decreased 4-fold on immunoblots (Figure 1D).

$SAMD9L^{-/-}$ (n = 15), $SAMD9L^{+/-}$ (n = 19), and $SAMD9L^{+/+}$ (n = 28) littermates were observed regularly for signs of illness, including routine examination of peripheral blood. Among 28 $SAMD9L^{+/+}$ mice, all but 2 maintained consistent WBC counts and hemoglobin (Hb) levels throughout the 24-month observation period (Figure 1E, shaded areas). Five of the $SAMD9L^{+/+}$ mice died during the observation period (Table S1 available online).

Among 34 $SAMD9L^{+/-}$ and $SAMD9L^{-/-}$ mice, all but 1 (M-13) showed normal WBC counts and Hb levels until the age of 12 months; thereafter, 12 mice (M-2, M-5, M-9, M-11, M-12, M-14, M-16, M-17, M-19, M-20, M-21, and M-22) developed neutropenia (WBC <4,000/μl), 3 mice (M-1, M-4, and M-7) suffered from anemia (Hb <10 g/dl) with normal WBC counts, whereas 3 mice (M-6, M-13, and M-23) showed an apparent WBC increase (>15,000/μl) (Figure 1E). Of 23 mice associated with those abnormal hematological findings, 18 had markedly enlarged spleen (Table S1), in which Gr1/Mac1-positive myeloid cells were proliferated (Figure 1F). All 15 mice developing cytopenia showed bone marrow (BM) with normal or even increased cellularity (Figure 1G, panel 1), and myelodysplasia included Pseudo-Pelger-Huet anomaly (panels 2 and 3), hypersegmented neutrophils (panel 4), erythroblasts with abnormal nuclei (panels 5–7), Howell-Jolly body, polychromasia, anisopoikilocytosis (panel 8), giant platelets (panel 9), and megakaryocytes with round shape nuclei (panels 10 and 11). BM frequently showed erythroid and/or myeloid maturation arrest (Figure 1G, panels 12 and 13). Based on Bethesda proposals for classification of nonlymphoid hematopoietic neoplasms in mice (Kogan et al., 2002), the types and frequencies of myeloid diseases included myeloid dysplasia (8 of 15 $SAMD9L^{-/-}$; 8 of 19 $SAMD9L^{+/-}$), myeloid leukemia (1 of 15 $SAMD9L^{-/-}$; 1 of 19 $SAMD9L^{+/-}$), and myeloproliferative disease (1 of 19 $SAMD9L^{+/-}$).

SAMD9L-deficient mice died of myeloid disease (Figure 1H; Table S1) at significantly higher frequency than $SAMD9L^{+/+}$ mice ($p < 0.05$, log rank test). $SAMD9L^{+/-}$ mice that developed myeloid diseases still expressed SAMD9L protein (Figure 1I), and no mutations were detected in the coding regions of the *SAMD9L* gene or mRNA.

MOL4070A Infection Accelerated Disease Latency and Frequency

MOL4070A retrovirus (Wolff et al., 2003), a derivative of Moloney murine leukemia virus, induces myeloid malignancies in

(C) 5′ Southern blot and 3′ genomic PCR to detect homologous recombination are shown. Germline (GL) and KO allele-derived bands are indicated by arrows (left panel), and the recombination-specific PCR product is indicated by the arrowhead (right).
(D) SAMD9L transcripts analyzed by quantitative real-time PCR and normalized by HPRT (left) are shown. Immunoblot analysis of kidney extract used SAMD9L (top) or β-actin (bottom) antibody (right). *SAMD9L* genotypes are indicated below (left) or above (right). The relative expression ratio of SAMD9L to β-actin is indicated between the two panels. Error bars, SD.
(E) Peripheral WBC count (left) or Hb level (right) is presented. Shaded areas indicate the range of values from −1 to +1 SD in $SAMD9L^{+/+}$ mice. Closed circles indicate $SAMD9L^{-/-}$ mice; open circles represent $SAMD9L^{+/-}$ mice.
(F) Flow cytometric analysis of splenic cells is shown.
(G) Hematoxylin-eosin staining of formalin-fixed BM (panel 1), Giemsa-stained peripheral blood (panels 2–4, 8, and 9), and BM smears (panels 5–7 and 10–13) from *SAMD9L*-deficient mice that developed MDS is shown. Arrows indicate Howell-Jolly bodies (panel 8). Scale bars, 5 μm.
(H) Myeloid disease-free survival curves are illustrated. Data from mice that died of causes other than myeloid malignancies are censored.
(I) Immunoblot analysis of mouse splenic cell extracts used SAMD9L (top) or β-actin (bottom) antibody. *SAMD9L* genotypes are indicated above. The arrow indicates the position of SAMD9L.
See also Table S1.

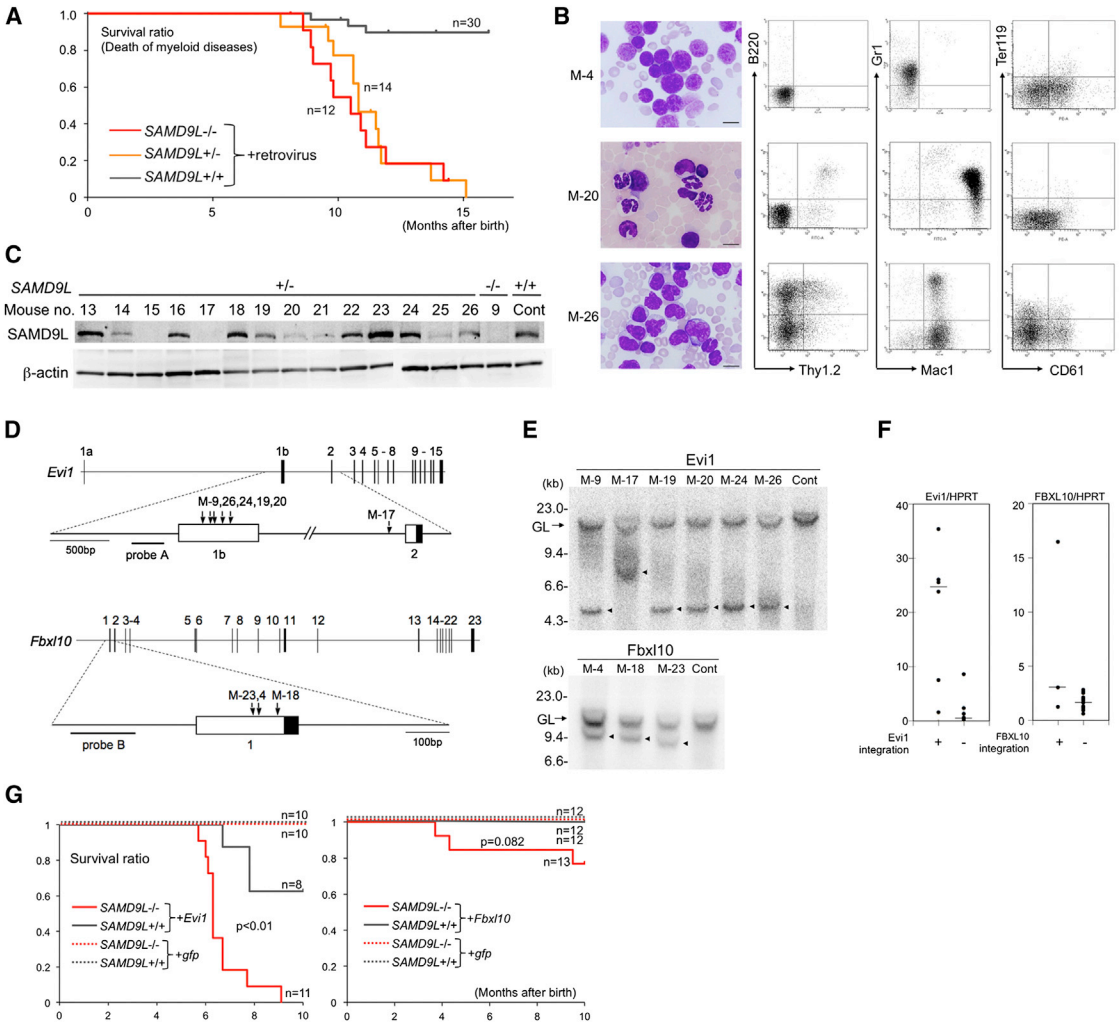

Figure 2. *SAMD9L* Deficiency Predisposes Mice to Myeloid Malignancies

(A) Myeloid disease-free survival curves of mice infected with MOL4070A retrovirus are presented. Data from mice that died of causes other than myeloid malignancies are censored.

(B) Representative phenotypes of myeloid leukemia are shown. Wright-Giemsa staining of peripheral blood smears and results of flow cytometric analysis of splenic cells are shown. Scale bars, 10 μm.

(C) Immunoblot analysis of extracts from splenic cells used SAMD9L (top) or β-actin (bottom) antibody. Mouse number and genotype are indicated above.

(D) Schematic illustration of the *Evi1* (top) and *Fbxl10* (bottom) genes identified as CISs is shown. Vertical arrows indicate viral integration sites.

(E) Southern blot analysis to detect retroviral integration is presented. Germline (GL) bands (arrows) and rearranged bands (arrowheads) are indicated.

(F) *Evi1* (left) and *Fbxl10* (right) transcripts analyzed by quantitative real-time PCR and normalized to the level of HPRT transcripts in splenic cells from mice with or without integration of the indicated gene are shown. Horizontal short lines indicate median values.

(G) Survival curves of lethally irradiated mice that had been transfused with BM cells from *SAMD9L*$^{-/-}$ or *SAMD9L*$^{+/+}$ mice infected with either *Evi1*- or control (*GFP*)-expressing retrovirus (left panel) or with either *Fbxl10*- or control (*GFP*)-expressing retrovirus (right panel) are illustrated.

See also Tables S2–S4.

mice harboring a propensity for myeloid diseases (Castilla et al., 2004). When newborn mice were injected intraperitoneally with MOL4070A retrovirus, almost all *SAMD9L*$^{+/-}$ (12 of 14) and *SAMD9L*$^{-/-}$ (10 of 12) mice died of nonlymphoid hematopoietic neoplasms (Figure 2A; Table S2), much earlier than mice that developed spontaneous myeloid malignancies (Figure 1F). In contrast, MOL4070A-infected *SAMD9L*$^{+/+}$ mice developed myeloid diseases at a significantly lower frequency (5 of 30; $p < 0.01$) within the 15-month observation period (Figure 2A).

Unlike uninfected *SAMD9L*-deficient mice, which preferentially developed MDS (13 of 30), 16 of 26 virus-infected mice showed myeloid leukemias of various types such as immature myeloid leukemia expressing myeloid (Gr1) and megakaryocyte (CD61) markers (Figure 2B, M-4), myelomonocytic leukemia with weak CD61 expression (M-20), and monocytic leukemia partially positive for B cell (B220), erythroid (Ter119), or megakaryocyte markers (M-26). Although leukemic cells from two *SAMD9L*$^{+/-}$ mice showed no SAMD9L protein (Figure 2C, M-15 and M-17) in immunoblots, long-distance PCR readily

amplified full-length *SAMD9L* DNA and mRNA that contained no mutation.

By the inverse PCR method (Yamashita et al., 2005), two common integration sites (CISs) were identified in leukemic samples from *SAMD9L*-deficient mice (Table S3), whereas no CIS was identified in samples from *SAMD9L*$^{+/+}$ mice. In six samples (M-9, M-17, M-19, M-20, M-24, and M-26), virus was found integrated into the *Evi1* gene (Figure 2D, upper) encoding a Zn finger transcription factor, whereas three additional samples (14%; M-4, M-18, and M-23) showed integration in the *Fbxl10* (also *JHDM1B*/*Ndy1*/*KDM2B*) gene (Frescas et al., 2007; Sánchez et al., 2007) (Figure 2D, lower), which encodes a histone H3K36 demethylase. Southern blot analysis showed polymorphic bands in all tumors (Figure 2E), indicating that the tumors were composed largely of cells with these integration sites. Quantitative real-time PCR analysis showed higher expression levels than the median level of *Evi1* mRNA in nonintegrated samples (Figure 2F, left), whereas two (M-4 and M-18) maintained higher *Fbxl10* mRNA levels relative to nonintegrated samples (Figure 2F, right panel).

Although Evi1 is well known to be overexpressed by retrovirus insertion in mouse myeloid leukemia, the frequency of 6 (27.2%) out of 22 myeloid malignancies carrying SAMD9L deficiency was remarkably high compared with other leukemogenic factors (usually around 5% or less) such as CBFβ-MYH11 (Castilla et al., 2004) and NUP98-HOXD13 (Slape et al., 2007). Enhancement of leukemia incidence in *SAMD9L*-deficient mice combined with *Evi1* or *Fbxl10* overexpression was further analyzed by retrovirus-mediated in vitro gene transfer experiments (see Experimental Procedures). Although no mice with transferred control *SAMD9L*$^{+/+}$GFP or *SAMD9L*$^{-/-}$GFP BM cells (BMCs) developed myeloid disorders during the 10-month observation period (Figure 2G), 3 of 11 mice with transferred *SAMD9L*$^{+/+}$*Evi1* cells died of hematopoietic malignancies (Table S4). This relatively low frequency of myeloid diseases induced by *Evi1* gene transfer is in agreement with previously published results by Buonamici et al. (2004), Cuenco and Ren (2004), and Watanabe-Okochi et al. (2008). In contrast, all mice (11 of 11) receiving transferred *SAMD9L*$^{-/-}$*Evi1* cells died of hematopoietic malignancies, particularly myeloid disorders (10 of 11; $p < 0.01$; Figure 2G, left). Although not a statistically significant result ($p = 0.082$), we also found that no mouse with transferred *SAMD9L*$^{+/+}$*Fbxl10* cells ($n = 12$) developed a hematopoietic malignancy, whereas 3 of 13 mice with transferred *SAMD9L*$^{-/-}$*Fbxl10* cells developed myeloid malignancies (Figure 2G, right panel).

SAMD9L Deficiency Affects Hematopoietic Stem Cells and Progenitors

Mouse (12 weeks old) BMCs were separated into three fractions: long term (LT)-LSK (CD34$^-$, CD135(Flt3)$^-$, lineage-negative [Lin$^-$], Sca-1$^+$, c-Kit$^+$); short term (ST)-LSK (CD34$^+$, CD135$^-$, LSK); and multipotent progenitor (MPP; CD34$^+$, CD135$^+$ LSK). Quantitative real-time PCR revealed that SAMD9L mRNA levels in *SAMD9L*$^{+/-}$ or *SAMD9L*$^{-/-}$ progenitors were roughly 50% or 0% of that in *SAMD9L*$^{+/+}$ cells, respectively (Figure 3A). Reduction of SAMD9L mRNA was supported by transcriptome analysis of LSK cells using a next-generation sequencer (Figure 3B), which also demonstrated that *SAMD9L* deficiency affects the expression of only a few genes (Table S5). In addition, the total number and proportion of the three LSK fractions in BM from *SAMD9L*-deficient mice were similar to those in BM from *SAMD9L*$^{+/+}$ mice (Figure 3C).

Despite these apparently small effects on the expression profile and the repertoire of early hematopoietic progenitors, colony-replating assay revealed prominent effects of *SAMD9L* deficiency. BMCs (12 weeks old) were grown in semisolid culture with appropriate cytokines, and colonies were counted and harvested for replating after 2 weeks. Although cells from *SAMD9L*$^{+/+}$ mice formed fewer colonies by the third replating (Figure 3D), cells from *SAMD9L*-deficient mice continued to form similar numbers and sizes of well-differentiated colonies beyond the seventh plating. The excess number of colonies formed was reduced by retrovirus-mediated forced expression of Samd9L (Figure 3E). These data suggested enhanced self-renewal and/or delays in differentiation of *SAMD9L*-deficient stem cells.

Enhanced reconstitution ability of stem cells was demonstrated by competitive repopulation assay using the Ly5 congenic mouse system. Irradiated Ly5.1 mice were transplanted with LT-LSK cells from *SAMD9L*$^{+/+}$ or *SAMD9L*-deficient Ly5.2 mice (10 weeks old) together with BMCs from *SAMD9L*$^{+/+}$Ly5.1 mice. Increased WBC numbers of *SAMD9L*-deficient cells relative to *SAMD9L*$^{+/+}$ cells were observed in recipient mice (Figure 3F). This was confirmed by limiting-dilution transplants using three dose concentrations of BMCs, results of which showed a higher frequency of multilineage repopulating cells (myeloid and T/B lymphocytes) at 8 weeks in *SAMD9L*$^{-/-}$ donor BM (Figure S1), suggesting enhanced reconstitution ability of stem cells and/or early hematopoietic progenitors.

In addition, growth advantage in the presence of cytokines was evident in liquid cultures of c-Kit$^+$ Lin$^-$ (KL) cells (Figure 3G), which were amplified by primary cultures of mouse BMCs using stem cell factor (SCF) and thrombopoietin (Kuribara et al., 2004). In this system, the level of SAMD9L expression in *SAMD9L*$^{+/-}$ KL cells was approximately 15% of that in *SAMD9L*$^{+/+}$ cells (Figure 3H).

Hypersensitivity of *SAMD9L*-deficient progenitors to cytokines was also shown in in vivo experiments (Figure 3I). Mice were injected with cyclophosphamide (CPA) (day 0) and human granulocyte colony-stimulating factor (hG-CSF) (days 1–4). WBC counts of control *SAMD9L*$^{+/+}$ mice without hG-CSF injection decreased rapidly until day 2 or 3 and then the counts gradually increased, whereas daily hG-CSF injection accelerated the recovery, as previously demonstrated by others (Hattori et al., 1990). *SAMD9L*-deficient mice showed significantly higher WBC counts at the nadir (day 3).

Because mice developed MDS at an old age, we examined the features of BM progenitors of old mice (26 months) by colony-replating assay. Cells from *SAMD9L*$^{+/+}$ non-MDS mice formed fewer primary colonies (Figure 3J), up to one-third of those from young mice (Figure 3D) probably due to aging, and colony formation potential was lost within replating five times. *SAMD9L*$^{+/-}$ non-MDS cells also formed fewer primary colonies; however, like *SAMD9L*-deficient cells from young mice, the colony formation potential was maintained during replating more than five times. Interestingly, cells from *SAMD9L*$^{+/-}$ MDS mice formed a reduced number of nonconcentric spread colonies, which were apparently different from colonies formed by non-MDS cells in shape (Figure 3K). These data suggested that additional abnormalities transform BM progenitors to MDS cells.

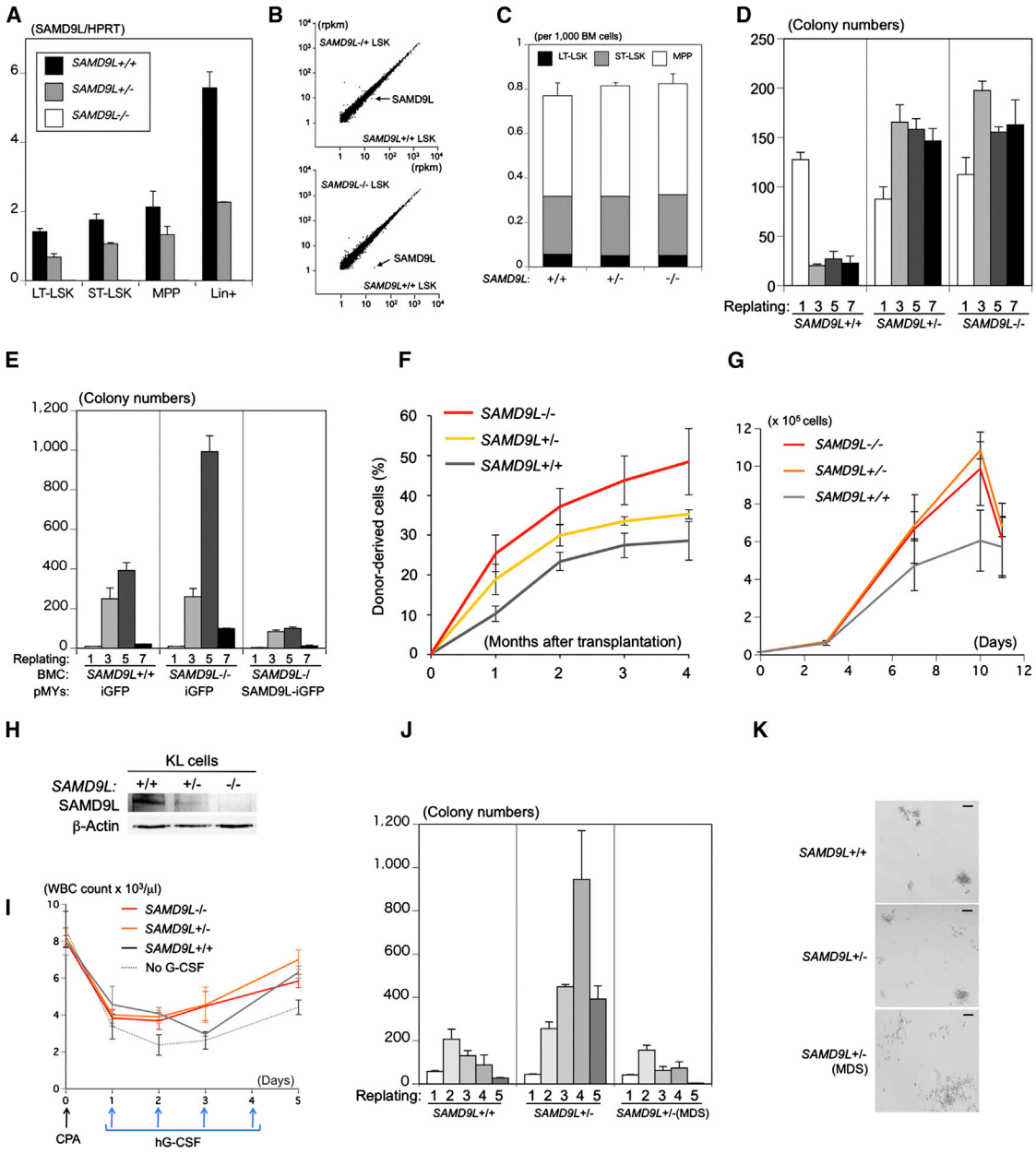

Figure 3. Hypersensitivity to Cytokines of SAMD9L-Deficient Hematopoietic Progenitors

(A) SAMD9 mRNA expression levels in hematopoietic cells are indicated below as a ratio relative to HPRT mRNA measured using quantitative real-time PCR. The mean and SD in four independent experiments are shown. Error bars, SD.

(B) Comprehensive identification and characterization of the transcriptome of LSK cells from *SAMD9L*-deficient BM are presented. Scatterplots of log10(rpkm) obtained for every transcript (>1 rpkm) in SAMD9L-deficient versus SAMD9L$^{+/+}$ LSK cells are shown.

(C) The numbers of each fraction of LSK cells per 1,000 BMCs are presented. A representative result is shown. Similar results were obtained in three independent experiments. Error bars, SD.

(D) The 2 × 10^4 BMCs obtained from 8-week-old *SAMD9L*$^{+/+}$, *SAMD9L*$^{+/-}$, and *SAMD9L*$^{-/-}$ mice were cultured in MethoCult M3434. Colonies were counted and replated at 2 × 10^4 cells every 2 weeks. Error bars, SD.

(E) BMCs were infected with pMYs retrovirus indicated below, and 0.7 × 10^4 c-Kit$^+$, GFP$^+$ cells were sorted and cultured in MethoCult M3434. Colonies were counted and replated at 2 × 10^4 cells every 10 days. iGFP, ires-GFP. Error bars, SD.

(F) Repopulation ability of *SAMD9L*$^{+/+}$, *SAMD9L*$^{+/-}$, and *SAMD9L*$^{-/-}$ LT-LSK cells isolated from 10-week-old mice is illustrated. The percentages of donor-derived (Ly5.2+) *SAMD9L*$^{+/-}$ and *SAMD9L*$^{-/-}$ cells in the total WBCs in the peripheral blood at periods indicated after transplantation are shown. Data are plotted as means with error bars (SD). Representative results from three independent experiments are shown.

(G) BMCs were harvested and cultured in the presence of SCF and thrombopoietin (TPO) for 5 days. KL cells were then selected and cultured in SCF- and TPO-containing medium. Cell numbers at the indicated period are shown. Error bars, SD.

(H) Immunoblot analysis of extracts from KL cells used SAMD9L (top) or β-actin (bottom) antibody. *SAMD9L* genotypes are indicated above.

(legend continued on next page)

To obtain candidates for such genomic abnormalities, we performed whole-exome sequencing on splenic cells from 17 mice that developed MDS or AML. We identified a total of 89 missense/nonsense/frameshift mutations that partially overlapped with genes (or closely related genes) mutated in human hematopoietic malignancies (Table S6).

SAMD9L Facilitates Homotypic Fusion of Endosomes

The above findings suggested that *SAMD9L* deficiency sensitizes hematopoietic progenitors to cytokines. KL cells (purity >90%) were harvested and starved of cytokines for 8 hr and then cultured in SCF-containing medium. In *SAMD9L*$^{+/+}$ KL cells, ERK was phosphorylated within 5 min of SCF stimulation (Figure 4A), followed by a rapid decline in phosphorylated-ERK (pERK) level. In contrast, KL cells obtained from *SAMD9L*-deficient mice maintained high levels of pERK even at 50 min after the addition of SCF. These data suggested that SAMD9L is involved in the turnover of cytokine receptors or negative feedback regulation for cytokine-derived signals.

A recent report demonstrated that hSAMD9L binds to an endosome protein, Rgl2 (Hershkovitz et al., 2011), which regulates cytokine receptor-derived signals (Takaya et al., 2007). Indeed, immunostaining using SAMD9L antibody showed a vesicular pattern of SAMD9L localization in approximately 15% of KL cells (Figure 4B, panel 1) or lung fibroblasts (panel 4) that overlapped with the localization of Rab5, an early endosomal protein (Bucci et al., 1992).

Ligand-bound cytokine/growth factor receptors are endocytosed and transitioned to endosomes and then degraded in lysosomes (Haas et al., 2005; Karlsson et al., 2006; Luzio et al., 2009). To analyze this process, we used lung fibroblasts expressing endogenous platelet-derived growth factor receptor (PDGFRβ) because sufficient numbers of cells can be obtained for pulse-chase experiments, and these cells have a large cytoplasmic volume allowing detailed observation of endosomes.

In pulse-chase studies, cell surface receptors were labeled with biotin, enabling us to discriminate cell surface and endocytosed receptors (Karlsson et al., 2006; Roberts et al., 2001) (see Experimental Procedures). Cell surface PDGFRβ was internalized within 5 min after PDGF stimulation of SAMD9$^{+/+}$ fibroblasts (Figure 4C, lanes 1–4), followed by an increase in endocytosed receptor levels after 15 min (lane 3), which then returned to low levels within 30 min (lane 4).

When we repeated this experiment using lung fibroblasts with reduced expression of SAMD9L by small hairpin RNA (sh#4 fibroblasts) (Figure 4D, lane 2), surface receptor levels in sh#4 fibroblasts behaved in a similar manner (Figure 4C, upper panel, lanes 5–8); however, these cells showed a 5-fold higher accumulation of endocytosed receptors relative to WT fibroblasts (lower panel, lanes 7 and 8). We established cells that coexpressed a FLAG-tagged sh#4-resistant SAMD9L (Figure 4D, lane 3) and found that endocytosed PDGFRβ accumulation was reduced to levels found in SAMD9L$^{+/+}$ fibroblasts (Figure 4C, lower panel, lanes 11 and 12), excluding the possibility of off-target effects.

We established lung fibroblasts from *SAMD9L*$^{+/-}$ and *SAMD9L*$^{-/-}$ mice, which expressed SAMD9L protein at levels of approximately 25% or 0%, respectively, of that in *SAMD9L*$^{+/+}$ mice (Figure 4E, top panel). Both *SAMD9L*$^{+/-}$ and *SAMD9L*$^{-/-}$ cells showed endocytosed receptor accumulation (Figure 4E, middle) and persistent phosphorylation of Akt (Figure 4E, bottom two panels) like sh#4 fibroblasts.

To elucidate the roles of SAMD9L in the metabolism of endocytosed PDGFRβ, we observed endosomes and lysosomes in lung fibroblasts expressing a myc-tagged PDGFRβ. In PDGF-starved fibroblasts, myc-PDGFRβ localized to the cell surface as well as to the cytoplasm with a diffuse and vesicular pattern (Figure 4F, panel 1), whereas an early endosome marker EEA1 localized to the cytoplasm (panel 5). PDGF stimulation for 5 min induced little change (Figure 4F, panels 2 and 6). However, upon PDGF treatment for 15 min, myc-PDGFRβ on the cell surface was barely visible, and relatively large vesicles (>1 μm) containing myc-PDGFRβ or EEA1 were observed in the perinuclear region (Figure 4F, panels 3, 3′, 7, and 7′; Figure 4G). Some regions (approximately 30%) within the large vesicles were positive for both EEA1 and PDGFR on immunostaining analyses (Figure 4F, panel 11′). Thirty minutes after the addition of PDGF, vesicle size decreased (Figure 4F, panels 4 and 8), and only a few vesicles were positive for both EEA1 and PDGFRβ (Figure 4F, panel 12). Instead of EEA1, lysosome-associated membrane protein 1 (Lamp1)-positive vesicles were fused to approximately 30% of those containing PDGFRβ (Figure 4H, panel 3). This time course is in agreement with a previous report by Karlsson et al. (2006), showing that early endosomes containing growth factor receptors increase in size via homotypic fusion and then transition to late endosomes that fuse with lysosomes.

We repeated this experiment using sh#4 fibroblasts. Although little difference was observed by PDGF stimulation for 5 min (Figure 4F, panel 14), after 15 min of PDGF treatment, PDGFRβ-containing vesicles moved to the perinuclear region, but these vesicles were noticeably smaller (Figure 4F, panels 15 and 15′; Figure 4G). Shrunken myc-PDGFR-containing vesicles in the perinuclear region were also observed in *SAMD9L*$^{+/-}$ and *SAMD9L*$^{-/-}$ fibroblasts 15 min after PDGF stimulation (Figure 4G). Thirty minutes after the addition of PDGF, few endosomes in sh#4 fibroblasts were positive for both Lamp1 and PDGFRβ (Figure 4H, panel 6), suggesting that SAMD9L promotes the fusion of early endosomes that will transition to late endosomes and/or lysosomes.

It was reported that EEA1 promotes homotypic fusion of endosomes (Christoforidis et al., 1999; Mills et al., 1998), and EEA1 downregulation delays the degradation of epidermal growth factor receptor (Leonard et al., 2008). Indeed, when EEA1 expression was downregulated using EEA1-specific siRNAs (Figure 5A), accumulation of endocytosed PDGFRβ and persistent phosphorylation of Akt were also evident 15 or 30 min after stimulation

(I) Mice (four each) were injected with CPA on day 0 and hG-CSF daily from day 1 to day 4. Average WBC counts and SD are shown.
(J) The 2 × 10^4 BMCs obtained from 26-month-old *SAMD9L*$^{+/+}$ non-MDS, *SAMD9L*$^{+/-}$ non-MDS, and *SAMD9L*$^{+/-}$ MDS mice were cultured in MethoCult M3434. Colonies were counted and replated at 2 × 10^4 cells every 10 days. Error bars, SD.
(K) Representative images show colonies obtained from 26-month-old mice. Scale bars, 100 μm.
See also Tables S5 and S6 and Figure S1.

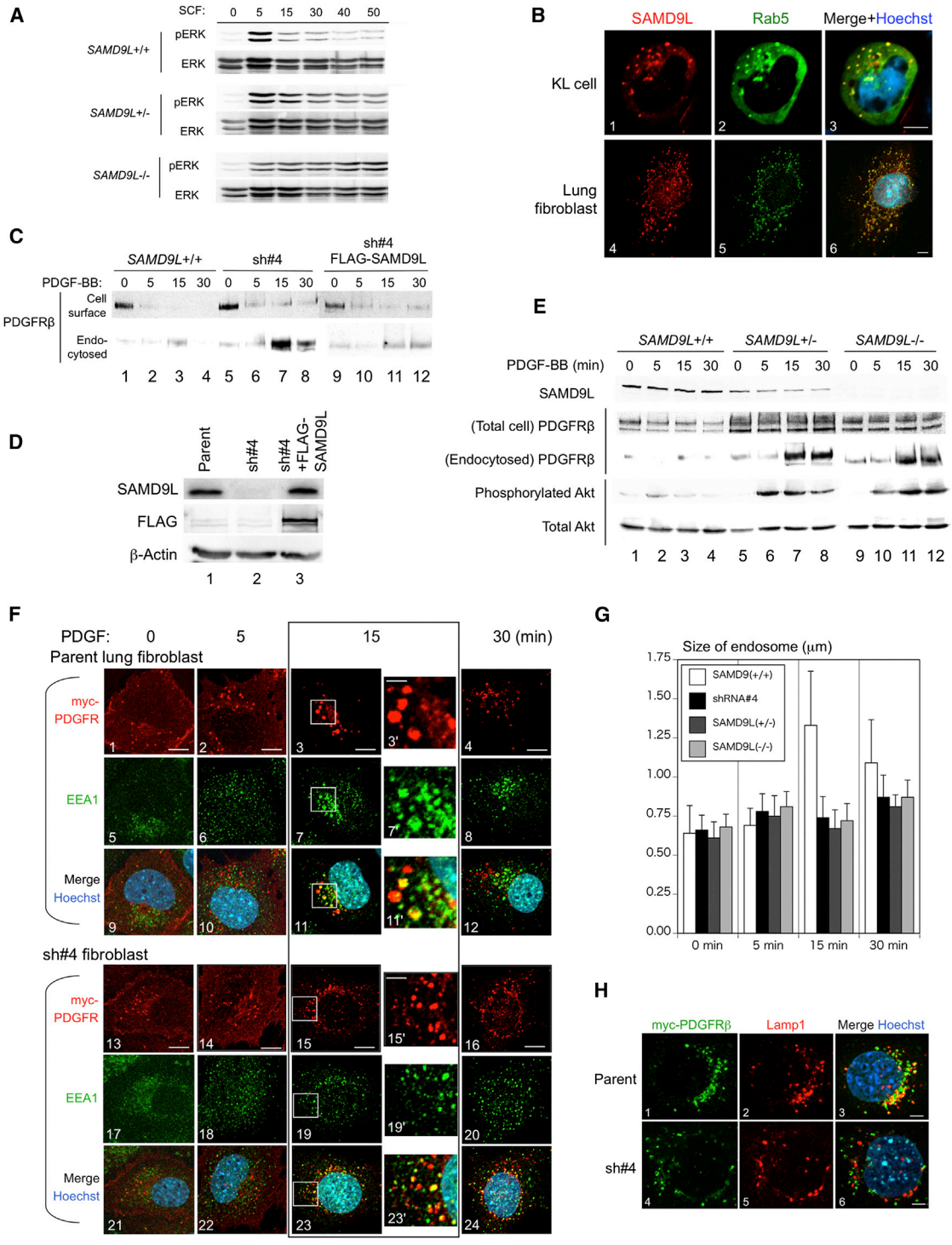

Figure 4. Involvement of SAMD9L in Homotypic Fusion of Endosomes

(A) KL cells from SAMD9L$^{+/+}$, SAMD9L$^{+/-}$, and SAMD9L$^{-/-}$ mice were SCF starved for 8 hr and then stimulated with SCF for the indicated number of minutes. The results of immunoblot detection of pERK and total ERK are shown.

(B) A KL cell (panels 1–3) or lung fibroblast (panels 4–6) was stained with SAMD9L and Rab5 antibodies. Scale bars, 5 μm.

(C) Immunoblot detection of cell surface and endosomal PDGFRβ that were biotinylated and precipitated separately is shown.

(D) Immunoblot analyses used SAMD9L (top), FLAG (middle), or β-actin (bottom) antibody to detect proteins in parent *SAMD9L*$^{+/+}$ lung fibroblasts (lane 1), cells in which SAMD9L expression was constitutively downregulated by sh#4 (lane 2), and cells simultaneously expressing sh#4 and FLAG-SAMD9L (sh#4 resistant) (lane 3).

(E) Immunoblot detection used the antibodies indicated on the left. Cell extracts from *SAMD9L*$^{+/+}$, *SAMD9L*$^{+/-}$, or *SAMD9L*$^{-/-}$ lung fibroblasts were subjected to immunoblot analysis except for the middle panel, in which biotinylated and precipitated endosomal PDGFRβ was used.

(legend continued on next page)

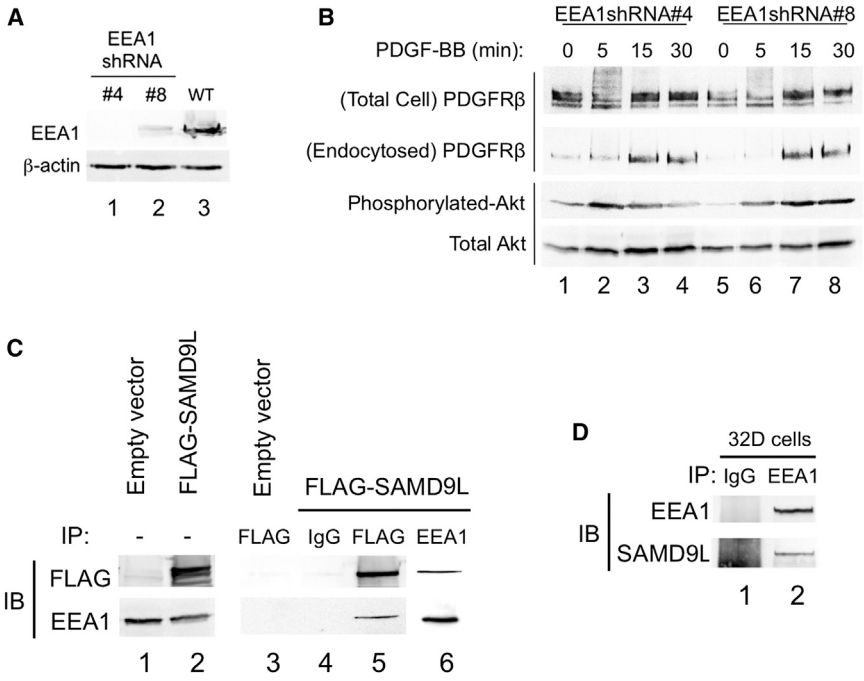

Figure 5. Involvement of SAMD9L in the Metabolism of Cytokine Receptor

(A) Immunoblot analyses used EEA1 (top) or β-actin (bottom) antibody to detect proteins in lung fibroblasts treated with EEA1 shRNA#4 (lane 1) or shRNA#8 (lane 2), and in parental cells (lane 3).

(B) Immunoblot detection used the antibodies indicated on the left. Cell extracts from lung fibroblasts expressing shRNA#4 (lanes 1–4) and shRNA#8 (lanes 5–8) were subjected to immunoblot analysis except for the middle panel, in which biotinylated and precipitated endosomal PDGFRβ was used.

(C) 293 cells were transiently transfected with either empty p3×FLAG-CMV10 or p3×FLAG-CMV10-SAMD9L vector. Whole-cell extracts (lanes 1 and 2) or immunoprecipitated products (IP) using control IgG, FLAG, or EEA1 antibody were subjected to immunoblot analysis (IB) using antibodies indicated on the left.

(D) IP of 32D cells using antibodies in (C) were subjected to IB using antibodies indicated on the left.

with PDGF (Figure 5B, upper- and lower-middle panels, lanes 3, 4, 7, and 8). By coimmunoprecipitation analyses, we obtained data showing that SAMD9L binds to EEA1 in 293 cells (Figure 5C, lanes 5 and 6) or 32D myeloid cells (Figure 5D), suggesting that SAMD9L and EEA1 are crucial components of a protein complex that facilitate the degradation of cytokine receptors through the homotypic fusion of endosomes.

Application of the Results in Mice to Human Myeloid Malignancies with –7/7q–

In human, the related *SAMD9* (*hSAMD9*) gene in addition to *SAMD9L* (*hSAMD9L*) was expressed in hematopoietic progenitors (Figure 6A). The unusual gene distribution among mammals (see Introduction) suggests that SAMD9 and SAMD9L at least partially complement each other's functions. We introduced FLAG-tagged *hSAMD9* or *hSAMD9L* transgenes into lung fibroblasts established from *SAMD9L*$^{-/-}$ mice (Figure 6B). Relative to *SAMD9L*$^{-/-}$ cells infected with empty virus (Figure 6C, lanes 7 and 8), those expressing hSAMD9 or hSAMD9L showed a 10- or 3-fold decrease in endosomal PDGFRβ (Figure 6C, lanes 11 and 12, and 15 and 16), respectively, suggesting that hSAMD9 or hSAMD9L also downregulates cytokine signalings. In addition, coimmunoprecipitation analyses revealed that both hSAMD9 and hSAMD9L interact with EEA1 (Figure 6D, lanes 4, 6, and 10).

To test whether SAMD9L plays roles in cytokine-emanating signal transduction in human leukemia cells harboring monosomy 7, F-36P cells (Chiba et al., 1991) were infected with virus containing SAMD9L cDNA (Figure 6E, left panel). In cells infected with empty virus, substantial levels of ERK phosphorylation continued to be observed more than 1 hr after GM-CSF stimulation (Figure 6E, middle panels). However, ERK phosphorylation decreased to less than 10% within 30 min in cells expressing SAMD9L (Figure 6E, right).

We determined the copy number of *SAMD9* and *SAMD9L* genes in 60 unselected MDS and AML samples using mCGH and qPCR (Asou et al., 2009). A total of 17 patients (17 of 60, 28%) carried one copy each of the *SAMD9* and *SAMD9L* genes. The remaining 43 patients had two or more copies of both *SAMD9* and *SAMD9L* genes, and no patient harbored missense or nonsense mutations. Quantitative real-time PCR revealed that *SAMD9* or *SAMD9L* mRNA expression levels in BM mononuclear cells in patients with MDS/AML with one gene copy were significantly reduced relative to those carrying two or more copies ($p < 0.01$; Figure 6F). Intriguingly, the mRNA expression level of *SAMD9* correlated with that of *SAMD9L* in MDS/AML cells (Figure 6G), suggesting that loss of one 7q allele results in simultaneous reductions in *SAMD9* and *SAMD9L* expression.

To test whether *Evi1* or *Fbxl10* overexpression contributes to human leukemogenesis associated with −7/7q−, as they did in *SAMD9L*-deficient mice (Figure 2F), we measured *Evi1* and *Fbxl10* mRNA levels in patients with MDS/AML. *Evi1* expression levels were higher (>0.5 of HPRT expression levels) in 5 of 17 (29%) and 3 of 43 (7.0%) samples carrying haploid or diploid/polyploid for *SAMD9*/*SAMD9L* genes, respectively

(F) Lung fibroblasts expressing myc-PDGFRβ (panels 1–12) and those expressing reduced levels of SAMD9L (sh#4; panels 13–24) were starved of PDGF for 16 hr, followed by stimulation with 100 ng/ml PDGF-BB for the indicated lengths of time. Cells were stained with the antibodies indicated on the left. Panels 3′, 7′, 11′, 15′, 19′, and 23′ show 5-fold enlargements of endosome-rich regions. Scale bars, 10 μm.

(G) Longitudinal diameter of PDGFR-positive endosomes was measured using ImageJ software (mean and SD of 200 endosomes).

(H) Cells stimulated with 100 ng/ml PDGF-BB for 30 min were stained with Myc and Lamp1 antibodies. Scale bars, 5 μm.

Nuclei were stained with Hoechst 33342 in (B), (F), and (H).

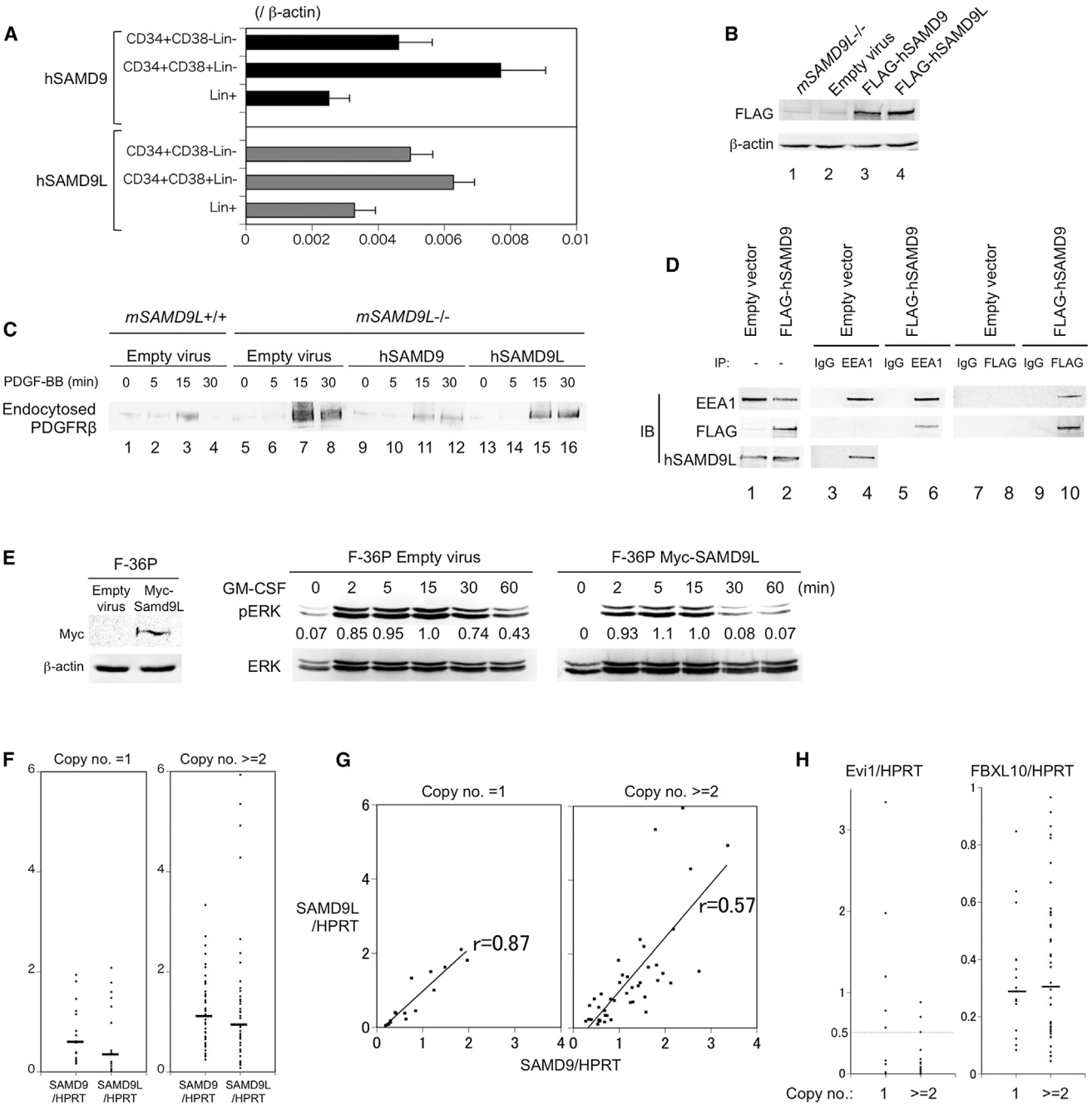

Figure 6. Function and Expression of hSAMD9 and hSAMD9L

(A) SAMD9 (top) and SAMD9L (bottom) mRNA expression levels in hematopoietic cells are indicated on the left as a ratio relative to β-actin mRNA measured using quantitative real-time PCR. The mean and SEM in four independent experiments are shown.

(B) Immunoblot analysis used FLAG (upper) or β-actin (bottom) antibody. Lung fibroblasts from *SAMD9L*$^{-/-}$ mice (lane 1), cells infected with the empty pMXs (lane 2), pMXs-FLAG-hSAMD9 (lane 3), or pMXs-FLAG-hSAMD9L (lane 4) virus are shown.

(C) Lung fibroblasts from SAMD9L$^{+/+}$ mice infected with the empty pMXs virus (lanes 1–4), fibroblasts from SAMD9L$^{-/-}$ mice infected with the empty pMXs (lanes 5–8), pMXs-FLAG-hSAMD9 (lanes 9–12), and pMXs-FLAG-hSAMD9L (lanes 13–16) virus are presented. Cells were starved of PDGF for 16 hr and then stimulated with PDGF-BB (100 ng/ml) for the periods indicated above. Immunoblot detection of endosomal PDGFRβ is shown.

(D) 293 cells were transiently transfected with either empty p3×FLAG-CMV10 or p3×FLAG-CMV10-SAMD9L vector. Whole-cell extracts (lanes 1 and 2) or immunoprecipitated products using control IgG, FLAG, or EEA1 antibody were subjected to immunoblot analysis using EEA1 (top), FLAG (middle), or hSAMD9L (bottom) antibody.

(E) F-36P cells were infected with empty retrovirus or virus containing mouse SAMD9L cDNA and cytokine starved for 12 hr and then stimulated with SCF for the indicated number of minutes. The results of immunoblot detection of pERK and total ERK (left and middle), and myc and β-actin (right) are shown.

(legend continued on next page)

($p < 0.05$, chi-square test; Figure 6H, left), consistent with previous reports by Barjesteh van Waalwijk van Doorn-Khosrovani et al. (2003) and Lugthart et al. (2008). In contrast, there was no significant difference in Fbxl10 mRNA expression levels (Figure 6H, right).

DISCUSSION

In this paper, we demonstrated that *SAMD9L* haploinsufficiency ultimately induces the development of myeloid diseases in mice. Because humans have the related *SAMD9* gene that encodes a protein that compensates for the function of SAMD9L at least in part, loss of one copy of each of the *SAMD9* and *SAMD9L* genes (i.e., *SAMD9*$^{+/-}$*SAMD9L*$^{+/-}$) as a result of −7/7q− may not correspond to *SAMD9L*$^{+/-}$ in mice. However, simultaneous reduction of SAMD9 and SAMD9L mRNA by loss of 7q (Figure 6F) suggests that SAMD9/SAMD9L function in human cells harboring −7/7q− is parallel to SAMD9L function in *SAMD9L*$^{+/-}$ mouse cells.

SAMD9L haploinsufficiency in the natural course induced the development of MDS in elderly mice (Figure 1F), mimicking the typical clinical association between monosomy 7 as a sole anomaly and sporadic MDS in elderly humans (Jaffe et al., 2001). Enhancement of stem cell self-renewal and/or delay in differentiation of early progenitors was observed in both young and old SAMD9L$^{+/-}$ non-MDS mice (Figures 3D and 3J); however, BMCs from old SAMD9L$^{+/-}$ MDS mice lost these features. This suggests that additional genetic and/or epigenetic alterations (other than age-related ones) that suppress stem cell self-renewal and/or induce differentiation of early progenitors play critical roles in the development of MDS. We consider that *SAMD9L* haploinsufficiency contributes to MDS by protecting stem cell(s) harboring such MDS-causative genetic and/or epigenetic alterations from depletion.

In addition to sporadic MDS in elderly individuals, −7/7q− frequently occurs in younger patients during the advancement of secondary AML/MDS in radiation-induced and therapy-related cases (Pedersen-Bjergaard et al., 2008), as well as during the development of AML/MDS among patients with a propensity for myeloid diseases such as patients with Fanconi anemia and congenital neutropenia. −7/7q− is also often detected as an additional chromosome abnormality in patients with AML harboring a variety of leukemogenic chromosome translocations and well-known gene abnormalities including Evi1 overexpression (Barjesteh van Waalwijk van Doorn-Khosrovani et al., 2003; Jaffe et al., 2001; Lugthart et al., 2008). The role of −7/7q− that promotes leukemogenesis caused by such a wide variety of genetic alterations to different subtypes of myeloid malignancies appears to correspond to the potential of *SAMD9L* haploinsufficiency that promotes diverse pathways activated by retrovirus insertion toward different types of myeloid leukemia in younger mice (Figures 2A and 2B; Table S2).

SAMD9L haploinsufficiency sensitized hematopoietic progenitors to cytokines both in vitro and in vivo (Figures 3G and 3I). This is consistent with a previous report indicating that G-CSF preferentially stimulates proliferation of monosomy 7 progenitors carrying nonmutated G-CSF receptor (Sloand et al., 2006). In addition, a correlation has been reported between the development of myeloid malignancies harboring monosomy 7 and LT treatment of aplastic anemia and congenital neutropenia with G-CSF (Kojima et al., 2002; Weinblatt et al., 1995), supporting that the loss of *SAMD9*/*SAMD9L* genes plays crucial roles in the growth advantage under the presence of cytokines and leukemogenic process of progenitors harboring −7/7q−.

The presence of broad and divergent deletion regions in patients with 7q− AML/MDS suggests that the total loss of one tumor suppressor gene (which usually occurs by the deletion of one allele and a mutation in the other) is unlikely to be responsible for myeloid transformation by −7/7q− (Jerez et al., 2012). Rather, like current models proposed for 5q− (another large deletion frequently found in MDS; Brunning et al., 2008), haploinsufficiencies of multiple genes play critical roles in the promotion of myeloid diseases (Ebert, 2009). The 5q− region encodes multiple (candidate) causative proteins that carry out a broad spectrum of biochemical functions. Haploinsufficiency of each gene is likely responsible for the corresponding clinical symptoms, such as anemia, thrombocytosis, clonal dominance, and response to lenalidomide (a key drug for treating 5q− MDS).

We consider that *SAMD9*/*SAMD9L* and *Miki*, the latter of which we recently reported as being involved in the abnormal morphology characteristic of MDS (Ozaki et al., 2012), are members of multiple causative genes on 7q, whose haploinsufficiency in combination plays crucial roles in the development of myeloid malignancies. Because SAMD9 and SAMD9L compensate each other's function at least in part, heterozygous loss of both *SAMD9* and *SAMD9L* genes may be required to develop human myeloid diseases, and that is why mutations have not been identified in either gene. Careful analysis of small deletions and mutations using high-throughput sequencing may help to identify other key genes in this region that contribute to myeloid transformation by loss of one 7q allele.

EXPERIMENTAL PROCEDURES

Mouse Experiments

SAMD9L-deficient mice were established according to standard procedures described in Supplemental Experimental Procedures. *Evi1* gene transduction was performed according to the method described previously by Jin et al. (2007). *Fbxl10* transduction was performed using the method described in Supplemental Experimental Procedures. Newborn mice were inoculated intraperitoneally with 100 μl MOL4070A retrovirus solution containing approximately 1×10^5 infectious particles. Retroviral integration sites were identified using iPCR as described previously by Yamashita et al. (2005). Peripheral blood chimerisms of the recipient mice were analyzed as previously described (Nagamachi et al., 2010). To analyze the effect of hG-CSF, mice (9 weeks of age) that had been intraperitoneally injected with CPA (Shionogi Pharmaceuticals, Osaka) at a dose of 100 mg/kg on day 0, were given 0.1 μg of human G-CSF (Miltenyi Biotec, Bergisch Gladbach) per mouse per day, or control vehicle for 4 days from day 1 to day 4. Blood samples for the measurement

(F) Ratios of *SAMD9* and *SAMD9L* mRNAs relative to HPRT mRNA in the BM-MNC of patients with MDS/AML that are *SAMD9*/*SAMD9L* haploid (left) or diploid/polyploid (right) are shown. Horizontal lines indicate the median.
(G) Correlation between the relative expression levels of *SAMD9* (horizontal) and *SAMD9L* (vertical) mRNA to HPRT mRNA from MNCs described in (F) is presented. Regression lines and correlation coefficient (r) are indicated.
(H) Relative expression levels of Evi1 (left) and Fbxl10 (right) mRNA to HPRT mRNA in MNCs of patients with MDS/AML described in (F) are shown.

of WBC count were obtained 5 hr after each injection and 30 hr after the injection on day 4. All mice were kept according to guidelines of the Institute of Laboratory Animal Science, Hiroshima University. The Animal Care Committee at the Japanese Foundation for Cancer Research approved all murine studies.

Cells and Cell Culture

F-36P cells were cultured in medium described by others (Chiba et al., 1991). Lung fibroblasts and 293 cells and their derivatives were grown in DMEM supplemented with 10% FBS. LSK cells were isolated and characterized (Honda et al., 2011; Mizuno et al., 2008), using antibodies listed in Supplemental Experimental Procedures. Human $CD34^+$ $CD38^-$ Lin^-, $CD34^+$ $CD38^+$ Lin^-, and Lin^+ cells were isolated from cryopreserved human BM cells (TaKaRa Bio, Shiga) (Shima et al., 2010). The stained cells were analyzed and sorted by FACSAria II (BD Biosciences). c-Kit^+ BM cells expressing Samd9L were obtained by infecting cells with pMYs retrovirus carrying *SAMD9L* cDNA and *IRES-GFP* followed by sorting with GFP. Cells stably expressing PDGFRβ and SAMD9/SAMD9L proteins were established by infecting cells with pMXs retrovirus carrying the corresponding cDNA followed by selection with neomycin. Cells expressing mouse SAMD9L or EEA1 at reduced levels were generated using U3-deleted pMX-puro retrovirus carrying a mouse U6 promoter and a small hairpin sequence specific for mouse SAMD9L mRNA (sh#4, target sequence: ACAATGGAGTGATCTACTACA), or EEA1 mRNA (sh#4, CAAGAAAGCATAAA GGAAATA; sh#8, CGGAGAAGCTGAAGAATCAGT). sh#4-resistant mouse *SAMD9L* cDNA was created by replacing nucleotides in the target sequence to CAgTGGAGcGAcCTtCTt (underline indicates replaced nucleotides), changes that do not affect the amino acid sequence. Murine colony formation assays were performed using MethoCult M3434 (STEMCELL Technologies, Vancouver) according to the manufacturer's instructions.

Quantitative Real-Time PCR, Transcriptome Analysis, Whole-Exome Sequencing, and Determination of Copy Number

Total RNA was extracted from sorted LSK cells using RNeasy Micro Kit (QIAGEN, Tokyo), and mRNA was purified using SuperScript VILO (Invitrogen, Venlo). Quantitative real-time PCR was performed as previously described by Kuribara et al. (2004) using the primer sets listed in a table in Supplemental Experimental Procedures. Transcriptome analysis was performed using a next-generation sequencer (GAIIx; Illumina, San Diego) according to the manufacturer's instructions. The generated sequence tags were mapped onto the mouse genomic sequence (UCSC Genome Browser, version mm9) using the sequence alignment program ELAND (Illumina). Whole-exome sequencing was performed according to the method described in Supplemental Experimental Procedures. Copy numbers of *hSAMD9* and *hSAMD9L* genes were determined using mCGH and qPCR techniques as previously described (Asou et al., 2009).

Protein Analysis

Immunoprecipitation and immunoblot analyses and immunostaining were performed according to standard procedures by Mizuno et al. (2008) and Shinjyo et al. (2001). Cell surface and internalized PDGFRβ were isolated as previously published procedures by others (Karlsson et al., 2006; Roberts et al., 2001) and are described in Supplemental Experimental Procedures.

Human Samples

Written informed consent was obtained from patients with AML/MDS in accordance with the Declaration of Helsinki for BM sampling, and analysis was undertaken with the approval of the Hiroshima University institutional review board.

ACCESSION NUMBERS

The short-read sequence archive data appearing in this paper were registered in GenBank/DDBJ under the following accession numbers: DRA000636, DRA000637, and DRA000638.

SUPPLEMENTAL INFORMATION

Supplemental Information includes Supplemental Experimental Procedures, one figure, and six tables and can be found with this article online at http://dx.doi.org/10.1016/j.ccr.2013.08.011.

ACKNOWLEDGMENTS

We would like to thank Drs. M. Iwama for providing virus and methods for gene transfer to mouse bone marrow cells and Y. Ebihara for useful discussion. We thank Mrs. M. Nakamura, Mr. N. Yamasaki, and Mrs. R. Tai for excellent technical assistance. This work was supported by Grants-in-Aid for Scientific Research from the Ministry of Education, Culture, Sports, Science and Technology of Japan.

Received: July 13, 2011
Revised: December 25, 2012
Accepted: August 15, 2013
Published: September 9, 2013

REFERENCES

Asou, H., Matsui, H., Ozaki, Y., Nagamachi, A., Nakamura, M., Aki, D., and Inaba, T. (2009). Identification of a common microdeletion cluster in 7q21.3 subband among patients with myeloid leukemia and myelodysplastic syndrome. Biochem. Biophys. Res. Commun. *383*, 245–251.

Barjesteh van Waalwijk van Doorn-Khosrovani, S., Erpelinck, C., van Putten, W.L., Valk, P.J., van der Poel-van de Luytgaarde, S., Hack, R., Slater, R., Smit, E.M., Beverloo, H.B., Verhoef, G., et al. (2003). High EVI1 expression predicts poor survival in acute myeloid leukemia: a study of 319 de novo AML patients. Blood *101*, 837–845.

Brunning, R., Germing, U., Le Beau, M.M., Porwit, A., Baumann, I., Vardiman, J.W., and Hellstrom-Lindberg, E. (2008). Myelodysplastic syndromes/neoplasms, overview. In WHO Classification of Tumours of Haematopoietic and Lymphoid Tissues, Fourth Edition, S.H. Swerdlow, International Agency for Research on Cancer., and World Health Organization., eds. (Lyon: IARC Press), pp. 62–73.

Bucci, C., Parton, R.G., Mather, I.H., Stunnenberg, H., Simons, K., Hoflack, B., and Zerial, M. (1992). The small GTPase rab5 functions as a regulatory factor in the early endocytic pathway. Cell *70*, 715–728.

Buonamici, S., Li, D., Chi, Y., Zhao, R., Wang, X., Brace, L., Ni, H., Saunthararajah, Y., and Nucifora, G. (2004). EVI1 induces myelodysplastic syndrome in mice. J. Clin. Invest. *114*, 713–719.

Castilla, L.H., Perrat, P., Martinez, N.J., Landrette, S.F., Keys, R., Oikemus, S., Flanegan, J., Heilman, S., Garrett, L., Dutra, A., et al. (2004). Identification of genes that synergize with Cbfb-MYH11 in the pathogenesis of acute myeloid leukemia. Proc. Natl. Acad. Sci. USA *101*, 4924–4929.

Chefetz, I., Ben Amitai, D., Browning, S., Skorecki, K., Adir, N., Thomas, M.G., Kogleck, L., Topaz, O., Indelman, M., Uitto, J., et al. (2008). Normophosphatemic familial tumoral calcinosis is caused by deleterious mutations in SAMD9, encoding a TNF-alpha responsive protein. J. Invest. Dermatol. *128*, 1423–1429.

Chiba, S., Takaku, F., Tange, T., Shibuya, K., Misawa, C., Sasaki, K., Miyagawa, K., Yazaki, Y., and Hirai, H. (1991). Establishment and erythroid differentiation of a cytokine-dependent human leukemic cell line F-36: a parental line requiring granulocyte-macrophage colony-stimulating factor or interleukin-3, and a subline requiring erythropoietin. Blood *78*, 2261–2268.

Christoforidis, S., McBride, H.M., Burgoyne, R.D., and Zerial, M. (1999). The Rab5 effector EEA1 is a core component of endosome docking. Nature *397*, 621–625.

Cuenco, G.M., and Ren, R. (2004). Both AML1 and EVI1 oncogenic components are required for the cooperation of AML1/MDS1/EVI1 with BCR/ABL in the induction of acute myelogenous leukemia in mice. Oncogene *23*, 569–579.

Ebert, B.L. (2009). Deletion 5q in myelodysplastic syndrome: a paradigm for the study of hemizygous deletions in cancer. Leukemia *23*, 1252–1256.

Frescas, D., Guardavaccaro, D., Bassermann, F., Koyama-Nasu, R., and Pagano, M. (2007). JHDM1B/FBXL10 is a nucleolar protein that represses transcription of ribosomal RNA genes. Nature *450*, 309–313.

Haas, A.K., Fuchs, E., Kopajtich, R., and Barr, F.A. (2005). A GTPase-activating protein controls Rab5 function in endocytic trafficking. Nat. Cell Biol. *7*, 887–893.

Hattori, K., Shimizu, K., Takahashi, M., Tamura, M., Oheda, M., Ohsawa, N., and Ono, M. (1990). Quantitative in vivo assay of human granulocyte colony-stimulating factor using cyclophosphamide-induced neutropenic mice. Blood *75*, 1228–1233.

Hershkovitz, D., Gross, Y., Nahum, S., Yehezkel, S., Sarig, O., Uitto, J., and Sprecher, E. (2011). Functional characterization of SAMD9, a protein deficient in normophosphatemic familial tumoral calcinosis. J. Invest. Dermatol. *131*, 662–669.

Honda, H., Takubo, K., Oda, H., Kosaki, K., Tazaki, T., Yamasaki, N., Miyazaki, K., Moore, K.A., Honda, Z., Suda, T., and Lemischka, I.R. (2011). Hemp, an mbt domain-containing protein, plays essential roles in hematopoietic stem cell function and skeletal formation. Proc. Natl. Acad. Sci. USA *108*, 2468–2473.

Jaffe, E.S., Harris, N.L., Stein, H., and Vardiman, J.M. (2001). Pathology and Genetics of Tumours of Haematopoietic and Lymphoid Tissues (Lyon: IARC press).

Jerez, A., Sugimoto, Y., Makishima, H., Verma, A., Jankowska, A.M., Przychodzen, B., Visconte, V., Tiu, R.V., O'Keefe, C.L., Mohamedali, A.M., et al. (2012). Loss of heterozygosity in 7q myeloid disorders: clinical associations and genomic pathogenesis. Blood *119*, 6109–6117.

Jiang, Q., Quaynor, B., Sun, A., Li, Q., Matsui, H., Honda, H., Inaba, T., Sprecher, E., and Uitto, J. (2011). The Samd9L gene: transcriptional regulation and tissue-specific expression in mouse development. J. Invest. Dermatol. *131*, 1428–1434.

Jin, G., Yamazaki, Y., Takuwa, M., Takahara, T., Kaneko, K., Kuwata, T., Miyata, S., and Nakamura, T. (2007). Trib1 and Evi1 cooperate with Hoxa and Meis1 in myeloid leukemogenesis. Blood *109*, 3998–4005.

Johnson, E., and Cotter, F.E. (1997). Monosomy 7 and 7q—associated with myeloid malignancy. Blood Rev. *11*, 46–55.

Karlsson, S., Kowanetz, K., Sandin, A., Persson, C., Ostman, A., Heldin, C.H., and Hellberg, C. (2006). Loss of T-cell protein tyrosine phosphatase induces recycling of the platelet-derived growth factor (PDGF) beta-receptor but not the PDGF alpha-receptor. Mol. Biol. Cell *17*, 4846–4855.

Kogan, S.C., Ward, J.M., Anver, M.R., Berman, J.J., Brayton, C., Cardiff, R.D., Carter, J.S., de Coronado, S., Downing, J.R., Fredrickson, T.N., et al.; Hematopathology subcommittee of the Mouse Models of Human Cancers Consortium. (2002). Bethesda proposals for classification of nonlymphoid hematopoietic neoplasms in mice. Blood *100*, 238–245.

Kojima, S., Ohara, A., Tsuchida, M., Kudoh, T., Hanada, R., Okimoto, Y., Kaneko, T., Takano, T., Ikuta, K., and Tsukimoto, I.; Japan Childhood Aplastic Anemia Study Group. (2002). Risk factors for evolution of acquired aplastic anemia into myelodysplastic syndrome and acute myeloid leukemia after immunosuppressive therapy in children. Blood *100*, 786–790.

Kuribara, R., Honda, H., Matsui, H., Shinjyo, T., Inukai, T., Sugita, K., Nakazawa, S., Hirai, H., Ozawa, K., and Inaba, T. (2004). Roles of Bim in apoptosis of normal and Bcr-Abl-expressing hematopoietic progenitors. Mol. Cell. Biol. *24*, 6172–6183.

Leonard, D., Hayakawa, A., Lawe, D., Lambright, D., Bellve, K.D., Standley, C., Lifshitz, L.M., Fogarty, K.E., and Corvera, S. (2008). Sorting of EGF and transferrin at the plasma membrane and by cargo-specific signaling to EEA1-enriched endosomes. J. Cell Sci. *121*, 3445–3458.

Li, C.F., MacDonald, J.R., Wei, R.Y., Ray, J., Lau, K., Kandel, C., Koffman, R., Bell, S., Scherer, S.W., and Alman, B.A. (2007). Human sterile alpha motif domain 9, a novel gene identified as down-regulated in aggressive fibromatosis, is absent in the mouse. BMC Genomics *8*, 92.

Lugthart, S., van Drunen, E., van Norden, Y., van Hoven, A., Erpelinck, C.A., Valk, P.J., Beverloo, H.B., Löwenberg, B., and Delwel, R. (2008). High EVI1 levels predict adverse outcome in acute myeloid leukemia: prevalence of EVI1 overexpression and chromosome 3q26 abnormalities underestimated. Blood *111*, 4329–4337.

Luzio, J.P., Parkinson, M.D., Gray, S.R., and Bright, N.A. (2009). The delivery of endocytosed cargo to lysosomes. Biochem. Soc. Trans. *37*, 1019–1021.

Mills, I.G., Jones, A.T., and Clague, M.J. (1998). Involvement of the endosomal autoantigen EEA1 in homotypic fusion of early endosomes. Curr. Biol. *8*, 881–884.

Mizuno, T., Yamasaki, N., Miyazaki, K., Tazaki, T., Koller, R., Oda, H., Honda, Z.I., Ochi, M., Wolff, L., and Honda, H. (2008). Overexpression/enhanced kinase activity of BCR/ABL and altered expression of Notch1 induced acute leukemia in p210BCR/ABL transgenic mice. Oncogene *27*, 3465–3474.

Nagamachi, A., Htun, P.W., Ma, F., Miyazaki, K., Yamasaki, N., Kanno, M., Inaba, T., Honda, Z., Okuda, T., Oda, H., et al. (2010). A 5′ untranslated region containing the IRES element in the Runx1 gene is required for angiogenesis, hematopoiesis and leukemogenesis in a knock-in mouse model. Dev. Biol. *345*, 226–236.

Ozaki, Y., Matsui, H., Asou, H., Nagamachi, A., Aki, D., Honda, H., Yasunaga, S., Takihara, Y., Yamamoto, T., Izumi, S., et al. (2012). Poly-ADP ribosylation of Miki by tankyrase-1 promotes centrosome maturation. Mol. Cell *47*, 694–706.

Pedersen-Bjergaard, J., Andersen, M.K., Andersen, M.T., and Christiansen, D.H. (2008). Genetics of therapy-related myelodysplasia and acute myeloid leukemia. Leukemia *22*, 240–248.

Roberts, M., Barry, S., Woods, A., van der Sluijs, P., and Norman, J. (2001). PDGF-regulated rab4-dependent recycling of alphavbeta3 integrin from early endosomes is necessary for cell adhesion and spreading. Curr. Biol. *11*, 1392–1402.

Sánchez, C., Sánchez, I., Demmers, J.A., Rodriguez, P., Strouboulis, J., and Vidal, M. (2007). Proteomics analysis of Ring1B/Rnf2 interactors identifies a novel complex with the Fbxl10/Jhdm1B histone demethylase and the Bcl6 interacting corepressor. Mol. Cell. Proteomics *6*, 820–834.

Shima, H., Takubo, K., Tago, N., Iwasaki, H., Arai, F., Takahashi, T., and Suda, T. (2010). Acquisition of G_0 state by CD34-positive cord blood cells after bone marrow transplantation. Exp. Hematol. *38*, 1231–1240.

Shinjyo, T., Kuribara, R., Inukai, T., Hosoi, H., Kinoshita, T., Miyajima, A., Houghton, P.J., Look, A.T., Ozawa, K., and Inaba, T. (2001). Downregulation of Bim, a proapoptotic relative of Bcl-2, is a pivotal step in cytokine-initiated survival signaling in murine hematopoietic progenitors. Mol. Cell. Biol. *21*, 854–864.

Slape, C., Hartung, H., Lin, Y.W., Bies, J., Wolff, L., and Aplan, P.D. (2007). Retroviral insertional mutagenesis identifies genes that collaborate with NUP98-HOXD13 during leukemic transformation. Cancer Res. *67*, 5148–5155.

Sloand, E.M., Yong, A.S., Ramkissoon, S., Solomou, E., Bruno, T.C., Kim, S., Fuhrer, M., Kajigaya, S., Barrett, A.J., and Young, N.S. (2006). Granulocyte colony-stimulating factor preferentially stimulates proliferation of monosomy 7 cells bearing the isoform IV receptor. Proc. Natl. Acad. Sci. USA *103*, 14483–14488.

Takaya, A., Kamio, T., Masuda, M., Mochizuki, N., Sawa, H., Sato, M., Nagashima, K., Mizutani, A., Matsuno, A., Kiyokawa, E., and Matsuda, M. (2007). R-Ras regulates exocytosis by Rgl2/Rlf-mediated activation of RalA on endosomes. Mol. Biol. Cell *18*, 1850–1860.

Topaz, O., Indelman, M., Chefetz, I., Geiger, D., Metzker, A., Altschuler, Y., Choder, M., Bercovich, D., Uitto, J., Bergman, R., et al. (2006). A deleterious mutation in SAMD9 causes normophosphatemic familial tumoral calcinosis. Am. J. Hum. Genet. *79*, 759–764.

Watanabe-Okochi, N., Kitaura, J., Ono, R., Harada, H., Harada, Y., Komeno, Y., Nakajima, H., Nosaka, T., Inaba, T., and Kitamura, T. (2008). AML1 mutations induced MDS and MDS/AML in a mouse BMT model. Blood *111*, 4297–4308.

Weinblatt, M.E., Scimeca, P., James-Herry, A., Sahdev, I., and Kochen, J. (1995). Transformation of congenital neutropenia into monosomy 7 and acute nonlymphoblastic leukemia in a child treated with granulocyte colony-stimulating factor. J. Pediatr. *126*, 263–265.

Wolff, L., Garin, M.T., Koller, R., Bies, J., Liao, W., Malumbres, M., Tessarollo, L., Powell, D., and Perella, C. (2003). Hypermethylation of the Ink4b locus in murine myeloid leukemia and increased susceptibility to leukemia in p15(Ink4b)-deficient mice. Oncogene *22*, 9265–9274.

Yamashita, N., Osato, M., Huang, L., Yanagida, M., Kogan, S.C., Iwasaki, M., Nakamura, T., Shigesada, K., Asou, N., and Ito, Y. (2005). Haploinsufficiency of Runx1/AML1 promotes myeloid features and leukaemogenesis in BXH2 mice. Br. J. Haematol. *131*, 495–507.

Cancer Cell
Article

p53 Acts as a Safeguard of Translational Control by Regulating Fibrillarin and rRNA Methylation in Cancer

Virginie Marcel,[1,2,9] Sandra E. Ghayad,[1,2,9] Stéphane Belin,[1,2,9] Gabriel Therizols,[1,2] Anne-Pierre Morel,[1,2] Eduardo Solano-Gonzàlez,[3] Julie A. Vendrell,[1,2,4,5] Sabine Hacot,[1,2] Hichem C. Mertani,[1,2] Marie Alexandra Albaret,[1,2] Jean-Christophe Bourdon,[5] Lee Jordan,[6] Alastair Thompson,[5] Yasmine Tafer,[1,2] Rong Cong,[7] Philippe Bouvet,[7] Jean-Christophe Saurin,[1,2,8] Frédéric Catez,[1,2] Anne-Catherine Prats,[3] Alain Puisieux,[1,2] and Jean-Jacques Diaz[1,2,*]

[1]Centre de Recherche en Cancérologie de Lyon UMR Inserm 1052 CNRS 5286, Centre Léon Bérard, F-69373, Lyon, France
[2]Université de Lyon, Université Lyon 1, ISPB, Lyon F-69622, France
[3]Université de Toulouse, UPS, TRADGENE, EA4554, Institut des Maladies Métaboliques et Cardiovasculaires, 1 Avenue Jean Poulhès, BP 84225, F-31432 Toulouse, France
[4]ISPB, Faculté de Pharmacie, Université Lyon 1, Lyon, France
[5]Dundee Cancer Centre, Clinical Research Centre, University of Dundee, Dundee DD1 9SY, UK
[6]Department of Pathology, Ninewells Hospital and Medical School, Dundee DD1 9SY, UK
[7]Laboratoire Joliot-Curie, Ecole Normale Supérieure de Lyon, Université de Lyon, CNRS USR 3010, SFR BioSciences UMS3444, Lyon 69364, France
[8]Gastroenterology Unit, Édouard Herriot Hospital, Hospices Civils de Lyon, 69002 Lyon, France
[9]These authors contributed equally to this work
*Correspondence: jean-jacques.diaz@lyon.unicancer.fr
http://dx.doi.org/10.1016/j.ccr.2013.08.013

SUMMARY

Ribosomes are specialized entities that participate in regulation of gene expression through their rRNAs carrying ribozyme activity. Ribosome biogenesis is overactivated in p53-inactivated cancer cells, although involvement of p53 on ribosome quality is unknown. Here, we show that p53 represses expression of the rRNA methyl-transferase fibrillarin (*FBL*) by binding directly to *FBL*. High levels of FBL are accompanied by modifications of the rRNA methylation pattern, impairment of translational fidelity, and an increase of internal ribosome entry site (IRES)-dependent translation initiation of key cancer genes. *FBL* overexpression contributes to tumorigenesis and is associated with poor survival in patients with breast cancer. Thus, p53 acts as a safeguard of protein synthesis by regulating *FBL* and the subsequent quality and intrinsic activity of ribosomes.

INTRODUCTION

Recent findings support the emerging notion that the dysregulation of ribosome biogenesis in cancer cells is not just a consequence of oncogenesis, but represents a key step in this complex process (Barna et al., 2008; Bywater et al., 2012; Yoon et al., 2006). Ribosome biogenesis is a multistage process that involves transcriptional and posttranscriptional regulation and a stringent quality control to produce functional ribosomes (Bashan and Yonath, 2008; Henras et al., 2008). Ribosome biogenesis is overactivated in cancer cells, notably by a loss of function of RNA polymerase I (Pol I) repressors such as p53 (Bywater et al., 2012; Zhai and Comai, 2000).

The posttranscriptional steps of ribosomal RNA (rRNA) processing determine the structure and function of the mature molecule (King et al., 2003; Baxter-Roshek et al., 2007; Puglisi, 2009). Indeed, rRNAs are ribozymes that support the decoding and proofreading steps and catalyze the formation of the peptide

Significance

Ribosome production is increased in cancer cells. This enhanced production of ribosomes plays a crucial role in tumor progression. Our results show that p53 regulates the pattern of ribosomal RNA posttranscriptional modification that impairs translational fidelity and increases the initiation of internal ribosome entry site (IRES)-dependent translation. By demonstrating that p53 regulates the biogenesis and intrinsic activity of ribosomes, our study demonstrates that p53 deficiency participates in the "translational reprogramming" in cancer cells and contributes to the uncontrolled expression of key oncogenic genes.

bond during translation (Cech, 2000; Demeshkina et al., 2012). rRNAs are subjected to intense and highly specific chemical modifications (methylations and pseudouridylations). The exact role of these modifications has not yet been fully elucidated, although it appears that they help optimize the complex ribosomal architecture required to produce an efficient ribosome (Baxter-Roshek et al., 2007).

Changes in the posttranscriptional modifications of rRNAs influence translational fidelity (i.e., nonsense suppression or amino acid misincorporation) and the mode of translation initiation (i.e., CAP versus internal ribosome entry site [IRES]) of key cancer genes (Ruggero, 2013; Basu et al., 2011; Baxter-Roshek et al., 2007). Moreover, a defect in rRNA methylation or pseudouridylation may cause specific clinical syndromes and is correlated with an increased incidence of cancer (Belin et al., 2009; Montanaro et al., 2008). This study aims to determine whether p53 controls rRNA methylation and subsequently affects translational regulation.

RESULTS

FBL Expression Is Inversely Associated with p53 Activity in Cell Lines and Human Breast Cancer Samples

Fibrillarin (FBL) is an indispensable, highly conserved protein essential in the processing of pre-rRNAs (Newton et al., 2003; Tollervey et al., 1993). In eukaryotes, it is the only known methyltransferase that performs the specific 2′-O-ribose-methylation directed by a large family of small *trans*-acting guide RNA (box C/D antisense snoRNAs). Because abnormal rRNA methylation could influence translational control and because p53 regulates rRNA transcription, we explored whether *FBL* expression was associated with p53 activity. We measured *FBL* mRNA and protein levels in different cell lines in which p53 expression and/or activity was modulated by different strategies. In immortalized human mammary epithelial cells (HME), p53 activity was impaired either by reducing its expression using an shRNA approach (HME-shp53) or by inactivation using an SV40 T/t antigen trapping strategy (HMLE; Elenbaas et al., 2001). In response to p53 knockdown or inactivation, there was a significant increase in *FBL* expression: 1.5-fold for the mRNA and 2-fold for the protein (Figures 1A–1D; Figures S1A and S1B available online). As expected, we observed a decrease in the expression of *CDKN1A,* which encodes p21, and *MDM2*, two p53 target genes, which validated the reduction in p53 activity in these cellular models (Figures 1B, 1D, S1A, and S1B). The inverse correlation between *FBL* and p53 expression was confirmed in a second series of immortalized HMEC lines (Figures S1C and S1D) and in an isogenic human HCT-116 colorectal cellular model: HCT-116-p53$^{+/+}$ cells that express wild-type p53 protein and HCT-116-p53$^{-/-}$ cells that lack p53 protein expression (Bunz et al., 1998). *FBL* mRNA and protein levels were increased in HCT-116-p53$^{-/-}$ cells compared to those of HCT-116-p53$^{+/+}$ cells (Figures 1E, 1F, and S1E), demonstrating that the increase in expression of *FBL* in response to p53 inactivation is not restricted to mammary cell lines.

To assess more directly the impact of p53 on *FBL* expression, HME cells were treated with a p53-specific siRNA instead of an shRNA to induce a transient knockdown of p53 expression (Figures 2A, 2B, S2A, and S2B). In this condition, increased *FBL* expression at the mRNA and protein levels correlated with the inhibition of p53 expression (Figures 2A and 2B). Taken together, these results exclude the possibility that the changes in *FBL* expression levels resulted from an off-target effect and firmly link *FBL* expression to p53 expression. Additionally, to investigate the impact of p53 activation on *FBL* expression, we treated HME cells with the topoisomerase inhibitors doxorubicin and camptothecin, which are prominent activators of p53. The results showed that the expected p53 induction in response to treatment was accompanied by a decrease in *FBL* mRNA and protein levels (Figures 2C and 2D). Quantification of the western blots demonstrated a significant association between the increase of p53 protein levels and the decrease of FBL protein levels (Figures S2C–S2E).

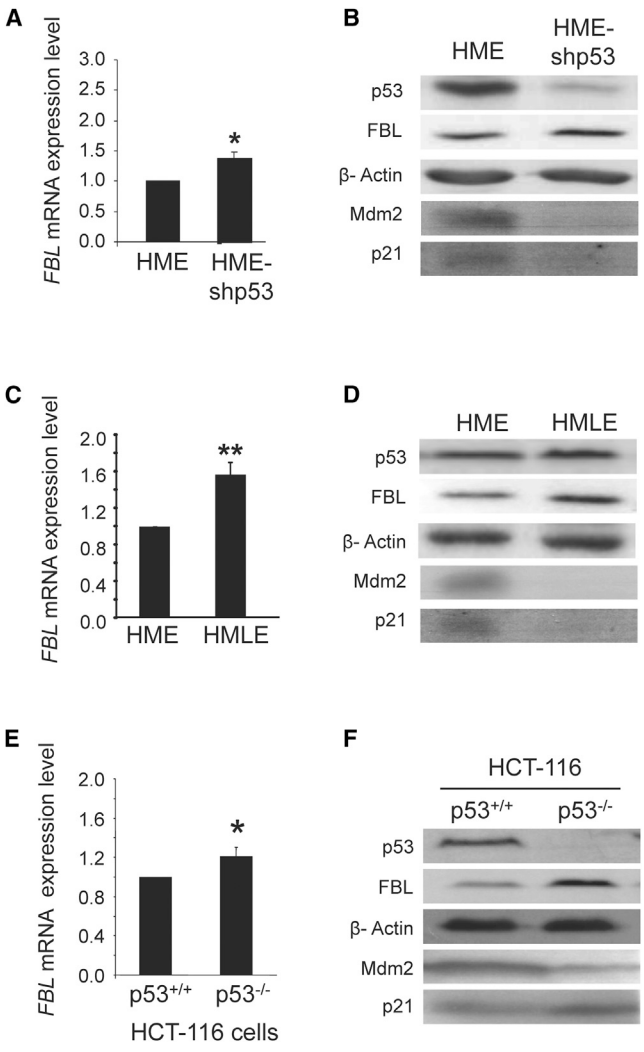

Figure 1. p53 Regulates *FBL* Expression at both the mRNA and Protein Levels

The expression of endogenous *FBL* in the indicated cell lines was analyzed at the mRNA level by RT-qPCR (A, C, and E) and at the protein level by western blot (B, D, and F). All graphs represent mean and SD of at least three experiments. *$p < 0.05$ and **$p < 0.01$ according to Student's t test.

See also Figure S1.

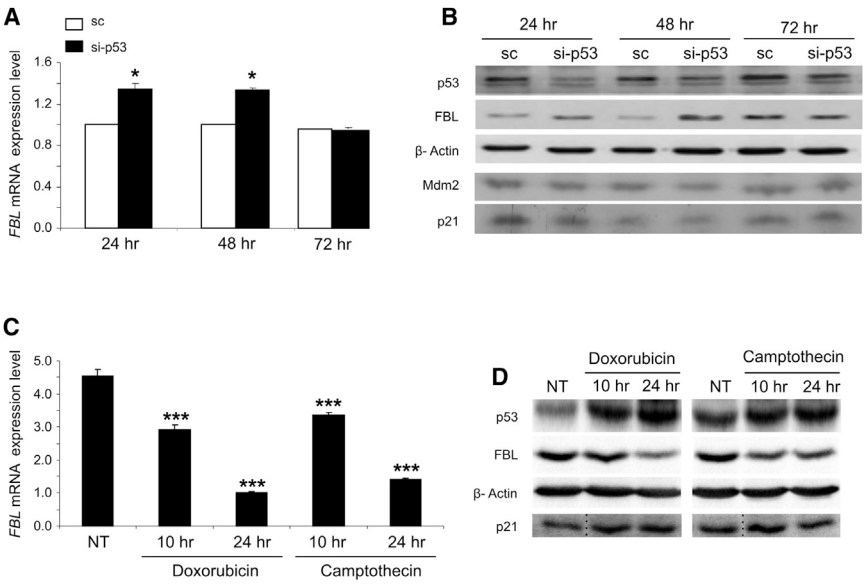

Figure 2. Modulation of p53 Expression Alters *FBL* Expression

Endogenous *FBL* expression was analyzed in HME cells at the mRNA level by RT-qPCR (A and C) and at the protein level by western blot (B and D). The p53 expression is modulated by using an siRNA (A and B) or by treating or not (NT) with 2 μg/ml doxorubicin or 1 nM camptothecin (C and D). The p21 lanes in (D) were spliced together from discontinuous lanes of the same blot as indicated by dotted lines. All graphs represent mean and SD of at least three experiments. *$p < 0.05$ and ***$p < 0.001$ according to Student's t test. See also Figure S2.

In human cancers, the *TP53* tumor suppressor gene is frequently inactivated, mainly by mutations (Olivier et al., 2006). To determine whether *FBL* expression is associated with p53 mutation status independently of other genetic variations in cell lines, we analyzed the *FBL* expression levels in a panel of three wild-type p53 breast cell lines and five mutant p53 breast cancer cell lines. High levels of *FBL* mRNA and protein were significantly associated with the expression of mutant p53 (Figures 3A, 3B, and S3). This result prompted us to investigate the clinical correlation between the p53 mutation status and *FBL* expression. We analyzed the *FBL* mRNA expression levels by RT-qPCR in relation to the p53 mutation status in a cohort of 80 randomly selected primary breast tumors (Table S1). Consistent with the results obtained in cell lines, *FBL* mRNA levels were significantly higher in mutant p53 tumors compared to wild-type p53 tumors (Figure 3C). We also performed a retrospective statistical analysis of the gene expression array data described by Miller and colleagues (Miller et al., 2005). *FBL* mRNA levels were significantly higher in mutant p53 tumors (n = 58) than in wild-type p53 tumors (n = 193; $p < 10^{-4}$, t test). Altogether, these results show a significant and reproducible inverse association between the p53 level and/or activity and the expression of *FBL* at both the mRNA and protein levels, suggesting that p53 can repress *FBL* expression in cellular models of breast and colon cancer as well as in human breast tumors.

p53 Represses *FBL* Expression by Directly Binding to DNA

Using the MatInspector software and the p53FamTag database, two putative p53 responsive elements (p53RE-1 and p53RE-2) were identified within the *FBL* intron 1, suggesting a direct transcriptional regulation of *FBL* expression by p53 (Cartharius et al., 2005; Sbisà et al., 2007; Figures 4A and S4A). Based on these predictions, we developed a luciferase reporter (p*FBL*-Luc) assay to assess whether p53 regulates *FBL* promoter activity. HCT-116-p53$^{-/-}$ cells were cotransfected with p*FBL*-Luc and a plasmid expressing either wild-type or mutant p53 protein at detectable protein levels (Figures 4B and S4B). The coexpression of wild-type p53 significantly decreased the luciferase activity by 80%, while no significant variation in luciferase activity was observed after co-expression of any p53 mutant. Similar results were observed in HME-shp53, the coexpression of wild-type, but not mutant, p53 protein reducing the luciferase activity (Figure 4C). These results suggest that p53 represses promoter activity through intron 1 of *FBL* in both breast and colon cellular models.

To determine whether p53 directly binds to *FBL* gene DNA, chromatin immunoprecipitation (ChIP) assays were performed in HME-derived cells (Figures 4D, 4E, S4C, and S4D). Compared to nontreated HME cells, camptothecin treatment increased p53 binding to both the *CDKN1A* promoter and the intron 1 of *FBL* at p53RE-1 and p53RE-2. In contrast, decrease in p53 expression in HME-shp53 cells was associated with a drastic reduction in p53 binding to both the *CDKN1A* promoter and intron 1 of *FBL* compared with nontreated HME cells (Figures 4D, 4E, S4C, and S4D). These data show that p53 binds the *FBL* intron 1 both in the basal condition and when p53 is activated. Altogether, these results demonstrate that *FBL* is a p53 target gene and that *FBL* expression is directly repressed by p53.

p53-Mediated Alteration of the rRNA Methylation Pattern

Because p53 directly represses *FBL* expression, we determined whether p53 inactivation alters rRNA methylation by using a previously described, site-specific semiquantitative RT-qPCR-based method (Belin et al., 2009; Maden, 1988). We analyzed the change of rRNA methylation at 18 sites distributed along the 5.8S, 18S, and 28S rRNAs that are known to be methylated. These sites include those localized within key functional domains of rRNAs, i.e., the decoding center (DC) in the 18S rRNA, and the peptidyl transferase center (PTC) and the helix 69 (H69) of 28S rRNA. In general, most of the sites were significantly more frequently methylated in HME-shp53 than in HME cells (Figures 5A and S5A). This overall increase in the site-specific rRNA methylation pattern is consistent with our finding that *FBL* expression level is higher in HME-shp53 than in HME cells, and suggests that methylation could be regulated in a site-by-site manner.

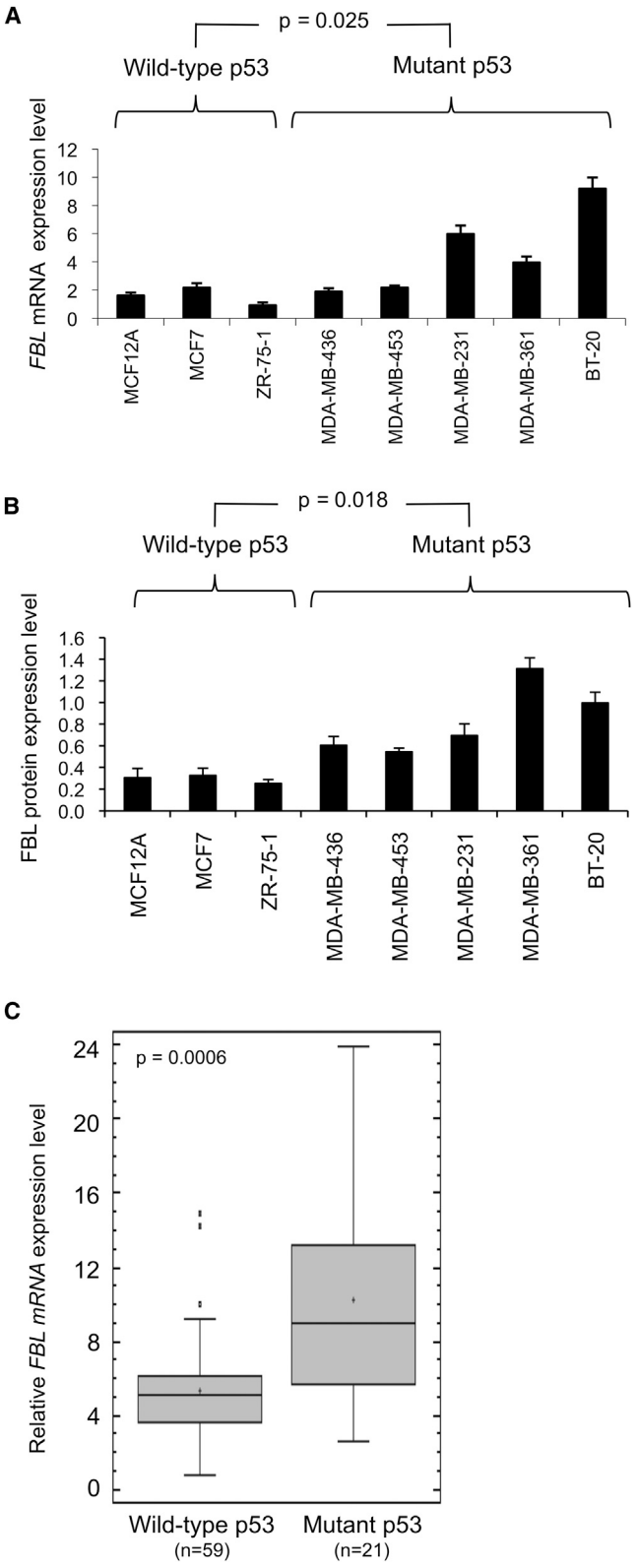

Figure 3. p53 Regulates *FBL* Expression in Human Breast Cell Lines and Tumors

(A) Quantification of *FBL* mRNA expression analyzed by RT-qPCR and normalized to *RNA18S*.

(B) Quantification of FBL protein expression analyzed by western blot. All graphs represent mean and SD of at least three experiments.

(C) Box-and-whisker plots of *FBL* mRNA expression quantification in wild-type p53 (n = 59) versus mutant p53 (n = 21) primary breast tumor samples. The bottom and the top of the boxes represent the 25th and 75th percentiles, respectively. The median values are visible as a line, the mean as a cross in the box and SD as error bars. The p value has been determined by a Mann-Whitney W test.

See also Figure S3 and Table S1.

As expected, metabolic labeling with [5,6-^{3}H]-uridine and L-[methyl-^{3}H]-methionine showed that p53 inactivation led to a significant increase in rRNA synthesis (Figure S5B; Zhai and Comai, 2000), with a faint increase in the global rRNA methylation rate (Figure S5C). This showed that the amount and/or activity of the rRNA methylation machinery was sufficient to sustain the global rRNA methylation rate following the increase in rRNA synthesis after p53 inactivation. In addition, because selection of site methylation is ensured by guide C/D-box snoRNAs that complex with FBL, we verified whether snoRNA expression levels were altered in p53-inactivated cells. Northern blot analyses revealed a modification of snoRNA levels according to p53 levels, suggesting that p53 could also be involved in the regulation of some C/D-box snoRNA as is the case for some H/ACA snoRNP (Figures S5D–S5F; Krastev et al., 2011). However, no correlation was found between the amount of snoRNA and the level of the corresponding rRNA methylation sites (Figures 5A and S5A). These results show that inactivation of p53 resulted in a site-specific modification of the rRNA methylation pattern that correlates with *FBL* expression.

p53 Alters the Translational Fidelity by Modulating *FBL* Expression

The chemical modifications of rRNA that have been conserved throughout evolution in all species are involved, at least in eukaryotes, in the control of translational fidelity and in the control of translation initiation modalities (i.e., CAP-dependent versus IRES-dependent; Ruggero, 2013; Baxter-Roshek et al., 2007; Chaudhuri et al., 2007; Ruggero et al., 2003). We first analyzed two different examples of translational fidelity, nonsense suppression and amino acid misincorporation (Belin et al., 2009). The bypass of a premature stop-codon (Figures 5B–5D) and the misincorporation of amino acids (Figures 5E–5G) were both significantly increased after p53 inhibition or inactivation in different cell lines. This suggested that the translational alteration could be due to p53-mediated increase of *FBL* expression level. To investigate this possibility, we analyzed the misincorporation of amino acids in response to knockdown of *FBL* expression. As shown in Figure 5G, reduction of *FBL* expression in HCT-116-p53$^{-/-}$ prevented the increase in amino acids misincorporation, demonstrating that the decrease in translational quality control in response to p53 inhibition is dependent on *FBL* overexpression. In contrast, the ability of ribosomes to induce a −1 frameshift from a severe acute respiratory syndrome-coronavirus (SARS-CoV)-1 programmed ribosome frameshift signal was similar in the three cell lines (Figures 5H–5J). These results suggest that p53 inactivation could decrease translational fidelity in an FBL-dependent manner.

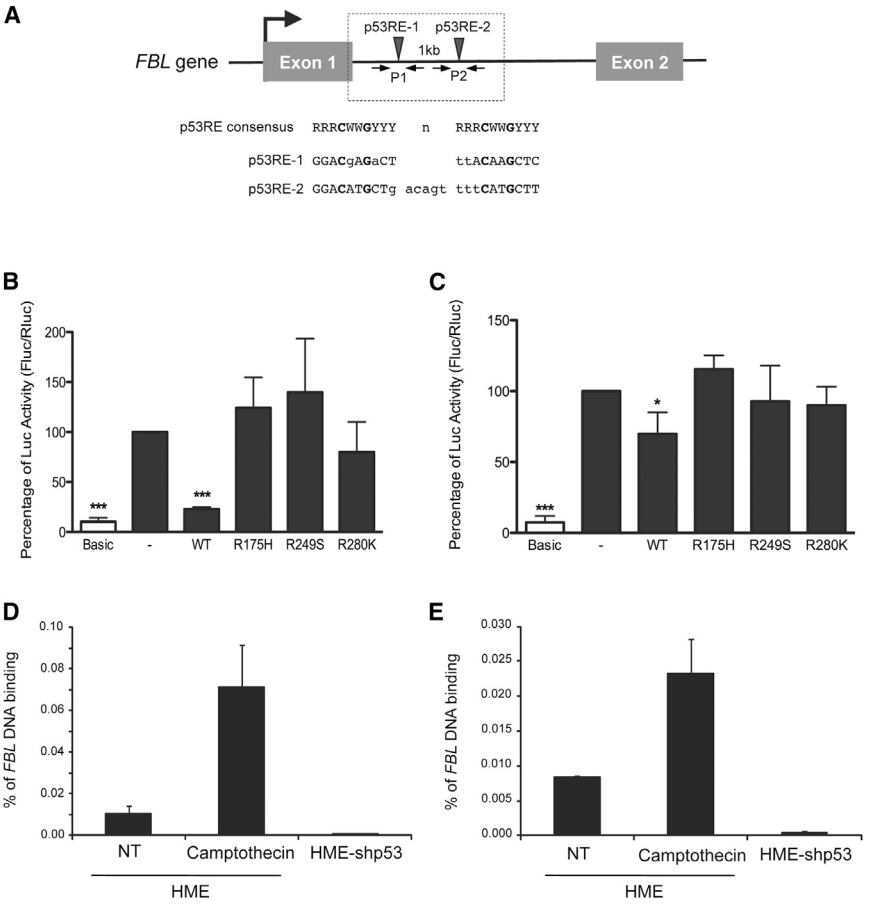

Figure 4. p53 Represses *FBL* Promoter Activity by Directly Binding to DNA

(A) Alignment of the two putative p53 response elements (p53RE-1 and p53RE-2, black arrows) located within the intron 1 of *FBL* with the p53RE consensus (R, G/A; W, A/T; Y, C/T). n, spacer within p53RE consensus; dotted box, nucleotide region of the *FBL* gene cloned in the p*FBL*-Luc reporter vector; P1 and P2, primers pairs used in ChIP assays.

(B and C) Luciferase reporter assays were performed in the absence of p53 (–) and in the presence of the wild-type (WT) or the indicated mutant p53 protein in HCT-116-p53$^{-/-}$ (B) and in HME-shp53 cells (C). *Firefly* luciferase activity is normalized to the *renilla* luciferase activity. Basic, luciferase reporter vector with no *FBL* sequence.

(D and E) ChIP using an anti-p53 antibody and primer pairs P1 (D) or P2 (E) were performed in nontreated (NT) or 1 nM camptothecin-treated HME cells, or in HME-shp53 cells. All graphs represent mean and SD of at least three experiments. *$p < 0.05$ and ***$p < 0.001$ according to Student's t test.

See also Figure S4.

p53 Increases IRES-Mediated Initiation of Translation by Modulating *FBL* Expression

To determine whether the CAP- or IRES-dependent mode of translation was modified, we used a bi-cistronic vector strategy that has been extensively used to identify a vast number of IRES-containing sequences (Belin et al., 2009; Komar and Hatzoglou, 2011). At this stage of the study, we focused our analysis on *IGF1R* due to its role in tumorigenesis and because *IGF1R* possesses the longest GC-rich 5′UTR that contains a well-identified IRES among all human transcripts yet characterized (Giraud et al., 2001; Pollak et al., 2004). Using a bi-cistronic luciferase assay, we observed a significant increase in the global luciferase activity in the p53-inactivated HME-shp53 and HCT-116-p53$^{-/-}$ cells compared with cells expressing wild-type p53 (Figure 6A). This increase was due to a preference to initiate IRES-dependent translation. Indeed, the translation of the *firefly* luciferase driven by the IRES of *IGF1R* was significantly increased, while no significant variation was detected for the *renilla* luciferase driven by a CAP-dependent mechanism (Figures S6A and S6B). Similar results were obtained in other HME-derived cell lines (Figures 6B, white bars; Figures S6C and S6D, sc bars). Moreover, HME and HMLE cells expressed similar levels of *firefly* luciferase mRNA and *renilla* luciferase mRNA independently of variations in p53 protein levels, which supports the hypothesis of IRES-mediated translational regulation rather than transcriptional regulation of *IGF1R* expression (Figure S6E).

To evaluate whether a similar regulation exists in human cell lines, we explored the *IGF1R* IRES activity in breast cell lines that express wild-type or mutant p53 protein (Figure 6C). The activity level of the *IGF1R* IRES was significantly higher in the mutant p53 cells that expressed high levels of *FBL* compared with the wild-type p53 cells that expressed low levels of *FBL*. Thus, translation initiation mediated by the *IGF1R* IRES was higher in breast cell lines that had inactivated p53 instead of wild-type p53.

To confirm that the IRES activity was modulated by rRNA methylation, we analyzed the *IGF1R* IRES activity after using an *FBL*-siRNA knockdown approach that reduced the FBL protein level (Figures S6C, S6D, and S6F). As shown in Figure 6B, reduction of *FBL* expression significantly decreases the IRES-dependent translation initiation of *IGF1R* in HME, HME-shp53 and HMLE cells. This result demonstrates that the efficiency of IRES-dependent translational initiation is modulated by rRNA methylation through modulation of *FBL* expression.

To determine whether the p53-mediated translational control of the *IGF1R* mRNA observed with recombinant expression vectors also occurs with endogenous *IGF1R* mRNA, we compared the distribution of the *IGF1R* mRNA within polysomal fractions of HME and HME-shp53 cells. The polysomal fraction corresponds to mRNA bound to more than one ribosome and therefore contains actively translated mRNA. As shown in Figure 6D, a significant 12-fold polysomal enrichment in *IGF1R* mRNA was observed in HME-shp53 compared with HME cells. In addition, a significant increase in the IGF1R protein level was observed in p53-inactivated HMLE cells compared to HME cells independently of any variation in *IGF1R* mRNA levels (Figures 6E and

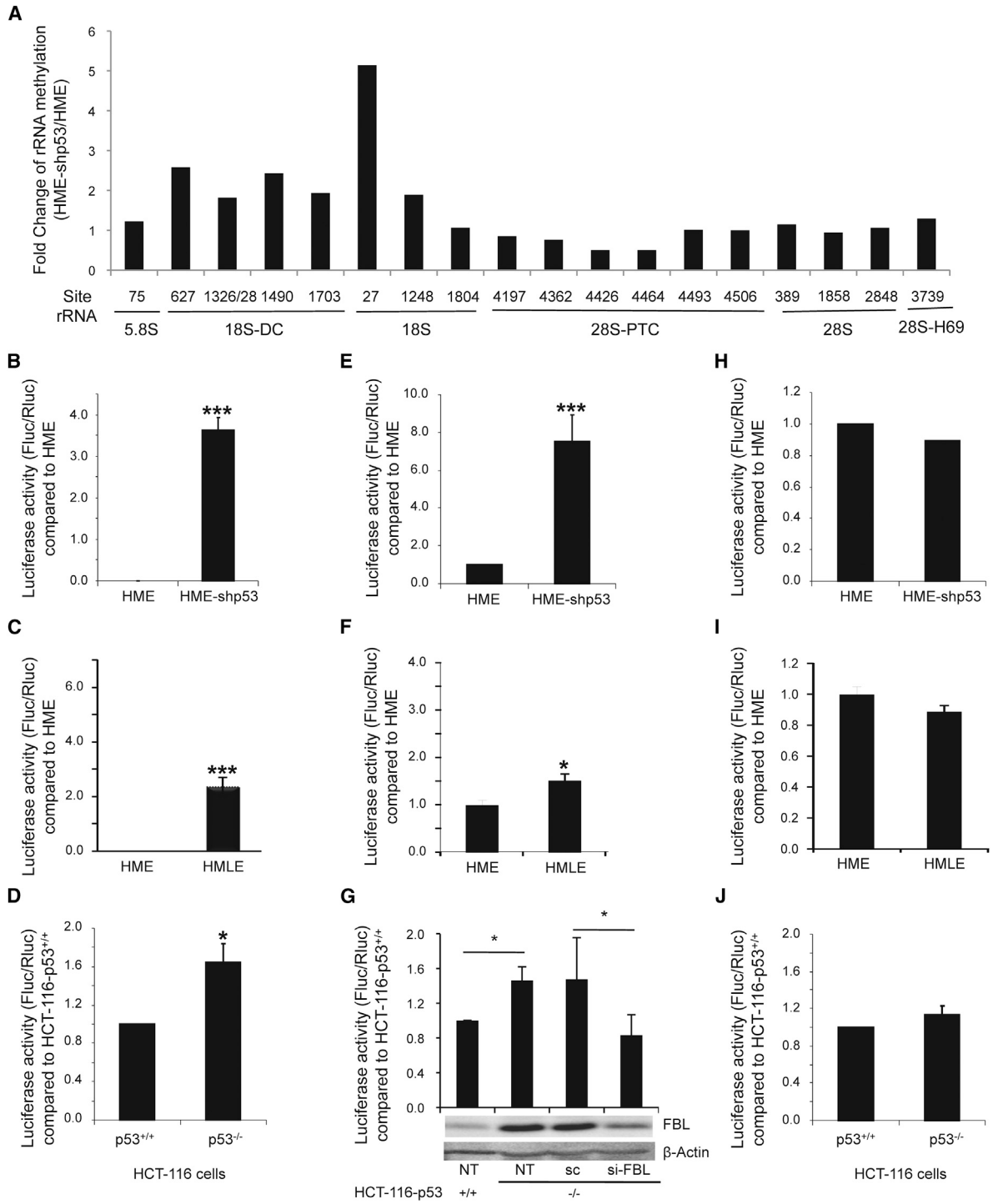

Figure 5. p53 Regulates the rRNA Methylation Pattern and the Translational Fidelity of Ribosomes

(A) The fold difference in rRNA methylation at 18 sites distributed throughout the 5.8S, 18S, and 28S rRNAs between HME-shp53 and HME cells were analyzed by RT-qPCR.

(B–J) Translational fidelity was analyzed by transfecting cells with the pGL3mut1 vector (premature stop mutant, B–D), the pGL3mut2 vector (amino acid substitution mutant, E–G), or the SARS-CoV −1 programmed ribosome frameshift vector (H–J) in the indicated cells. (G) Translational fidelity was analyzed in nontransfected cells (NT) and after transfection of siRNA control (sc) or siRNA targeting *FBL* (si-FBL). FBL expression levels were verified by western blot (G, lower panel). All graphs represent mean and SD of at least three experiments. *$p < 0.05$ and ***$p < 0.001$ according to Student's t test.

See also Figure S5.

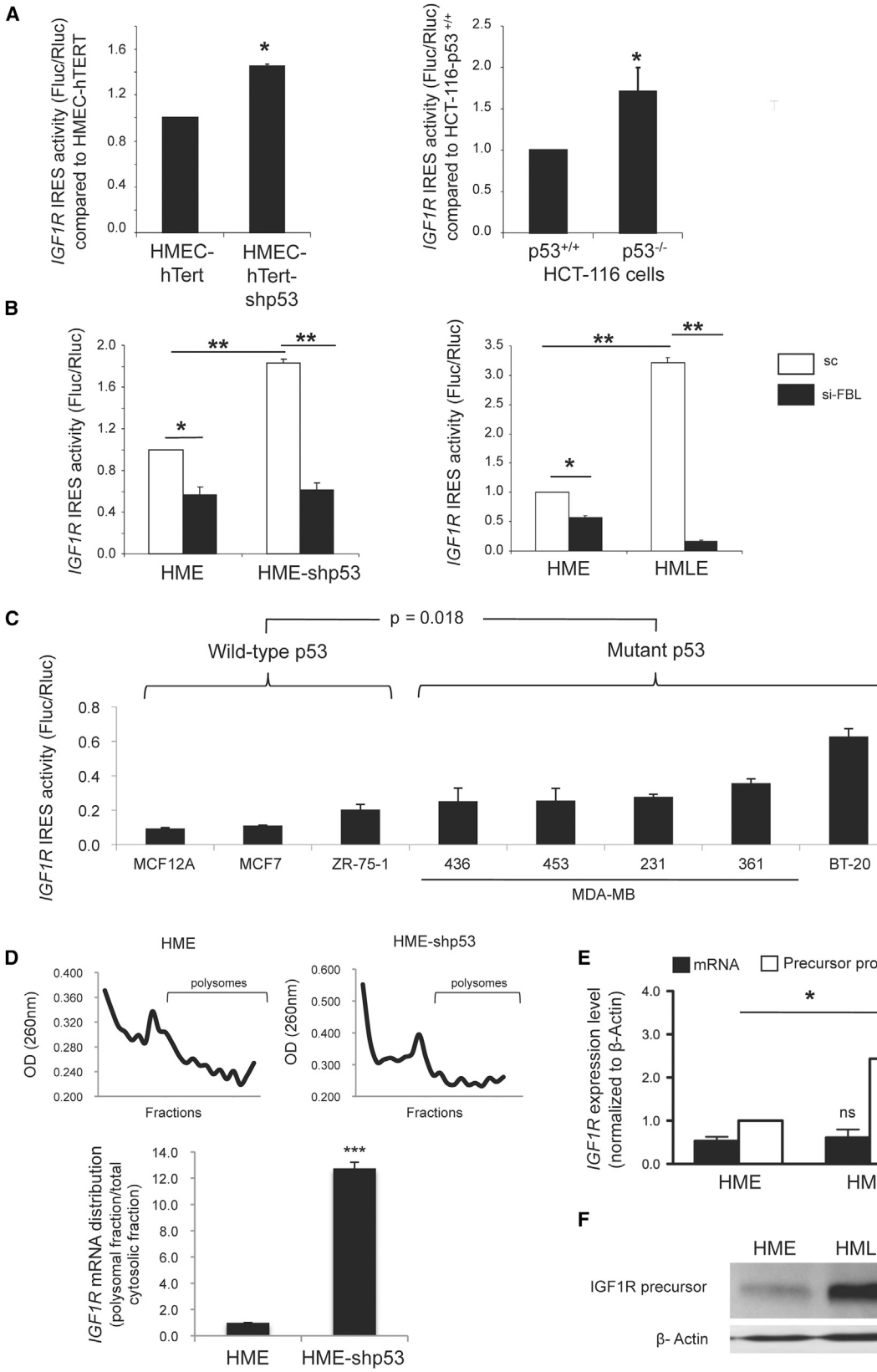

(legend on next page)

6F). These results demonstrate that p53 inactivation increases the translation of *IGF1R* mRNA.

To investigate whether this p53-mediated translational control is restricted to *IGF1R* mRNA, we analyzed translational control of several other known cellular and viral mRNAs containing IRESs, including *MYC*, *FGF1*, *FGF2*, and *VEGFA* that play key roles in oncogenesis (Dang, 2012; Turner and Grose, 2010; Carmeliet and Jain, 2011) and encephalomyocarditis virus. Bi-cistronic luciferase assays and mRNA polysomal profiling assays showed an increase of translational efficiency of these mRNA in p53 inactivated cells compared to p53 wild-type cells (Figures S6G–S6I). Altogether these results show that p53 inactivation impacts the translational control of several genes involved in tumorigenesis through deregulation of *FBL* expression.

FBL Overexpression Contributes to Tumorigenesis

Six independent stable clones derived from MCF7 cells overexpressing either a FBL-GFP protein or a GFP protein were developed (Figure S7A) to determine the effect of *FBL* overexpression on several characteristics of cancer cells. Cell proliferation of the stable clones was first monitored for 72 hr and the index of cell proliferation was calculated from the slope of the growth curve (Figure 7A). Cells overexpressing FBL-GFP exhibit a significant 2-fold increase in proliferation rate compared with GFP control cells. To determine whether the FBL-induced cell proliferation is mediated by *IGF1R*, whose translation is increased in *FBL*-overexpressing cells, proliferation of two clones was monitored in response to Osi-906, an IGF1R tyrosine kinase activity inhibitor (Figure 7B; Mulvihill et al., 2009). Inhibition of IGF1R pathway activity abolished the difference in proliferation rate between GFP-G3 and FBL-GFP-F2 clones, suggesting that IGF1R pathway activity is required in these cells, for FBL-induced cell proliferation.

Anchorage-independent cell proliferation was then investigated using soft agar assays. Compared to GFP control clones, those overexpressing FBL-GFP formed significantly more colonies (Figures 7C and 7D). Finally, the effect of *FBL* overexpression on cell growth in response to doxorubicin treatment was investigated (Figure 7E). A significantly higher concentration of doxorubicin is required to reach 50% of inhibitory effect in FBL-GFP cells compared to GFP control cells (mean half-maximal inhibitory concentration [IC_{50}]: 24.6 μM versus 53.1 μM, respectively). Altogether, these data show that *FBL* overexpression promotes cell proliferation in both an anchorage-dependent and -independent manner and protects the MCF7 breast cancer cells from doxorubicin. Moreover, the FBL-induced cell proliferation required IGF1R pathway, supporting the notion that *FBL* overexpression can directly contribute to tumorigenesis by altering translational control of key cancer genes.

High Levels of *FBL* Are an Independent Marker of a Poor Outcome in Breast Cancer

To investigate whether the level of *FBL* mRNA in tumors is associated with prognosis, we analyzed the relapse-free survival and the breast cancer-specific survival of patients with breast cancer in regard to *FBL* expression. High expression of *FBL* mRNA was significantly associated with a poor relapse-free survival rate and poor breast cancer-specific survival rate (Figures 7F and 7G). We also performed retrospective statistical analyses of published gene expression array data (Györffy et al., 2010; Sabatier et al., 2011; Weigelt et al., 2005). This investigation confirmed that the high levels of *FBL* mRNA are associated with poor breast cancer-specific survival and relapse-free survival rates (Figures S7B–S7F).

However, because the high levels of *FBL* expression are associated with p53 mutations and because p53 mutations are known to be associated with poor disease-free and overall survival rates (Olivier et al., 2006), a multivariate analysis was conducted to adjust for possible confounding variables. The analysis included the number of invaded lymph nodes, histological grade, estrogen and progesterone receptors status, ErbB2 status, p53 mutation status, and *FBL* mRNA levels. The best model associated with poor survival contained two independent markers: progesterone receptor-negative status and high *FBL* expression (Table S2). These analyses showed that *FBL* expression is associated with poor survival independent of other commonly used clinical markers.

DISCUSSION

It is now clearly established that ribosome synthesis is increased in cancers due to the overexpression of oncogenes or the inactivation of tumor suppressor genes leading to a sustained increase in RNA Pol I activity (Bywater et al., 2012). Moreover, studies performed in different animal and cellular models of various eukaryotic organisms have shown that heterogeneity in ribosome composition, due to regulated posttranscriptional modifications of ribosomal proteins and rRNA, is likely to be the more common mechanism (Xue and Barna, 2012). Xue and Barna have made detailed contributions to extend the concept of "specialized ribosomes" to eukaryotes and highlighted the adaptive capabilities of the ribosomes in the control of cell fate through selective protein synthesis. Moreover, it is now well demonstrated that within the ribosomes, the rRNAs catalyze and control protein synthesis through their ribozyme activity that could be finely optimized by their rRNAs methylations and pseudouridylations (Baxter-Roshek et al., 2007; Belin et al., 2009). In this study, we show a p53-mediated alteration of ribosome biogenesis and translational control of cancer cells that

Figure 6. p53 Regulates the *IGF1R* IRES-Dependent Translation

(A and B) The *IGF1R* IRES-dependent translation initiation was determined by using luciferase bi-cistonic vectors in the indicated cells (A) and in cells after the downregulation of *FBL* by siRNA approach (B).

(C) Analysis of the *IGF1R* IRES-dependent translation initiation in a panel of breast cell lines expressing either wild-type or mutant p53 proteins.

(D) Typical polysomal profiles after fractionation of postmitochondrial supernatants from HME and HME-shp53 cells in a 10%–40% sucrose gradient are shown (upper). The distribution of the *IGF1R* mRNA within polysomes was determined by RT-qPCR (lower).

(E and F) Endogenous *IGF1R* expression at mRNA (E, black bars) and protein levels (E, white bars; and F) was analyzed in HME and HMLE cells. All graphs represent mean and SD of at least three experiments. *$p < 0.05$, **$p < 0.01$ and ***$p < 0.001$ according to Student's t test.

See also Figure S6.

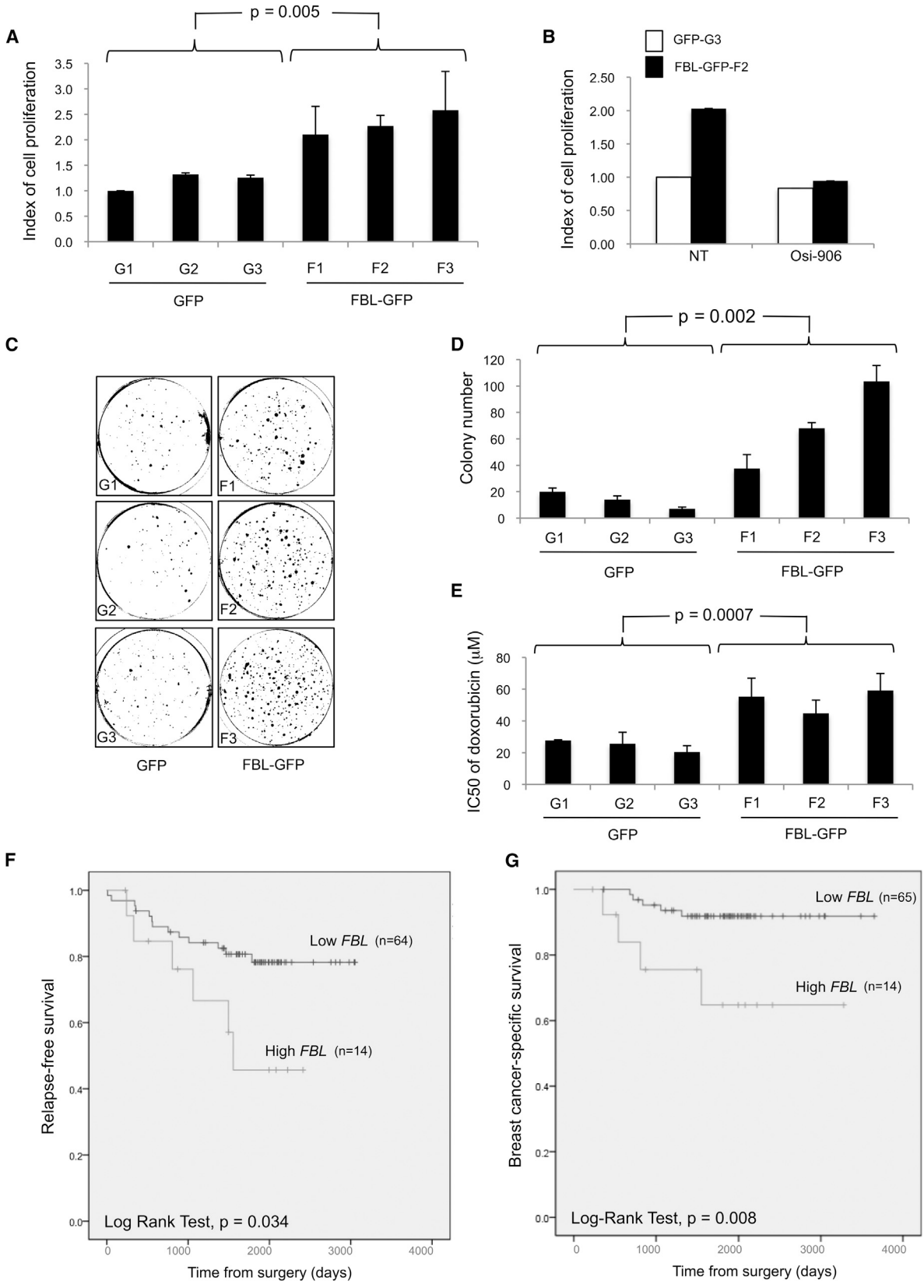

(legend on next page)

could contribute in gene expression dysregulation and cancer development (Ruggero, 2013).

We demonstrate a role of p53 in the control of rRNA methylation patterning by directly regulating *FBL* expression levels that leads to the synthesis of modified "cancer ribosomes." The notion that *FBL* is a p53-target gene is supported by genome-wide analyses, such as ChIP-seq assays showing that p53 binds the *FBL* gene (ENCODE database, Nikulenkov et al., 2012) and by transcriptomic analysis showing an inverse expression of *FBL* in response to p53 inactivation by siRNA or activation by doxorubicin in several cell lines (Troester et al., 2006). p53 response elements have also been identified in the first intron of approximately 25% of p53 target genes, some of them being associated with gene repression, including genes involved in ribosome biogenesis such as *NOLC1*, a snoRNP chaperone gene (Menendez et al., 2009; Krastev et al., 2011).

We found that the methylation pattern of rRNAs varies between sites, which is consistent with published data (Baxter-Roshek et al., 2007; Belin et al., 2009; Basu et al., 2011) and suggests that the rRNA modification pattern is modulated in a site-by-site manner. Our data showed that p53 inactivation is sufficient to alter rRNA methylation patterning. In addition to regulating *FBL* expression, the role of p53 in optimizing the rRNA functional quality is reinforced by our observations that the level of some C/D-box snoRNAs is modulated according to the p53 status and that p53 is involved in the assembly process of the other major family of snoRNP (H/ACA box; Krastev et al., 2011). Deciphering the mechanisms by which p53 inactivation alters the site-specific rRNA methylation pattern through *FBL* induction will require biochemical and structural studies dedicated to the understanding of formation, dynamics, and activities of the rRNA methylation complex. However, we can hypothesize that the improper induction of *FBL* expression observed in cancer cells leads to an alteration of the coordination between pre-rRNA production and the rRNA methylation enzymatic machineries.

Today, several pieces of data, including ours, indicate that modulation of methylation at only some rRNA sites is sufficient to affect the translational regulation process and that it could alter cellular behavior without inducing a lethal phenotype (King et al., 2003; Baudin-Baillieu et al., 2009; Higa-Nakamine et al., 2012). Indeed, the depletion of methylation of several rRNA methylation sites in yeast and human cells has been associated with a decrease in translation fidelity (such as an increase in nonsense suppression, frameshifts, and amino acid misincorporation; Baxter-Roshek et al., 2007; Baudin-Baillieu et al., 2009). Moreover, modulating rRNA methylation by RPL13a depletion in HeLa cells modified the control of the translation initiation by IRES (Basu et al., 2011). Modification in the rRNA methylation pattern in breast cancer cells exhibiting an induced aggressive phenotype was also associated with the alteration of IRES activity of key factors such as vascular endothelial growth factor (VEGF) and p53 (Belin et al., 2009). In the present study, we demonstrate that the repression of *FBL* expression by p53 is accompanied by an increase of IRES-dependent translation initiation, affecting cellular as well as a viral IRES-containing mRNAs. These data are consistent with previous reports showing that the *FGF2* mRNA translation is inhibited by p53, whereas the *FGF2* mRNA IRES is aberrantly activated in transformed cells when p53 is inactivated (Galy et al., 2001). It remains to systematically explore the effect of methylation sites, individually and as a pattern, in the intrinsic activity of the ribosome.

Modulation of intrinsic activity of the ribosome by altering rRNA methylation may involve structural changes of ribosomes. The inhibition of rRNA methylation altered the IRES translation initiation by impairing the association of the 40S and 60S subunits (Basu et al., 2011). Moreover, structural and biochemical studies showed that ribose methylation modifies the conformational state of the RNA backbone, stabilizes the RNA loops, and influences the overall structure of the modified RNA regions. Ribose methylation helps maintain the tertiary structure of rRNAs and potentially the rRNA-mRNA, rRNA-tRNA or rRNA-protein interactions (Blanchard and Puglisi, 2001; Liang et al., 2009). Consistently, several 18S rRNA regions promote structural modifications when a viral IRES is bound to the 40S subunit (Spahn et al., 2004) and the efficient translation of *IGF1R* mRNA results from its IRES directly contacting an 18S rRNA domain through a Shine-Dalgarno-like interaction (Meng et al., 2010). These data support the notion that rRNA methylation could participate in translational control by regulating IRES translation initiation.

Our clinical analysis shows that a high level of *FBL* in primary breast tumors is associated with poor survival independent of other biological markers. Elevated expression levels of *FBL* were previously reported in primary and metastatic prostate cancers compared with normal prostate epithelium and in squamous cell cervical carcinoma compared with normal cervix samples (Choi et al., 2007; Koh et al., 2011; Su et al., 2013). Furthermore, we have shown the direct contribution of *FBL* overexpression in tumorigenesis. The maintenance and progression of cancer phenotype induced by FBL-mediated enhanced translation may involve several key cancer proteins whose synthesis is dependent upon IRES-containing mRNA. As shown here,

Figure 7. Contribution of *FBL* Overexpression to Cancer Phenotype

(A) Cell proliferation of three each independent stable MCF7 clones expressing FBL-GFP (F1, F2, and F3) or GFP (G1, G2, and G3).

(B) Proliferation of the indicated cell clones not treated (NT) or treated with 1 μM Osi-906 for 72 hr.

(C and D) Anchorage-independent growth of MCF7 clones using soft agar assay. Representative images are shown in (C) and the numbers of colonies determined in three experiments are shown in (D).

(E) Impact of *FBL* overexpression on drug response was investigated by determining the IC_{50} of doxorubicin using MTS assays. Error bars represent SD. The p values have been determined by a Mann-Whitney W test.

(F and G) Kaplan-Meier analysis of relapse-free survival rates (event = relapse) (F) and of breast cancer-specific survival rates (event = death related to breast cancer disease) (G) according to *FBL* mRNA level in primary breast tumor samples. The data are dichotomized at the upper quartile value into high and low expression groups.

See also Figure S7 and Table S2.

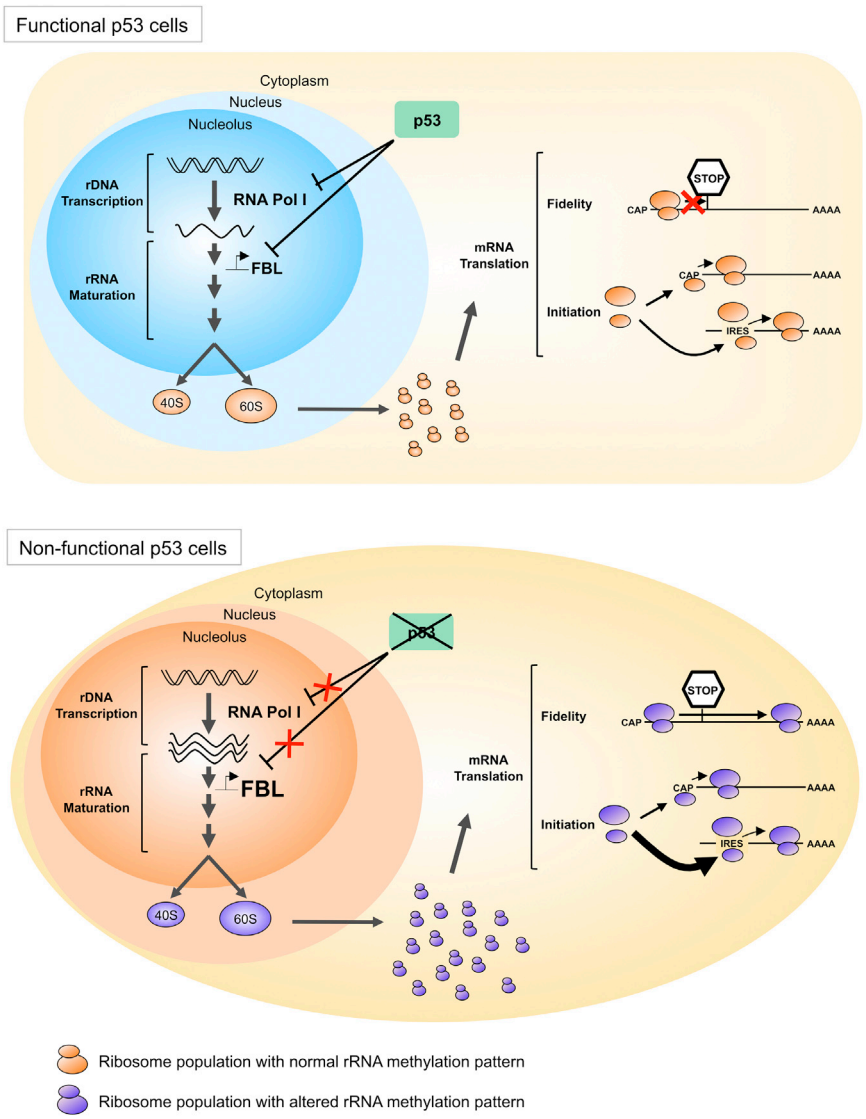

Figure 8. Model of the Implication of p53 in the Control of Ribosomes Quantity and Ribosomes Quality, and Their Consequences on Translation

In cells expressing functional p53 (top), p53 negatively regulates RNA Pol I activity to control ribosome quantity and *FBL* expression levels to control ribosome quality. This regulation would aim to coordinate the methylation of ribosomes and the rate of ribosome production according to the cell needs. These quality-controlled ribosomes allow a high translational fidelity together with a correct control of the balance between CAP- and IRES-dependent initiation of translation. In cells expressing a mutant or nonfunctional p53 (bottom), loss of the repression of RNA Pol I activity leads to an increase in rRNA synthesis. In parallel, p53 inactivation leads to an increase in *FBL* expression levels, resulting in a modification of the rRNA methylation patterns. Ribosomes with modified rRNA methylated translate mRNA with a lower fidelity (bypass of stop codon, amino acid misincorporation) and are more likely to initiate translation through IRES of mRNA coding for pro-oncogenic, anti-apoptotic, and survival proteins.

these proteins may include IGF1R, which is involved in tumor progression, cell survival, and response to chemotherapy (Pollak et al., 2004), c-Myc, which exhibits pleiotropic pro-oncogenic functions (Dang, 2012), FGF1/2, which are involved in epithelial-mesenchymal transition (Sakuma et al., 2012), and VEGFA, which is involved in tumoral angiogenesis (Carmeliet and Jain, 2011). Thus, high levels of *FBL* observed in human samples could have a role in tumor progression and could affect the clinical outcome of patients through alteration of translational regulation.

Our results allow us to propose a model in which p53 regulates not only the ribosome production rate, but also their structure, function, and intrinsic activity (Figure 8). In this model, p53 alteration in pathological cells results in the production of ribosomes with decreased translational fidelity and increased translation of the IRES-containing mRNAs selectively. Thus, the p53-mediated ribosome alterations could be in part responsible for the "translational instability" of cancer cells and contribute to the expression of the continuously growing class of translationally regulated cancer-promoting genes (Ruggero, 2013).

Finally, the detailed description of rRNA chemical modification patterning in cancer cells, occurring in part through the p53-mediated regulation of ribosome biogenesis enzymatic machineries, and the increasing knowledge of the ribosome structure at the atomic level (Anger et al., 2013), opens up the possibility to target these "cancer ribosomes" to develop anticancer molecules using strategies similar to those used for the development of antibiotics specifically targeting prokaryotic ribosomes (Yonath, 2009).

EXPERIMENTAL PROCEDURES

Cell Culture, Transfection, and Luciferase Assay

Cells were maintained in culture following ATCC recommendations. siRNA and plasmids (Belin et al., 2009) were transfected using lipofectamine 2000 (Invitrogen). Cells were treated with 2 μg/ml doxorubicin or 1 nM camptothecin (Sigma). Luciferase activity was measured using the Dual Luciferase Reporter Assay kit (Promega). Anchorage-dependent cell proliferation was analyzed using a real-time monitoring cell proliferation assay based on variation of electric impedance using the xCELLigence RTCA system (ACEA Biosciences) for 72 hr in nontreated cells or in presence of 1 μM Osi-906 (Selleckchen). Anchorage-independent cell proliferation was analyzed by soft agar assays. The IC_{50} values for doxorubicin were determined by MTS assays (Promega).

Western Blot and Chromatin Immunoprecipitation

Protein extraction and western blot were performed as described (Belin et al., 2010) using the following antibodies: anti-FBL (38F3, Abcam); anti-p53 (DO-1, Santa Cruz); anti-β-actin (AC-15, Sigma); anti-Mdm2 (4B2, Bethyl

Laboratories); anti-p21 (F-5, Santa Cruz); and anti-IGF1Rα (N20, Santa Cruz). For ChIP assays, chromatin was prepared from 1% formaldehyde fixed cells by sonication. Immunoprecipitation was performed on 200-1000 bp DNA fragments using the DO-1 anti-p53 antibody and immunoprecipitated DNA was quantified by qPCR using Sybr Green technology.

Total mRNA, Polysomal mRNA, and rRNA Methylation Quantification

Total RNA and RNA issued from cytosolic and polysomal fractions was extracted and purified using either Trizol reagent (Invitrogen) or TriPure Isolation reagent (Roche). Cytosolic ribosomes were obtained from postmitochondrial fractions, and polysomal ribosomes by separation of postmitochondrial fractions on a 10%–40% sucrose gradient by ultracentrifugation. Total, cytosolic, and polysomal mRNA levels were quantified by RT-qPCR using M-MLV and Sybr Green technologies as described (Ghayad et al., 2009). Site-specific rRNA methylation was quantified using a RT-qPCR based method, which relies on the inhibition of reverse transcription reaction by ribose methylation at low dNTP concentration and on the detection of total rRNA as an internal reference, by reverse transcription at high dNTP concentration (Belin et al., 2009). RT products were then quantified by qPCR.

Breast Tumor Samples

FBL mRNA expression was analyzed in a cohort of 80 primary breast tumors collected at Ninewells Hospital from white women who received no neoadjuvant treatment prior surgery (Tayside Tissue Bank, Dundee; Table S1). Informed consent was obtained from all patients and ethical approval was received from the Tayside Tissue Bank (REC Reference 07/S1402/90) under delegated authority from the Local Research Ethics Committee. Relapse-free survival was calculated among breast cancer patients from the date of diagnosis to the date of relapse (event = relapse). Breast cancer-specific survival was calculated from the date of diagnosis to the date of breast cancer specific death (event = death related to breast cancer disease). The characterization of the classical molecular markers (histological grade, invaded lymph node, p53 mutation as well as estrogen, progesterone, and errB2 status) was previously determined and reported (Bourdon et al., 2011).

Statistical Analyses

Statistical analyses were performed using the Statgraphics 3 plus software (Statgraphics Centurion). The log-rank test (univariate analysis), Kaplan-Meier plots, and Cox proportional hazards model (multivariate analysis) were performed using SPSS Software. A p value < 0.05 was considered to be statistically significant. All graphs present the mean and standard variations of at least three independent experiments and Student's t test has been performed for experimental data.

Experimental procedures are detailed in the Supplemental Experimental Procedures.

SUPPLEMENTAL INFORMATION

Supplemental Information includes Supplemental Experimental Procedures, seven figures, and two tables and can be found with this article online at http://dx.doi.org/10.1016/j.ccr.2013.08.013.

ACKNOWLEDGMENTS

This work was supported by Centre Léon Bérard, CNRS, INSERM, Université Claude Bernard Lyon 1, Ecole Normale Supérieure de Lyon, Cancéropôles GSO and CLARA, ARC, FRM, ANR (Oncoscreen), and Ligue Contre le Cancer. It was funded by grants from Région Rhône-Alpes (thématiques prioritaires and Cluster 10), Ligue Contre le Cancer (Comité du Rhône), Institut National contre le Cancer (RIBOCAN). V.M. is a recipient of a postdoctoral fellowship from the Centre Léon Bérard. S.B. and G.T. are recipients of doctoral fellowships from the Ligue Contre le Cancer and from ARC for S.B. We thank Carine Jolyon for her technical assistance.

Received: June 20, 2012
Revised: July 8, 2013
Accepted: August 12, 2013
Published: September 9, 2013

REFERENCES

Anger, A.M., Armache, J.P., Berninghausen, O., Habeck, M., Subklewe, M., Wilson, D.N., and Beckmann, R. (2013). Structures of the human and Drosophila 80S ribosome. Nature *497*, 80–85.

Barna, M., Pusic, A., Zollo, O., Costa, M., Kondrashov, N., Rego, E., Rao, P.H., and Ruggero, D. (2008). Suppression of Myc oncogenic activity by ribosomal protein haploinsufficiency. Nature *456*, 971–975.

Bashan, A., and Yonath, A. (2008). Correlating ribosome function with high-resolution structures. Trends Microbiol. *16*, 326–335.

Basu, A., Das, P., Chaudhuri, S., Bevilacqua, E., Andrews, J., Barik, S., Hatzoglou, M., Komar, A.A., and Mazumder, B. (2011). Requirement of rRNA methylation for 80S ribosome assembly on a cohort of cellular internal ribosome entry sites. Mol. Cell. Biol. *31*, 4482–4499.

Baudin-Baillieu, A., Fabret, C., Liang, X.-H., Piekna-Przybylska, D., Fournier, M.J., and Rousset, J.-P. (2009). Nucleotide modifications in three functionally important regions of the Saccharomyces cerevisiae ribosome affect translation accuracy. Nucleic Acids Res. *37*, 7665–7677.

Baxter-Roshek, J.L., Petrov, A.N., and Dinman, J.D. (2007). Optimization of ribosome structure and function by rRNA base modification. PLoS ONE *2*, e174.

Belin, S., Beghin, A., Solano-Gonzàlez, E., Bezin, L., Brunet-Manquat, S., Textoris, J., Prats, A.-C., Mertani, H.C., Dumontet, C., and Diaz, J.-J. (2009). Dysregulation of ribosome biogenesis and translational capacity is associated with tumor progression of human breast cancer cells. PLoS ONE *4*, e7147.

Belin, S., Kindbeiter, K., Hacot, S., Albaret, M.A., Roca-Martinez, J.X., Thérizols, G., Grosso, O., and Diaz, J.-J. (2010). Uncoupling ribosome biogenesis regulation from RNA polymerase I activity during herpes simplex virus type 1 infection. RNA *16*, 131–140.

Blanchard, S.C., and Puglisi, J.D. (2001). Solution structure of the A loop of 23S ribosomal RNA. Proc. Natl. Acad. Sci. USA *98*, 3720–3725.

Bourdon, J.-C., Khoury, M.P., Diot, A., Baker, L., Fernandes, K., Aoubala, M., Quinlan, P., Purdie, C.A., Jordan, L.B., Prats, A.-C., et al. (2011). p53 mutant breast cancer patients expressing p53γ have as good a prognosis as wild-type p53 breast cancer patients. Breast Cancer Res. *13*, R7.

Bunz, F., Dutriaux, A., Lengauer, C., Waldman, T., Zhou, S., Brown, J.P., Sedivy, J.M., Kinzler, K.W., and Vogelstein, B. (1998). Requirement for p53 and p21 to sustain G2 arrest after DNA damage. Science *282*, 1497–1501.

Bywater, M.J., Poortinga, G., Sanij, E., Hein, N., Peck, A., Cullinane, C., Wall, M., Cluse, L., Drygin, D., Anderes, K., et al. (2012). Inhibition of RNA polymerase I as a therapeutic strategy to promote cancer-specific activation of p53. Cancer Cell *22*, 51–65.

Carmeliet, P., and Jain, R.K. (2011). Molecular mechanisms and clinical applications of angiogenesis. Nature *473*, 298–307.

Cartharius, K., Frech, K., Grote, K., Klocke, B., Haltmeier, M., Klingenhoff, A., Frisch, M., Bayerlein, M., and Werner, T. (2005). MatInspector and beyond: promoter analysis based on transcription factor binding sites. Bioinformatics *21*, 2933–2942.

Cech, T.R. (2000). Structural biology. The ribosome is a ribozyme. Science *289*, 878–879.

Chaudhuri, S., Vyas, K., Kapasi, P., Komar, A.A., Dinman, J.D., Barik, S., and Mazumder, B. (2007). Human ribosomal protein L13a is dispensable for canonical ribosome function but indispensable for efficient rRNA methylation. RNA *13*, 2224–2237.

Choi, Y.W., Kim, Y.W., Bae, S.M., Kwak, S.Y., Chun, H.J., Tong, S.Y., Lee, H.N., Shin, J.C., Kim, K.T., Kim, Y.J., and Ahn, W.S. (2007). Identification of differentially expressed genes using annealing control primer-based GeneFishing in human squamous cell cervical carcinoma. Clin. Oncol. (R Coll Radiol) *19*, 308–318.

Dang, C.V. (2012). MYC on the path to cancer. Cell *149*, 22–35.

Demeshkina, N., Jenner, L., Westhof, E., Yusupov, M., and Yusupova, G. (2012). A new understanding of the decoding principle on the ribosome. Nature *484*, 256–259.

Elenbaas, B., Spirio, L., Koerner, F., Fleming, M.D., Zimonjic, D.B., Donaher, J.L., Popescu, N.C., Hahn, W.C., and Weinberg, R.A. (2001). Human breast cancer cells generated by oncogenic transformation of primary mammary epithelial cells. Genes Dev. *15*, 50–65.

Galy, B., Créancier, L., Zanibellato, C., Prats, A.-C., and Prats, H. (2001). Tumour suppressor p53 inhibits human fibroblast growth factor 2 expression by a post-transcriptional mechanism. Oncogene *20*, 1669–1677.

Ghayad, S.E., Vendrell, J.A., Bieche, I., Spyratos, F., Dumontet, C., Treilleux, I., Lidereau, R., and Cohen, P.A. (2009). Identification of TACC1, NOV, and PTTG1 as new candidate genes associated with endocrine therapy resistance in breast cancer. J. Mol. Endocrinol. *42*, 87–103.

Giraud, S., Greco, A., Brink, M., Diaz, J.-J., and Delafontaine, P. (2001). Translation initiation of the insulin-like growth factor I receptor mRNA is mediated by an internal ribosome entry site. J. Biol. Chem. *276*, 5668–5675.

Györffy, B., Lanczky, A., Eklund, A.C., Denkert, C., Budczies, J., Li, Q., and Szallasi, Z. (2010). An online survival analysis tool to rapidly assess the effect of 22,277 genes on breast cancer prognosis using microarray data of 1,809 patients. Breast Cancer Res. Treat. *123*, 725–731.

Henras, A.K., Soudet, J., Gérus, M., Lebaron, S., Caizergues-Ferrer, M., Mougin, A., and Henry, Y. (2008). The post-transcriptional steps of eukaryotic ribosome biogenesis. Cell. Mol. Life Sci. *65*, 2334–2359.

Higa-Nakamine, S., Suzuki, T., Uechi, T., Chakraborty, A., Nakajima, Y., Nakamura, M., Hirano, N., Suzuki, T., and Kenmochi, N. (2012). Loss of ribosomal RNA modification causes developmental defects in zebrafish. Nucleic Acids Res. *40*, 391–398.

King, T.H., Liu, B., McCully, R.R., and Fournier, M.J. (2003). Ribosome structure and activity are altered in cells lacking snoRNPs that form pseudouridines in the peptidyl transferase center. Mol. Cell *11*, 425–435.

Koh, C.M., Gurel, B., Sutcliffe, S., Aryee, M.J., Schultz, D., Iwata, T., Uemura, M., Zeller, K.I., Anele, U., Zheng, Q., et al. (2011). Alterations in nucleolar structure and gene expression programs in prostatic neoplasia are driven by the MYC oncogene. Am. J. Pathol. *178*, 1824–1834.

Komar, A.A., and Hatzoglou, M. (2011). Cellular IRES-mediated translation: the war of ITAFs in pathophysiological states. Cell Cycle *10*, 229–240.

Krastev, D.B., Slabicki, M., Paszkowski-Rogacz, M., Hubner, N.C., Junqueira, M., Shevchenko, A., Mann, M., Neugebauer, K.M., and Buchholz, F. (2011). A systematic RNAi synthetic interaction screen reveals a link between p53 and snoRNP assembly. Nat. Cell Biol. *13*, 809–818.

Liang, X.H., Liu, Q., and Fournier, M.J. (2009). Loss of rRNA modifications in the decoding center of the ribosome impairs translation and strongly delays pre-rRNA processing. RNA *15*, 1716–1728.

Maden, B.E. (1988). Locations of methyl groups in 28 S rRNA of Xenopus laevis and man. Clustering in the conserved core of molecule. J. Mol. Biol. *201*, 289–314.

Menendez, D., Inga, A., and Resnick, M.A. (2009). The expanding universe of p53 targets. Nat. Rev. Cancer *9*, 724–737.

Meng, Z., Jackson, N.L., Shcherbakov, O.D., Choi, H., and Blume, S.W. (2010). The human IGF1R IRES likely operates through a Shine-Dalgarno-like interaction with the G961 loop (E-site) of the 18S rRNA and is kinetically modulated by a naturally polymorphic polyU loop. J. Cell. Biochem. *110*, 531–544.

Miller, L.D., Smeds, J., George, J., Vega, V.B., Vergara, L., Ploner, A., Pawitan, Y., Hall, P., Klaar, S., Liu, E.T., and Bergh, J. (2005). An expression signature for p53 status in human breast cancer predicts mutation status, transcriptional effects, and patient survival. Proc. Natl. Acad. Sci. USA *102*, 13550–13555.

Montanaro, L., Calienni, M., Ceccarelli, C., Santini, D., Taffurelli, M., Pileri, S., Treré, D., and Derenzini, M. (2008). Relationship between dyskerin expression and telomerase activity in human breast cancer. Cell. Oncol. *30*, 483–490.

Mulvihill, M.J., Cooke, A., Rosenfeld-Franklin, M., Buck, E., Foreman, K., Landfair, D., O'Connor, M., Pirritt, C., Sun, Y., Yao, Y., et al. (2009). Discovery of OSI-906: a selective and orally efficacious dual inhibitor of the IGF-1 receptor and insulin receptor. Future Med Chem *1*, 1153–1171.

Newton, K., Petfalski, E., Tollervey, D., and Cáceres, J.F. (2003). Fibrillarin is essential for early development and required for accumulation of an intron-encoded small nucleolar RNA in the mouse. Mol. Cell. Biol. *23*, 8519–8527.

Nikulenkov, F., Spinnler, C., Li, H., Tonelli, C., Shi, Y., Turunen, M., Kivioja, T., Ignatiev, I., Kel, A., Taipale, J., and Selivanova, G. (2012). Insights into p53 transcriptional function via genome-wide chromatin occupancy and gene expression analysis. Cell Death Differ. *19*, 1992–2002.

Olivier, M., Langerød, A., Carrieri, P., Bergh, J., Klaar, S., Eyfjord, J., Theillet, C., Rodriguez, C., Lidereau, R., Bièche, I., et al. (2006). The clinical value of somatic TP53 gene mutations in 1,794 patients with breast cancer. Clin. Cancer Res. *12*, 1157–1167.

Pollak, M.N., Schernhammer, E.S., and Hankinson, S.E. (2004). Insulin-like growth factors and neoplasia. Nat. Rev. Cancer *4*, 505–518.

Puglisi, J.D. (2009). Resolving the elegant architecture of the ribosome. Mol. Cell *36*, 720–723.

Ruggero, D. (2013). Translational control in cancer etiology. Cold Spring Harb. Perspect. Biol. *5*, a012336–a012336.

Ruggero, D., Grisendi, S., Piazza, F., Rego, E., Mari, F., Rao, P.H., Cordon-Cardo, C., and Pandolfi, P.P. (2003). Dyskeratosis congenita and cancer in mice deficient in ribosomal RNA modification. Science *299*, 259–262.

Sabatier, R., Finetti, P., Cervera, N., Lambaudie, E., Esterni, B., Mamessier, E., Tallet, A., Chabannon, C., Extra, J.M., Jacquemier, J., et al. (2011). A gene expression signature identifies two prognostic subgroups of basal breast cancer. Breast Cancer Res. Treat. *126*, 407–420.

Sakuma, K., Aoki, M., and Kannagi, R. (2012). Transcription factors c-Myc and CDX2 mediate E-selectin ligand expression in colon cancer cells undergoing EGF/bFGF-induced epithelial-mesenchymal transition. Proc. Natl. Acad. Sci. USA *109*, 7776–7781.

Sbisà, E., Catalano, D., Grillo, G., Licciulli, F., Turi, A., Liuni, S., Pesole, G., De Grassi, A., Caratozzolo, M.F., D'Erchia, A.M., et al. (2007). p53FamTaG: a database resource of human p53, p63 and p73 direct target genes combining in silico prediction and microarray data. BMC Bioinformatics *8*(*Suppl 1*), S20.

Spahn, C.M., Jan, E., Mulder, A., Grassucci, R.A., Sarnow, P., and Frank, J. (2004). Cryo-EM visualization of a viral internal ribosome entry site bound to human ribosomes: the IRES functions as an RNA-based translation factor. Cell *118*, 465–475.

Su, H., Xu, T., Ganapathy, S., Shadfan, M., Long, M., Huang, T.H., Thompson, I., and Yuan, Z.M. (2013). Elevated snoRNA biogenesis is essential in breast cancer. Oncogene. Published online April 1, 2013. http://dx.doi.org/10.1038/onc.2013.89.

Tollervey, D., Lehtonen, H., Jansen, R., Kern, H., and Hurt, E.C. (1993). Temperature-sensitive mutations demonstrate roles for yeast fibrillarin in pre-rRNA processing, pre-rRNA methylation, and ribosome assembly. Cell *72*, 443–457.

Troester, M.A., Herschkowitz, J.I., Oh, D.S., He, X., Hoadley, K.A., Barbier, C.S., and Perou, C.M. (2006). Gene expression patterns associated with p53 status in breast cancer. BMC Cancer *6*, 276.

Turner, N., and Grose, R. (2010). Fibroblast growth factor signalling: from development to cancer. Nat. Rev. Cancer *10*, 116–129.

Weigelt, B., Hu, Z., He, X., Livasy, C., Carey, L.A., Ewend, M.G., Glas, A.M., Perou, C.M., and Van't Veer, L.J. (2005). Molecular portraits and 70-gene prognosis signature are preserved throughout the metastatic process of breast cancer. Cancer Res. *65*, 9155–9158.

Xue, S., and Barna, M. (2012). Specialized ribosomes: a new frontier in gene regulation and organismal biology. Nat. Rev. Mol. Cell Biol. *13*, 355–369.

Yonath, A. (2009). Large facilities and the evolving ribosome, the cellular machine for genetic-code translation. J. R. Soc. Interface *6*(*Suppl 5*), S575–S585.

Yoon, A., Peng, G., Brandenburger, Y., Zollo, O., Xu, W., Rego, E., and Ruggero, D. (2006). Impaired control of IRES-mediated translation in X-linked dyskeratosis congenita. Science *312*, 902–906.

Zhai, W., and Comai, L. (2000). Repression of RNA polymerase I transcription by the tumor suppressor p53. Mol. Cell. Biol. *20*, 5930–5938.

Cancer Cell
Article

Mesenchymal Differentiation Mediated by NF-κB Promotes Radiation Resistance in Glioblastoma

Krishna P.L. Bhat,[1,16,*] Veerakumar Balasubramaniyan,[5,16] Brian Vaillant,[7,16] Ravesanker Ezhilarasan,[2,16] Karlijn Hummelink,[1] Faith Hollingsworth,[1] Khalida Wani,[1] Lindsey Heathcock,[1] Johanna D. James,[1] Lindsey D. Goodman,[2] Siobhan Conroy,[6] Lihong Long,[1] Nina Lelic,[8] Suzhen Wang,[3] Joy Gumin,[4] Divya Raj,[5] Yoshinori Kodama,[9] Aditya Raghunathan,[10] Adriana Olar,[1] Kaushal Joshi,[11] Christopher E. Pelloski,[12] Amy Heimberger,[4] Se Hoon Kim,[13] Daniel P. Cahill,[8] Ganesh Rao,[4] Wilfred F.A. Den Dunnen,[6] Hendrikus W.G.M. Boddeke,[5] Heidi S. Phillips,[14] Ichiro Nakano,[11] Frederick F. Lang,[4] Howard Colman,[15,17] Erik P. Sulman,[2,17,*] and Kenneth Aldape[1,17,*]
[1]Department of Pathology
[2]Department of Radiation Oncology
[3]Department of Neuro-Oncology
[4]Department of Neurosurgery
The University of Texas, M.D. Anderson Cancer Center, Houston, TX 77030, USA
[5]Department of Neuroscience
[6]Department of Pathology and Medical Biology
University of Groningen, University Medical Center Groningen, Groningen 9713 AV, the Netherlands
[7]Department of Neurology, Seton Brain and Spine Institute, Austin, TX 78701, USA
[8]Deparment of Neurosurgery, Massachusetts General Hospital/Brain Tumor Center, Boston, MA 02114, USA
[9]Division of Pathology, Osaka National Hospital, National Hospital Organization, Chuo-ku, Osaka 540-0006, Japan
[10]Department of Pathology, Henry Ford Hospital, Detroit, MI 48202, USA
[11]Department of Neurosurgery
[12]Department of Radiation Oncology
The Ohio State University, Columbus, OH 43210, USA
[13]Department of Pathology, Yonsei University College of Medicine, Seoul 120-752, Korea
[14]Department of Tumor Biology and Angiogenesis, Genentech, Inc., South San Francisco, CA 94080, USA
[15]Department of Neurosurgery, and Huntsman Cancer Institute, University of Utah, Salt Lake City, UT 84132, USA
[16]These authors contributed equally to this work
[17]These authors contributed equally to this work
*Correspondence: kbhat@mdanderson.org (K.P.L.B.), epsulman@mdanderson.org (E.P.S.), kaldape@mdanderson.org (K.A.)
http://dx.doi.org/10.1016/j.ccr.2013.08.001

SUMMARY

Despite extensive study, few therapeutic targets have been identified for glioblastoma (GBM). Here we show that patient-derived glioma sphere cultures (GSCs) that resemble either the proneural (PN) or mesenchymal (MES) transcriptomal subtypes differ significantly in their biological characteristics. Moreover, we found that a subset of the PN GSCs undergoes differentiation to a MES state in a TNF-α/NF-κB-dependent manner with an associated enrichment of CD44 subpopulations and radioresistant phenotypes. We present data to suggest that the tumor microenvironment cell types such as macrophages/microglia may play an integral role in this process. We further show that the MES signature, CD44 expression, and NF-κB activation correlate with poor radiation response and shorter survival in patients with GBM.

Significance

In this study, we characterize plasticity between the proneural (PN) and mesenchymal (MES) transcriptome signatures observed in glioblastoma (GBM). Specifically, we show that PN glioma sphere cultures (GSCs) can be induced to a MES state with an associated enrichment of CD44 expressing cells and a gain of radioresistance, in an NF-κB-dependent fashion. Newly diagnosed GBM samples show a direct correlation among radiation response, higher MES metagene, CD44 expression, and NF-κB activation, and we propose macrophages/microglia as a potential microenvironmental component that can regulate this transition. Our results reveal a mechanistic link between transcriptome plasticity, radiation resistance, and NF-κB signaling. Inhibition of NF-κB activation can directly affect radioresistance and presents an attractive therapeutic target for GBM.

INTRODUCTION

Glioblastoma (GBM) is the most common malignant primary central nervous system tumor in adults and remains resistant to current therapies (Furnari et al., 2007) Ample evidence exists to argue that GBM, as defined by histopathologic criteria, actually represents multiple distinct molecular entities (Huse et al., 2011). GBM can be segregated into subtypes based on gene expression signatures. Although the precise classifications have varied in the literature (Cooper et al., 2010; Huse et al., 2011; Phillips et al., 2006; Verhaak et al., 2010), two subtypes, termed proneural (PN) and mesenchymal (MES), appear robust and generally consistent among the classification schemes. GBMs in the MES subclass are predominantly primary tumors that arise de novo and, in some studies, exhibit a worse prognosis compared to PN tumors (Colman et al., 2010; Pelloski et al., 2005; Phillips et al., 2006), which may be related to the fact that a subset of the PN tumors displays mutations in the isocitrate dehydrogenase 1 gene (*IDH1*) as well as the glioma-CpG island methylator phenotype (G-CIMP), both favorable prognostic factors (Noushmehr et al., 2010; Verhaak et al., 2010). Conversely, MES tumors are G-CIMP^{-}, exhibit wild-type (WT) *IDH1*, and contain alterations in *NF1* (Noushmehr et al., 2010; Verhaak et al., 2010).

Although a wealth of data on molecular alterations in GBM continues to accumulate, the availability of relevant models that mirror these alterations is limited. Current evidence points toward the existence of a small fraction of tumor-initiating cells in the bulk tumor that also exhibit radioresistant properties (reviewed in Chen et al., 2012). However, the genetic and epigenetic alterations underlying TICs derived from glioma sphere cultures (GSCs) are less characterized. Whereas initial studies identified CD133 as a tumor-initiating marker, CD133^{-} subpopulations that resemble the MES subtype also retain the capacity to form tumors in orthotopic transplantation models (reviewed in Stopschinski et al., 2012). Consequently, additional cell surface antigens have been proposed as tumor-initiating markers for GSCs including CD44 (Brescia et al., 2012; Jijiwa et al., 2011), a marker that is enriched in cancer stem cells as well as those that undergo epithelial to MES transition (EMT; Zöller, 2011). Interestingly, MES transition has also been shown to occur in GBM and can be induced by master transcription factors (TFs), STAT3, C/EBPβ, and TAZ (Bhat et al., 2011; Carro et al., 2010). Whether this transition occurs in a cell-intrinsic manner or can be influenced by factors secreted in the tumor microenvironment is not known. Furthermore, whether MES differentiation leads to enrichment of the CD44 subpopulation in a fashion similar to other solid tumors remains unexplored. Finally, PN tumors have been found to give rise to MES recurrences, suggestive of a PN to MES transition (Phillips et al., 2006). Therefore, understanding the mechanistic basis of MES differentiation may have implications for the treatment of GBM.

RESULTS

Patient-Derived GSCs Bear Resemblance to PN and MES Signatures

In the context of molecular subtypes reported for GBM, we examined whether GSCs isolated from patient-derived tumors show similar characteristics. Forty-one GBM tumors were subjected to culture conditions according to published protocols and successful expansion as neurospheres was observed in 33 cases (Table S1 available online). Seventeen GSCs that were expanded earliest were chosen for microarray analysis to identify molecular subtypes using unsupervised algorithms. Using 500 probe sets with the highest variability in gene expression, two clusters of coexpressed genes were readily apparent by hierarchical clustering (Figure 1A). These two clusters for the most part were well defined, although some GSCs did not readily fit in this pattern (e.g., GSC6-27, 30, and 46). The primary or recurrent status of the parental tumor of origin had no bearing on the cluster segregation (cluster 1 = 33% versus cluster 2 = 36% recurrent tumors; Figure 1A). To understand the functional significance of these two gene clusters, we performed Gene Ontology (GO) analysis using the Database for Annotation, Visualization and Integrated Discovery (DAVID) webtool (Dennis et al., 2003). Cluster 1 GO terms were enriched for wound response, vasculature formation, and cell motility gene signatures (Figure 1B), whereas cluster 2 showed predominant association with differentiated neural or glial cell functions and homeostatic activities (Figure 1B). Importantly, cluster 1 showed significant similarity only to the MES GBM subclass by Gene Set Enrichment Analysis (GSEA; Subramanian et al., 2005; Figure 1C), with 89 out of the top 500 enriched genes being MES (Figure S1A; Table S2). Similarly, cluster 2 predominantly comprised PN genes (98/500; Figures 1C and S1A; Table S2). Supervised clustering using the TCGA classification (Verhaak et al., 2010) showed a similar grouping of the GSCs at the first branch of the dendrogram compared to the unsupervised clustering (Figure S1B). GSC6-27 and 30 displayed characteristics of both MES and PN gene signatures. GSC11 and 30 were also enriched for Classical (CL) signatures. EGFR amplification, usually restricted to the CL subtype, was seen in 5 out of the 14 GSCs and appeared distributed between the PN and MES subtypes (3 PN and 2 MES; Figure S1C). *NF1* homozygous inactivating mutations were observed in GSC6-27 (exon 39) and GSC28 (exon 50 and exon 38; Figure S1D), both GSCs that had MES characteristics consistent with the TCGA analyses (Verhaak et al., 2010). Quantitative RT-PCR (qRT-PCR) and immunoblotting of basal expression of key PN/MES markers (Table S3) were concordant with microarray results (Figures S1E and S1F).

To rule out the possibility of nonneoplastic cells being enriched in the GSC isolation procedure, we tested for loss of heterozygosity (LOH) on chromosome 10q, a frequently deleted region in adult GBM (Pietsch and Wiestler, 1997), and found LOH in 12 out of the 13 GSCs, confirming their neoplastic origin (Figure S1G). Implantation of 5×10^5 or fewer unsorted GSCs caused formation of high-grade gliomas (HGGs) in a majority of the cases (13/17) with predominant histologic features of this disease (Tables S4 and S5; Figure S1H). A subset of the tumors exhibited microvascular proliferation and/or pseudopalisading necrosis, both hallmarks of GBM (Figure S1H). Thus, despite differential gene expression signatures, GSCs formed tumors that were histologically similar.

GSCs Differ in the Transcriptome and Epigenetic Profiles When Compared to the Originating Tumor

Next, we examined whether gene expression patterns observed in the GSCs and xenografts matched with the respective

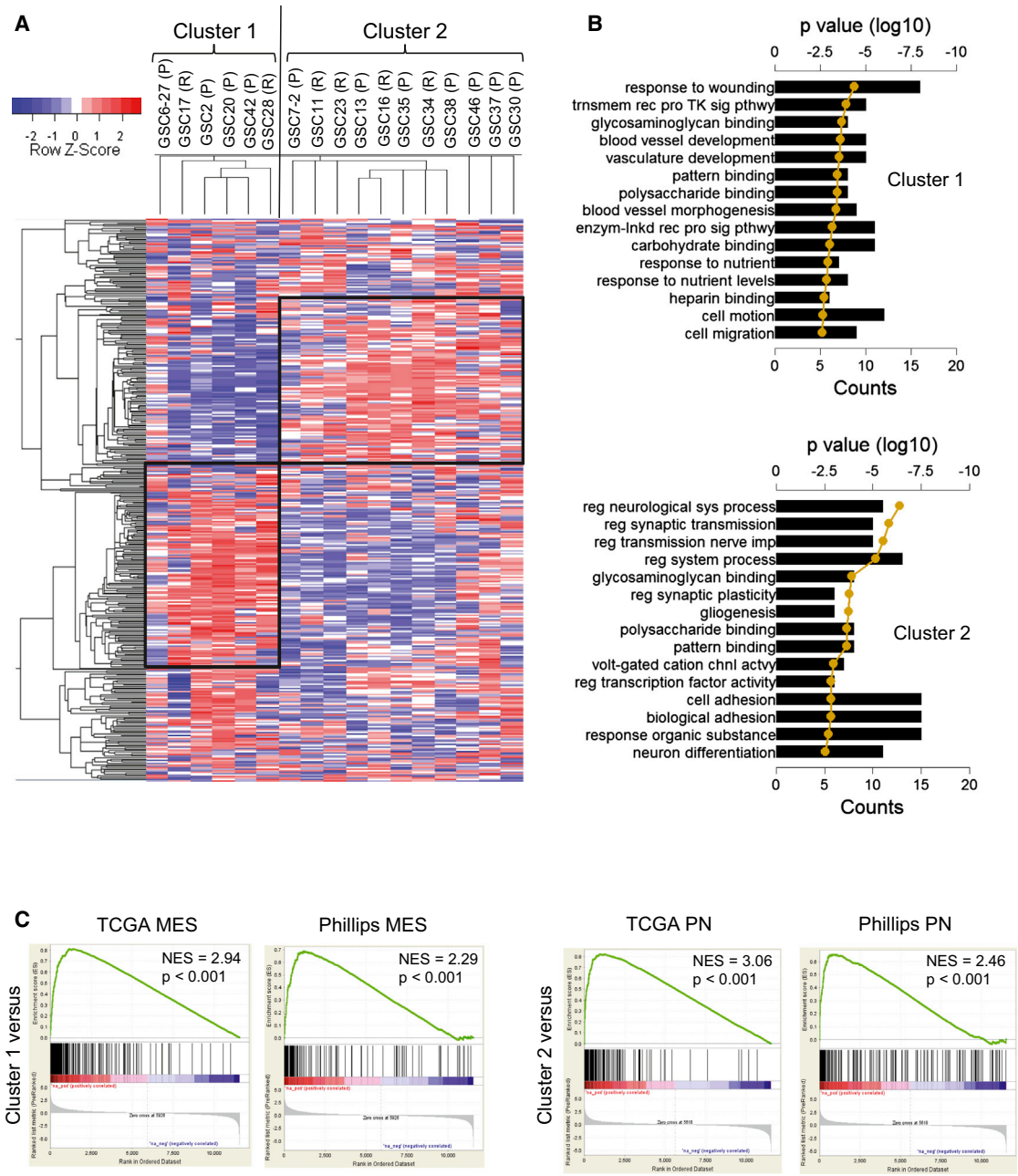

Figure 1. Patient-Derived GSCs Bear Resemblance to PN and MES Signatures

(A) Unsupervised hierarchical analysis of the top 500 highest median absolute deviation genes from expression microarray of 17 GSCs is shown. Expression data was Z score corrected for display; relatively lower expression is shown in blue and higher expression is shown in red (see color key). Two large clusters, cluster 1 (128 genes) and cluster 2 (102 genes), were identified (shown as black boxes). The vertical black line identifies the first dendrogram splitting of the GSCs. Primary (P) or recurrent (R) status of the GSCs is indicated.

(B) The top 20 gene ontology (GO) terms associated with cluster 1 (left) and cluster 2 (right) from the unsupervised GSC hierarchical cluster analysis are shown. GO terms are ranked by p value. The black bars show the number of genes that is common between the GO term's gene set and the respective cluster gene set. The golden line is the $\log_{10}$ of the p value as determined by DAVID functional analysis.

(C) GSEA enrichment plots of GSC cluster 1 high (top row) and cluster 2 high (bottom row) gene lists versus queried gene lists are shown (see Supplemental Experimental Procedures for data source). The normalized enrichment scores (NES) and the p values are shown for each plot.

See also Figure S1 and Tables S1, S2, and S3–S5.

parental GBMs from which they were derived. To determine the association of a sample with either a PN or MES gene expression signature, we calculated a metagene score for each sample using a set of four PN (*DLL3*, *OLIG2*, *ASCL1*, and *NCAM1*) and four MES (*YKL40*, *SERPINE1*, *TIMP1*, and *TGFBI*) genes, seven out of the eight of which were subset defining in published data

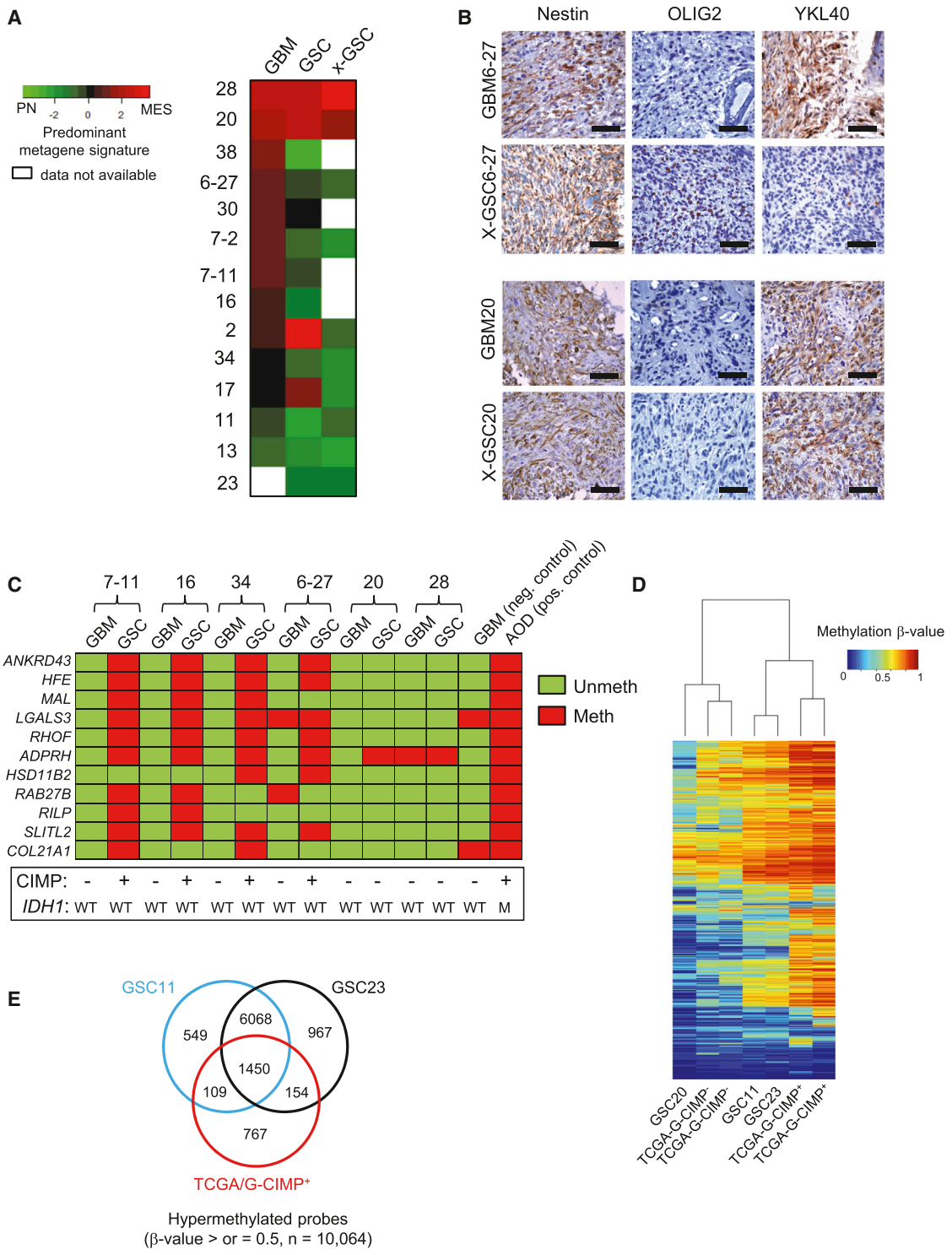

Figure 2. GSCs Differ in the Transcriptome and Epigenetic Profiles when Compared to the Originating Tumor

(A) Heatmap of the predominant signature of initiating GBM, derived GSC, and xenograft for 14 samples is shown. A PN and MES qRT-PCR-based metagene was calculated for each sample and then compared to each other after Z score correction. Green shades represent a predominantly PN signature, red a MES one, and black a relatively balanced expression of both, as indicated in the figure.

(B) IHC analysis of Nestin, OLIG2, and YKL40 expression in patient-matched GBM and xenografts of GSCs is shown. Scale bar: 50 μm.

(C) Methylight profiling of GBMs and their derivative GSCs for G-CIMP status is shown. Eleven markers were tested for presence of methylation on their promoters and coded as red if methylated and green if unmethylated. Samples were deduced as G-CIMP if >50% of the loci showed methylation. A GBM and

(legend continued on next page)

sets (Phillips et al., 2006; Verhaak et al., 2010). Using this approach, each sample could be ranked according to its metagene score as being predominantly PN or MES. Surprisingly, we found that most GSCs that arose from MES tumors lost MES characteristics and exhibited a higher PN metagene (Figure 2A). GSC20 and GSC28, both of which originated from highly MES tumors with histological hallmarks of gliosarcoma (Figure S2A), maintained their MES state in culture and as xenografts. With the exception of GSC2 and GSC17 (which lost MES features gained in culture), all PN GSCs maintained their PN status when examined in xenografts. Alterations in growth factor supplements to culture media did not influence gene expression signatures in established GSCs, although neurosphere formation was dependent on EGF (Figures S2B and S2C). Immunohistochemical (IHC) analysis on xenografts showed absence of the MES marker YKL40 in GSCs derived from MES tumors, which instead acquired the PN marker OLIG2 (Figures 2B and S2D). This contrast was not observed in the MES GSC20 that retained YKL40 expression in the xenograft, similar to the parental tumor, but lacked OLIG2 expression in both (Figure 2B). These findings imply that the GSC isolation protocol generally favors a loss of MES and gain of PN features from patient to xenograft.

Given the tight association of the G-CIMP signature with the PN subtype (Noushmehr et al., 2010), we asked whether PN GSCs are G-CIMP$^+$. To test this, we used a previously reported G-CIMP signature panel that shows correlation with array-based methylation platforms (Noushmehr et al., 2010). Eleven hypermethylated gene regions were chosen based on feasibility and reproducibility in archival tumor-derived DNA and deemed G-CIMP$^+$ based on percentage loci that were hypermethylated (>50%). Consistent with a drift toward a PN signature from tumor to GSC, we observed that PN GSCs were G-CIMP$^+$ compared to their parental tumors that were G-CIMP$^-$ (Figures 2C and S2E). To the contrary, MES GSCs 20 and 28 remained G-CIMP$^-$ similar to their parental tumors (Figure 2C). To test for the extent of similarity to the previously described G-CIMP signature on a genome-wide scale, we profiled three GSCs using the Illumina Infinium methylation array (Figure 2D). Upon cross-examination with TCGA tumors, PN GSCs 11 and 23 segregated with G-CIMP$^+$ tumors, while GSC20 clustered with the G-CIMP$^-$ cases. Overall, GSCs 11 and 23 showed greater hypermethylation compared to GSC20 (Figure S2F) and showed an ~70% enrichment of G-CIMP signature genes, although numerous distinct non-G-CIMP loci also appeared hypermethylated in these GSCs (Figure 2E). Taken together, our data suggest that PN GSCs can exhibit hypermethylation patterns (henceforth named CIMP) with similarities to G-CIMP even in the absence of *IDH1* mutations.

Molecular Signatures Differ between GBM and Their Derivative GSCs Even in Early Passages

Based on our initial findings, two possibilities were considered: (1) culturing of freshly resected GBMs in serum-free media supplemented with growth factors preferentially induces a PN/CIMP$^+$ signature in culture, or (2) most undifferentiated GSCs are innately PN/CIMP$^+$, but the microenvironment in human tumors induces a reversible MES/CIMP$^-$ differentiation, which is not entirely recapitulated in vitro or in xenografts of immunocompromised mice. To discern which one of these can be attributed to a general MES/CIMP$^-$ to PN/CIMP$^+$ drift, and to reduce the potential of artifacts from long-term culture, we examined freshly resected tissues and their derivative serial passage GSCs for gene expression and methylation signatures as soon as sufficient starting material was available for analyses. Strikingly, even in early passages (fewer than five), we observed that GSCs showed PN characteristics despite having a MES origin (Figure S2G). Moreover, these early passage GSCs were CIMP$^+$ in contrast to their parental tumors, which were CIMP$^-$ (Figure S2H). These observations, taken together with previous studies showing requirement of extended passages for the induction of the G-CIMP phenotype by *IDH1* mutation (Lu et al., 2012; Turcan et al., 2012), favor a model in which a majority of undifferentiated GSCs already exist in a PN/CIMP$^+$ state and are selectively enriched under proliferating conditions.

CD44 Is Enriched in the MES Subtype and Is Inversely Correlated with OLIG2 Expression

Next, to test whether the differential molecular signatures have a bearing on their biological properties, we expanded our repertoire of GSCs. We first examined the expression of cell surface markers that have been used to define tumor-initiating potential. We observed enrichment of CD15 specifically in the PN/CIMP$^+$ subclass of GSCs (e.g., GSC11, GSC23, and GSC34) that also expressed equal or smaller percentages of CD44 (Figure 3A), although the ratio of CD15 to CD44 varied with passage or confluence of spheres. MES/CIMP$^-$ GSCs (e.g., GSC20, GSC28, and GSC2) did not express appreciable levels of CD15 but predominantly expressed CD44 (Figure 3A). Comparison of CD15 and CD44 expression among GSCs with a range of passage times showed no correlation (Figures S3A and S3B). Using OLIG2 as a surrogate for CD15 (Figure S3C) as previously shown (Son et al., 2009), we found a mutually exclusive pattern of inter- and intratumoral staining with CD44 (Figures 3B, 3C, and S3D), implying that these were indeed distinct tumor populations. Furthermore, PN tumors expressed higher levels of *OLIG2* whereas MES tumors predominantly expressed *CD44* and the expression of *OLIG2* and *CD44* was inversely correlated (Figures 3D and S3E). Additionally, CD44^{high} subpopulations within PN/CIMP$^+$ GSCs showed enrichment of MES markers (Figure S3F). Thus, whereas unsorted GSCs formed tumors upon transplantation irrespective of exclusive expression of tumor initiation markers, CD15 (e.g., GSC7-11) or CD44 (e.g., GSC20), the proportion of the cell surface expression of CD44 appeared to correlate with a MES state.

an anaplastic oligodendroglioma (AOD) sample were used as negative and positive controls, respectively. The *IDH1* and G-CIMP status of all samples is shown below.

(D) Heatmap shows the unsupervised clustering of 1,138 differentially hypermethylated probes from the G-CIMP signature.

(E) Venn diagram shows the number of hypermethylated probes (β values ≥ 0.5) in GSCs 11, 23, and TCGA G-CIMP$^+$ tumors.

See also Figure S2.

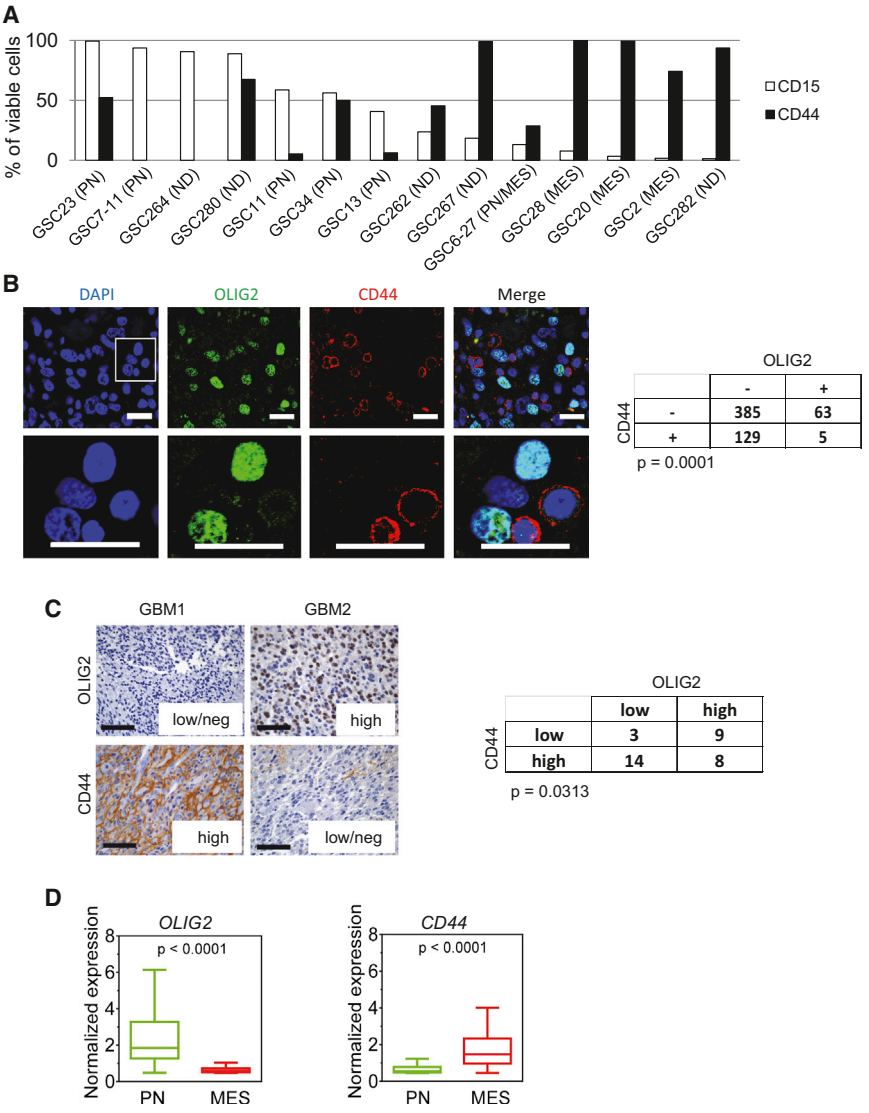

Figure 3. CD44 Is Enriched in the MES Subtype and Is Inversely Correlated with OLIG2 Expression

(A) CD15 and CD44 of various GSCs were determined by flow cytometry. Bar graph indicates percentage of viable cells that express these markers at the earliest passage tested. ND, not determined.

(B) Immunofluorescent staining of OLIG2 (green) and CD44 (red) in human GBM tumors shows a mutually exclusive pattern of staining. Scale bar: 20 μm. The merged image of CD44/OLIG2 is shown on the right against 4′,6-diamidino-2-phenylindole (DAPI)-stained nuclei (blue). Enlarged inset is shown in the lower panel (scale bar: 20 μm). Quantification of staining in three random fields of three independent tumors and the p value from chi-square test are shown on the right.

(C) Representative IHC images of OLIG2 and CD44 expression in human GBM samples are shown. Scale bar: 50 μm. The table to the right shows the number of tumors expressing OLIG2/CD44. Tumors were classified as low/negative, intermediate, or high depending on the extent of expression in the overall tumors. p value was calculated using chi-square test.

(D) Box plots show the normalized median expression of *OLIG2* and *CD44* in TCGA tumors based on Phillips and TCGA classification. Boxes show median 25th and 75th percentiles, while whiskers show the 5th and the 95th percentiles. The p value was determined using a nonparametric Wilcoxon test.

See also Figure S3.

PN/CIMP$^+$ and MES/CIMP$^-$ GSCs Display Differential Sensitivity to Radiation

To test whether GSCs with varied transcriptome, methylation, and cell surface antigen expression patterns also exhibit differential treatment responses, we examined the consequence of clinically relevant fractionated ionizing radiation (IR; 2.5 Gy × 4) on mice 2–3 weeks after orthotopic implantation of GSCs. PN/CIMP$^+$ GSCs (7-11 and 23) showed significantly improved median survival (5–9 weeks) upon IR treatment, whereas GSC20 showed no statistical difference and GSC267 showed modest survival (~2 weeks) improvement compared to untreated controls (Figure 4A). Because glioma cells predominantly arrest in the G2/M phase of cell cycle in response to IR (Mir et al., 2010), we asked whether the two subtypes of GSCs showed fundamental differences in this mode of arrest. Indeed, PN/CIMP$^+$ GSCs showed dramatic accumulation of cells in G2/M, whereas MES/CIMP$^-$ GSCs showed only a modest arrest (Figure 4B). In addition, although both subtypes of GSCs showed comparable γ-H2AX foci formation at early time points, MES/CIMP$^-$ GSCs (2, 20, and 267) showed enhanced repair ability as evidenced by the reduced number of foci at 24 hr compared to PN/CIMP$^+$ GSCs (Figure 4C), consistent with the lack of G2/M arrest. Consequently, the PN/CIMP$^+$ GSCs underwent profound apoptosis (Figure 4D) with reduced neurosphere formation compared to MES/CIMP$^-$ GSCs (Figure 4E). We further observed a similar radioresistant CD44^{high} population within the PN/CIMP$^+$ GSCs (Figures S4A–S4C).

TNF-α Mediates MES Differentiation in an NF-κB-Dependent Fashion

Despite originating from MES tumors, the lack of MES signature in xenografts led us to hypothesize that specific factors in the human tumor microenvironment could alter the transcriptome and epigenetic signatures of GSCs, but these features are not entirely recapitulated in immunocompromised mice. In search of such signaling molecules, we noted that the TCGA analyses showed specific enrichment of genes in the TNF-α receptor superfamily and the NF-κB pathway in the MES subclass of tumors that also expressed high levels of *YKL40* and *CD44* (Riddick and Fine, 2011; Verhaak et al., 2010). Additionally, prior studies have shown the association of a hypoxic signature and the NF-κB pathway to HGGs (Murat et al., 2009). We

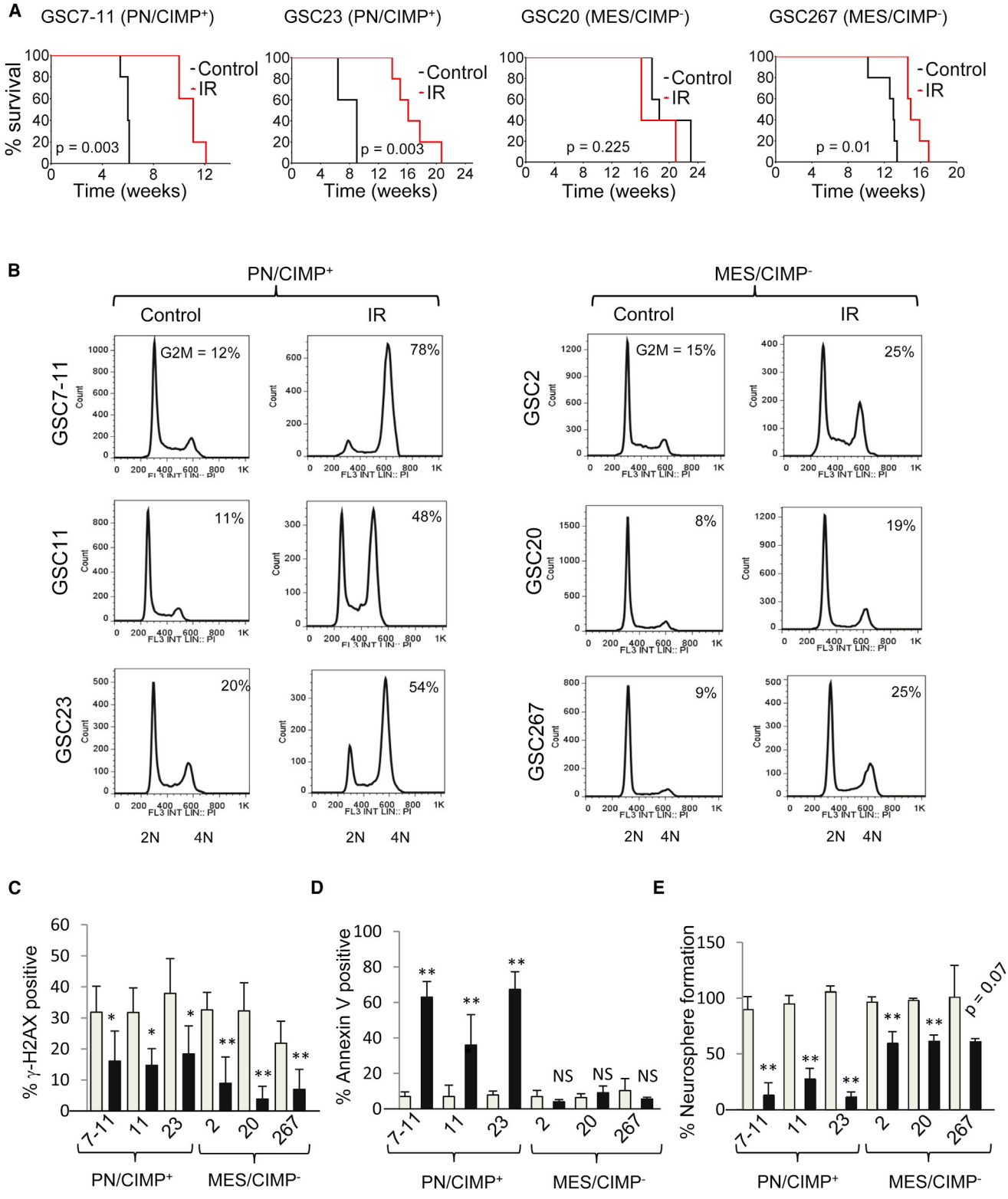

Figure 4. PN/CIMP$^+$ and MES/CIMP$^-$ GSCs Display Differential Sensitivity to Radiation

(A) Kaplan Meier curves show the survival of mice implanted with PN/CIMP$^+$ (7-11 and 23) or MES/CIMP$^-$ (20 and 267) GSCs at 5 × 10^5 cells per mouse with or without fractioned intracranial radiation (2.5 Gy × 4). t test was used to assess statistical significance.

(B) Cell cycle analysis of GSCs treated with 6 Gy IR is shown. The percentage of cells in the G2/M phase is indicated within each cell cycle plot.

(legend continued on next page)

hypothesized that cytokines that can trigger NF-κB or alternative TF signaling pathways could result in MES differentiation and influence the proportion of CD44^{high} subpopulations. To test this, we treated PN/CIMP^{+} GSCs 11, 23, and 34 with similar concentrations of interleukin (IL)-6, IL-8, IL-10, TGF-β, or TNF-α, all of which are constituents of the GBM microenvironment (Charles et al., 2011). TNF-α treatment resulted in a dramatic gain of CD44 expression, an effect not seen with any of the other cytokines tested (GSC34, Figure 5A; GSC11 and 23, data not shown), and this effect was blunted by transduction with a nondegradable mutant form of IκB (IκB superrepressor [IκB-SR]), indicating an NF-κB-dependent effect (Figure 5B). Interestingly, the CIMP positivity of the GSCs remained unaltered in response to TNF-α treatment (Figure 5C), implying that the regulation of CIMP can be uncoupled from NF-κB-mediated MES differentiation in GSCs. However, long-term effects of TNF-α and/or other potential modifiers of CIMP status are worthy of further exploration.

To further characterize the extent of MES differentiation, we performed microarray analysis of GSCs treated with TNF-α and found significant enrichment of genes involved in wound healing and vasculature development, as well as the NF-κB cascade and regulation of cell-death-related genes (Figure 5D), suggesting that in addition to the canonical NF-κB pathway, TNF-α induces a parallel MES differentiation in GSCs, which was further confirmed by qRT-PCR (Figure S5A). Moreover, genes induced by TNF-α were significantly similar to the GBM MES subclass (Figure S5B). Interestingly, although a global reduction of the PN signature was not observed, a significant downregulation of *OLIG2*, *PDGFRA*, and *DLL3* transcripts were seen with TNF-α treatment (data not shown). Physiological concentrations (100 pg/ml) of TNF-α were sufficient to cause induction of YKL40 and CD44 (Figures S5C and S5D), which was temporally preceded by activation of NF-κB, as judged by serine 536 (ser 536) phosphorylation (Figure S5D). Furthermore, we identified macrophages/microglia as the stromal cell type that can potentially induce MES differentiation (Figures S5E–S5I) and that MES/CIMP^{-} GSCs show selective susceptibility to minocycline, an inhibitor of microglial activation and NF-κB signaling (Figures S5J–S5N; Daginakatte and Gutmann, 2007; Markovic et al., 2011).

Pretreatment of PN/CIMP^{+} GSCs with TNF-α strongly reduced the G2/M accumulation in response to IR (Figure 5E) as well as the number of γ-H2AX foci (Figure S5O), and these effects were inhibited by pretreatment with IκB-SR, indicating that TNF-α promotes MES differentiation coupled with increased radioresistance in an NF-κB-dependent manner. We noted that although long-term treatment of GSCs with TNF-α (5 ng/ml) reduced the neurosphere formation (Figure S5P), exposure of GSCs to IR caused significantly higher neurosphere efficiency in the presence of TNF-α compared to untreated controls, suggesting a radioprotective effect of TNF-α (Figure S5P). To examine this in vivo, we expressed firefly luciferase in GSC23 to monitor tumor kinetics using bioluminescent imaging. As expected, IR caused a strong decrease in tumor volume (Figure 5F), and a similar growth inhibition was seen with TNF-α treatment alone, consistent with our in vitro observations. However, a combination of TNF-α and IR caused significant expansion of the tumor, and the cells appeared similar in volume to the control group. Overall, our findings indicate that the induction of MES differentiation and enrichment of CD44 by NF-κB activation promotes radioresistance in PN/CIMP^{+} GSCs.

NF-κB Controls Master TFs of MES Differentiation in GSCs

Next, we explored how NF-κB pathway activation integrates into the MES signaling network and its relation to master TFs (STAT3, C/EBPβ, and TAZ) known to induce this signature. We found that both total and phosphorylated forms of p65 (ser 536) were significantly higher in MES/CIMP-GSCs 2 and 20 when compared to PN/CIMP^{+} GSCs 11 and 23 (Figure 6A). The expression of STAT3 and C/EBPβ as well as phosphorylation at tyrosine 705 of STAT3 (which promotes nuclear translocation and DNA binding of STAT3) were also higher in the MES/CIMP^{-} GSCs (Figure 6A). Similar increases in MES proteins and master TFs were seen in the CD44^{high} subpopulation when compared to those that were CD44^{low} (Figures 6B and 6C). CD44 expression also positively correlated with *STAT3*, *CEBPB*, and *TAZ* expression as well as NF-κB pathway activation in human GBMs (Figure 6D). Although these TFs showed strong association with the MES signature, classic EMT inducers *SNAIL*, *SLUG*, and *TWIST1* were not robustly associated (Figure S6A).

To test whether NF-κB mediates MES reprogramming via master TFs, we treated GSC11 with TNF-α at various time points and analyzed the temporal expression of these proteins by western blotting. TNF-α-induced phosphorylation of p65 preceded the induction of YKL40, STAT3, C/EBPβ, and TAZ, an effect that was negated by pretreatment with IκB-SR, indicating that the master TFs act downstream of the NF-κB pathway (Figures 6E and S6B). Furthermore, upregulation of *STAT3*, *CEBPB*, and *TAZ* mRNA was significantly inhibited by IκB-SR pretreatment (Figures 6F and S6B). Finally, concomitant silencing of STAT3, C/EBPβ, and TAZ caused strong reduction of *CD44* and *YKL40* induced by TNF-α (Figures 6G and S6B). Taken together, these data indicate that NF-κB promotes MES differentiation in GSCs via induction of master TFs. Interestingly, GSC13, which originated from a PN tumor (Figure 1C), did not exhibit MES differentiation even upon long-term culture in TNF-α, suggesting that some PN GSCs are resistant to NF-κB-mediated MES differentiation (Figure S2C).

(C) γ-H2AX foci formation assay is shown. Gray bars indicate number of foci after 6 hr irradiation whereas black bars show foci after 24 hr. At least 25 nuclei were counted. Error bar indicates ± SEM. t test was used to assess statistical significant differences. *$p < 0.05$, **$p < 0.005$.
(D) Percentage of cells that were positive for annexin V staining 96 hr post irradiation is shown as bar graphs. Gray bars indicate percentage of cells in untreated population whereas black bars show percentage of annexin-V-positive cells exposed to 6 Gy IR. Error bar indicates ± SD. t test was used for statistical significance. **$p < 0.005$; NS, not significant.
(E) Neurosphere formation efficiency was determined by setting the number of spheres formed in control groups at 100% (gray bars) and compared to those exposed to 3 Gy IR (black bars). Error bar indicates ± SD. t test was used for statistical significance. **$p < 0.005$.
See also Figure S4.

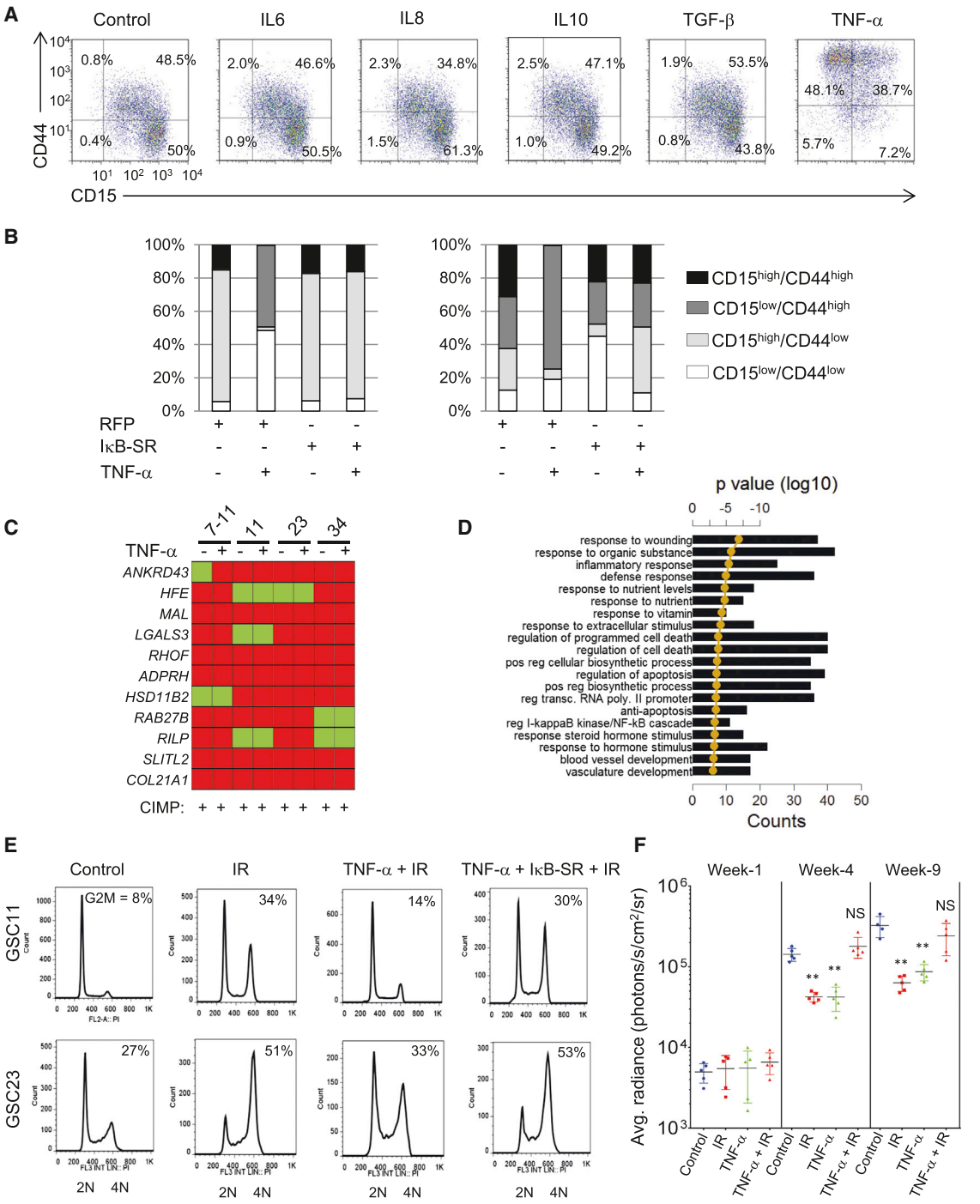

Figure 5. TNF-α Mediates MES Differentiation and Radioresistance in an NF-κB-Dependent Fashion

(A) FACS analysis of expression of CD15 and CD44 in GSC34 after 96 hr treatment with 10 ng/ml of indicated cytokines is shown. Percentage of cells in each quadrant is shown.

(B) Expression of CD15 and CD44 after TNF-α (96 hr, 10 ng/ml) with or without pretreatment with IκB-SR adenovirus or control RFP adenovirus 24 hr prior to TNF-α treatment by flow cytometry is shown. The stacked bar shows the percentage of CD15/CD44-expressing cells after various treatments.

(C) Methylight profiling of GSCs after 2 weeks of TNF-α treatment is shown.

(D) The top 20 GO terms associated with 1.5-fold or greater TNF-α-induced genes in GSC11 are ranked by lowest p value. Bar graphs show the number of genes overlapping between the GO category and the query gene list. The golden line is the DAVID functional analysis determined $\log_{10}$ of p values.

(E) Cell cycle analysis of GSCs after treatments is indicated. The percentage of cells in the G2/M phase is indicated within each cell cycle plot.

(F) Tumor volume measurement of GSC23-pCignal lenti-CMV-luc cells injected intracranially into Foxn1^{nu} mice is shown. Mice were imaged 2–3 weeks after implantation as the first time point (denoted as week 1), after which the radiation group received four cycles of 2.5 Gy IR on consecutive days. Mice were subject to

(legend continued on next page)

MES Differentiation, CD44 Levels, and NF-κB Activation Are Predictive of Radiation Response in GBM

Because activation of NF-κB caused both MES differentiation and enrichment of CD44 populations in GSCs, we performed in-depth analyses of NF-κB activation in GBM. Among previously annotated direct targets of NF-κB, MES GSCs as well as tumors (Table S6) showed a 36% enrichment (induced to a 1.5-fold or greater expression) of these targets when compared to PN counterparts, which showed only a 6% enrichment (Figure S7A). Seventeen NF-κB target genes appeared commonly induced in both MES GSCs and GBMs, which included *CD44*, proinflammatory cytokines *IL1B* and *IL8*, chemokines *CCL2* and *CXCL5*, prostaglandin enzyme cyclooxygenase 2 (*COX2*), and the downstream target of TNF-α stimulation *TNFAIP3* that has been previously shown to be associated with GBM (Hjelmeland et al., 2010; Murat et al., 2009). Thus, the MES phenotype in GSCs and GBM was accompanied by activated NF-κB signaling, and CD44 is an integral component of this signature.

We next examined the association of these variables with radiation response and treatment outcome in a cohort of newly diagnosed GBM patients (Table S7). We used a previously defined radiation response scoring criteria (Pelloski et al., 2005) by comparing the maximal area of enhancement between the pre- (i.e., within 1 month of the start of radiation) and the post-RT magnetic resonance imaging (MRI; Figure 7A). Examination of the PN/MES status showed correlation between MES composite metagene (see Supplemental Experimental Procedures for details) and progression following RT (nonresponders) whereas a PN composite metagene correlated to patients with stable or reduced disease following RT, even in patients with WT *IDH1* tumors (Figures 7B and 7C). After adjusting for patient age (≤50 years versus >50 years), *IDH1* status (mutant versus WT), and Karnofsky Performance Status (KPS; ≤70 versus >70), only the MES metagene remained a significant predictor of RT response (Table S8). Patients with a higher MES metagene (upper two-thirds of the metagene quartile) also showed reduced survival irrespective of *IDH1* status (Figures 7D and 7E). Next, we evaluated whether CD44 and OLIG2 expression could be used as serviceable markers for MES and PN states, respectively. Patients with higher expression of CD44 showed a striking association with poor response to radiation and lower survival compared to those with lower CD44, and conversely, patients with high OLIG2 were more likely to be responders to radiation and better survivors (Figures 7F–7I; Figures S7B–S7E). Additionally, using an antibody specific for phosphorylated p65 (ser 276), a transcriptionally active form of NF-κB, as well as its target COX2 (Figure S7F), we found significant association of the expression of these proteins to nonresponders compared to those with a favorable response to radiation (Figures 7J and 7K; Figures S7G and S7H). Whereas intermediate and high COX2 expression were associated with poor survival (Figures 7L and S7I), p-p65 expression showed a similar trend but did not reach statistical significance (data not shown).

Finally, to characterize intratumoral PN to MES transition in human GBMs, we closely examined the temporal distribution of multiple markers by IHC on serial paraffin-embedded sections (Table S9). The expression of these markers ranged from pockets of negative expression to those with strong positivity. Importantly, $OLIG2^{low}$ and $CD44^{high}$ areas (MES signature) coincided with p-p65 positivity (Figure 8A; Table S9). The extent of macrophages/microglia infiltration (as judged by IBA staining) also correlated with the MES regions. This finding highlights intratumoral PN/MES heterogeneity that correlates with activation of NF-κB and macrophages/microglial involvement in GBM.

DISCUSSION

Differential Molecular Signatures in GSCs and GBMs

Whereas gene expression profiling of GBM has consistently shown the PN and MES subtypes, parallel efforts on GSCs have been limited, and mouse models representative of transcriptome subtypes of GBM are only beginning to emerge (Chow et al., 2011; Friedmann-Morvinski et al., 2012; Koso et al., 2012; Liu et al., 2011). In this report, we demonstrate that with the exception of a few, GSCs in general show gene expression and epigenetic profile differences from their parental tumors and that the majority of the GSCs exhibit an overall PN/$CIMP^+$ signature despite originating from predominantly MES/$CIMP^-$ GBMs. Placement of these PN/$CIMP^+$ GSCs in intracranial xenografts did not restore the MES phenotype of the parental tumor, indicating a potential shortcoming of immunocompromised xenograft models to fully recapitulate the human tumor microenvironment (Magee et al., 2012). We could not ascertain the CIMP status of the xenografts because of technical difficulties given the small size of these tumors. Although TNF-α/NF-κB activation induced MES differentiation, it did not alter CIMP methylation patterns, suggesting that other tumor microenvironment-derived cytokines could play a role in this process. Coupled with recent reports that resetting the epigenome of GSCs can cause remarkable changes in their malignant behavior (Stricker et al., 2013), future studies utilizing GSCs as a model system should take these factors into consideration.

MES Differentiation Is Mediated by NF-κB Induction of Master TFs

In addition to the identification of a role for NF-κB in inducing the MES signature, we show that this occurs via the induction of STAT3, C/EBPβ, and TAZ, although it remains to be seen if the radioresistance mediated by NF-κB is also dependent on these master TFs. Interestingly, these same TFs (with the exception of TAZ) play prominent roles in inflammatory response, and past studies have shown considerable crosstalk between these TFs. For example, NF-κB promotes an inflammatory response through secretion of TNF-α, IL-1β, and IL-6, of which IL-6 triggers STAT3 activation (Ben-Neriah and Karin, 2011; Hayden and Ghosh, 2012). Conversely, studies have shown that nuclear translocation of NF-κB is dependent on acetylation of NF-κB by

intracranial administration of TNF-α (2 ng/mouse) 72 hr prior to irradiation and once every 2 weeks thereafter. Horizontal black bar shows average radiance (photons/s/cm^2/sr) with various treatments and time points. Error bar indicates ± SEM. t test was used to assess statistical significance. **$p < 0.005$; NS, not significant.
See also Figure S5.

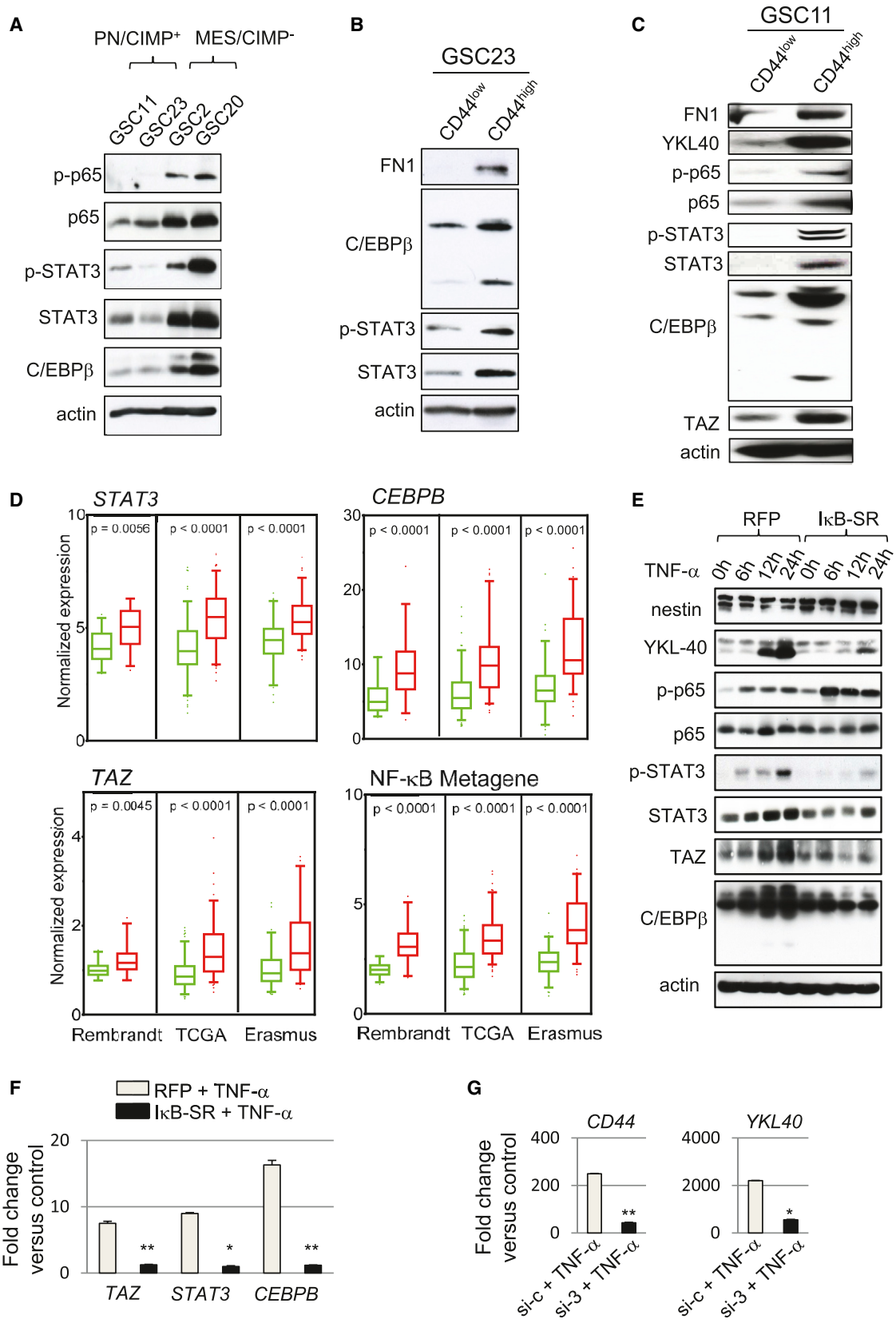

(legend on next page)

p300, which requires STAT3 activation (Gravendeel et al., 2009). The interdependency of NF-κB and C/EBPβ has also been previously reported in other studies (Acosta et al., 2008; Kuilman et al., 2008). While we show that TNF-α can be derived from macrophages/microglia, it is noteworthy that these cell types themselves exhibit plasticity and can be polarized to a proinflammatory (M1) or anti-inflammatory (M2) phenotype in the brain microenvironment (Li and Graeber, 2012; Wu et al., 2010). Because most GBMs arise de novo without prior clinical history of a lower grade tumor, it is difficult to study tumor evolution in GBM, that is, whether a MES tumor evolved from an early stage PN tumor is difficult to ascertain and the characteristics and the influence of the microenvironment in the early stages of a GBM are virtually unknown. Here we show evidence for the transcriptomic plasticity of the PN and MES states by IHC analysis of tumors that had regions of both PN and MES markers and their correlation to NF-κB activation and infiltration of macrophages/microglia. Consistent with our findings, recent studies have shown that the MES subclass of GBMs exhibit a high degree of necrosis (Cooper et al., 2012) and macrophages/microglial infiltration (Engler et al., 2012; Li et al., 2012). In addition, tumor evolutionary dynamics have been shown in a recent report wherein multiple transcriptome signatures were found within the same tumor (Sottoriva et al., 2013). We found that in some cases, MES/CIMP$^-$ GSCs showed constitutive MES signatures even in instances where *NF1* mutations were not seen (e.g., GSCs 2 and 20) and when removed from the microenvironment, suggesting that cell intrinsic mechanisms that sustain the MES network also exist.

Association of the MES Signature, CD44, and NF-κB Signaling with Radiation Resistance

Patients with GBM currently undergo standard treatment consisting of maximal surgical resection, combined radiation and chemotherapy, and adjuvant chemotherapy with temozolomide (Furnari et al., 2007; Hegi et al., 2005). Radiation has been a mainstay of GBM treatment for decades and the exact molecular mechanisms driving resistance in GBMs is unknown. Our previous studies have shown that patients with a MES signature belong to the poor prognosis subclass and are resistant to standard treatments (Colman et al., 2010) and that PN tumors can recur in a MES state (Phillips et al., 2006). Here we show that PN/CIMP$^+$ GSCs under specific conditions can undergo MES differentiation, with associated radioresistance. Importantly, we show that in newly diagnosed GBM, an increased MES metagene, CD44 expression, or NF-κB activation is associated with poor radiation response and shorter survival even in the absence of *IDH1* mutation. Although NF-κB has been previously implicated in GBM (Bredel et al., 2006, 2011; Park et al., 2009), our studies identify a role for NF-κB in mediating radiation resistance. We speculate that global MES differentiation induced by NF-κB parallels activation of checkpoint pathways, leading to enhanced DNA damage repair and unperturbed cell cycle progression in response to IR. Moreover, given that NF-κB has been shown to mediate antiapoptotic effects and DNA damage repair (Magné et al., 2006), it is conceivable that this pathway acts as a potential link between MES differentiation and radioresistance. In the context of previous studies showing that the CD133$^+$ GSCs are resistant to radiation (Bao et al., 2006), and even more efficiently under the influence of the brain microenvironment (Jamal et al., 2012), it remains to be seen whether CD133$^+$ subpopulation within the CD44^{high} GSCs represents a refinement of the radioresistant cell types.

In summary (Figure 8B), we show that although GBM patient tumors appear predominantly MES/CIMP$^-$ at presentation or progression, the GSCs derived from these tumors using a standard isolation procedure tend to be PN/CIMP$^+$ (despite absence of the *IDH1* mutation), suggesting that tumor microenvironmental factors in humans may induce a MES/CIMP$^-$ signature. We further show that in a subset of the PN/CIMP$^-$ GSCs, MES differentiation with associated enrichment of CD44-expressing subpopulations and radioresistance can be induced in an NF-κB-dependent fashion. Our data suggest that inhibition of NF-κB activation can directly affect radioresistance and presents an attractive therapeutic target for GBM.

EXPERIMENTAL PROCEDURES

GSCs Isolation and Cell Culture

Freshly resected tumor tissues were enzymatically and mechanically dissociated into single cells and grown in DMEM/F12 media supplemented with B27 (Invitrogen), EGF (20 ng/ml), and bFGF (20 ng/ml). After 2 to 4 weeks, free-floating neurospheres were collected and thereafter routinely cultured in the above-mentioned neurosphere media, with dissociation to single cells every 5–6 days. For growth factor comparison, PDGF (R&D Systems) was used at a final concentration of 10 ng/ml. For cytokine treatment, GSCs were dissociated into single cells with Accutase (Sigma Aldrich) and treated with various concentrations and durations as indicated in figure legends. IL-6, IL-8, IL-10, and TGF-β were obtained from R&D Systems, and TNF-α was from Sigma

Figure 6. NF-κB Controls Master TFs of MES Differentiation in GSCs

(A) Western blot analysis of phosphorylated p65 (ser 536), total p65, phosphorylated STAT3 (Tyr 705), STAT3, and C/EBPβ in GSCs is shown.

(B and C) Western blot analysis using indicated antibodies was performed on GSC23 (B) and 11 (C) sorted for CD44^{high} or CD44^{low} subpopulations.

(D) Box plots of normalized expression of *STAT3*, *CEBPB*, *TAZ*, and NF-κB metagene in *CD44*^{low} (green boxes) or *CD44*^{high} (red boxes) tumors from multiple data sets as indicated are shown. Boxes show median 25th and 75th percentiles, while whiskers represent the 5th and the 95th percentiles. Outliers are shown as individual points. p value was determined using a nonparametric Wilcoxon test. For the NF-κB metagene, the average expression of 38 NF-κB family members and targets (see Supplemental Experimental Procedures) was condensed into a metagene and plotted. Wilcoxon signed-rank test was used to test statistical significance.

(E) Time course western blot analysis of indicated antibodies after TNF-α treatment in GSC11 transduced with RFP or IκB-SR adenovirus 24 hr prior to TNF-α treatment is shown.

(F) qRT-PCR analysis of MES signature master TFs *STAT3*, *CEBPB*, and *TAZ* in GSC11 treated with TNF-α with or without pretreatment with RFP or IκB-SR adenovirus is shown. Error bar indicates ± SD. t test was used for statistical significance. *$p < 0.05$ and **$p < 0.005$.

(G) qRT-PCR analysis of *YKL40* and *CD44* after knockdown of all three master TFs (STAT3, C/EBPβ, and TAZ) in GSC11 is shown. Cells were treated with siRNA 72 hr prior to treatment with TNF-α for an additional 24 hr. Error bar indicates ± SD. t test was used for statistical significance. *$p < 0.05$ and **$p < 0.005$.

See also Figure S6.

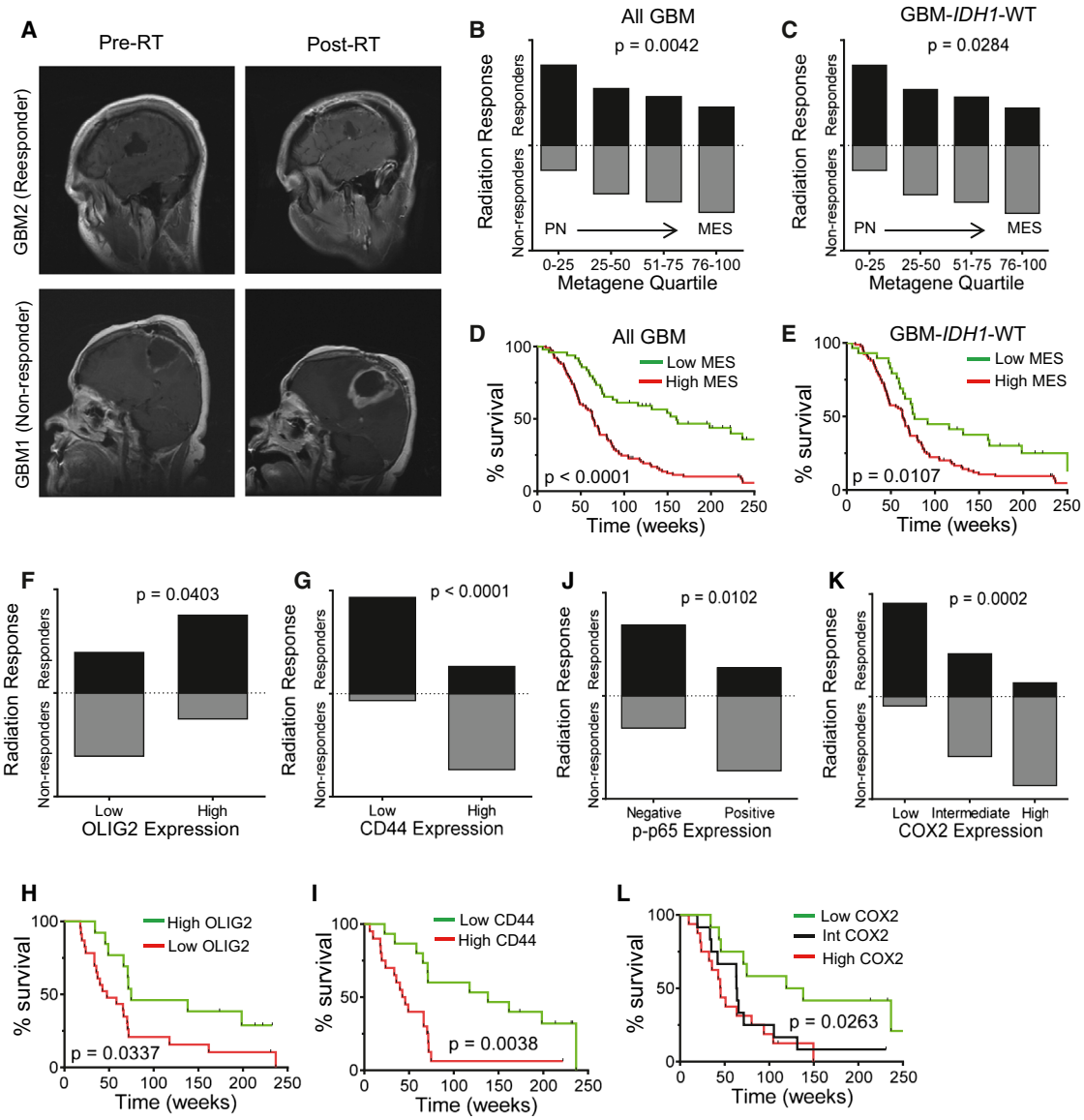

Figure 7. MES Differentiation, CD44 Levels, and NF-κB Activation Are Predictive of Radiation Response in GBM

(A) Representative MRI scans of postoperative/pre-RT and post-RT responses of patients typically classified as responders or nonresponders are shown.

(B) Box plots show the proportion of patients classified as responders or nonresponders against the PN/MES metagene quartiles in all newly diagnosed GBM cases (n = 149). Chi-square test was used to assess statistical significance.

(C) Box plot is shown for *IDH1* WT cases (n = 121).

(D) Kaplan Meier curves show survival of newly diagnosed patients based on PN/MES metagene scores. Low MES represents the bottom one-third of the cases whereas high MES was the top two-thirds. Log rank test was used to assess statistical significance.

(E) Kaplan Meier curves showing survival of newly diagnosed GBM-*IDH1* WT patients based on PN/MES metagene scores.

(F–L) Bar graph shows the proportion of OLIG2 (F), CD44 (G), p-p65 (J), and COX2 (K) expression in newly diagnosed GBM-*IDH1* WT patients classified as radiation responders or nonresponders. Proportions of patients who responded or did not respond were compared using chi-square test. Kaplan Meier curves show survival of newly diagnosed GBM-*IDH1* WT patients based on OLIG2 (H), CD44 (I), and COX2 (L).

See also Figure S7 and Tables S6–S8.

Aldrich. RFP and IκB-SR adenovirus were obtained from Vector Biolabs. The use of human tumor tissue samples and all other tumor-related studies were conducted in accordance with the protocols approved by the Institutional Review Board at the UT, M.D. Anderson Cancer Center, or the Medical Ethical Committee at the University Medical Center Groningen. The use of the tissues for the experiments involving isolation of GSCs, DNA and RNA isolation, and/or IHC on human tumors was exempt from requiring consent as per the MDACC Institutional Review Board. Patient materials at UMCG were obtained after routine diagnostics, coded according to the National Code for the Good Use of Patient Material, and were exempt from informed consent.

Microarray and Bioinformatic Analyses

RNA labeling and hybridization to Affymetrix HGU133 version 2.0 genechips was performed by Expression Analysis (Durham, NC). Raw .cel files

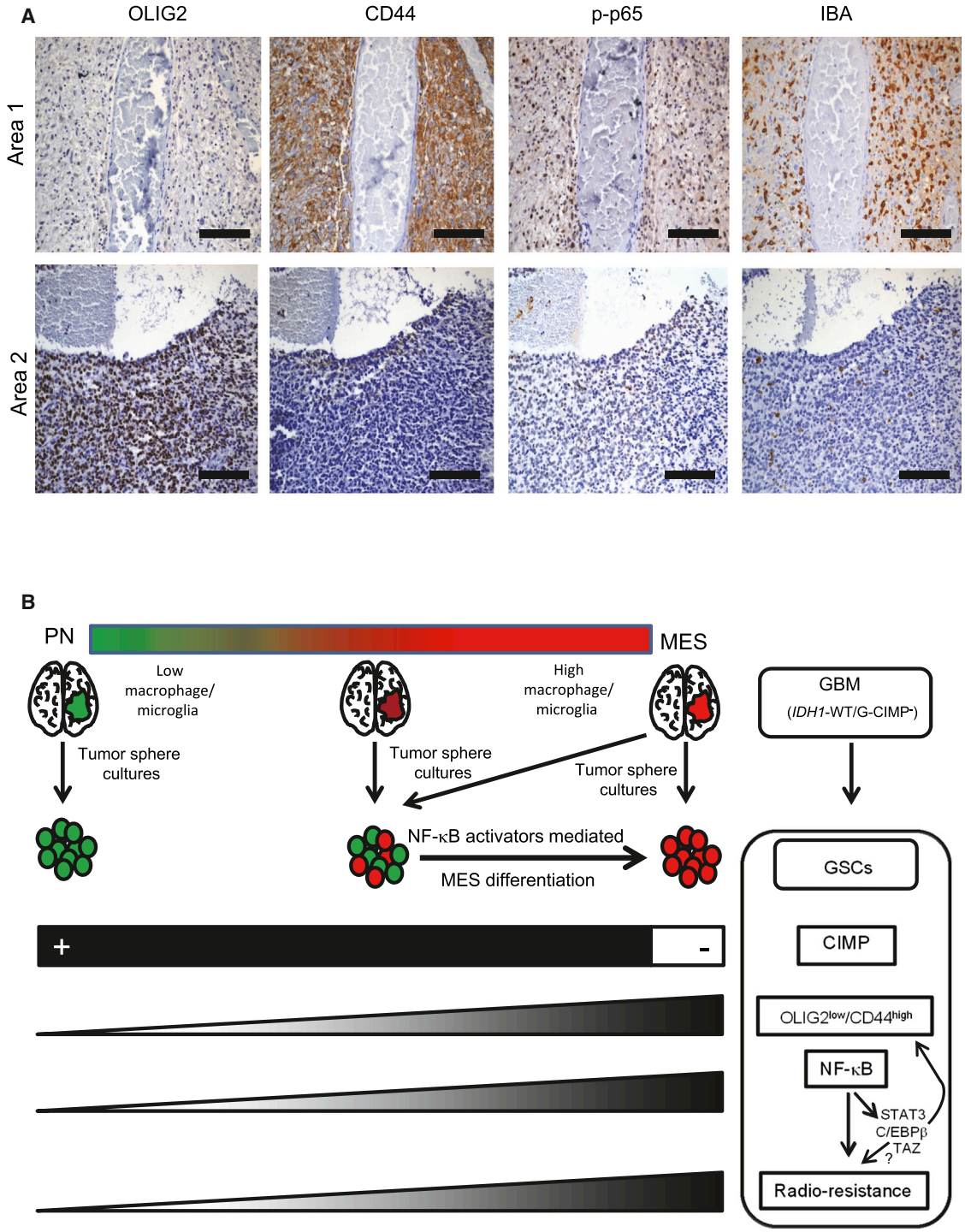

Figure 8. Features Associated with MES Differentiation Induced by NF-κB in GBM

(A) Consecutive 5 μm sections were stained for various markers by IHC. Two independent areas within a same tumor are shown for mutual exclusive expression of OLIG2 from CD44, p-p65, and IBA. Scale bar: 100 μm.

(B) Cartoon shows a summary of our findings. We propose that GSCs when isolated from the microenvironment may differ in their molecular signatures from the parental tumor. Whereas GBMs at the extreme ends of the PN/MES axis will likely contain (and enrich for) GSCs with similar signatures to the parental tumor, GBMs with intermediate to high MES signatures enrich for PN GSCs that are maintained in a MES state in the human tumor microenvironment (by cell types such as macrophages/microglia). These PN GSCs also tend to be $CIMP^{+}$ although derived from G-$CIMP^{-}$ tumors that lack the *IDH1* mutation. MES differentiation, CD44 enrichment, and radioresistance can be induced in PN/$CIMP^{-}$ GSCs by activation of NF-κB and downstream master TFs (STAT3, C/EBPβ, and TAZ). In contrast, MES GSCs are $CIMP^{-}$, predominantly express CD44, are radioresistant, and exhibit constitutive activation of NF-κB and downstream master TFs. See also Table S9.

(GSE49009) were processed using R and Bioconductor (Gentleman et al., 2004), using a custom CDF (Sandberg and Larsson, 2007), with background correction, log transformation, and quantile normalization performed using the RMA algorithm. Detailed description of all other bioinformatic analyses is described in Supplemental Experimental Procedures.

Xenograft Models and Treatments

GSCs were implanted intracranially using the guide screw system in 4- to 5-week-old NOD/SCID or Foxn1^{nu} mice. After 1 week of guide screw implantation, 5 × 10^5 cells or fewer (as indicated) were injected intracranially in each mouse and randomly distributed between groups. A minimum of five mice was used in each group. For in vivo bioluminescent imaging, GSCs were engineered to express luciferase by transducing with pCignal lenti-CMV-luc viral particles (SABiosciences). Kinetics of tumor growth was monitored using IVIS 200 system bioluminescent imaging and tumor volume measured using Living Image 4.1 software. IR was delivered using fractionated doses (2.5 Gy × 4) using a ^{60}Co teletherapy unit and a custom gig with validated dosimetry. Mice that presented neurological symptoms (i.e., hydrocephalus, seizures, inactivity, and/or ataxia) or that were moribund were sacrificed, and brains were fixed in formalin, stained with H&E to confirm the presence of tumor, and subject to IHC. All animal procedures were reviewed and approved by the Institutional Animal Care and Use Committee at the M.D. Anderson Cancer Center.

ACCESSION NUMBERS

The Gene Expression Omnibus accession number for the microarray experiments is GSE49009.

SUPPLEMENTAL INFORMATION

Supplemental Information includes Supplemental Experimental Procedures, seven figures, and nine tables and can be found with this article online at http://dx.doi.org/10.1016/j.ccr.2013.08.001.

ACKNOWLEDGMENTS

We would like to acknowledge the Caroline Ross Endowment Fellowship, the American Brain Tumor Association Basic Research Fellowship, the Odyssey Special Fellowship, and the MDACC Brain Tumor SPORE Career Development grant (to K.P.L.B.); the Brain Tumor Funders' Collaborative, the Dr. Marnie Rose Foundation, and the National Brain Tumor Society (to K.A.); the V Foundation and SPORE grant P50CA127001 from NIH/NCI (to K.A. and H.C.); the Huntsman Cancer Foundation (to H.C.); the Ben and Cathy Ivy Foundation Research Award (to F.F.L., K.A., and E.P.S.); the SPORE Animal Core grant (to F.F.L.); grant R01-CA1208113 from NIH/NCI (to A.H.); and Dutch Cancer Society grant RUG 2011-5150 (to V.B., H.W.B., and W.F.D.) for their generous support. We thank Alicia Ledoux, Bhavna Singh, and Susan Cweren for histology; Verlene Henry for animal injections; and the Flow Cytometry & Cellular Imaging Core Facility, Small Animal Imaging Facility, and the Division of Surgery Pathology Core Facility (all at MDACC supported by P30-CA016672) for technical support. We apologize for not citing some original references because of space limitations. H.S.P. is an employee and stockholder of Roche/Genentech.

Received: May 11, 2012
Revised: June 24, 2013
Accepted: August 1, 2013
Published: August 29, 2013

REFERENCES

Acosta, J.C., O'Loghlen, A., Banito, A., Guijarro, M.V., Augert, A., Raguz, S., Fumagalli, M., Da Costa, M., Brown, C., Popov, N., et al. (2008). Chemokine signaling via the CXCR2 receptor reinforces senescence. Cell *133*, 1006–1018.

Bao, S., Wu, Q., McLendon, R.E., Hao, Y., Shi, Q., Hjelmeland, A.B., Dewhirst, M.W., Bigner, D.D., and Rich, J.N. (2006). Glioma stem cells promote radioresistance by preferential activation of the DNA damage response. Nature *444*, 756–760.

Ben-Neriah, Y., and Karin, M. (2011). Inflammation meets cancer, with NF-κB as the matchmaker. Nat. Immunol. *12*, 715–723.

Bhat, K.P., Salazar, K.L., Balasubramaniyan, V., Wani, K., Heathcock, L., Hollingsworth, F., James, J.D., Gumin, J., Diefes, K.L., Kim, S.H., et al. (2011). The transcriptional coactivator TAZ regulates mesenchymal differentiation in malignant glioma. Genes Dev. *25*, 2594–2609.

Bredel, M., Bredel, C., Juric, D., Duran, G.E., Yu, R.X., Harsh, G.R., Vogel, H., Recht, L.D., Scheck, A.C., and Sikic, B.I. (2006). Tumor necrosis factor-alpha-induced protein 3 as a putative regulator of nuclear factor-kappaB-mediated resistance to O6-alkylating agents in human glioblastomas. J. Clin. Oncol. *24*, 274–287.

Bredel, M., Scholtens, D.M., Yadav, A.K., Alvarez, A.A., Renfrow, J.J., Chandler, J.P., Yu, I.L., Carro, M.S., Dai, F., Tagge, M.J., et al. (2011). NFKBIA deletion in glioblastomas. N. Engl. J. Med. *364*, 627–637.

Brescia, P., Richichi, C., and Pelicci, G. (2012). Current strategies for identification of glioma stem cells: adequate or unsatisfactory? J. Oncol. *2012*, 376894.

Carro, M.S., Lim, W.K., Alvarez, M.J., Bollo, R.J., Zhao, X., Snyder, E.Y., Sulman, E.P., Anne, S.L., Doetsch, F., Colman, H., et al. (2010). The transcriptional network for mesenchymal transformation of brain tumours. Nature *463*, 318–325.

Charles, N.A., Holland, E.C., Gilbertson, R., Glass, R., and Kettenmann, H. (2011). The brain tumor microenvironment. Glia *59*, 1169–1180.

Chen, J., McKay, R.M., and Parada, L.F. (2012). Malignant glioma: lessons from genomics, mouse models, and stem cells. Cell *149*, 36–47.

Chow, L.M., Endersby, R., Zhu, X., Rankin, S., Qu, C., Zhang, J., Broniscer, A., Ellison, D.W., and Baker, S.J. (2011). Cooperativity within and among Pten, p53, and Rb pathways induces high-grade astrocytoma in adult brain. Cancer Cell *19*, 305–316.

Colman, H., Zhang, L., Sulman, E.P., McDonald, J.M., Shooshtari, N.L., Rivera, A., Popoff, S., Nutt, C.L., Louis, D.N., Cairncross, J.G., et al. (2010). A multigene predictor of outcome in glioblastoma. Neuro-oncol. *12*, 49–57.

Cooper, L.A., Gutman, D.A., Long, Q., Johnson, B.A., Cholleti, S.R., Kurc, T., Saltz, J.H., Brat, D.J., and Moreno, C.S. (2010). The proneural molecular signature is enriched in oligodendrogliomas and predicts improved survival among diffuse gliomas. PLoS ONE *5*, e12548.

Cooper, L.A., Gutman, D.A., Chisolm, C., Appin, C., Kong, J., Rong, Y., Kurc, T., Van Meir, E.G., Saltz, J.H., Moreno, C.S., and Brat, D.J. (2012). The tumor microenvironment strongly impacts master transcriptional regulators and gene expression class of glioblastoma. Am. J. Pathol. *180*, 2108–2119.

Daginakatte, G.C., and Gutmann, D.H. (2007). Neurofibromatosis-1 (Nf1) heterozygous brain microglia elaborate paracrine factors that promote Nf1-deficient astrocyte and glioma growth. Hum. Mol. Genet. *16*, 1098–1112.

Dennis, G., Jr., Sherman, B.T., Hosack, D.A., Yang, J., Gao, W., Lane, H.C., and Lempicki, R.A. (2003). DAVID: Database for Annotation, Visualization, and Integrated Discovery. Genome Biol. *4*, 3.

Engler, J.R., Robinson, A.E., Smirnov, I., Hodgson, J.G., Berger, M.S., Gupta, N., James, C.D., Molinaro, A., and Phillips, J.J. (2012). Increased microglia/macrophage gene expression in a subset of adult and pediatric astrocytomas. PLoS ONE *7*, e43339.

Friedmann-Morvinski, D., Bushong, E.A., Ke, E., Soda, Y., Marumoto, T., Singer, O., Ellisman, M.H., and Verma, I.M. (2012). Dedifferentiation of neurons and astrocytes by oncogenes can induce gliomas in mice. Science *338*, 1080–1084.

Furnari, F.B., Fenton, T., Bachoo, R.M., Mukasa, A., Stommel, J.M., Stegh, A., Hahn, W.C., Ligon, K.L., Louis, D.N., Brennan, C., et al. (2007). Malignant astrocytic glioma: genetics, biology, and paths to treatment. Genes Dev. *21*, 2683–2710.

Gentleman, R.C., Carey, V.J., Bates, D.M., Bolstad, B., Dettling, M., Dudoit, S., Ellis, B., Gautier, L., Ge, Y., Gentry, J., et al. (2004). Bioconductor: open software development for computational biology and bioinformatics. Genome Biol. *5*, R80.

Gravendeel, L.A., Kouwenhoven, M.C., Gevaert, O., de Rooi, J.J., Stubbs, A.P., Duijm, J.E., Daemen, A., Bleeker, F.E., Bralten, L.B., Kloosterhof, N.K., et al. (2009). Intrinsic gene expression profiles of gliomas are a better predictor of survival than histology. Cancer Res. *69*, 9065–9072.

Hayden, M.S., and Ghosh, S. (2012). NF-κB, the first quarter-century: remarkable progress and outstanding questions. Genes Dev. *26*, 203–234.

Hegi, M.E., Diserens, A.C., Gorlia, T., Hamou, M.F., de Tribolet, N., Weller, M., Kros, J.M., Hainfellner, J.A., Mason, W., Mariani, L., et al. (2005). MGMT gene silencing and benefit from temozolomide in glioblastoma. N. Engl. J. Med. *352*, 997–1003.

Hjelmeland, A.B., Wu, Q., Wickman, S., Eyler, C., Heddleston, J., Shi, Q., Lathia, J.D., Macswords, J., Lee, J., McLendon, R.E., and Rich, J.N. (2010). Targeting A20 decreases glioma stem cell survival and tumor growth. PLoS Biol. *8*, e1000319.

Huse, J.T., Phillips, H.S., and Brennan, C.W. (2011). Molecular subclassification of diffuse gliomas: seeing order in the chaos. Glia *59*, 1190–1199.

Jamal, M., Rath, B.H., Tsang, P.S., Camphausen, K., and Tofilon, P.J. (2012). The brain microenvironment preferentially enhances the radioresistance of CD133(+) glioblastoma stem-like cells. Neoplasia *14*, 150–158.

Jijiwa, M., Demir, H., Gupta, S., Leung, C., Joshi, K., Orozco, N., Huang, T., Yildiz, V.O., Shibahara, I., de Jesus, J.A., et al. (2011). CD44v6 regulates growth of brain tumor stem cells partially through the AKT-mediated pathway. PLoS ONE *6*, e24217.

Koso, H., Takeda, H., Yew, C.C., Ward, J.M., Nariai, N., Ueno, K., Nagasaki, M., Watanabe, S., Rust, A.G., Adams, D.J., et al. (2012). Transposon mutagenesis identifies genes that transform neural stem cells into glioma-initiating cells. Proc. Natl. Acad. Sci. USA *109*, E2998–E3007.

Kuilman, T., Michaloglou, C., Vredeveld, L.C., Douma, S., van Doorn, R., Desmet, C.J., Aarden, L.A., Mooi, W.J., and Peeper, D.S. (2008). Oncogene-induced senescence relayed by an interleukin-dependent inflammatory network. Cell *133*, 1019–1031.

Li, W., and Graeber, M.B. (2012). The molecular profile of microglia under the influence of glioma. Neuro-oncol. *14*, 958–978.

Li, B., Senbabaoglu, Y., Peng, W., Yang, M.L., Xu, J., and Li, J.Z. (2012). Genomic estimates of aneuploid content in glioblastoma multiforme and improved classification. Clin. Cancer Res. *18*, 5595–5605.

Liu, C., Sage, J.C., Miller, M.R., Verhaak, R.G., Hippenmeyer, S., Vogel, H., Foreman, O., Bronson, R.T., Nishiyama, A., Luo, L., and Zong, H. (2011). Mosaic analysis with double markers reveals tumor cell of origin in glioma. Cell *146*, 209–221.

Lu, C., Ward, P.S., Kapoor, G.S., Rohle, D., Turcan, S., Abdel-Wahab, O., Edwards, C.R., Khanin, R., Figueroa, M.E., Melnick, A., et al. (2012). IDH mutation impairs histone demethylation and results in a block to cell differentiation. Nature *483*, 474–478.

Magee, J.A., Piskounova, E., and Morrison, S.J. (2012). Cancer stem cells: impact, heterogeneity, and uncertainty. Cancer Cell *21*, 283–296.

Magné, N., Toillon, R.A., Bottero, V., Didelot, C., Houtte, P.V., Gérard, J.P., and Peyron, J.F. (2006). NF-kappaB modulation and ionizing radiation: mechanisms and future directions for cancer treatment. Cancer Lett. *231*, 158–168.

Markovic, D.S., Vinnakota, K., van Rooijen, N., Kiwit, J., Synowitz, M., Glass, R., and Kettenmann, H. (2011). Minocycline reduces glioma expansion and invasion by attenuating microglial MT1-MMP expression. Brain Behav. Immun. *25*, 624–628.

Mir, S.E., De Witt Hamer, P.C., Krawczyk, P.M., Balaj, L., Claes, A., Niers, J.M., Van Tilborg, A.A., Zwinderman, A.H., Geerts, D., Kaspers, G.J., et al. (2010). In silico analysis of kinase expression identifies WEE1 as a gatekeeper against mitotic catastrophe in glioblastoma. Cancer Cell *18*, 244–257.

Murat, A., Migliavacca, E., Hussain, S.F., Heimberger, A.B., Desbaillets, I., Hamou, M.F., Rüegg, C., Stupp, R., Delorenzi, M., and Hegi, M.E. (2009). Modulation of angiogenic and inflammatory response in glioblastoma by hypoxia. PLoS ONE *4*, e5947.

Noushmehr, H., Weisenberger, D.J., Diefes, K., Phillips, H.S., Pujara, K., Berman, B.P., Pan, F., Pelloski, C.E., Sulman, E.P., Bhat, K.P., et al.; Cancer Genome Atlas Research Network. (2010). Identification of a CpG island methylator phenotype that defines a distinct subgroup of glioma. Cancer Cell *17*, 510–522.

Park, S., Hatanpaa, K.J., Xie, Y., Mickey, B.E., Madden, C.J., Raisanen, J.M., Ramnarain, D.B., Xiao, G., Saha, D., Boothman, D.A., et al. (2009). The receptor interacting protein 1 inhibits p53 induction through NF-kappaB activation and confers a worse prognosis in glioblastoma. Cancer Res. *69*, 2809–2816.

Pelloski, C.E., Mahajan, A., Maor, M., Chang, E.L., Woo, S., Gilbert, M., Colman, H., Yang, H., Ledoux, A., Blair, H., et al. (2005). YKL-40 expression is associated with poorer response to radiation and shorter overall survival in glioblastoma. Clin. Cancer Res. *11*, 3326–3334.

Phillips, H.S., Kharbanda, S., Chen, R., Forrest, W.F., Soriano, R.H., Wu, T.D., Misra, A., Nigro, J.M., Colman, H., Soroceanu, L., et al. (2006). Molecular subclasses of high-grade glioma predict prognosis, delineate a pattern of disease progression, and resemble stages in neurogenesis. Cancer Cell *9*, 157–173.

Pietsch, T., and Wiestler, O.D. (1997). Molecular neuropathology of astrocytic brain tumors. J. Neurooncol. *35*, 211–222.

Riddick, G., and Fine, H.A. (2011). Integration and analysis of genome-scale data from gliomas. Nat Rev Neurol *7*, 439–450.

Sandberg, R., and Larsson, O. (2007). Improved precision and accuracy for microarrays using updated probe set definitions. BMC Bioinformatics *8*, 48.

Son, M.J., Woolard, K., Nam, D.H., Lee, J., and Fine, H.A. (2009). SSEA-1 is an enrichment marker for tumor-initiating cells in human glioblastoma. Cell Stem Cell *4*, 440–452.

Sottoriva, A., Spiteri, I., Piccirillo, S.G., Touloumis, A., Collins, V.P., Marioni, J.C., Curtis, C., Watts, C., and Tavaré, S. (2013). Intratumor heterogeneity in human glioblastoma reflects cancer evolutionary dynamics. Proc. Natl. Acad. Sci. USA *110*, 4009–4014.

Stopschinski, B.E., Beier, C.P., and Beier, D. (2012). Glioblastoma cancer stem cells - From concept to clinical application. Cancer Lett. Published online June 2, 2012. http://dx.doi.org/10.1016/j.canlet.2012.05.033.

Stricker, S.H., Feber, A., Engström, P.G., Carén, H., Kurian, K.M., Takashima, Y., Watts, C., Way, M., Dirks, P., Bertone, P., et al. (2013). Widespread resetting of DNA methylation in glioblastoma-initiating cells suppresses malignant cellular behavior in a lineage-dependent manner. Genes Dev. *27*, 654–669.

Subramanian, A., Tamayo, P., Mootha, V.K., Mukherjee, S., Ebert, B.L., Gillette, M.A., Paulovich, A., Pomeroy, S.L., Golub, T.R., Lander, E.S., and Mesirov, J.P. (2005). Gene set enrichment analysis: a knowledge-based approach for interpreting genome-wide expression profiles. Proc. Natl. Acad. Sci. USA *102*, 15545–15550.

Turcan, S., Rohle, D., Goenka, A., Walsh, L.A., Fang, F., Yilmaz, E., Campos, C., Fabius, A.W., Lu, C., Ward, P.S., et al. (2012). IDH1 mutation is sufficient to establish the glioma hypermethylator phenotype. Nature *483*, 479–483.

Verhaak, R.G., Hoadley, K.A., Purdom, E., Wang, V., Qi, Y., Wilkerson, M.D., Miller, C.R., Ding, L., Golub, T., Mesirov, J.P., et al.; Cancer Genome Atlas Research Network. (2010). Integrated genomic analysis identifies clinically relevant subtypes of glioblastoma characterized by abnormalities in PDGFRA, IDH1, EGFR, and NF1. Cancer Cell *17*, 98–110.

Wu, A., Wei, J., Kong, L.Y., Wang, Y., Priebe, W., Qiao, W., Sawaya, R., and Heimberger, A.B. (2010). Glioma cancer stem cells induce immunosuppressive macrophages/microglia. Neuro-oncol. *12*, 1113–1125.

Zöller, M. (2011). CD44: can a cancer-initiating cell profit from an abundantly expressed molecule? Nat. Rev. Cancer *11*, 254–267.

Cancer Cell
Article

Protein Kinase C α Is a Central Signaling Node and Therapeutic Target for Breast Cancer Stem Cells

Wai Leong Tam,[1,8] Haihui Lu,[1] Joyce Buikhuisen,[1] Boon Seng Soh,[2] Elgene Lim,[3] Ferenc Reinhardt,[1] Zhenhua Jeremy Wu,[4] Jordan A. Krall,[1] Brian Bierie,[1] Wenjun Guo,[5] Xi Chen,[6] Xiaole Shirley Liu,[4] Myles Brown,[3] Bing Lim,[2] and Robert A. Weinberg[1,7,8,*]

[1]Whitehead Institute for Biomedical Research, Cambridge, MA 02142, USA
[2]Genome Institute of Singapore, 60 Biopolis Street, Singapore 138672, Singapore
[3]Department of Medical Oncology
[4]Department of Biostatistics and Computational Biology
Dana Farber Cancer Institute and Harvard School of Public Health, Boston, MA 02115, USA
[5]Gottesman Institute for Stem Cell and Regenerative Medicine Research, Albert Einstein College of Medicine, Bronx, NY 10461, USA
[6]Department of Medicine, Weill Cornell Medical College, New York, NY 10065, USA
[7]Department of Biology, Massachusetts Institute of Technology, Cambridge, MA 02142, USA
[8]MIT Ludwig Center for Molecular Oncology, Cambridge, MA 02139, USA
*Correspondence: weinberg@wi.mit.edu
http://dx.doi.org/10.1016/j.ccr.2013.08.005

SUMMARY

The epithelial-mesenchymal transition program becomes activated during malignant progression and can enrich for cancer stem cells (CSCs). We report that inhibition of protein kinase C α (PKCα) specifically targets CSCs but has little effect on non-CSCs. The formation of CSCs from non-stem cells involves a shift from EGFR to PDGFR signaling and results in the PKCα-dependent activation of FRA1. We identified an AP-1 molecular switch in which c-FOS and FRA1 are preferentially utilized in non-CSCs and CSCs, respectively. PKCα and FRA1 expression is associated with the aggressive triple-negative breast cancers, and the depletion of FRA1 results in a mesenchymal-epithelial transition. Hence, identifying molecular features that shift between cell states can be exploited to target signaling components critical to CSCs.

INTRODUCTION

Cancer stem cells (CSCs), which are defined by their tumor-initiating properties, have been identified within breast, colon, head and neck, lung, and prostate carcinomas (Ailles and Weissman, 2007). These cells appear to be responsible for driving tumor growth, recurrence, and metastasis (Al-Hajj et al., 2003; Dalerba et al., 2007). In experimental models of cancer development, treatment of bulk cancer cell populations within tumors or cancer cell lines propagated in culture with chemotherapy or radiotherapy has been shown to select for the outgrowth of therapy-resistant subpopulations of cancer cells that are more tumorigenic, invasive, and stem like (Creighton et al., 2009; Gupta et al., 2009). Hence, cancer therapies may be rendered ineffective because the bulk of cancer cells within a tumor may be eliminated while leaving behind CSC-enriched cells that proceed to regenerate tumors. These tumors are often more malignant than was observed prior to treatment, underscoring the need for a detailed understanding of the molecular differences between CSCs and non-CSCs to discover and exploit cell-state-specific features that may render CSCs susceptible to selective therapeutic intervention.

Numerous studies have used existing cancer cell lines to identify compounds that target cells bearing specific gene mutations or exhibiting a more malignant phenotype; these studies did not, however, address the specific effects of certain treatments on CSCs because the representation of CSCs within these cell lines was poorly defined. In the case of breast cancer, several

Significance

Conventional cancer therapeutics tend to preferentially eliminate the non-CSCs within a tumor, leaving behind residues of more resistant CSCs that can subsequently generate clinical relapses, indicating the need to specifically target the CSCs within tumors. The identification of key regulatory mechanisms that distinguish CSCs from non-CSCs is therefore critical for CSC-targeted therapy. We find that the PKCα signaling network is activated specifically in CSCs, rendering them preferentially susceptible to specific pharmacologic agents. In addition, we uncovered FRA1 to be a key transcription factor downstream of PKCα that drives CSC function. The inhibition of either PKCα or FRA1 can abolish tumor initiation, highlighting the potential therapeutic value of targeting these proteins in epithelial cancers such as breast cancer.

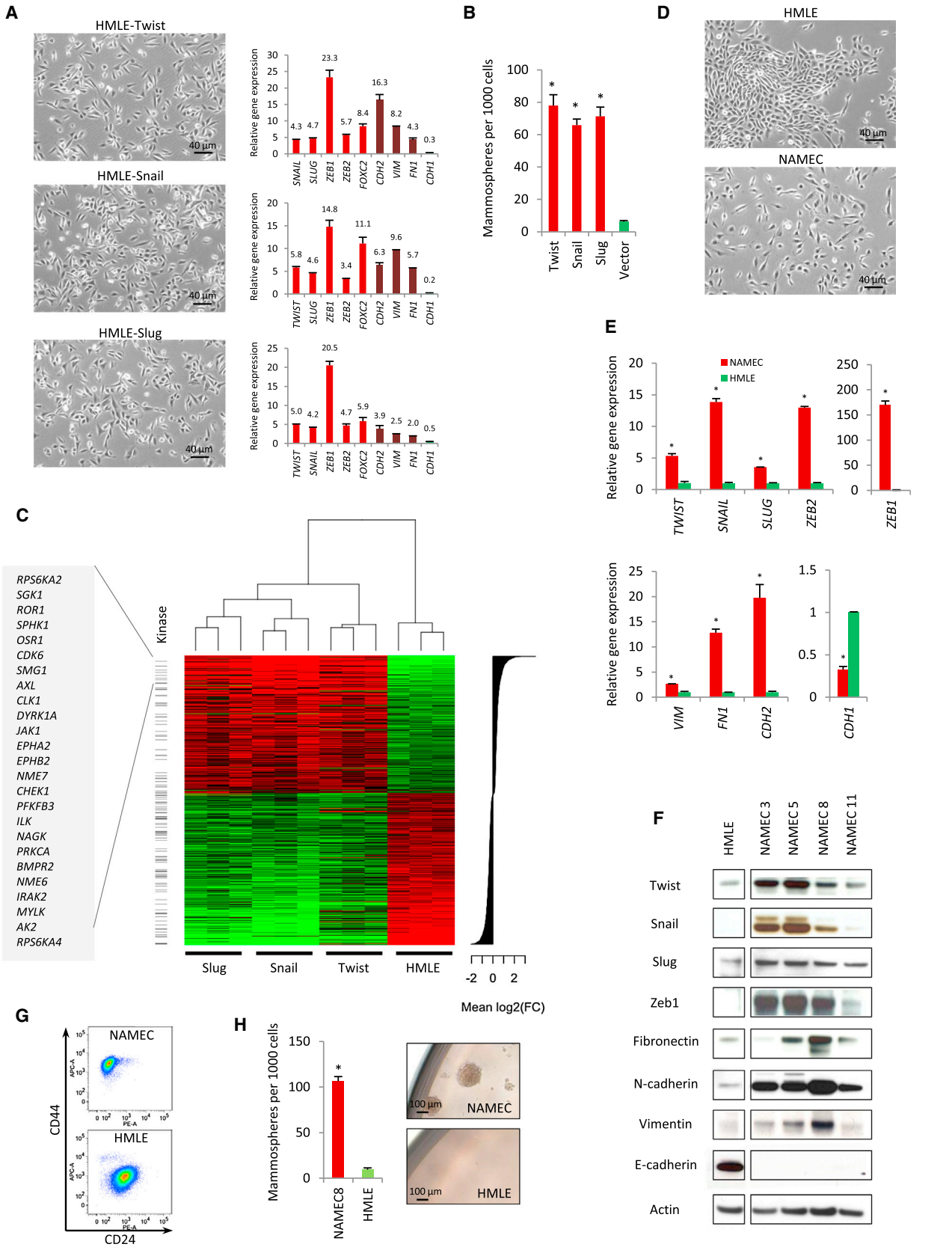

(legend on next page)

markers, including $CD44^{hi}/CD24^{lo}$, aldehyde dehydrogenase, Hoechst dye efflux, and the retention of the PKH26 lipophilic dye, have been shown to enrich for CSCs in various cell lines (Al-Hajj et al., 2003; Ginestier et al., 2007; Pece et al., 2010). However, regardless of the enrichment procedure, these initially purified cells with CSC properties often differentiate rapidly into cells exhibiting a non-CSC profile, making it difficult to identify cell-state-specific inhibitors in vitro.

CSCs are generated in some and perhaps all carcinomas as one of the products of an epithelial-mesenchymal transition (EMT), indicating that these cells possess a more mesenchymal phenotype that is associated with highly aggressive traits (Nieto, 2011; Thiery et al., 2009). We undertook to develop a method by which we could clearly distinguish chemical inhibitors that target breast CSCs from those that affect non-CSCs. Within normal mammary epithelial cells (MECs), the forced expression of EMT-inducing transcription factors (EMT-TFs) endows cells with mesenchymal traits accompanied by the loss of epithelial markers. These cells were shown to possess enhanced stem cell activity in vitro and in vivo (Mani et al., 2008; Morel et al., 2008). Likewise, in populations of weakly or non-tumorigenic breast cancer cells, passage through the EMT program dramatically increases CSC frequency along with the acquisition of mesenchymal properties that include a distinctive $CD44^{hi}/CD24^{lo}$ cell-surface marker profile, mammosphere-forming ability, heightened resistance to chemotherapeutics, and increased tumor-initiating ability (Nieto, 2011; Thiery et al., 2009).

In the present work, we took a directed approach to discover key regulatory genes unique to the mesenchymal state whose expression is elevated in CSCs.

RESULTS

Identification of Kinases Expressed Differentially in EMT-Induced Cells

To understand the molecular changes associated with epithelial cells that have passed through an EMT, we transduced genes encoding the Twist, Snail, and Slug EMT-TFs into HMLE human MECs that had previously been immortalized through the introduction of the hTERT and SV40 early-region genes (Mani et al., 2008). As anticipated, the resulting cells (HMLE-Twist, HMLE-Snail, and HMLE-Slug) displayed a set of mesenchymal markers and were judged by these criteria to have undergone an EMT (Figure 1A and Figure S1A available online). These cells were predominantly $CD44^{hi}/CD24^{lo}$ (data not shown) and formed mammospheres more efficiently than did the parental epithelial cells (Figure 1B), indicating they were enriched for stem cell activity.

Using microarray gene expression analyses (GSE43495), we searched for kinase-encoding genes that exhibited the greatest differences in expression in the EMT-TF-induced mesenchymal cells relative to the parental HMLE cells. A group of kinase-encoding genes was overexpressed at least 2-fold in HMLE-Twist, HMLE-Snail, and HMLE-Slug cells relative to the HMLE population (Figure 1C; Table S1). Several of these genes, including *CLK1*, *EPHA2*, *NME7*, *PRKCA* (hereafter referred as *PKCα*), *SGK1*, *SPHK1*, and *CDK6*, have been reported to promote cancer cell invasion and motility but were not previously implicated either as components of the EMT transcription program or in the maintenance of mesenchymal and CSC states. We validated the expression of the top selected kinase mRNAs by quantitative PCR (Figure S1B).

The changes in the expression patterns of these kinases during the EMT suggested an opportunity for selective therapeutic intervention using kinase inhibitors. We wished to develop an assay that could be used to determine whether any of the upregulated kinases could be pharmacologically targeted to preferentially kill the mesenchymal cells. Because the mesenchymal cells analyzed above carried constitutively expressed EMT-TFs and were therefore locked in the mesenchymal state, we reasoned their response to chemical inhibitors might not be representative of mesenchymal cells that arise in vivo through the physiological and presumably reversible upregulation of endogenous EMT-TFs, limiting the utility of the EMT-TF vector-transduced cells in chemical inhibitor screens.

Therefore, we derived populations of HMLE cells that had spontaneously undergone an EMT and stably resided thereafter in a mesenchymal state (Figure 1D). Hence, their phenotypic state was governed by endogenously expressed EMT-TFs. We derived 11 such lines, termed *n*aturally *a*rising *me*senchymal *c*ells (NAMECs), from bulk cultures of HMLE cells. We found that NAMECs expressed elevated levels of endogenous EMT-TFs (Twist, Snail, Slug, and Zeb1) and associated markers (vimentin, N-cadherin, and fibronectin) as well as loss of the key epithelial adherens junction protein, E-cadherin (encoded by *CDH1*) (Figures 1E, 1F, S1A, and S1C). Similar to EMT-TF-induced cells and the resident mammary epithelial stem cells that are naturally present within HMLE populations, NAMECs were also predominately $CD44^{hi}/CD24^{lo}$ (Figure 1G). They exhibited an 11.3-fold higher mammosphere-forming ability relative to HMLE cells (Figure 1H). Thus, NAMECs exhibited characteristics of cells that have passed through an EMT and differed greatly from parental HMLE cells.

Figure 1. Global Gene Expression Analyses Reveal Differentially Regulated Kinases Whose mRNA Expression Are Altered following EMT

(A) Representative phase contrast images of the indicated cell lines (left) and quantitative PCR for gene expression of EMT markers in these cell lines are shown relative to HMLE-vector cells (right). Numbers denote fold change. Scale bar: 40 μm.

(B) Mammosphere-forming ability of HMLE cells transduced with Twist, Snail, or Slug is shown.

(C) Heatmap of the top differentially regulated genes among HMLE-Twist, HMLE-Snail, HMLE-Slug, and control cells is shown (fold change > 1.2).

(D) Phase contrast images of NAMEC and HMLE cells are shown. Scale bar: 40 μm.

(E) Quantitative PCR for gene expression of EMT markers in NAMEC8 and HMLE cells is shown.

(F) Western blots of EMT-associated proteins in NAMECs and HMLE cells are shown. Samples were loaded and analyzed on the same blot.

(G) Flow cytometry analysis for the expression of CD44 and CD24 surface antigens on NAMECs and HMLE cells.

(H) Mammosphere-forming ability of NAMECs and HMLE cells is depicted.

*$p < 0.05$. Data are presented as mean ± SEM. See also Table S1 and Figure S1.

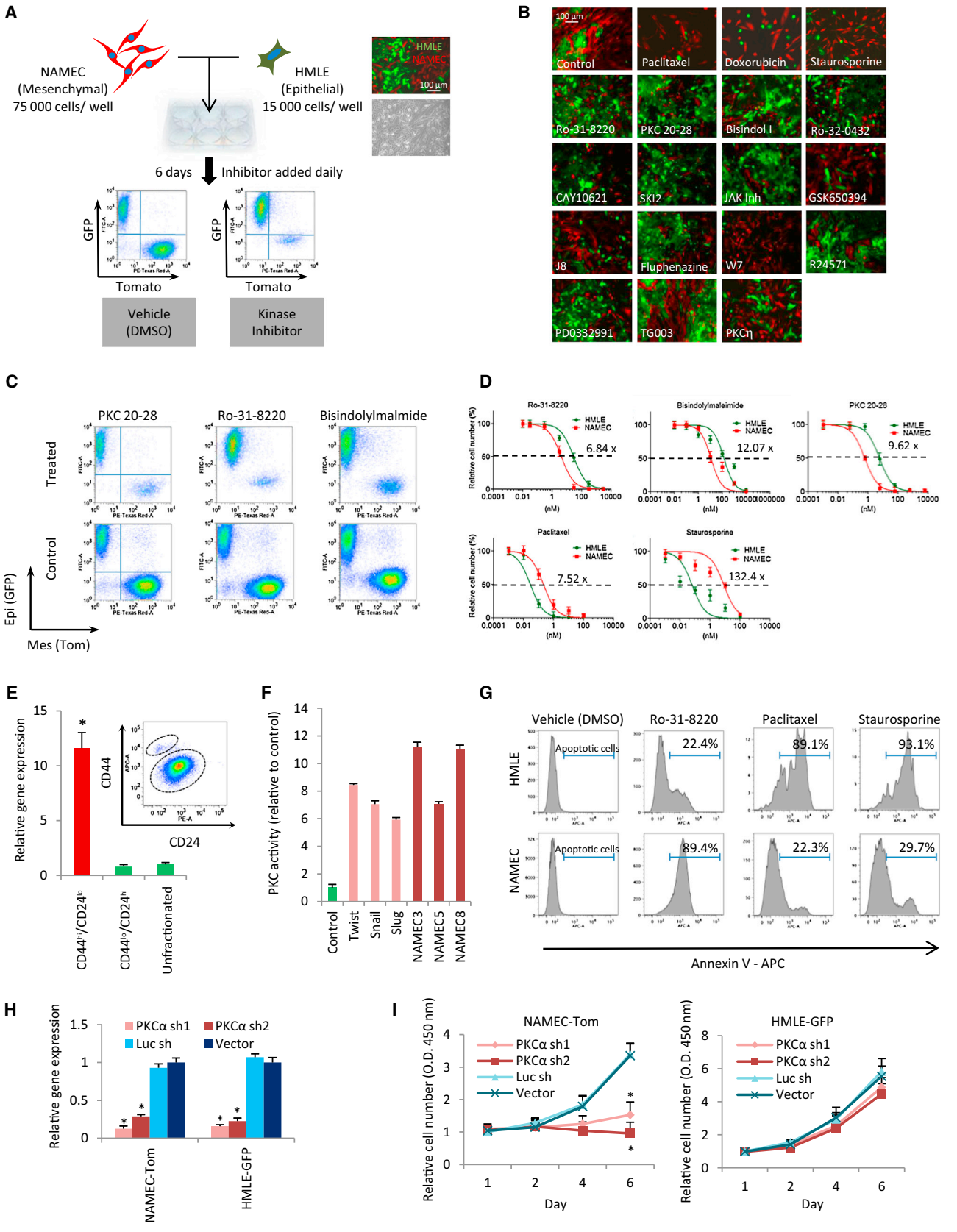

(legend on next page)

Depletion of Stem-like Cells by Select Kinase Inhibitors

To identify kinase inhibitors that selectively targeted mesenchymal-like cells bearing stem cell properties, we established a screen that measured the ability of candidate inhibitors to preferentially deplete mesenchymal NAMECs but not HMLE cells. We labeled one of the NAMEC lines (NAMEC8) with the tdTomato red fluorescent protein (NAMEC-Tom) and the HMLE cells with green fluorescent protein (HMLE-GFP). We then attempted to reconstitute certain stem cell and non-stem-cell interactions that might operate in vivo by mixing the two cell populations in culture in a 5:1 ratio (Figures 2A and S2A). We then challenged these cultures with a panel of kinase inhibitors. We initially targeted several protein kinases that were elevated in HMLE-Twist, HMLE-Snail, and HMLE-Slug cells and NAMECs relative to HMLE using of a panel of 15 commercially available kinase inhibitors (Figures 1C, S1B, and S2B). Figure 2B illustrates their effects on the proportion of surviving NAMEC-Tom and HMLE-GFP cells at the end of a 6-day treatment period. The numbers of viable cells were quantified with flow cytometry to determine the fraction of NAMEC-Tom or HMLE-GFP cells in inhibitor-treated populations relative to vehicle-treated controls.

The four inhibitors targeting PKCα (PKC 20-28, Ro-31-8220, Ro-32-0432, and bisindolylmaleimide I) showed a 6.8- to 12.1-fold lower lethal concentration (LC_{50}, 50%) against NAMEC-Tom cells relative to HMLE-GFP cells (Figures 2C and 2D). These findings were validated in three other NAMEC cell lines (Figures S2C and S2D). Because PKCα was also elevated in $CD44^{hi}/CD24^{lo}$ HMLE cells (Figure 2E), we tested whether these stem-like cells were sensitive to the inhibitors. Indeed, treatment of bulk HMLE cells with two different PKCα inhibitors reduced the $CD44^{hi}/CD24^{lo}$ cell compartment, whereas the $CD44^{lo}/CD24^{hi}$ population remained unaffected (Figure S2E).

Although total and phosphorylated PKCα were overexpressed in a variety of derived mesenchymal cells (Figure S2F), the phosphorylation status of PKCα is constitutive and not a useful indicator of its activity (Newton, 2001). Furthermore, active site inhibitors, such as bisindolylmaleimide, could paradoxically stabilize phosphorylated PKC (Cameron et al., 2009; Gould et al., 2011). Accordingly, we validated PKC enzymatic activity in these cells and found that the derived mesenchymal cells possessed on average 8.5-fold higher levels of total PKC activity relative to HMLE cells (Figure 2F).

The inhibitors targeting PKCη, CLK1, CDK6, and JAK1 also appeared to deplete NAMEC-Tom cells preferentially (Figure 2B). However, these agents were not included in subsequent studies because only a single inhibitor was available against each of these kinases, preventing us from controlling for possible off-target effects. In stark contrast to the effect of the pathway-specific inhibitors, three non-pathway-specific compounds, staurosporine, doxorubicin, and paclitaxel, preferentially depleted HMLE-GFP cells instead (Figures 2B and 2D). This supported previous observations that non-cell-state-specific inhibitors can enhance the representation of more aggressive cancer stem-like cells within heterogeneous cell populations following treatment (Creighton et al., 2009; Gupta et al., 2009).

To determine how PKCα inhibitors affected these more susceptible cell populations, we tested whether they induced apoptosis. The mixed cell populations were treated with Ro-31-8220 for 3 days; 89.4% of NAMEC-Tom cells underwent apoptosis in comparison to 22.4% of the HMLE-GFP cells (Figure 2G). Conversely, paclitaxel and staurosporine resulted in HMLE-GFP cell apoptosis, leaving NAMEC-Tom cells less affected.

Because it remained possible that the four PKCα inhibitors used in our analyses acted in an off-target manner, we depleted PKCα with shRNA (Figure 2H). Mixed NAMEC-Tom and HMLE-GFP cultures were infected with lentiviral shRNAs targeting PKCα and then seeded separately, after sorting for either Tom^+ or GFP^+ expression. Consistent with the use of chemical inhibitors, depletion of PKCα resulted in the substantial loss of NAMECs, whereas HMLE cells were less affected (Figure 2I). These observations confirmed the greater dependence on PKCα-regulated signaling networks in cells that have passed through an EMT program.

Conservation of Cell-State-Specific Features upon Oncogenic Transformation

To test whether neoplastic cells that have passed through an EMT program acquire a greater potential to generate CSCs, we ectopically expressed comparable levels of $H\text{-}RAS^{G12V}$ in NAMECs and HMLE cells (Figure 3A). As few as 500 of the resulting NAMEC-RAS cells, when implanted into NOD-SCID mice, were sufficient for tumor initiation in 6 out of 10 hosts, whereas

Figure 2. PKCα Inhibition Selectively Targets Cells that Have Undergone an EMT and Are Enriched for Stem Cell Properties

(A) This is the approach for testing kinase inhibitors to identify stem-cell-specific compounds. NAMEC-Tom and HMLE-GFP cells were comixed and seeded for 24 hr prior to daily inhibitor treatment. Viable cells were analyzed after 6 days by flow cytometry to determine the proportion of NAMEC-Tom or HMLE-GFP cells.

(B) The proportion of surviving NAMEC-Tom and HMLE-GFP cells is shown as visualized by fluorescence microscopy after 6 days of inhibitor treatment.

(C) Viable cell populations were analyzed by flow cytometry that segregated and counted NAMEC-Tom and HMLE-GFP cells after treatment with PKCα inhibitors. Cell numbers of each population were normalized to corresponding NAMEC-Tom or HMLE-GFP cells of DMSO-treated controls.

(D) Dose-response curves of NAMEC-Tom and HMLE-GFP cells treated with PKCα inhibitors, paclitaxel, or staurosporine are shown. The difference in LC_{50} between NAMEC-Tom and HMLE-GFP cells at each inhibitor is indicated. Curves for each cell type were generated using non-linear-regression curve fit with the variable slope model.

(E) Quantitative PCR for *PKCα* mRNA level in $CD44^{hi}/CD24^{lo}$, $CD44^{lo}/CD24^{hi}$, and unfractionated cell compartments of HMLE cells is shown.

(F) Levels of total PKC kinase activity in EMT-TF-induced HMLE and NAMEC cells relative to HMLE control cells are shown.

(G) Measurement of apoptosis by Annexin V-APC in mixed NAMEC-Tom and HMLE-GFP cells treated with Ro-31-8220 for 3 days is depicted.

(H) Quantitative PCR for validation of PKCα RNAi knockdown in NAMEC-Tom and HMLE-GFP cells 3 days after puromycin selection is shown. The asterisk (*) denotes a significant difference from the Luc sh control.

(I) Effects of PKCα RNAi on the growth kinetics of NAMEC-Tom and HMLE-GFP cells as measured by WST assay are shown. The asterisk (*) denotes a significant difference from the Luc sh control.

*$p < 0.05$. Data are presented as mean ± SEM. See also Figure S2.

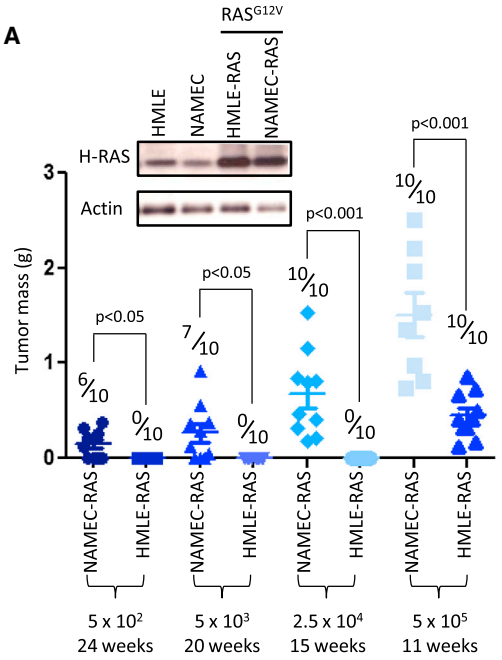

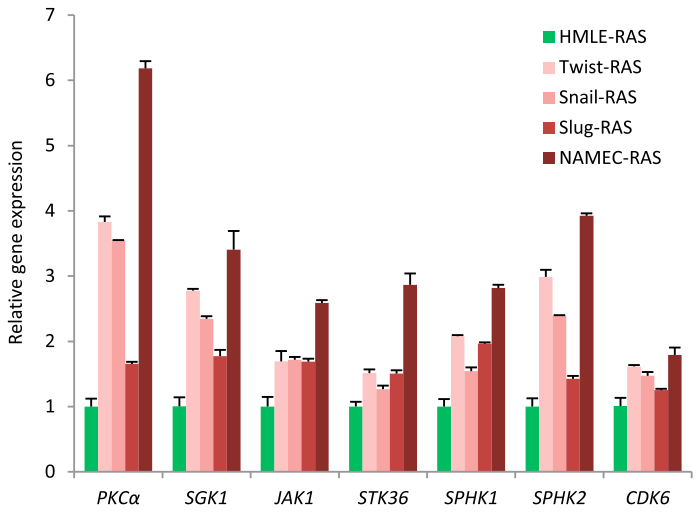

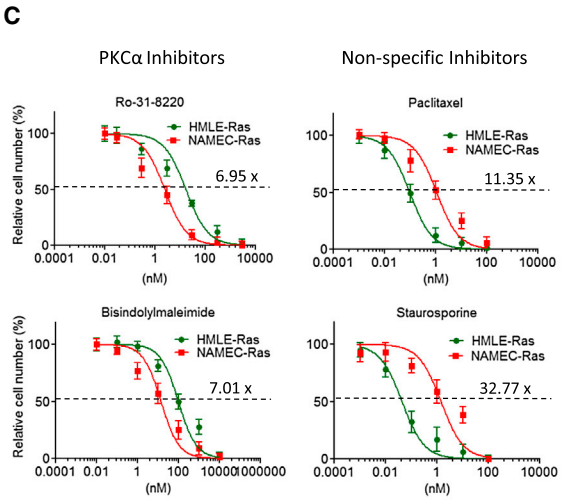

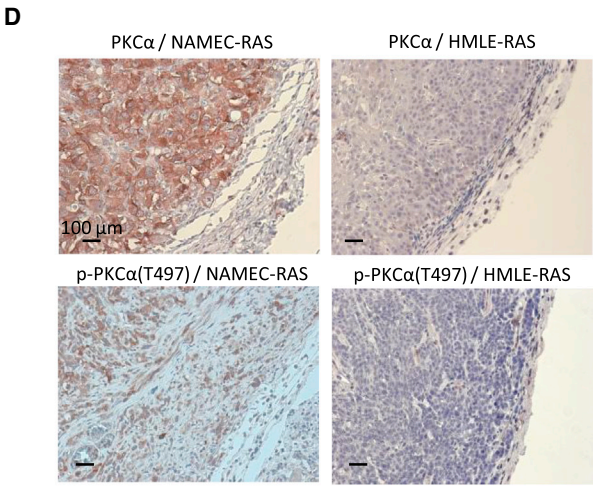

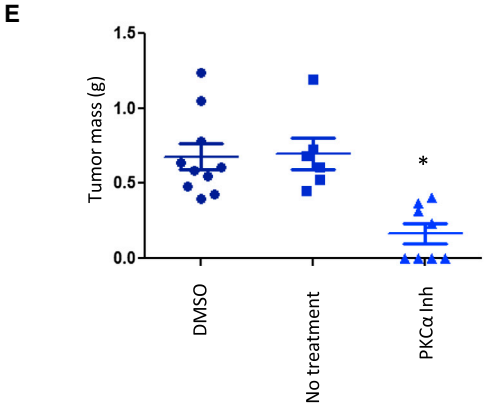

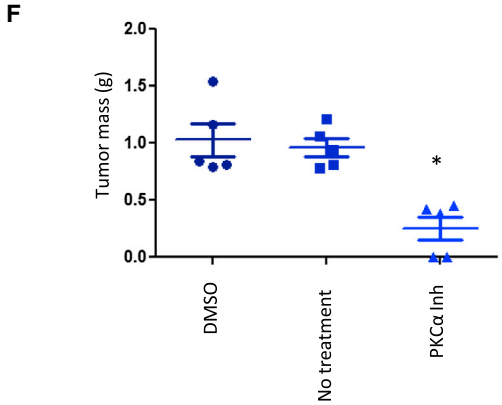

(legend on next page)

as many as 25,000 of the corresponding HMLE-RAS cells failed to form tumors (Figure 3A). Based on a limiting dilution assay, the frequency of CSCs was calculated to be approximately 1/2,314 for NAMEC-RAS and 1/463,783 for HMLE-RAS cells. Thus, transformation of preneoplastic stem cells expressing mesenchymal traits gave rise to CSCs far more efficiently than bulk epithelial cells.

To investigate whether PKCα inhibition would also preferentially affect CSC-enriched NAMEC-RAS cells, we first determined whether *PKCα* mRNA levels remained differentially regulated between NAMEC-RAS and HMLE-RAS cell populations. We found that the mRNA levels of *PKCα* and other kinase-encoding genes that were examined previously remained higher in NAMEC-RAS cells compared to the HMLE-RAS cells; this echoed the behavior of EMT-TF-induced mesenchymal cells that had been transduced with the RAS^{G12V} vector (Figure 3B). We then mixed NAMEC-RAS cells labeled with tdTomato (NAMEC-Tom-RAS) and HMLE-RAS cells labeled with GFP (HMLE-GFP-RAS), retested the effects of kinase inhibition, and found that NAMEC-Tom-RAS cells were more sensitive to PKCα inhibition relative to HMLE-GFP-RAS cells (Figure 3C). In contrast, NAMEC-Tom-RAS cells were more resistant to paclitaxel and staurosporine than were HMLE-GFP-RAS cells (Figure 3C). When these various transformed cell populations were implanted into NOD-SCID mice, NAMEC-RAS-derived tumors continued to express PKCα, but HMLE-RAS tumors did not (Figure 3D).

To assess the therapeutic utility of PKCα inhibitors, NAMEC-RAS cells were implanted in NOD-SCID mice and treated for 30 days with a daily intraperitoneal dose of either a PKCα inhibitor (Ro-31-8220) or a DMSO solvent control; additional control animals were left untreated. These dosages were well tolerated in mice and had no adverse effects after 30 days of treatment followed by 8 weeks of observation. Significant tumor burdens were observed after 15 weeks in all control-treated mice, whereas only four of eight mice treated with PKCα inhibitor formed tumors (Figure 3E). Hence, PKCα inhibition reduced tumor-initiating frequency and tumor growth of the CSC-enriched populations in vivo. We also examined whether PKCα inhibition would have any effect on the growth of already established tumors. Xenografted NAMEC-RAS tumors were allowed to reach approximately 2 mm in diameter (assessed by palpation) 4 weeks after implantation and then exposed to treatments. Tumors from control-treated mice reached ~1.03 g 6 weeks later, whereas those from PKCα-inhibitor-treated mice only weighed ~0.25 g (Figure 3F). These results demonstrated the therapeutic effects of PKCα inhibition on the continued growth of already-established tumors.

A Switch from EGFR to PDGFR Signaling Is Induced upon EMT

The greater reliance of CSCs on PKCα led us to question whether cells that have passed through an EMT respond to mitogenic and trophic signals differently from those that have not. We attempted to trace the sources of the upstream signals that might be responsible for activating PKCα and postulated that certain receptor tyrosine kinases induced by the EMT program might be involved. We speculated that the EGF receptor (EGFR) might activate PKCα in cells that had undergone an EMT because EGFR overexpression and amplification are positively associated with breast cancer progression (Carey et al., 2010). However, in mesenchymal cell populations, the expression of endogenous total and phosphorylated $EGFR^{Y1068}$ was reduced relative to HMLE cells (Figure 4A). Treatment of comixed NAMEC-RAS-Tom and HMLE-RAS-GFP cells with either of two EGFR inhibitors preferentially selected against HMLE-RAS-GFP cells (Figure 4B). Hence, the more epithelial, non-CSC-enriched populations depended more strongly upon sustained EGFR signaling than did the mesenchymal CSC-enriched cell populations.

We used proteome analysis to identify potential RTKs associated with an EMT and responsible for the activation of PKCα. The most differentially expressed RTK, exhibiting a 13-fold increase in representative peptides in HMLE-Twist cells relative to HMLE cells, was PDGFRβ (encoded by *PDGFRB*) (data not shown). In addition, mRNAs of *PDGFRA* (encoding PDGFRα) and *PDGFRB*, as well as their ligand *PDGFC*, were highly expressed in basal B subtype of breast cancer cell lines bearing mesenchymal properties but not in luminal-like cell counterparts bearing more epithelial features (Figure 4C). *PKCα* mRNA was also highly expressed in basal B, and not luminal-like, breast cancer cells (Figure 4C). This is consistent with the notion that basal-like tumors contain cells that behave as if they have undergone at least a partial EMT (Blick et al., 2008; Sarrió et al., 2008).

To determine whether PDGF autocrine signaling might be activated following an EMT, we surveyed the expression of

Figure 3. Cell-State-Specific Kinase Expression Is Conserved upon Oncogenic RAS^{G12V} Transformation and in CSCs

(A) Assessment of the tumorigenicity of NAMEC-RAS or HMLE-RAS cells injected subcutaneously into NOD-SCID mice at limiting dilutions of cells, as determined by tumor mass, is shown. Numbers indicate the frequency of tumor formation. Western blot indicates levels of RAS expression.

(B) Quantitative PCR for gene expression of selected kinases in HMLE-Twist-RAS, HMLE-Snail-RAS, HMLE-Slug-RAS, and NAMEC-RAS cells is shown relative to HMLE-RAS cells.

(C) Dose-response curves of NAMEC-Tom-RAS and HMLE-GFP-RAS cells treated with PKCα inhibitors, paclitaxel, or staurosporine are shown. Differential sensitivity to treatment at LC_{50} is indicated.

(D) Immunohistochemistry detection of total PKCα and p-$PKC\alpha^{T497}$ in sections of equivalent size (~0.3 g) NAMEC-RAS and HMLE-RAS tumors is depicted. NAMEC-RAS tumors were 15 weeks after inoculation of 2.5×10^4 cells, and HMLE-RAS tumors were 11 weeks after inoculation of 5×10^5 cells.

(E) Assessment of the tumorigenicity of subcutaneously xenografted NAMEC-RAS cells (5×10^4) in mice treated with daily intraperitoneal administration of the indicated agents, as determined by tumor mass, is shown. Treatments began on the same day as the cells were implanted. Tumors were collected 15 weeks post implantation.

(F) Assessment of the tumorigenicity of established NAMEC-RAS tumors following treatment with the indicated agents is shown. NAMEC-RAS cells (5×10^4) were subcutaneously xenografted in mice and allowed to reach approximately 2 mm in diameter after 4 weeks. Subsequently, mice were treated with daily intraperitoneal administration of the indicated agents for 30 days. Tumors were collected 6 weeks later and tumor masses were determined.

*$p < 0.005$. Data are presented as mean ± SEM.

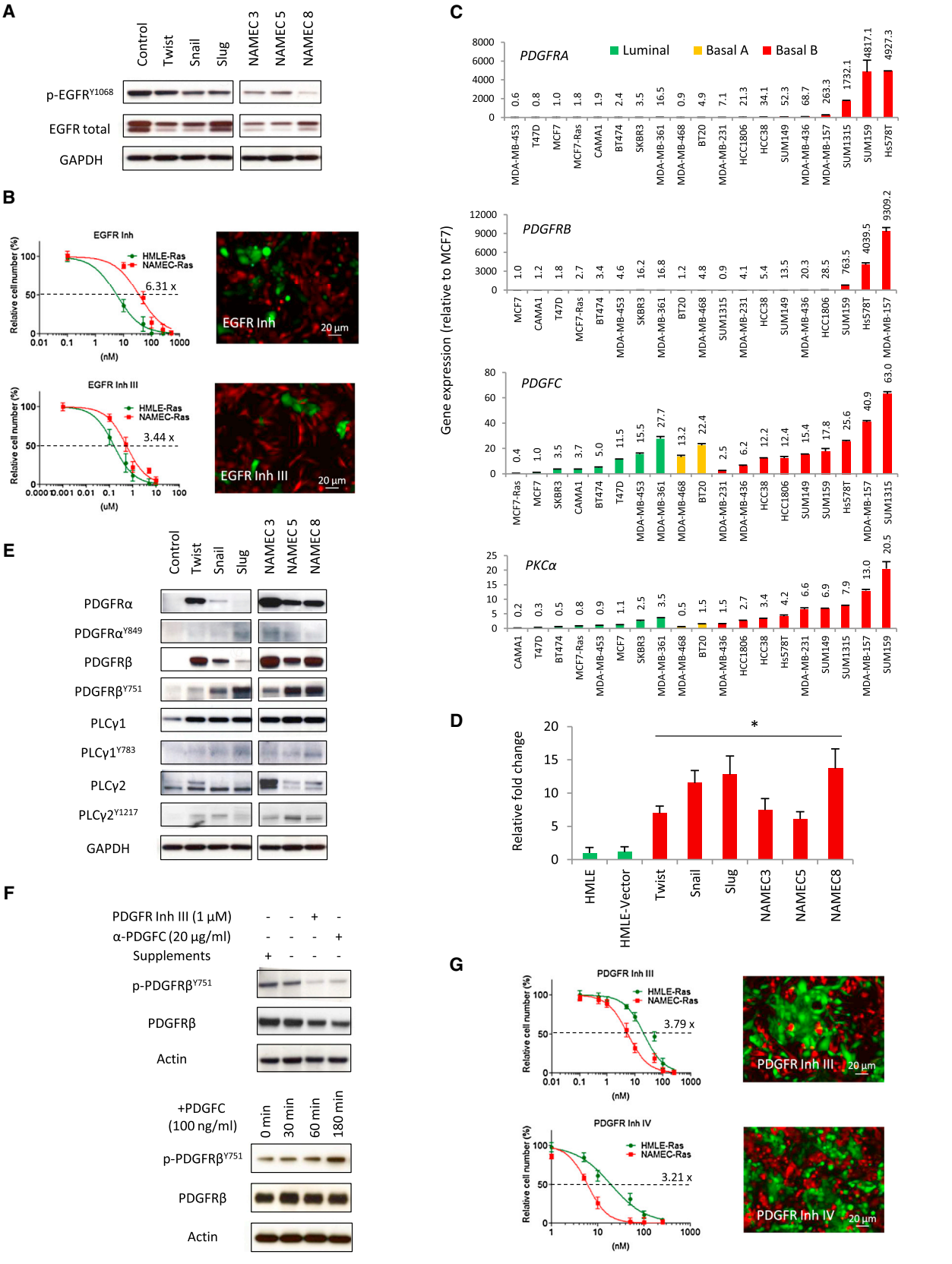

(legend on next page)

PDGFR ligands in the mesenchymal and epithelial cell populations. *PDGFA*, *PDGFB*, and *PDGFD* mRNAs were not expressed in either cell state (data not shown), indicating that only PDGFC could participate in such autocrine signaling. In mesenchymal cell populations, *PDGFC* mRNA was indeed upregulated (Figure 4D); total and phosphorylated PDGFRα/β proteins were also induced in these cells (Figure 4E). Additionally, *PDGFRA*, *PDGFRB*, and *PDGFC* mRNAs were upregulated specifically in the $CD44^{hi}/CD24^{lo}$ stem-cell-enriched subpopulation (Figure S3A).

We also monitored the activity of PDGFR in the mesenchymal cell populations. Culturing NAMECs for 24 hr in serum-free, growth-factor-depleted medium reduced phosphorylation of PDGFRβ modestly relative to NAMECs maintained in complete medium, whereas application of either a PDGFR-neutralizing antibody or a PDGFR pharmacologic inhibitor led to a 4.3- and 6.8-fold reduction, respectively, in p-PDGFRβ^{Y751} (Figure 4F). Conversely, the exposure of the growth-factor-depleted NAMECs to PDGFC resulted in increased phosphorylation of PDGFRβ (Figure 4F), whereas HMLE cells showed no response to PDGFC (data not shown). This provided further support for the specific activation of autocrine PDGF signaling activity following induction EMT.

Levels of phospholipase C γ 1 and 2 (PLCγ1 and PLCγ2) proteins, which are known to transduce signals from PDGFRα/β to PKCα (Rhee, 2001), were also elevated in the EMT-TF-transduced and NAMEC cells (Figure 4E). To examine whether PLCγ was activated by PDGFR, NAMECs were treated with either of two PDGFR inhibitors (PDGFR Inh III and PDGFR Inh IV). Levels of the two p-PLCγ1^{Y783} and p-PLCγ2^{Y1217} activated forms were reduced, whereas total PLCγ1 and PLCγ2 protein levels remained unaltered (Figure S3B). We next sought to determine whether PKCα activation was dependent on the observed activations of PDGFR and PLCγ, the latter of which activates PKCα through its production of diacylglycerol (Saito et al., 2002). Exposure of NAMECs to a PLCγ inhibitor (U73122) reduced total PKC enzymatic activity (Figure S3C). Likewise, pharmacologic inhibition of PDGFR in NAMECs reduced PKC activity (Figure S3C). Together, these results confirmed that PKCα activity operated downstream of PDGFR and depended on the actions of PLCγ.

Because PDGF autocrine signaling was activated in cells that had undergone an EMT, we reasoned that this might be important for their survival and that the inhibition of PDGFR could be useful for the selective killing of CSCs. Comixed NAMEC-Tom-RAS and HMLE-GFP-RAS cells were treated with each of these inhibitors. NAMEC-Tom-RAS cells exhibited a 3.2- to 3.8-fold lower LC_{50} for the PDGFR inhibitors tested relative to HMLE-GFP-RAS cells (Figure 4G). It thus appeared that the EMT, along with the acquisition of CSC-like traits, was accompanied by a downregulation of EGFR and concomitant upregulation of PDGFR, highlighting the preferential utilization of different signaling networks in different cellular states. We noted that a pharmacologic inhibitor that is completely specific to inhibition of PDGFRα/β is currently unavailable and the two PDGFRα/β inhibitors used here cross-inhibited c-KIT- and VEGFR-associated tyrosine kinases.

Cell-State-Dependent Utilization of c-FOS or FRA1 during EMT

We sought to elucidate the mechanism(s) through which PKCα acts to support the mesenchymal cell state and to identify downstream mediators of PKCα in cells that have undergone an EMT. We surveyed for PKCα substrates identified by others in various cellular contexts (Abate et al., 1991; Gruda et al., 1994; Kang et al., 2012) and focused on those upregulated together with PKCα expression during an EMT (Figure S4A). Among genes examined, *FOSL1* mRNA (encoding the FRA1 protein) was the most upregulated target of PKCα in the HMLE-Twist, HMLE-Snail, and HMLE-Slug cells. This prompted us to further examine the connection between PKCα and FRA1. Of note, we could not exclude the possible functional importance of other genes encoding PKCα substrates that were not transcriptionally upregulated.

FRA1 is a member of the FOS family of transcription factors that when phosphorylated downstream of PKCα signaling associate with members of the JUN family of transcription factors to form heterodimeric activator protein-1 (AP-1) complexes to transcriptionally regulate target gene expression (Abate et al., 1991). To confirm that FRA1 operated downstream of PKCα, NAMECs were treated with either of two PKCα inhibitors. Levels of p-FRA1^{S265} were strongly downregulated, whereas total FRA1 levels remained unchanged, indicating that FRA1 phosphorylation was indeed dependent on PKCα activity (Figure 5A).

We speculated that c-JUN (encoded by *JUN*) was a binding partner of FRA1 because our previous work demonstrated

Figure 4. EMT Induces a Switch from EGFR to PDGFR Signaling

(A) Western blots of total and p-EGFR^{Y1068} in the indicated EMT-TF-induced HMLE and NAMEC cells are shown. Samples were loaded and analyzed on the same blot.

(B) Dose-response curves (left) of the sensitivities of HMLE-RAS-GFP and NAMEC-RAS-Tom cells to EGFR inhibitors are shown. The difference in fold sensitivity between both cell types at LC_{50} is indicated. Representative immunofluorescent images are shown at the right.

(C) Quantitative PCR for *PDGFRA*, *PDGFRB*, *PDGFC*, and *PKCα* mRNA expression in breast cancer cell lines is shown. Numbers indicate fold change.

(D) Quantitative PCR for *PDGFC* expression in mesenchymal and epithelial cells. The asterisk (*) denotes a significant difference from HMLE or HMLE-vector; $p < 0.05$.

(E) Western blots of PDGFRα, PDGFRβ, PLCγ1, and PLCγ2, along with protein phosphorylation, in NAMECs and EMT-TF-induced cells are shown. Sample loading controls (GAPDH) were the same as Figure 4A. Samples were loaded and analyzed on the same blot.

(F) Shown is the western blot analysis of NAMECs cultured in the absence of growth supplements (bovine pituitary extract, EGF, hydrocortisone, and insulin) and treated with either a PDGFC-neutralizing antibody (20 μg/ml) or a PDGFR inhibitor (1 μM) (top), or upon exposure to PDGFC (100 ng/ml) (bottom). PDGFR activity is represented by the phosphorylation of PDGFRβ^{Y751}.

(G) Dose-response curves (left) of HMLE-RAS-GFP and NAMEC-RAS-Tom cells to PDGFR inhibitors are shown. The difference in fold sensitivity between both cell types at LC_{50} is indicated. Representative immunofluorescent images are shown at the right.

Data are presented as mean ± SEM. See also Figure S3.

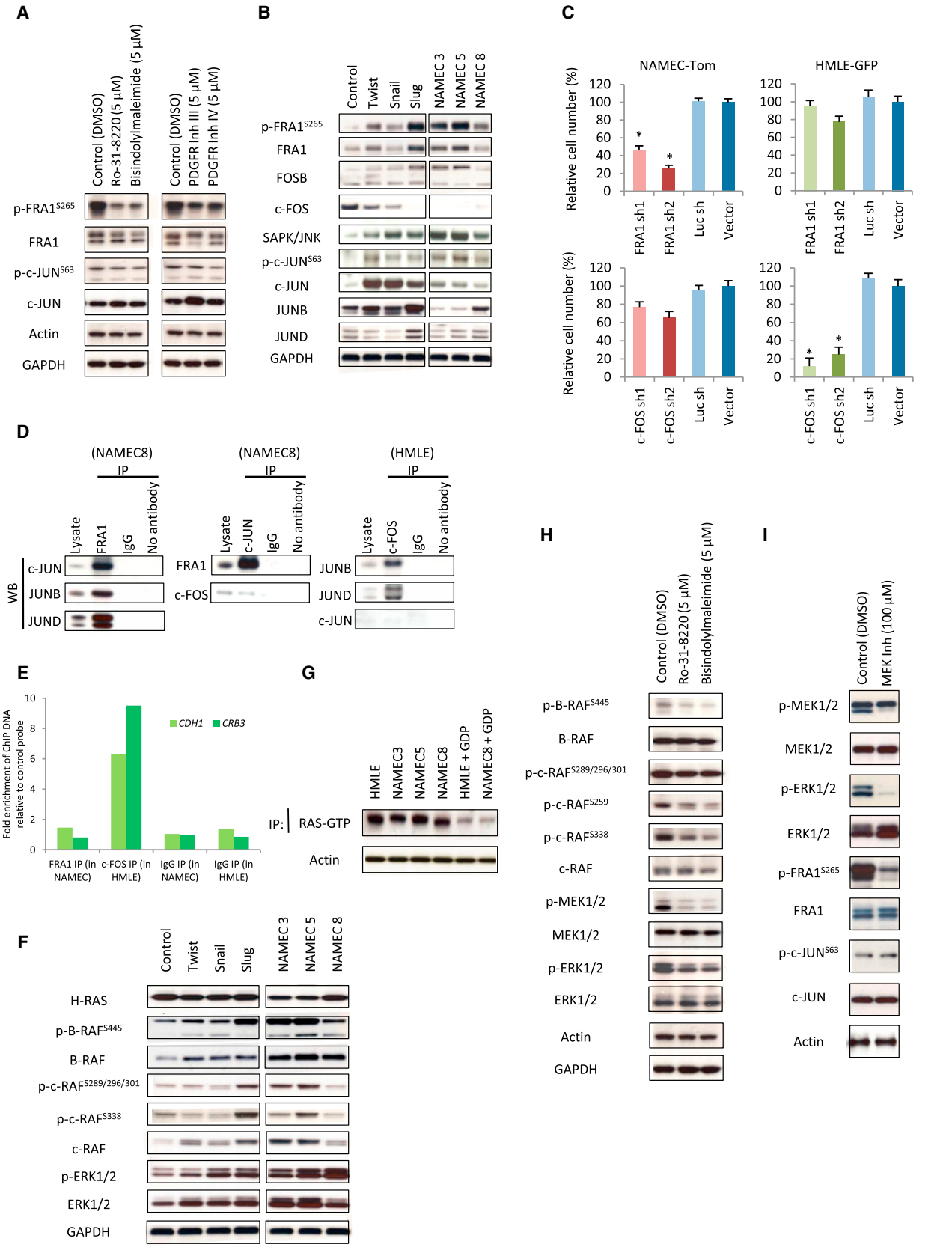

(legend on next page)

induction of c-JUN during passage through an EMT (Scheel et al., 2011). Indeed, we found that total and phospho-c-JUN^{S63} as well as the Jun N-terminal kinase (JNK), which is required for the activation of c-JUN, were upregulated in mesenchymal cell populations (Figures 5B and S4B). Other JUN family members, JUNB and JUND, did not exhibit consistent up- or downregulation following passage through an EMT, indicating that their expression was not cell-state dependent. Unexpectedly, c-FOS (encoded by *FOS*), which has been extensively documented as a partner of c-JUN (Eferl and Wagner, 2003), was downregulated during passage through an EMT (Figures 5B and S4B). Total and phospho-FRA1^{S265} levels, by contrast, were increased. Hence, epithelial and mesenchymal cells appeared capable of assembling AP-1 complexes, but of quite different composition in that FRA1 seemed to replace c-FOS as the partner of JUN following passage through an EMT.

We sought to understand the functional significance of the c-FOS-FRA1 molecular switch during the EMT. Knockdown of FRA1 with two independent shRNAs preferentially reduced NAMEC-Tom cell numbers but had a lesser impact on HMLE-GFP cells (Figures 5C and S4C). In contrast, HMLE-GFP cells were preferentially depleted upon c-FOS knockdown, whereas NAMEC-Tom cells were significantly less affected. This highlighted the cell-state-specific dependence on either c-FOS or FRA1 for maintaining cell viability (Figure 5C). We performed coimmunoprecipitation experiments to validate the formation of AP-1 complexes and the nature of their constituent subunits. In NAMECs, immunoprecipitation of FRA1 showed physical association with c-JUN, JUNB, and JUND (Figure 5D). In a reciprocal manner, pull-down of c-JUN demonstrated its interaction with FRA1 but not c-FOS (Figure 5D). The converse pattern was observed in HMLE cells, in which c-FOS strongly associated with JUNB and JUND but not c-JUN, which was downregulated in the epithelial state (Figure 5D). Furthermore, chromatin immunoprecipitation analyses revealed c-FOS binding to the promoters of genes encoding E-cadherin and Crumb3, two key epithelial proteins, in HMLE cells. The same promoters, however, were not bound by FRA1 in NAMECs, which did not express either protein (Figure 5E). Hence, during execution of the EMT program, there is a switch from the use of c-FOS to FRA1 as the preferred component of AP-1 transcription factor complexes.

Control of FRA1 Activation by ERK Signaling

We sought to uncover additional downstream targets of PKCα beyond FRA1 that might be crucial for supporting the EMT program. c-Raf is another substrate of PKCα that sustains activation of ERK signaling and helps to promote mesenchymal cell phenotypes (Kolch et al., 1993). Examination of proteins involved in the ERK pathway revealed increased expression of both total and phosphorylated levels of B-RAF, c-RAF, and ERK1/2 in the mesenchymal cell populations (Figure 5F).

Because ERK signaling is commonly controlled by RAS activity, we tested whether mesenchymal cells contained higher RAS expression or activated RAS than did epithelial cells. Interestingly, levels of total RAS and activated GTP-bound RAS were similar among epithelial and mesenchymal cell types (Figures 5F and 5G). This led us to propose that the enhanced ERK signaling in the mesenchymal cell state was primarily mediated by PKCα signaling rather than through the RAS-RAF pathway. To test this notion, we exposed NAMECs to PKCα inhibitors and found reduced p-c-RAF, p-MEK1/2, and p-ERK1/2 levels (Figures 5H and S4D). Inhibitors of PDGFR signaling, likewise, blunted ERK signaling as indicated by decreased p-c-RAF, p-MEK1/2, and p-ERK1/2 levels (Figure S4E). Hence, enhanced activity of ERK signaling during EMT was conferred in part by signaling through PDGFR and PKCα.

FRA1, which we showed earlier to be downstream of PKCα, has also been reported to serve as a direct substrate of p-ERK1/2 (Kakumoto et al., 2006). Thus, we speculated that the increased p-FRA1 activity in the mesenchymal cells could be further augmented by elevated ERK signaling. Accordingly, blockade of ERK1/2 phosphorylation with a MEK inhibitor in NAMECs decreased p-FRA1 levels but did not affect the levels of total FRA1 or p-c-JUN (Figure 5I), confirming that ERK1/2 signaling promoted the phosphorylation of FRA1. Together, these observations indicate that PKCα signaling in mesenchymal cells leads to activation of FRA1, downstream of both PKCα and ERK1/2.

Role of FRA1 in Tumor Initiation by Breast Cancer Cells

We sought to understand whether FRA1 might be functionally important for the subset of human breast cancer cells that exhibit mesenchymal traits. Accordingly, we depleted FRA1 by RNAi in

Figure 5. PDGFR Signaling Results in PKCα and ERK1/2 Activation that Induces FRA1

(A) Western blot analysis shows the effects of inhibiting PKCα (using Ro-31-8220 or bisindolylmalmide I) or PDGFRα/β (using PDGFR Inh III or PDGFR Inh IV) for 30 min on the phosphorylation status of FRA1 and c-JUN in NAMECs.

(B) Western blots of AP-1 family member subunits in epithelial and mesenchymal cell lines are shown. Samples were loaded and analyzed on the same blot.

(C) Relative cell number analyses of the effects of FRA1 or c-FOS knockdown on the viability of NAMEC-Tom and HMLE-GFP cells are shown. The asterisk (*) denotes a significant difference from vector control; $p < 0.05$. Data are presented as mean ± SEM.

(D) Western blots for proteins immunoprecipitated with FRA1 or c-JUN antibodies in NAMECs and with c-FOS antibody in HMLE cells are shown. Whole cell lysates were used as positive controls, whereas pull-down with IgG or without an antibody was performed as negative controls.

(E) Occupancy of c-FOS and FRA1 on the promoters of *CDH1* and *CRB3* (encoding Crumb3) is shown. A normalization probe for the non-enriched region is located within intron 1 (*CDH1*) or intron 3 (*CRB3*). Control ChIP was performed with an IgG antibody.

(F) Western blots of total and phosphorylated B-RAF, c-RAF, and ERK1/2 in TF-induced EMT and NAMEC cells are shown. Sample loading controls (GAPDH) were the same as in Figure 5B. Samples were loaded and analyzed on the same blot.

(G) The amount of GTP-bound Ras was compared between epithelial and mesenchymal cell states by immunoprecipitation with Raf-Ras Binding Domain (RBD) beads followed by blotting with a pan-Ras antibody. As a negative control, lysates were treated with GDP, which blocked the ability of Ras to bind Raf-RBD beads. β-actin from whole-cell lysate (prior to IP) was used as a loading control.

(H) Western blots of phosphorylated proteins of B-RAF, c-RAF, MEK1/2, and ERK1/2 in NAMEC cells following treatment with PKCα inhibitors for 30 min are shown.

(I) Western blots of p-FRA1 levels in NAMEC cells following MEK inhibition for 30 min are shown.

See also Figure S4.

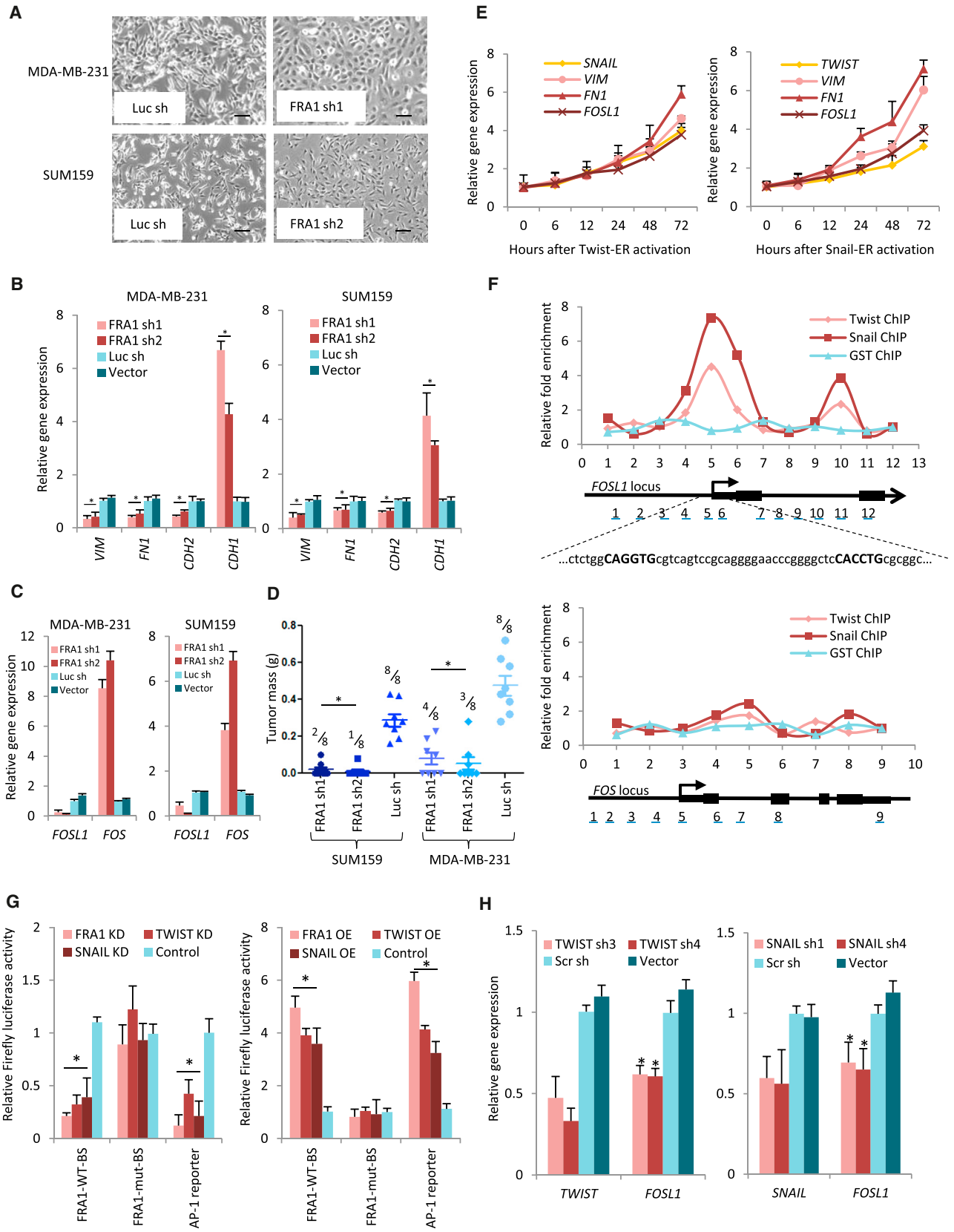

(legend on next page)

two basal-like (basal B) breast cancer cell lines, MDA-MB-231 and SUM159, both of which do not express HER2, estrogen receptor (ER), or progesterone receptor (PR). In both cell lines, FRA1 depletion resulted in a morphologic response resembling a mesenchymal-epithelial transition (MET), in which otherwise mesenchymal-like cancer cells formed cobblestone sheets resembling those assembled by epithelial cells (Figure 6A). The loss of *VIM*, *FN1*, and *CDH2* mRNA expression accompanied by the gain of *CDH1* mRNA expression was observed (Figure 6B). Moreover, in both cell lines depleted of FRA1, *FOS* mRNA expression, which we had previously associated with the epithelial cell phenotype, was strikingly increased (Figure 6C).

FRA1 knockdown did not significantly affect proliferation of MDA-MB-231 or SUM159 cells in vitro (Figure S5A). However, FRA1-depleted cells formed tumors with a reduced frequency and were a substantially smaller size relative to shRNA controls when xenografted into female NOD-SCID mice (Figure 6D). In contrast, depletion of FRA1 in two luminal-like, hormone-receptor-positive (ER^+/PR^+) breast cancer cell lines, MCF7-Ras and T47D, did not affect their proliferation, expression of EMT-associated markers, tumor formation, or tumor growth (Figures S5A–S5C). These observations suggested that FRA1 was important for the tumorigenic potential of breast cancer cells forming basal-like or triple-negative tumors but not those forming luminal tumors.

This led us to speculate that FRA1 expression might be restricted to the more mesenchymal, CSC-enriched compartments within basal-like human breast tumors. Previous studies have shown that purified $CD44^+$ or protein C receptor-positive ($PROCR^+$) cells tend to be enriched for CSCs in primary human tumors, whereas the $CD24^+$ fraction was depleted of these cells (Al-Hajj et al., 2003; Shipitsin et al., 2007). Both $CD44^+$- and $PROCR^+$-purified cells also demonstrated elevated mRNA expression of *VIM* (403×), *FN1* (48×), and *TWIST* (6.6×) (Shipitsin et al., 2007). Thus, we further analyzed the expression of *FOSL1* and *FOS* in these $CD44^+/PROCR^+$ or $CD24^+$ cells isolated from human tumors (Shipitsin et al., 2007). Across multiple specimens, *FOSL1* was upregulated in the $CD44^+/PROCR^+$ fraction, whereas *FOS* was elevated in the $CD24^+$ fraction (Figure S5D), providing additional support that *FOSL1* expression is associated with CSC-enriched $CD44^+$ populations bearing mesenchymal properties.

Effects of the Twist and Snail EMT-TFs on FRA1 Expression

The increased expression of FRA1 in the EMT-TF-induced mesenchymal cells and NAMECs correlated closely with the abundance of several EMT-TFs, suggesting that the latter might directly induce *FOSL1* mRNA expression. To test this notion, we fused ER to either Twist or Snail (HMLE-Twist-ER and HMLE-Snail-ER) (Mani et al., 2008) and demonstrated that activation of Twist or Snail upon tamoxifen exposure led to increased levels of *FOSL1* mRNA in a time-dependent manner (Figure 6E). We next assessed using chromatin immunoprecipitation (ChIP) whether Twist and Snail bound at the *FOSL1* promoter and could detect their binding at the transcription start site and within the first intron of *FOSL1* (Figure 6F). These regions contained E-box motifs (CANNTG), which Twist and Snail are known to bind. In contrast, the promoter of *FOS* was only weakly enriched for Twist and Snail binding (Figure 6F). Together, these data suggested that *FOSL1* was a direct target of Twist and Snail.

To determine whether the ability of FRA1 to drive gene transcription was dependent on the expression of EMT-TFs, we utilized a luciferase reporter containing the sequence of a previously reported FRA1-bound gene promoter (FRA1-wild-type binding site: FRA1-WT-BS) as well as a mutant FRA1 binding construct (FRA1-mut-BS) (Stinson et al., 2011). In NAMECs, knockdown of FRA1 abrogated luciferase activity of the FRA1-WT-BS but not FRA1-mut-BS (Figure 6G, left). Similarly, knockdown of TWIST or SNAIL diminished FRA1-dependent expression of the FRA1-WT-BS reporter (Figure 6G, left). *FOSL1* mRNA expression was also reduced upon either TWIST or SNAIL knockdown (Figure 6H).

In a reverse experiment, we overexpressed FRA1 in the NAMEC11 cell line, which had undergone a partial EMT. Overexpression of FRA1 induced FRA1-WT-BS but not FRA1-mut-BS luciferase activity (Figure 6G, right). Likewise, Twist and Snail overexpression in these cells was able to induce transcription of the FRA1-WT-BS reporter (Figure 6G, right). The wild-type AP-1 reporter containing tandem repeats of AP-1 response element was used as a positive control (Figure 6G). Therefore, these various lines of evidence confirmed that *FOSL1* levels were transcriptionally regulated by two master EMT-TFs and in a direct manner.

To demonstrate that FRA1 plays a functionally significant role downstream of EMT-TFs, we activated Twist or Snail in

Figure 6. FRA1 Is a Transcriptional Target of Twist and Snail that Is Indispensible for Tumorigenicity of Basal-like Breast Cancer Cells

(A) Phase contrast images show the morphology of MDA-MB-231 or SUM159 cells after FRA1 knockdown for 10 days. Scale bar: 40 μm.

(B) Quantitative PCR for gene expression of mesenchymal markers in FRA1-depleted cells is shown. The asterisk (*) denotes a significant difference from Luc sh.

(C) Quantitative PCR for gene expression of *FOS* and *FOSL1* after FRA1 knockdown in MDA-MB-231 and SUM159 cells is shown.

(D) Assessment of the tumorgenicity of cancer cells following FRA1 knockdown is shown. Subcutaneously, 1×10^6 MDA-MB-231 or SUM159 cells were implanted into female NOD-SCID mice, tumors were extracted after 4 weeks, and tumor masses were determined. Numbers indicate the frequency of tumor formation. The asterisk (*) denotes a significant difference from Luc-sh-derived tumors.

(E) Changes in gene expression of EMT markers in Twist-ER and Snail-ER cells after the addition of 4-OHT are depicted. Cells were exposed to 4-OHT for the duration examined.

(F) Occupancy of Twist and Snail on the *FOSL1* or *FOS* promoter is shown. Binding enrichment was normalized to input DNA and plotted relative to probe 12 (*FOSL1*) or probe 9 (*FOS*).

(G) Effect of Twist and Snail on FRA1-reporter luciferase activity is shown. Firefly luciferase was normalized against SV40-*Renilla*-luciferase transfection control and the values were compared to control Scr sh or vector overexpression. The asterisk (*) denotes a significant difference from Scr sh or the vector control; n = 6.

(H) This is the quantitative PCR for *FOSL1* expression after Twist or Snail knockdown in NAMECs. The asterisk (*) denotes a significant difference from vector control.

*$p < 0.05$. Data are presented as mean ± SEM. See also Figure S5.

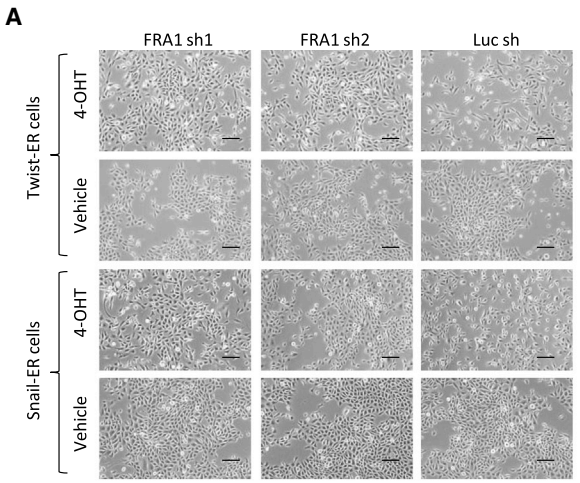

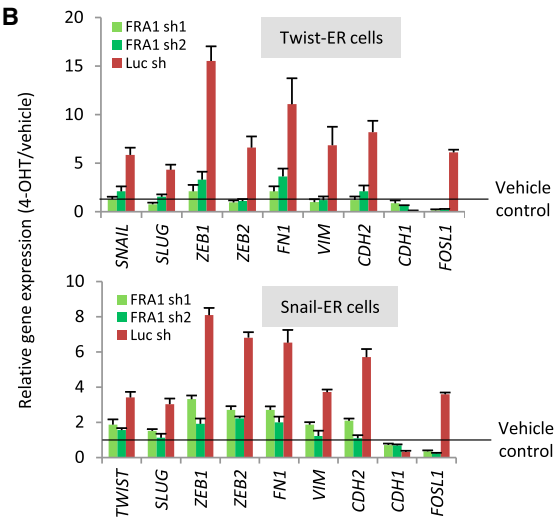

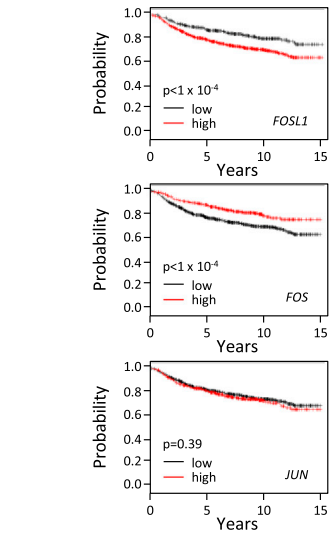

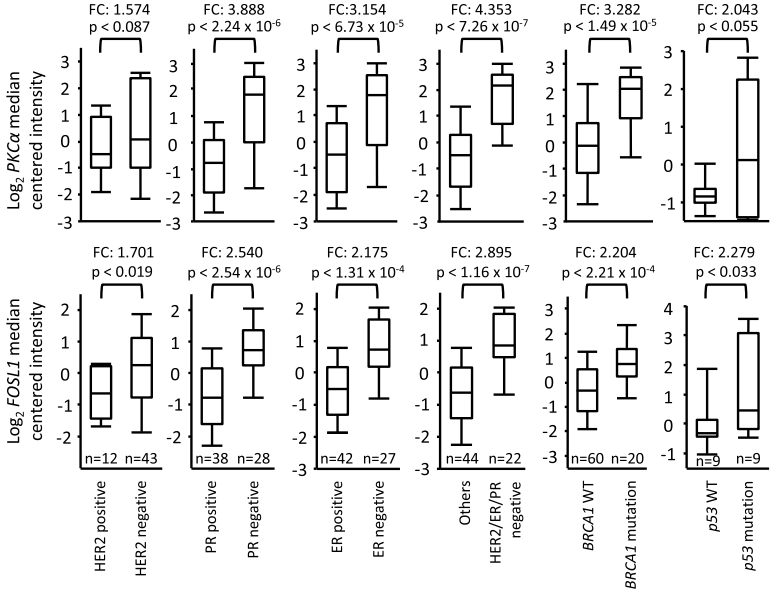

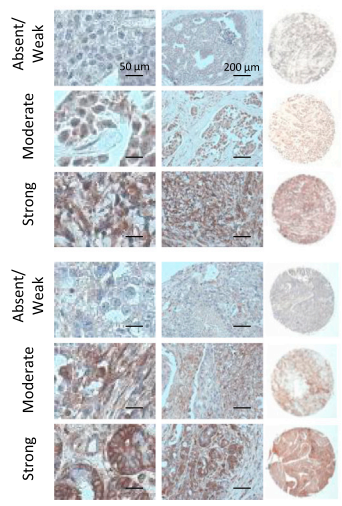

FRA1

	Absent/ Weak	Moderate	Strong
Grade 1	39	7	1
Grade 2	45	9	3
Grade 3	18*	23*	15*
Normal	26	0	1

PKCα

	Absent/ Weak	Moderate	Strong
Grade 1	28	17	3
Grade 2	27	24	6
Grade 3	19	21	16*
Normal	23	3	1

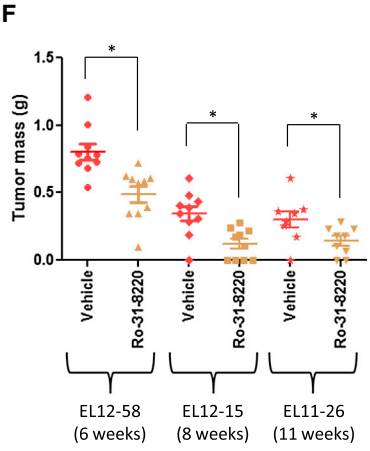

(legend on next page)

HMLE-Twist-ER or HMLE-Snail-ER cells in the presence or absence of two different FRA1 shRNAs and assessed the ability of these cells to transit into the mesenchymal state. HMLE-Twist-ER and HMLE-Snail-ER cells that expressed control shRNA underwent an EMT within 1 week after 4-OH-tamoxifen exposure (Figures 7A and 7B). However, FRA1-depleted cells were blocked in their ability to undergo an EMT upon Twist or Snail activation and retained their epithelial phenotype (Figures 7A and 7B). These observations reinforced our conclusion that FRA1 acts as an effector of the EMT program that is required for its execution.

Relevance of FRA1 and PKCα Expression to Clinical Breast Cancer

The functional significance of FRA1 in mediating cell-state transition and in maintaining CSCs led us to wonder whether its expression might also be relevant to clinical breast cancer. We speculated that *FOSL1* expression was restricted to basal B and triple-negative breast cancer (TNBC) tumors and cell lines because these bear strong molecular hallmarks of cells that have activated an EMT program (Shipitsin et al., 2007). These subtypes are also thought to contain a high representation of CSCs, thereby favoring relapse, metastasis, and poor overall survival. Indeed, *FOSL1* mRNA levels, but not those of other AP-1 subunits, were elevated in the basal B subtype of breast cancer cell lines surveyed, whereas *FOSL1* mRNA levels were reduced in the basal A cell lines and were essentially undetectable in all luminal subtype cell lines (Neve et al., 2006) (Figure S6A).

From a compendium of clinical data sets, we observed high *FOSL1* expression significantly correlated with poor distant metastasis-free survival (DMFS), whereas high *FOS* or *FOSB* expression associated with better survival (Figures 7C and S6B). The expression levels of other AP-1 subunits did not predict patient outcome (Figure S6B). Additionally, higher *PKCα* and *FOSL1* mRNA expression was significantly associated with $HER2^-$, ER^- or PR^- status, as well as with triple-negative tumors (Figure 7D). Their expression was also elevated in tumors bearing *BRCA1* mutations and in breast cancer cell lines containing *p53* mutations (Figure 7D). Moreover, *FOSL1*, *PDGFRA*, and *PDGFRB* mRNAs were more highly expressed in the claudin-low subtype of breast cancer that is thought to express the most mesenchymal properties (Figure S6C).

To exclude the possibility that *FOSL1* mRNA expression was derived from infiltrating stromal cells, we examined its protein expression in breast tumor microarrays derived from patients whose tumors had been scored for tumor grade. Moderate-to-strong nuclear FRA1 staining was present predominantly in the neoplastic cells of Grade 3 tumors that were typically hormone receptors negative but far less commonly in Grade 1 and Grade 2 tumors or in the normal mammary epithelium (Figure 7E). A similar trend could be observed with cytoplasmic and membrane-localized PKCα in which moderate-strong staining was most common in Grade 3 tumors relative to Grade 1 and Grade 2 tumors (Figure 7E). Taken together, these results reinforced the notion that FRA1, along with PKCα, functions as an important mediator of the behavior of aggressive basal-like and TNBCs.

In light of the findings that PKCα inhibitors, administered systemically, could inhibit the growth of breast cancer cells bearing mesenchymal traits and the observation that triple-negative breast tumors tend to express elevated levels of PKCα, we tested whether PKCα inhibition could be useful therapeutically against patient-derived tumor samples. We generated three patient-derived breast cancer xenografts from triple-negative tumors (EL12-58, EL12-15, and EL11-26) that had been serially passaged in NOD-SCID mice following their removal from patients. We then transplanted these tumor fragments orthotopically into a fresh set of female NOD-SCID mice and, on the same day, subjected them to either a PKCα inhibitor or vehicle control that was administered intraperitoneally daily for 6 weeks. With all three xenograft lines, tumors that formed in the PKCα-inhibitor-treated mice were consistently smaller (EL12-15: 65.7%, EL11-26: 53.3%, and EL12-58: 39.5%) than the control group (Figure 7F). Thus, inhibition of PKCα appeared to be a potentially useful strategy for targeting triple-negative breast tumors.

DISCUSSION

We and others have argued previously that effective treatment of carcinomas depends upon the elimination of minority CSCs in addition to the majority non-CSC cells in these tumors (Creighton et al., 2009; Dalerba et al., 2007; Gupta et al., 2009). This led us to exploit the observation that the EMT program generates cells that are enriched for stem cell and CSC properties to identify signaling networks that are preferentially utilized in the cellular products of an EMT (Figure 8). Our present findings demonstrate that PKCα is a central regulatory node activated by PDGFR in CSC-enriched populations. Although PKCα has been implicated in promoting cancer progression (Griner and Kazanietz, 2007;

Figure 7. FRA1 Is a Gatekeeper of the EMT Program and Is Clinically Correlated with Basal-like or Triple-Negative Breast Tumors

(A) Phase contrast images show the morphology of Twist- or Snail-induced EMT cells after FRA1 depletion. Scale bar: 40 μm.

(B) Quantitative PCR for gene expression of EMT-associated mRNAs in Twist-ER and Snail-ER cells following FRA1 knockdown after 7 days of 4-OHT exposure is shown.

(C) Kaplan-Meier plots of distant metastasis-free survival of breast cancer patients. Patient groups were separated based on *FOSL1* (top), *FOS* (middle), or *JUN* (bottom) mRNA expression.

(D) Microarray meta-analyses of *PKCα* and *FOSL1* mRNA expression in human primary breast cancer tumor subtypes (Waddell et al., 2010) and in breast cancer cell lines bearing *p53* mutation (Neve et al., 2006) are shown.

(E) Immunohistochemistry analyses of human breast cancer samples for PKCα and FRA1 protein expression in breast tumors with different grades are shown. Representative staining results are shown at the left. The numbers of graded tumors or normal tissues that were classified based on FRA1 or PKCα expression are depicted at the right. The asterisk (*) denotes a significant difference from Grade 1, Grade 2, or normal specimens.

(F) Effects of PKCα inhibitor administration (5 mg/kg/day) on the growth of patient-derived breast tumor xenografts in NOD-SCID mice are shown. Treatment was initiated immediately following implantation and continued for 5 weeks; tumor masses were then determined. The asterisk (*) denotes a significant difference from the vehicle.

*$p < 0.05$. Data are presented as mean ± SEM. See also Figure S6.

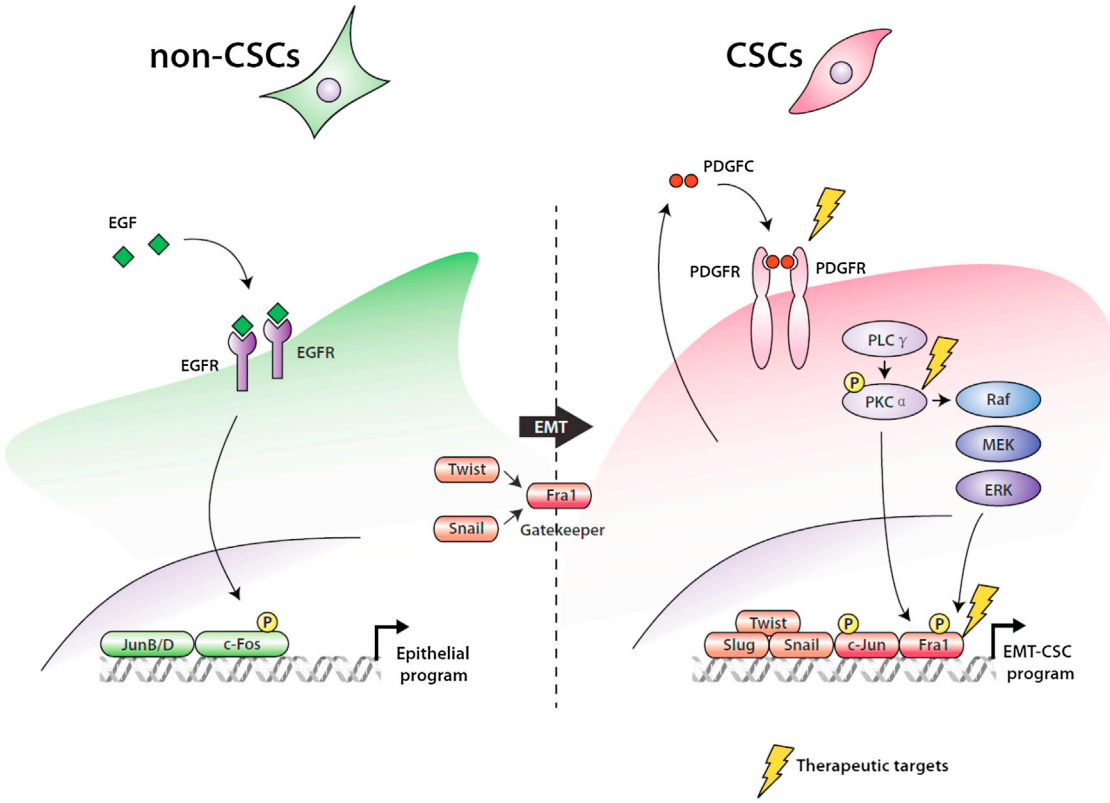

Figure 8. Scheme Depicting the Differential Utilization of Signaling Networks between Non-CSCs and CSCs upon the Activation of an EMT Program

Lønne et al., 2010), its connection to cell-state transitions and CSCs has been unclear. As a proof-of-principle, we showed that the pharmacologic inhibition of PKCα can target breast CSCs selectively and that clinically effective compounds inhibiting PKCα may prove therapeutically useful for treating certain breast tumors.

The selective dependence of the epithelial versus mesenchymal MECs on the function of EGFR and PDGFR is clinically relevant because EGFR inhibitors are being tested in clinical trials or in clinical use but often are resulting in limited clinical responses (Carey et al., 2010). Several studies have pointed out that such inhibitors enrich for CSCs and can lead to the outgrowth of more aggressive, chemotherapy-resistant tumor cell populations (Buck et al., 2007; Thomson et al., 2005). These studies suggest that the presence of epithelial- and mesenchymal-like carcinoma cells within tumors requires the elimination of both cell types.

The EMT program is initially required for invasion and dissemination of tumor cells, whereas MET has been demonstrated to promote colonization and metastatic outgrowth (Ocaña et al., 2012; Tsai et al., 2012). An increasing number of observations suggest that both tumor initiation and metastatic outgrowth depend on coexisting epithelial and mesenchymal subpopulations; conversely, tumors containing exclusively one or the other subpopulation appear to be poorly suited in enabling both of these processes (Brabletz, 2012; Celià-Terrassa et al., 2012; Ocaña et al., 2012). This implies that although the inhibition of cancer cells bearing a mesenchymal phenotype could be useful for preventing tumor initiation and/or dissemination, such a therapeutic strategy needs to be complemented with treatments that target already-established metastases and their complements of non-CSC epithelial cells. Moreover, the EMT should be viewed as generating a spectrum of phenotypic states depending on the extent to which this program is completed by epithelial cells, and partial completion of this program may be essential for the formation of CSCs and thus the founding of metastases. Future work will require more detailed measurements of the extent to which the various intermediate states depend on the epithelial versus mesenchymal signaling circuits described here.

Our initial efforts to distinguish molecular features between mammary CSCs and non-CSCs have led to the identification of kinase inhibitors that may be useful in preclinical models of human breast cancer. We speculate that the EMT program may also be adopted by other carcinoma cell types to drive tumor progression and metastasis. If so, the approach used to identify therapeutic compounds and pathways unique to mammary carcinoma CSCs described here may be extended to target CSCs present in the tumors arising from other epithelial tissues.

EXPERIMENTAL PROCEDURES

Kinase Inhibitor Screen

Kinase inhibitors and other biochemicals were obtained from sources listed in the Supplemental Information. To set up the screen, 75,000 NAMEC-Tom

and 15,000 HMLE-GFP cells were seeded into each well of a 6-well tissue culture plate. The following day, fresh media containing inhibitors were added. For control treatment, DMSO was added. Fresh media containing inhibitors were replaced daily during the 6-day period. For analysis, cells were trypsinized and flow cytometry was performed to analyze the proportion of surviving cells relative to DMSO-treated control for NAMEC-Tom or HMLE-GFP cells. To test the effects of these inhibitors on CSCs and non-CSCs, NAMEC-RAS-Tom and HMLE-RAS-GFP were used in similar comixed experiments.

Cell Lines and Cell Culture

HMLE cells and NAMECs were maintained in MEGM (Lonza). Other commonly used breast cancer cell lines are listed in Supplemental Information. HMLE were generated from HMECs immortalized using retroviral vectors to express the catalytic subunit of the human telomerase enzyme, hTERT, and the SV-40 Large T antigen. NAMECs were isolated based on the observation that mesenchymal cells were less adherent than epithelial cells to tissue culture surfaces. HMLE cells were grown to 50% confluency, followed by differential trypsinization for 1 min with 0.05% trypsin. Detached cells were collected and replated at approximately 200 cells per well of a 24-well plate. Upon expansion, wells were screened for populations with a mesenchymal phenotype that could be stably propagated.

Gene Expression Microarray and Analyses

Total RNA was extracted and expression profiling of coding genes was carried out using Illumina HumanRef-8 v2 BeadArrays. Gene expression data from Illumina array are normalized by quantile normalization. Differential genes are called using LIMMA with $p < 0.05$ and fold change > 1.2.

Patient-Derived Breast Cancer Xenograft Establishment and Therapy

Primary human breast cancer samples were obtained from the Dana-Farber Cancer Institute with patients' consent and institutional review board approval. These samples were subsequently deidentified to protect patient confidentiality. Patient-derived breast tumor fragments (approximately 3 × 1 × 1 mm) were inserted bilaterally into the inguinal mammary fat pads of 6- to 8-week-old NOD-SCID-IL2Rγc$^{-/-}$ female mice for initial establishment of tumors within 2 hr of surgery and subsequently expanded in NOD-SCID mice once established. Established TNBC tumors (EL12-15, EL12-58, and EL11-26) were implanted into cohorts of 6- to 8-week-old female NOD-SCID mice. Treatment was initiated at the time of tumor implantation and the mice were randomized into two groups: vehicle (10% DMSO in saline) and treatment (Ro-31-8220, 5 mg/kg/day intraperitoneally). Tumors were collected and weighed after 6, 8, or 11 weeks. All research involving animals complied with protocols approved by the MIT Committee on Animal Care.

ACCESSION NUMBERS

Microarray data are deposited in the NCBI GEO repository with accession number GSE43495.

SUPPLEMENTAL INFORMATION

Supplemental Information includes Supplemental Experimental Procedures, six figures, and one table and can be found with this article online at http://dx.doi.org/10.1016/j.ccr.2013.08.005.

ACKNOWLEDGMENTS

We thank Tsukasa Shibue for helpful comments and Tom DiCesare for illustrations. This research was supported by grants from the Breast Cancer Research Foundation, National Cancer Institute Program (P01-CA080111), and National Institutes of Health (R01-CA078461). R.A.W. is an American Cancer Society and Ludwig Foundation professor. W.L.T. is supported by the MIT Ludwig Center for Molecular Oncology and the Agency for Science, Technology and Research (Singapore).

Received: December 26, 2012
Revised: May 3, 2013
Accepted: August 6, 2013
Published: September 9, 2013

REFERENCES

Abate, C., Marshak, D.R., and Curran, T. (1991). Fos is phosphorylated by p34cdc2, cAMP-dependent protein kinase and protein kinase C at multiple sites clustered within regulatory regions. Oncogene *6*, 2179–2185.

Ailles, L.E., and Weissman, I.L. (2007). Cancer stem cells in solid tumors. Curr. Opin. Biotechnol. *18*, 460–466.

Al-Hajj, M., Wicha, M.S., Benito-Hernandez, A., Morrison, S.J., and Clarke, M.F. (2003). Prospective identification of tumorigenic breast cancer cells. Proc. Natl. Acad. Sci. USA *100*, 3983–3988.

Blick, T., Widodo, E., Hugo, H., Waltham, M., Lenburg, M.E., Neve, R.M., and Thompson, E.W. (2008). Epithelial mesenchymal transition traits in human breast cancer cell lines. Clin. Exp. Metastasis *25*, 629–642.

Brabletz, T. (2012). To differentiate or not—routes towards metastasis. Nat. Rev. Cancer *12*, 425–436.

Buck, E., Eyzaguirre, A., Barr, S., Thompson, S., Sennello, R., Young, D., Iwata, K.K., Gibson, N.W., Cagnoni, P., and Haley, J.D. (2007). Loss of homotypic cell adhesion by epithelial-mesenchymal transition or mutation limits sensitivity to epidermal growth factor receptor inhibition. Mol. Cancer Ther. *6*, 532–541.

Cameron, A.J., Escribano, C., Saurin, A.T., Kostelecky, B., and Parker, P.J. (2009). PKC maturation is promoted by nucleotide pocket occupation independently of intrinsic kinase activity. Nat. Struct. Mol. Biol. *16*, 624–630.

Carey, L., Winer, E., Viale, G., Cameron, D., and Gianni, L. (2010). Triple-negative breast cancer: disease entity or title of convenience? Nat Rev Clin Oncol *7*, 683–692.

Celià-Terrassa, T., Meca-Cortés, O., Mateo, F., de Paz, A.M., Rubio, N., Arnal-Estapé, A., Ell, B.J., Bermudo, R., Díaz, A., Guerra-Rebollo, M., et al. (2012). Epithelial-mesenchymal transition can suppress major attributes of human epithelial tumor-initiating cells. J. Clin. Invest. *122*, 1849–1868.

Creighton, C.J., Li, X., Landis, M., Dixon, J.M., Neumeister, V.M., Sjolund, A., Rimm, D.L., Wong, H., Rodriguez, A., Herschkowitz, J.I., et al. (2009). Residual breast cancers after conventional therapy display mesenchymal as well as tumor-initiating features. Proc. Natl. Acad. Sci. USA *106*, 13820–13825.

Dalerba, P., Cho, R.W., and Clarke, M.F. (2007). Cancer stem cells: models and concepts. Annu. Rev. Med. *58*, 267–284.

Eferl, R., and Wagner, E.F. (2003). AP-1: a double-edged sword in tumorigenesis. Nat. Rev. Cancer *3*, 859–868.

Ginestier, C., Hur, M.H., Charafe-Jauffret, E., Monville, F., Dutcher, J., Brown, M., Jacquemier, J., Viens, P., Kleer, C.G., Liu, S., et al. (2007). ALDH1 is a marker of normal and malignant human mammary stem cells and a predictor of poor clinical outcome. Cell Stem Cell *1*, 555–567.

Gould, C.M., Antal, C.E., Reyes, G., Kunkel, M.T., Adams, R.A., Ziyar, A., Riveros, T., and Newton, A.C. (2011). Active site inhibitors protect protein kinase C from dephosphorylation and stabilize its mature form. J. Biol. Chem. *286*, 28922–28930.

Griner, E.M., and Kazanietz, M.G. (2007). Protein kinase C and other diacylglycerol effectors in cancer. Nat. Rev. Cancer *7*, 281–294.

Gruda, M.C., Kovary, K., Metz, R., and Bravo, R. (1994). Regulation of Fra-1 and Fra-2 phosphorylation differs during the cell cycle of fibroblasts and phosphorylation in vitro by MAP kinase affects DNA binding activity. Oncogene *9*, 2537–2547.

Gupta, P.B., Onder, T.T., Jiang, G., Tao, K., Kuperwasser, C., Weinberg, R.A., and Lander, E.S. (2009). Identification of selective inhibitors of cancer stem cells by high-throughput screening. Cell *138*, 645–659.

Kakumoto, K., Sasai, K., Sukezane, T., Oneyama, C., Ishimaru, S., Shibutani, K., Mizushima, H., Mekada, E., Hanafusa, H., and Akagi, T. (2006). FRA1 is a determinant for the difference in RAS-induced transformation between human and rat fibroblasts. Proc. Natl. Acad. Sci. USA *103*, 5490–5495.

Kang, J.H., Toita, R., Kim, C.W., and Katayama, Y. (2012). Protein kinase C (PKC) isozyme-specific substrates and their design. Biotechnol Adv. *30*, 1662–1672.

Kolch, W., Heidecker, G., Kochs, G., Hummel, R., Vahidi, H., Mischak, H., Finkenzeller, G., Marmé, D., and Rapp, U.R. (1993). Protein kinase C alpha activates RAF-1 by direct phosphorylation. Nature *364*, 249–252.

Lønne, G.K., Cornmark, L., Zahirovic, I.O., Landberg, G., Jirström, K., and Larsson, C. (2010). PKCalpha expression is a marker for breast cancer aggressiveness. Mol. Cancer *9*, 76.

Mani, S.A., Guo, W., Liao, M.J., Eaton, E.N., Ayyanan, A., Zhou, A.Y., Brooks, M., Reinhard, F., Zhang, C.C., Shipitsin, M., et al. (2008). The epithelial-mesenchymal transition generates cells with properties of stem cells. Cell *133*, 704–715.

Morel, A.P., Lièvre, M., Thomas, C., Hinkal, G., Ansieau, S., and Puisieux, A. (2008). Generation of breast cancer stem cells through epithelial-mesenchymal transition. PLoS ONE *3*, e2888.

Neve, R.M., Chin, K., Fridlyand, J., Yeh, J., Baehner, F.L., Fevr, T., Clark, L., Bayani, N., Coppe, J.P., Tong, F., et al. (2006). A collection of breast cancer cell lines for the study of functionally distinct cancer subtypes. Cancer Cell *10*, 515–527.

Newton, A.C. (2001). Protein kinase C: structural and spatial regulation by phosphorylation, cofactors, and macromolecular interactions. Chem. Rev. *101*, 2353–2364.

Nieto, M.A. (2011). The ins and outs of the epithelial to mesenchymal transition in health and disease. Annu. Rev. Cell Dev. Biol. *27*, 347–376.

Ocaña, O.H., Córcoles, R., Fabra, A., Moreno-Bueno, G., Acloque, H., Vega, S., Barrallo-Gimeno, A., Cano, A., and Nieto, M.A. (2012). Metastatic colonization requires the repression of the epithelial-mesenchymal transition inducer Prrx1. Cancer Cell *22*, 709–724.

Pece, S., Tosoni, D., Confalonieri, S., Mazzarol, G., Vecchi, M., Ronzoni, S., Bernard, L., Viale, G., Pelicci, P.G., and Di Fiore, P.P. (2010). Biological and molecular heterogeneity of breast cancers correlates with their cancer stem cell content. Cell *140*, 62–73.

Rhee, S.G. (2001). Regulation of phosphoinositide-specific phospholipase C. Annu. Rev. Biochem. *70*, 281–312.

Saito, Y., Hojo, Y., Tanimoto, T., Abe, J., and Berk, B.C. (2002). Protein kinase C-alpha and protein kinase C-epsilon are required for Grb2-associated binder-1 tyrosine phosphorylation in response to platelet-derived growth factor. J. Biol. Chem. *277*, 23216–23222.

Sarrió, D., Rodriguez-Pinilla, S.M., Hardisson, D., Cano, A., Moreno-Bueno, G., and Palacios, J. (2008). Epithelial-mesenchymal transition in breast cancer relates to the basal-like phenotype. Cancer Res. *68*, 989–997.

Scheel, C., Eaton, E.N., Li, S.H., Chaffer, C.L., Reinhardt, F., Kah, K.J., Bell, G., Guo, W., Rubin, J., Richardson, A.L., and Weinberg, R.A. (2011). Paracrine and autocrine signals induce and maintain mesenchymal and stem cell states in the breast. Cell *145*, 926–940.

Shipitsin, M., Campbell, L.L., Argani, P., Weremowicz, S., Bloushtain-Qimron, N., Yao, J., Nikolskaya, T., Serebryiskaya, T., Beroukhim, R., Hu, M., et al. (2007). Molecular definition of breast tumor heterogeneity. Cancer Cell *11*, 259–273.

Stinson, S., Lackner, M.R., Adai, A.T., Yu, N., Kim, H.J., O'Brien, C., Spoerke, J., Jhunjhunwala, S., Boyd, Z., Januario, T., et al. (2011). TRPS1 targeting by miR-221/222 promotes the epithelial-to-mesenchymal transition in breast cancer. Sci. Signal. *4*, ra41.

Thiery, J.P., Acloque, H., Huang, R.Y., and Nieto, M.A. (2009). Epithelial-mesenchymal transitions in development and disease. Cell *139*, 871–890.

Thomson, S., Buck, E., Petti, F., Griffin, G., Brown, E., Ramnarine, N., Iwata, K.K., Gibson, N., and Haley, J.D. (2005). Epithelial to mesenchymal transition is a determinant of sensitivity of non-small-cell lung carcinoma cell lines and xenografts to epidermal growth factor receptor inhibition. Cancer Res. *65*, 9455–9462.

Tsai, J.H., Donaher, J.L., Murphy, D.A., Chau, S., and Yang, J. (2012). Spatiotemporal regulation of epithelial-mesenchymal transition is essential for squamous cell carcinoma metastasis. Cancer Cell *22*, 725–736.

Waddell, N., Cocciardi, S., Johnson, J., Healey, S., Marsh, A., Riley, J., da Silva, L., Vargas, A.C., Reid, L., Simpson, P.T., et al.; kConFab Investigators. (2010). Gene expression profiling of formalin-fixed, paraffin-embedded familial breast tumours using the whole genome-DASL assay. J. Pathol. *221*, 452–461.

Cancer Cell
Article

The RasGAP Gene, *RASAL2*, Is a Tumor and Metastasis Suppressor

Sara Koenig McLaughlin,[1,2,3] Sarah Naomi Olsen,[1,2,3] Benjamin Dake,[4,5] Thomas De Raedt,[1,2,3,9] Elgene Lim,[2,3,6] Roderick Terry Bronson,[3] Rameen Beroukhim,[2,3,7,8] Kornelia Polyak,[2,3,6] Myles Brown,[2,3,6] Charlotte Kuperwasser,[4,5] and Karen Cichowski[1,2,3,9,*]
[1]Genetics Division
[2]Department of Medicine
Brigham and Women's Hospital, Boston, MA 02115, USA
[3]Harvard Medical School, Boston, MA 02115, USA
[4]Department of Developmental, Molecular, and Biochemical Biology, Sackler School of Graduate Biomedical Sciences, Tufts University School of Medicine, 136 Harrison Avenue, Boston, MA 02111, USA
[5]Molecular Oncology Research Institute, Tufts Medical Center, 800 Washington Street, Boston, MA 02111, USA
[6]Division of Molecular and Cellular Oncology, Department of Medical Oncology
[7]Department of Cancer Biology
Dana-Farber Cancer Institute, Boston, MA 02215, USA
[8]Broad Institute of Massachusetts Institute of Technology and Harvard University, Cambridge, MA 02142, USA
[9]Ludwig Center at Dana-Farber/Harvard Cancer Center, Boston, MA 02115, USA
*Correspondence: kcichowski@rics.bwh.harvard.edu
http://dx.doi.org/10.1016/j.ccr.2013.08.004

SUMMARY

RAS genes are commonly mutated in cancer; however, *RAS* mutations are rare in breast cancer, despite frequent hyperactivation of Ras and ERK. Here, we report that the RasGAP gene, *RASAL2*, functions as a tumor and metastasis suppressor. *RASAL2* is mutated or suppressed in human breast cancer, and *RASAL2* ablation promotes tumor growth, progression, and metastasis in mouse models. In human breast cancer, *RASAL2* loss is associated with metastatic disease; low *RASAL2* levels correlate with recurrence of luminal B tumors; and *RASAL2* ablation promotes metastasis of luminal mouse tumors. Additional data reveal a broader role for *RASAL2* inactivation in other tumor types. These studies highlight the expanding role of RasGAPs and reveal an alternative mechanism of activating Ras in cancer.

INTRODUCTION

The Ras pathway is one of the most commonly deregulated pathways in human cancer (Downward, 2003). Mutations in *RAS* genes occur in a variety of tumor types (Karnoub and Weinberg, 2008; Pylayeva-Gupta et al., 2011); however, the Ras pathway is also frequently activated as a consequence of alterations in upstream regulators and downstream effectors, underscoring the importance of this pathway in cancer (Downward, 2003).

Ras is negatively regulated by Ras *G*TPase-*a*ctivating *p*roteins (RasGAPs), which catalyze the hydrolysis of Ras-GTP to Ras-GDP (Bernards, 2003). As such, RasGAPs are poised to function as potential tumor suppressors. Indeed, the *NF1* tumor suppressor encodes a RasGAP and is mutated in the familial cancer syndrome neurofibromatosis type 1 (Cawthon et al., 1990). *NF1* also is lost or suppressed in sporadic cancers, including glioblastoma (Cancer Genome Atlas Research Network, 2008; Parsons et al., 2008; McGillicuddy et al., 2009), nonsmall cell lung cancer (Ding et al., 2008), neuroblastoma (Hölzel et al., 2010), and melanoma (Krauthammer et al., 2012; Maertens et al., 2012). More recently, the RasGAP gene, *DAB2IP*, has been shown to function as a potent tumor and metastasis suppressor in prostate cancer (Min et al., 2010). In total, there are 14 RasGAP genes in the human genome (Bernards, 2003). All contain a RasGAP domain but exhibit little similarity elsewhere. It is currently unknown whether any of these other genes may also function as human tumor suppressors.

Breast cancer is the most common cancer in women worldwide (Kamangar et al., 2006). *K*-, *H*-, and *N-RAS* mutations are

Significance

The RasGAPs are direct negative regulators of Ras and are therefore poised to function as potential tumor suppressors. Here, we identify a RasGAP gene, *RASAL2*, as a tumor suppressor within this gene family. Our data suggest that *RASAL2* loss plays a causal role in the development, progression, and metastasis of breast cancer and may play a broader role in the metastasis of other solid tumors as well. Collectively, these data reveal an alternative mechanism by which Ras becomes activated in cancer and identify a role for *RASAL2* and Ras in breast cancer progression and metastasis.

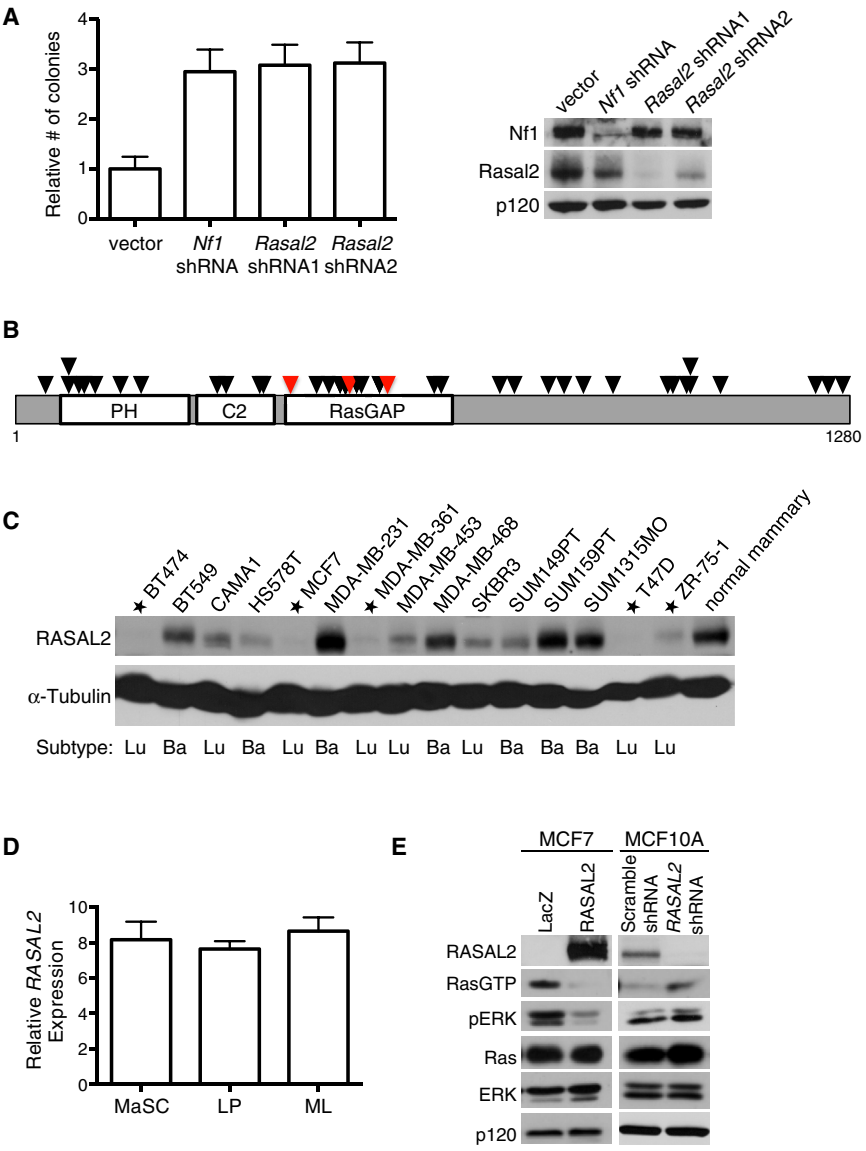

Figure 1. *RASAL2* Is a Candidate Tumor Suppressor

(A) Left: immortalized MEFs were infected with lentiviral shRNAs that target *Rasal2*, *Nf1*, or control and were plated in soft agar. Data are reported as relative number of colonies ± SEM. Inactivation of *Nf1* or *Rasal2* induced a statistically significant increase in anchorage-independent growth ($p \leq 0.0001$). Right: western blot confirming knockdown.

(B) *RASAL2* mutations in human tumor samples (Bamford et al., 2004). Each triangle represents a nonsynonymous mutation. Red triangles indicate breast cancer mutations. See also Tables S1 and S2.

(C) RASAL2 expression in a panel of human breast cancer cell lines in comparison to normal human mammary epithelial cells. Cell lines with very low or no RASAL2 are starred. Luminal (Lu) or basal (Ba) subtype categorization is indicated.

(D) Relative *RASAL2* expression in subsets of sorted human mammary epithelial cells (Lim et al., 2009). MaSC, mammary stem cell enriched: (CD49hi EpCAM$^-$). LP: luminal progenitor (CD49f$^+$ EpCAM$^+$). ML, mature luminal (CD49f$^-$ EpCAM$^+$). Data show relative expression ± SD. Similar results were obtained using two additional *RASAL2* probes. There were no statistically significant differences in *RASAL2* expression between subsets of cells.

(E) Left: western blot of Ras-GTP and phospho-ERK (pERK) levels in MCF7 cells following expression of LacZ or RASAL2. Right: western blot of Ras-GTP and phospho-ERK (pERK) levels in MCF10A cells following shRNA-mediated inactivation of *RASAL2* or control (nontargeting "Scramble" shRNA).

RESULTS

The RasGAP Gene, *RASAL2*, Is a Candidate Tumor Suppressor

We previously developed a cell-based screen to identify additional RasGAPs that might function as tumor suppressors (Min et al., 2010). Distinct small hairpin RNAs (shRNAs) that recognize individual RasGAP genes were introduced into immortalized mouse embryonic fibroblasts (MEFs), and cells were evaluated for the ability to grow in soft agar. Three genes scored in this screen: *Nf1*, a well-documented tumor suppressor gene, *Dab2ip*, which we have since shown is a tumor suppressor in prostate cancer, and *Rasal2*, a third RasGAP gene (Min et al., 2010). Several *Rasal2*-specific shRNA sequences promoted colony growth in this assay and did so as well as *Nf1*- and *Dab2ip*-specific shRNAs (Figure 1A; Min et al., 2010). Notably, transformation was not generally promoted by the loss of any RasGAP, suggesting that only a subset of RasGAPs may function as tumor suppressors (Min et al., 2010). Upon identifying *RASAL2* as a candidate tumor suppressor, we searched publicly available databases and found mutations within the catalytic RasGAP domain in human breast cancers (Figure 1B; Table S1 available online) (Sjöblom et al., 2006; Shah et al., 2012). Current genomic mutation databases indicate that *RASAL2* is also mutated in several other tumor relatively rare in this tumor type, and together they have been detected in only ~3.2% of all breast lesions (Bamford et al., 2004). Nevertheless, the Ras/ERK pathway is hyperactivated in ≥50% of breast cancers and has been proposed to be involved in tumor progression and recurrence, suggesting that Ras may be more frequently activated by other mechanisms in these tumors (Sivaraman et al., 1997; von Lintig et al., 2000; Mueller et al., 2000). In this study, we demonstrate that the RasGAP gene, *RASAL2*, functions as a tumor suppressor in breast cancer. Through the analysis of human tumor samples, human xenografts, and genetically engineered mouse models, we show that *RASAL2* loss plays a causal role in breast cancer development and metastasis. Additional mouse modeling studies reveal a broader potential role for *RASAL2* in other tumor types. Together, these studies highlight the expanding role of RasGAP genes in cancer and reveal an important mechanism by which Ras becomes activated in breast tumors.

types, including colorectal, lung, and ovarian tumors (Figure 1B; Table S2). In total, 42 nonsynonymous mutations have been detected in *RASAL2*, 31% of which reside in the catalytic RasGAP domain, many of which are predicted to be deleterious (Tables S2 and S3). Because the mechanism by which Ras becomes activated in breast cancer is largely unknown, and because mutations in breast tumors were among the first to be identified, we began by investigating a potential role for *RASAL2* inactivation in breast cancer development.

Work from our laboratory and others have shown that the RasGAP genes *NF1* and *DAB2IP* are inactivated in cancer by genetic, epigenetic, and proteasomal mechanisms (Dote et al., 2004; McGillicuddy et al., 2009; Min et al., 2010). Moreover, in many instances the nongenetic mechanisms of inactivation of these tumor suppressors appear to be more prevalent than mutational events in sporadic tumors (McGillicuddy et al., 2009; Min et al., 2010; Maertens et al., 2012). Therefore, we began by examining RASAL2 protein expression in a panel of breast cancer cell lines. In comparison to normal mammary epithelial cells, in at least 5 out of 15 breast cancer cell lines RASAL2 was absent or minimally expressed, suggesting that RASAL2 may be lost or suppressed in this tumor type (Figure 1C). RASAL2 levels were high in MDA-MB-231 and SUM159PT cells, which are known to harbor mutations in *KRAS* and *HRAS*, respectively (Hollestelle et al., 2007). We also noted that RASAL2 was frequently absent in cells derived from luminal cancers in this panel of lines. Cell sorting studies indicate that there are no inherent differences in *RASAL2* expression in any specific cell population within the mammary cell hierarchy: luminal progenitor, mature luminal, or mammary stem cell enriched, suggesting that the low RASAL2 levels associated with luminal cancer cell lines are not inherently associated with a pre-existing reduction in RASAL2 levels due to a specific cell of origin or fate, as has been suggested for other genes (Figure 1D) (Lim et al., 2009). When RASAL2 was reconstituted in MCF7 cells, which express little to no endogenous RASAL2, Ras-GTP and phospho-ERK levels were suppressed (Figure 1E). Conversely, acute inactivation of *RASAL2* via shRNA sequences in immortalized mammary epithelial cells (MCF10A) increased Ras-GTP and phospho-ERK levels (Figure 1E). These data confirm that RASAL2 is a functional RasGAP and that loss of RASAL2 activates Ras and ERK in this tumor type.

RASAL2 Functions as a Tumor Suppressor in Breast Cancer

We next investigated the biological consequences of reconstituting or suppressing *RASAL2* in breast cancer cell lines. When RASAL2 was introduced into human breast cancer cells that lack endogenous RASAL2, proliferation was largely unaffected (Figure 2A); however, RASAL2 reconstitution significantly inhibited anchorage-independent colony growth (Figure 2B). In contrast, RASAL2 did not inhibit colony growth of SUM159PT cells, which retain RASAL2 expression but harbor an activating *RAS* mutation (Figure 2B). RASAL2 also potently suppressed the growth of *RASAL2*-deficient breast cancer xenografts in vivo but again had no effect on *RAS* mutant tumors (Figure 2C). Conversely, shRNA-mediated suppression of endogenous *RASAL2* in a breast cancer cell line that normally does not grow well as a xenograft promoted tumor growth in vivo (Figure 2D). Together, these gain- and loss-of-function studies suggest that RASAL2 can function as a tumor suppressor in the mammary epithelium and that inactivation or loss of RASAL2 can contribute to mammary tumor development. Notably, like *NF1* and *DAB2IP*, *RASAL2* appears to restrict transformation and/or anchorage-independent growth, rather than generally suppressing cell proliferation in two-dimensional culture systems (Johannessen et al., 2005; Min et al., 2010).

RASAL2 Functions via Its Effects on Ras

To determine whether the RasGAP domain of RASAL2 and effects on Ras were critical for tumor suppression, we first evaluated the effects of *RASAL2* mutations identified in human breast cancer samples. Two of the three RasGAP domain mutants (K417E and K567X) failed to suppress anchorage-independent growth, demonstrating that these two mutations result in a clear loss of function (Figure 3A). The third mutation, which resulted in a more conservative amino acid change (E509D), still retained activity in this assay and therefore does not appear to be pathogenic; however, a number of additional nonconservative mutations have been detected in the RasGAP domain in other tumor types (Table S3). Consistent with these biological observations, both the K417E and the K567X mutations were defective in their ability to suppress activation of the Ras/ERK pathway (Figure 3B). Phospho-ERK levels in xenograft tumors further illustrate the difference in activity between pathogenic and nonpathogenic mutations (Figure 3C). To complement these studies, we investigated which Ras isoforms were activated in response to *RASAL2* suppression and found that both K-Ras and H-Ras-GTP levels were elevated (Figure 3D). Accordingly, ablation of either *KRAS* or *HRAS* suppressed colony growth by more than 50% (Figure 3E). Together, these results demonstrate that the RasGAP domain is essential for RASAL2 tumor suppressor function and that both H- and K-Ras contribute to the pathogenesis caused by *RASAL2* inactivation.

RASAL2 Inactivation Promotes Migration, Invasion, and Tumor Progression

To fully characterize the oncogenic effects of *RASAL2* loss, we investigated whether *RASAL2* suppression might also promote migration, invasion, and tumor progression. *RASAL2* suppression promoted the migration of MCF10A cells in a wound-healing assay (Figures 4A and 4B) and significantly enhanced invasion through Matrigel (Figure 4C, $p = 0.002$). Similar to what was observed in colony assays shown in Figure 3E, ablation of *HRAS* or *KRAS* reduced invasiveness (Figure S1). We also utilized a xenograft model of breast cancer progression that mimics the progression of ductal carcinoma in situ (DCIS) to invasive carcinoma (Miller et al., 2000; Hu et al., 2008). Specifically, MCF10ADCIS cells, derivatives of MCF10A cells that are enriched for a progenitor population of cells (Miller et al., 2000), develop into DCIS-like lesions when grown as xenografts in mice. However, after a latency of approximately 8 weeks, they progress to invasive carcinoma, characterized by the loss of the myoepithelial cell layer and basement membrane (Hu et al., 2008). We acutely inactivated *RASAL2*, using two distinct shRNAs in these cells, and found that *RASAL2* inactivation accelerated tumor progression, resulting in a rapid disruption of the myoepithelium and basement membrane and the

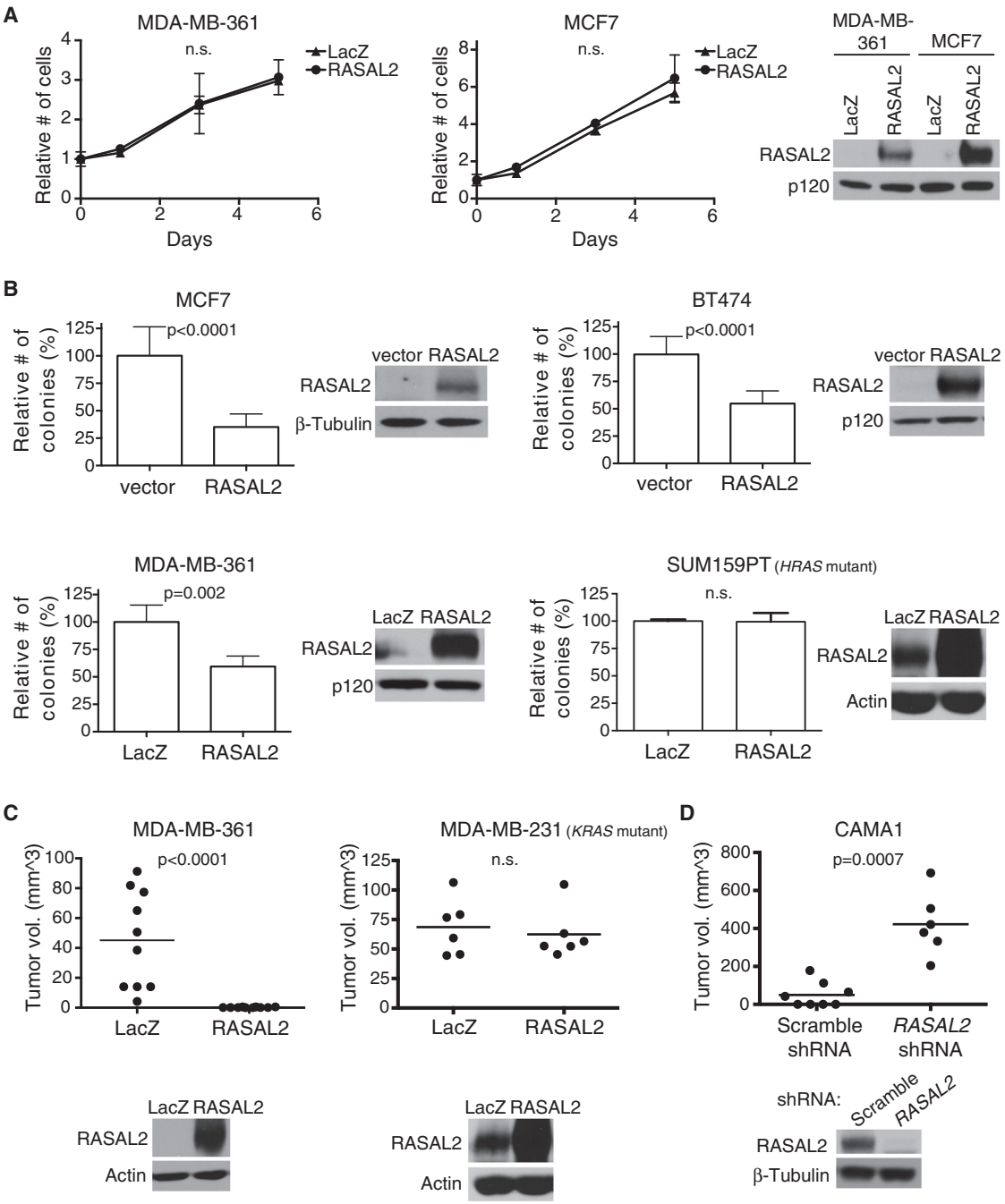

Figure 2. *RASAL2* Functions as a Tumor Suppressor in Breast Cancer

(A) Growth curves of MDA-MB-361 and MCF7 cells expressing RASAL2 or LacZ. Data points show triplicate averages ± SD. There were no statistically significant differences in proliferation. Western blot on right confirms ectopic RASAL2 expression.

(B) Soft agar colony formation of MCF7, BT474, MDA-MB-361, and SUM159PT cells expressing RASAL2 or LacZ. Data show relative number of colonies ± SD. There was a statistically significant decrease in anchorage-independent growth upon ectopic RASAL2 expression in *RAS* wild-type cell lines (MCF7 and BT474 $p < 0.0001$; MDA-MB-361 $p = 0.002$), but not in the *HRAS* mutant cell line SUM159PT. Western blots confirm ectopic RASAL2 expression.

(C) Xenograft tumor formation of MDA-MB-361 and MDA-MB-231 cells expressing RASAL2 or LacZ. MDA-MB-361 cells were injected orthotopically into female NOD/SCID mice; MDA-MB-231 cells were injected subcutaneously into female nude mice. Horizontal bars indicate mean tumor volume. There was a statistically significant decrease in tumor growth upon ectopic RASAL2 expression ($p < 0.0001$) in the *RAS* wild-type cell line MDA-MB-361, but not in the *KRAS* mutant cell line MDA-MB-231. Western blots below confirm ectopic RASAL2 expression.

(D) Xenograft tumor formation of CAMA1 cells infected with shRNAs targeting *RASAL2* or nontargeting control shRNA and injected subcutaneously into female NOD/SCID mice. Horizontal bars indicate mean tumor volume. There was a statistically significant increase in tumor growth upon *RASAL2* inactivation ($p = 0.0007$). Western blot confirms RASAL2 knockdown.

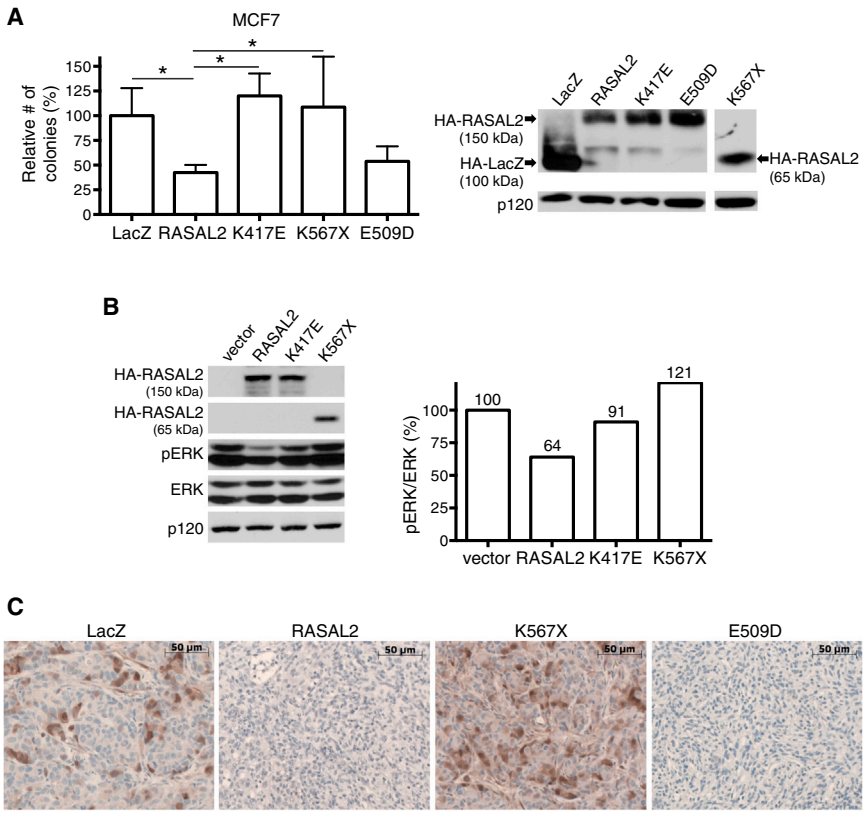

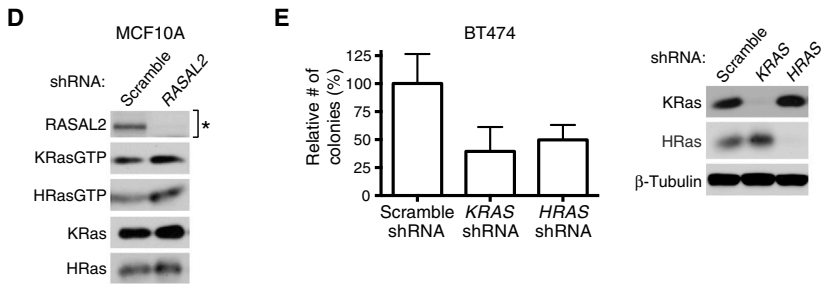

Figure 3. RASAL2 Functions as a Tumor Suppressor via Its Effects on Ras

(A) Soft agar colony formation of MCF7 cells expressing HA-tagged LacZ, wild-type, or mutant RASAL2 (see also Table S3). Data show relative number of colonies ± SD. *p ≤ 0.05. Western blot confirms expression of constructs.

(B) Western blot reflecting the relative activation of the Ras/ERK pathway in the presence of HA-tagged wild-type or mutant RASAL2. The pERK/ERK ratio of each sample was calculated and normalized to the vector control.

(C) Phospho-ERK (pERK) expression in MDA-MB-361 xenograft tumors. LacZ, RASAL2, or mutant RASAL2 was expressed in MDA-MB-361 cells, and cells were injected orthotopically into female NOD/SCID mice. pERK levels were assessed by immunohistochemistry.

(D) Western blot showing HRas-GTP and KRas-GTP levels in MCF10A cells following shRNA-mediated inactivation of *RASAL2* or control shRNA. As indicated by the asterisk, the blot confirming RASAL2 knockdown is a duplicate from Figure 1E, as these immunoblots were generated from the same samples.

(E) Soft agar colony formation of BT474 cells infected with an shRNA targeting *HRAS* or *KRAS* or a nontargeting control. Data show relative number of colonies ± SD. Western blot confirms Ras isoform-specific knockdown.

development of invasive adenocarcinoma after just 3 weeks (Figure 4D). These results suggest that *RASAL2* inactivation may also play a role in breast cancer progression. Notably, tumors in which RASAL2 had been depleted also exhibited a marked elevation of phospho-ERK as compared to control tumors (Figure 4E).

Loss of *Rasal2* Promotes Metastasis and Ras Activation in a Genetically Engineered Mouse Model of Luminal Breast Cancer

As a rigorous and complementary means of investigating the biological consequences of *RASAL2* inactivation in vivo, we generated genetically engineered mice that lack *Rasal2*. Mouse embryonic stem cells that contain a gene-trap cassette within the third intron of *Rasal2* were used to generate *Rasal2*-deficient mice (Figure 5A). Appropriate integration and loss of Rasal2 expression were confirmed in heterozygous and homozygous mutant animals (Figures 5B and 5C). *Rasal2*$^{-/-}$ mice were viable, fertile, and born at Mendelian ratios. We found that mutant animals did exhibit shorter overall survival as compared to control animals (77.8 compared to 95.6 weeks; p = 0.007, Figure S2A). However, there was no obvious difference in phenotype between wild-type and *Rasal2*$^{-/-}$ mice. A subset of animals from both cohorts developed tumors associated with old age. Whereas *Rasal2* mutant mice developed these tumors earlier, the tumor spectrum was similar to wild-type animals, and they did not develop mammary lesions (Figure S2B). These results indicate that *Rasal2* loss is not sufficient to drive breast cancer in mice but may play a more general role in enhancing the development of other spontaneous tumors.

To examine the effects of *RASAL2* loss on mammary tumorigenesis, we crossed *Rasal2*$^{-/-}$ mice to animals that constitutively overexpress a wild-type *Her2 (Erbb2)* transgene in the mammary epithelium (*MMTVneu* mice) (Guy et al., 1992): a mouse model of luminal tumors (Herschkowitz et al., 2007). These tumors exhibit some differences from human luminal cancers, as they do not express estrogen receptor; however, unsupervised hierarchical clustering analysis and tumor pathology demonstrate that lesions from these animals recapitulate many of the key features of human luminal tumors (Guy et al., 1992; Herschkowitz et al., 2007). As such, these animals are currently the best available genetically engineered mouse model for luminal cancer (Guy et al., 1992; Herschkowitz et al., 2007). Female *MMTVneu* mice develop focal luminal mammary tumors,

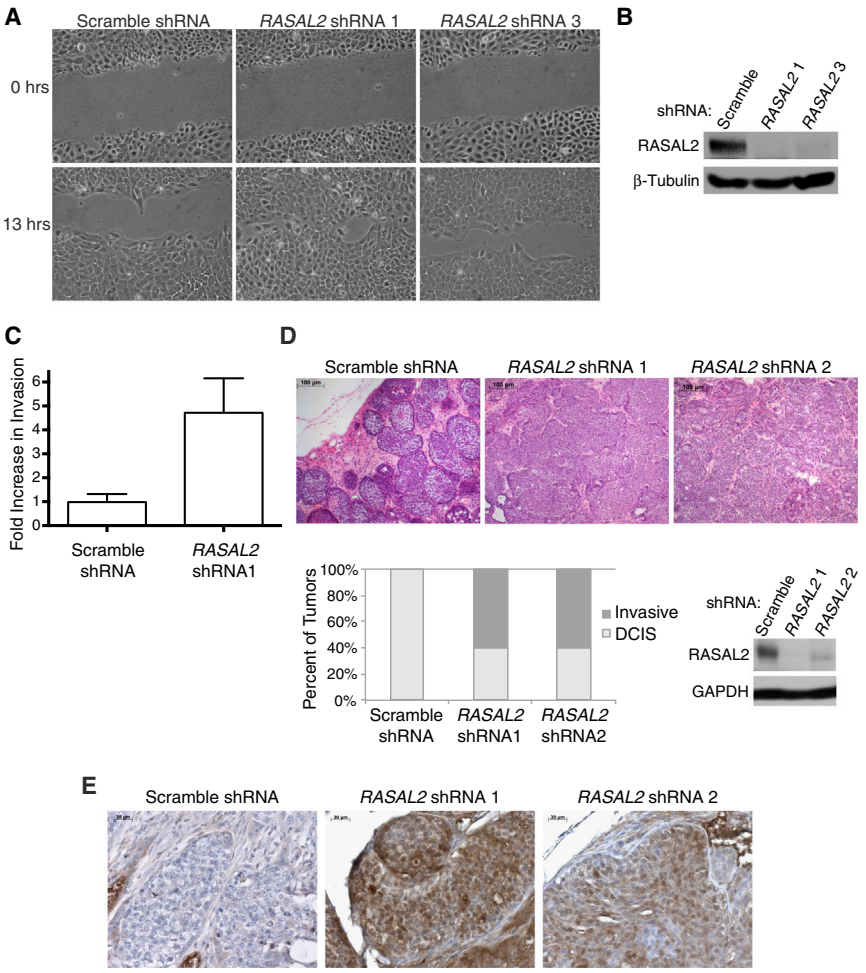

Figure 4. *RASAL2* Inactivation Promotes Migration, Invasion, and Tumor Progression

(A) Cell migration of MCF10A cells infected with shRNAs targeting *RASAL2* or a nontargeting control.

(B) Western blot confirming RASAL2 knockdown in MCF10A cells used in (A) and (C).

(C) Transwell invasion of MCF10A cells infected with an shRNA targeting *RASAL2* or a nontargeting control. Invasion was measured after 24 hr and reported as average ± SD ($p = 0.002$).

(D) Xenograft tumor progression of MCF10ADCIS cells infected with shRNAs targeting *RASAL2* or a nontargeting control. Top: H&E images of xenograft tumors. Bottom left: quantification of xenograft tumor progression. Bottom right: western blot confirming RASAL2 knockdown.

(E) Phospho-ERK (pERK) expression in MCF10ADCIS xenograft tumors from (D) as assessed via immunohistochemistry.

See also Figure S1.

and a fraction of tumor-bearing females develop lung metastases (Guy et al., 1992). As expected, *MMTVneu* and *MMTVneu; Rasal2*$^{-/-}$ compound mice developed mammary adenocarcinomas and did so at a similar high frequency (Figure 5D, top panels; Figure S2E). Strikingly, however, we found that *MMTVneu; Rasal2*$^{-/-}$ mice developed substantially more metastases than *MMTVneu* animals. First, a higher fraction of compound mutant mice developed lung metastases (Figure 5E, 74% versus 46%, $p = 0.05$). Second, compound mutant mice developed more metastases per lung than *MMTVneu* animals (Figure 5E, 30 per mouse versus 8 per mouse, $p = 0.04$). Finally, the metastases were significantly larger in *MMTVneu; Rasal2*$^{-/-}$ mice as compared to *MMTVneu* mice (Figure 5D, bottom panels; Figure 5E, $p = 0.04$). Interestingly, a subset of compound mutant mice developed tumors that metastasized to other organs, including brain, kidney, ovary, and gastrointestinal tract, a phenomenon not observed in *MMTVneu* animals historically or in our cohort (Figure 5F). Moreover, in most autochthonous mouse models of mammary adenocarcinoma, metastasis is typically limited to the lung and occasionally lymph nodes (Kim and Baek, 2010). However, human breast cancers do frequently metastasize to the brain and these other distal sites, underscoring the significance of these observations and the potential utility of this mouse model (Weigelt et al., 2005). Despite the dramatic increase in metastasis, no differences in primary tumor incidence, growth rate, or tumor size were observed in *MMTVneu* versus *MMTVneu; Rasal2*$^{-/-}$ mice, indicating that the differences in metastatic burden were not due to underlying differences in primary tumor onset or growth (Figures S2C, S2D, and S2F). Importantly, when we compared primary tumors from *MMTVneu; Rasal2*$^{-/-}$ mice and *MMTVneu* animals, higher levels of phospho-ERK and phospho-AKT were more consistently observed in *MMTVneu; Rasal2*$^{-/-}$ lesions (Figure 5G). In addition, we found that Rasal2 was spontaneously lost or suppressed in a subset of *MMTVneu* tumors, and this loss or suppression was accompanied by a substantial increase in phospho-ERK and phospho-AKT levels (Figure 5G). Finally, the primary tumor that spontaneously lost/suppressed Rasal2 and exhibited the most robust activation of the Ras pathway was a metastatic outlier within the *MMTVneu* cohort (Tumor 6, Figure 5G; Figure S2G). Taken together, these findings indicate that *Rasal2* loss enhances Ras activity in mammary tumors and that it promotes tumor progression, invasion, and metastasis in both autochthonous mouse models of breast cancer and human xenografts.

RASAL2 in Primary Human Breast Cancers

Genomic analyses demonstrate that *RASAL2* mutations do occur in human breast cancer but are relatively rare (Bamford et al., 2004; Sjöblom et al., 2006; Shah et al., 2012; Table S1). However, the two other known RasGAP tumor suppressors appear to be more frequently inactivated in cancer via nongenetic mechanisms. To more accurately determine how frequently *RASAL2* is lost or suppressed in human breast cancers, we directly examined RASAL2 protein levels in primary human tumors. Existing RASAL2 antibodies cannot be used for immunohistochemistry; therefore, we obtained breast cancer

arrays comprised of 55 sets of protein lysates (in triplicate) from matched primary breast tumors and adjacent normal mammary tissue taken from naive patients (Mueller et al., 2010). These tumor samples were histologically verified to contain at least 80% cancer cells and the normal tissue is cancer cell free. We first validated our purified RASAL2 antibody in this assay and found that dot blots from RASAL2-expressing and nonexpressing human breast cancer cell lines exhibited the expected pattern of expression (Figure 6A, top). *RASAL2*-specific shRNA sequences also effectively ablated expression in this assay (Figure 6A, bottom). Using the tumor arrays, we found that RASAL2 expression was decreased by 75%–100% in 20% of human breast tumors as compared to adjacent normal mammary tissue (Figures 6B and 6C). These results confirm our findings in breast cancer cell lines, suggesting that RASAL2 expression is lost or suppressed in a significant fraction of human breast cancers at a frequency that is much greater than indicated by mutation analysis alone. More importantly, however, low RASAL2 protein levels were significantly associated with metastasis (Figures 6C and 6D, $p = 0.006$).

Because the cell line analysis indicated that RASAL2 expression was low or undetectable in a subset of luminal breast cancer cell lines (Figure 1), and mouse modeling studies further demonstrated that *RASAL2* loss promoted the metastasis of luminal tumors, we evaluated *RASAL2* expression in different breast cancer subtypes. Human breast cancers can be molecularly classified into five distinct subtypes: basal-like, HER2-positive, luminal A, luminal B, and normal breast-like (Perou et al., 2000; Sørlie et al., 2001; Hu et al., 2006). Notably, molecular subtype association analysis of transcriptional profiles from primary breast cancers revealed that *RASAL2* expression was low in luminal B breast cancers; 50% of luminal B tumors expressed the lowest levels of *RASAL2*, consistent with a potential role for *RASAL2* loss in this subtype (Figures 6E and 6F). Moreover, low *RASAL2* expression was also associated with both increased tumor recurrence (Figure 6G, log rank $p = 0.0133$) and decreased overall survival (Figure 6H, log rank $p = 0.0131$) in patients with luminal B cancers. Finally, using publicly available TCGA methylation 450 data, we found that two CpG sites in the *RASAL2* promoter region are differentially methylated in primary breast tumors. Specifically, *RASAL2* promoter methylation is enriched in luminal B tumors ($p < 0.05$, Mann-Whitney U test). These luminal B tumors also showed the lowest expression of *RASAL2*. Notably, both sites exhibit a significant increase in methylation when comparing luminal B samples with the lowest expression of *RASAL2* (bottom 33%) to luminal B samples with highest expression (top 33%) ($p < 0.05$, t test). Taken together, cellular, xenograft, mouse modeling, and human tumor studies suggest that *RASAL2* loss promotes breast cancer development and metastasis and may play a particularly important role in the progression of luminal B tumors. In this context, the general lack of *KRAS* amplifications in luminal tumors but their frequent occurrence in basal-like breast cancers is notable (Cancer Genome Atlas Network, 2012), suggesting that *RASAL2* suppression may provide an alternative mechanism of Ras activation in the luminal subtype. Nevertheless, although the models used in this study provide functional evidence to support a role for *RASAL2* inactivation in luminal B tumors, these data do not preclude its involvement in a fraction of other subtypes.

Rasal2 Mutations Promote Tumor Development and Widespread Metastasis in *p53* Mutant Mice

To determine whether *RASAL2* inactivation might also contribute to the development of other sporadic tumors, *Rasal2*$^{-/-}$ mice were crossed to mice mutant for p53, one of the most commonly inactivated tumor suppressors in human cancer (Vousden and Lane, 2007). *Trp53* mutant mice develop a spectrum of lymphomas and sarcomas, and some carcinomas arise in heterozygotes (Donehower et al., 1992; Jacks et al., 1994). In addition to the classical tumors observed in *Trp53* mutant mice, *Rasal2*/*Trp53* compound mutant mice developed several other lesions that were not found in *Trp53* mutant controls, historically or in our cohort (Figure 7A). Specifically, *Rasal2*/*Trp53* mutant mice developed hepatocellular carcinomas and other liver tumors, colonic adenomas, and oral and stomach tumors (Figure 7A). These findings are of particular interest because *RASAL2* mutations have been found in related human cancers, namely, hepatocellular carcinoma, colorectal carcinoma, head and neck squamous cell carcinoma, and stomach cancer (Table S2). Notably, the *Rasal2*$^{-/-}$; *p53*$^{-/-}$ tumors exhibited higher levels of pERK as compared to *Rasal2*$^{+/+}$; *p53*$^{-/-}$ tumors (Figure 7B).

However, the most striking phenotype in *Rasal2*/*Trp53* mutant mice was that *Rasal2* loss potently promoted metastasis. The *Trp53*$^{-/-}$ mice, either with or without functional Rasal2, typically died from the primary tumor, which was frequently lymphoma. Nevertheless, 60% of the solid tumors that developed in *Rasal2*$^{+/-}$; *Trp53*$^{+/-}$ mice and 83% of the solid tumors from *Rasal2*$^{-/-}$; *Trp53*$^{+/-}$ mice were metastatic, as compared to 18% of tumors in *Trp53*$^{+/-}$ mice (Figure 7C, $p = 0.003$). Specifically, *Rasal2*/*Trp53* mutant animals developed highly metastatic mammary adenocarcinomas, hepatocellular carcinomas, lung adenocarcinomas, and various sarcomas, again tumor types in which *RASAL2* mutations have been detected in humans (Figure 7D). Thus, these findings further underscore the role of RASAL2 loss as a driver of metastasis and suggest that its inactivation may play a role in the progression of breast and other human cancers.

DISCUSSION

The Ras pathway plays a well-established role in cancer (Downward, 2003). However, the primary mechanism(s) by which Ras becomes activated in breast cancers has remained elusive. Here, we report that *RASAL2*, which encodes a RasGAP, functions as a tumor and metastasis suppressor in breast and other cancers. Specifically, we have shown that loss-of-function mutations in *RASAL2* are found in human breast cancers and other tumor types; however, like other RasGAP genes *RASAL2* appears to be more frequently inactivated by nongenetic mechanisms, and it is substantially repressed in at least 20% of primary human breast cancers. We also showed that *RASAL2* ablation promotes tumor growth and progression in two different human xenograft models, whereas *RASAL2* reconstitution suppresses mammary tumor growth. Notably, *RASAL2* mutations activate Ras and dramatically enhance metastasis in a genetically engineered mouse model of luminal mammary cancer. *RASAL2* mutations also cooperate with *p53* mutations to promote the development and metastasis of several tumor types, including mammary tumors, in a second mouse model. Finally, we show

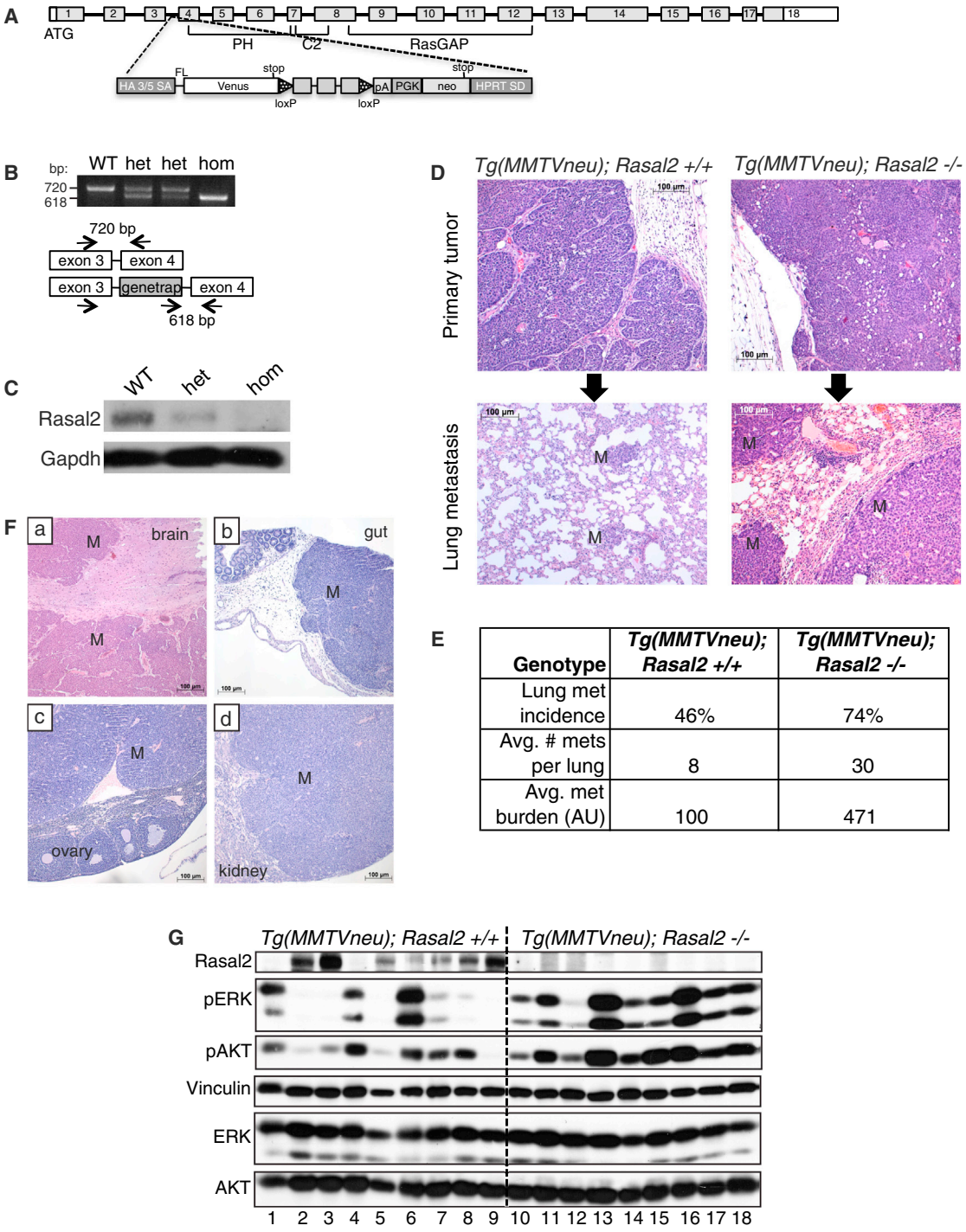

Genotype	*Tg(MMTVneu); Rasal2 +/+*	*Tg(MMTVneu); Rasal2 -/-*
Lung met incidence	46%	74%
Avg. # mets per lung	8	30
Avg. met burden (AU)	100	471

Figure 5. Loss of *Rasal2* Promotes Metastasis and Ras Activation in a Genetically Engineered Mouse Model of Breast Cancer

(A) Schematic of *Rasal2* genomic locus and pNMDi4 genetrap cassette. Unshaded regions in exons 1 and 18 mark 5′ and 3′ UTRs, respectively. Known domains of *Rasal2* are noted (PH, C2, and RasGAP). See the Experimental Procedures for detailed description of pNMDi4. The genetrap cassette targets the third intron of *Rasal2*.

(B) Genotyping of *Rasal2* mice to distinguish wild-type (WT), heterozygous mutant (het), and homozygous mutant (hom).

(C) Western blot confirming loss of Rasal2 protein in genetrap animals (mammary gland tissue). WT, wild-type; het, heterozygous; hom, homozygous mutant.

(D) Top: H&E images of primary mammary adenocarcinomas from *MMTVneu*; *Rasal2*$^{+/+}$ and *MMTVneu*; *Rasal2*$^{-/-}$ animals. Bottom: H&E images of lung metastases from *MMTVneu*; *Rasal2*$^{+/+}$ and *MMTVneu*; *Rasal2*$^{-/-}$ animals. M, metastases.

(E) Lung metastasis burden in *MMTVneu*; *Rasal2*$^{+/+}$ and *MMTVneu*; *Rasal2*$^{-/-}$ animals. Lung metastasis incidence: percent of tumor-bearing females with lung metastases at sacrifice ($p = 0.05$; n = 24 *MMTVneu*; *Rasal2*$^{+/+}$, n = 23 *MMTVneu*; *Rasal2*$^{-/-}$). Average number of lung metastases per animal: counted per

(legend continued on next page)

that low RASAL2 levels are associated with metastasis in human breast cancer.

Notably, the lowest *RASAL2* messenger RNA (mRNA) expression levels are most frequently observed in luminal B human breast cancers and are associated with recurrence and reduced survival of patients with this tumor subtype. Collectively, these data suggest that RASAL2 loss plays a causal role in breast cancer pathogenesis. Whereas the breast cancer xenograft studies and the overall increase in tumor incidence in *Rasal2/p53* mice suggest that RASAL2 may play a role in primary tumor development, the dramatic metastatic phenotype in *Rasal2/MMTVneu* and *Rasal2/p53* mutant animals demonstrates a role for *RASAL2* loss in metastasis. Similarly, the Ras pathway has been shown to play a role in both primary tumor development and metastasis, depending on context. As such, we hypothesize that *RASAL2* inactivation may play a role in one or both processes, depending on the presence of other mutations in a given tumor. Nevertheless, the human breast cancer data presented in this study suggest that *RASAL2* loss may play a more prominent role in progression and metastasis in this tumor type.

It should be noted that although *RAS* mutations are rare in breast cancer, they do occur. Moreover, amplifications of wild-type *RAS* are frequently observed in basal breast cancers, the most aggressive subtype of human breast cancer, underscoring the connection between Ras activation and breast cancer progression (Cancer Genome Atlas Network, 2012). Our data indicate that overall *RASAL2* is suppressed or lost in at least 20% of human breast cancers. However, expression and DNA methylation analysis of different breast cancer subtypes suggests that *RASAL2* loss may play a particularly important role in the progression of luminal B tumors. The observation that *RASAL2* ablation promotes metastasis in a mouse model of luminal tumors provides important functional data to support this conclusion. In this respect, the fact that luminal B tumors have poorer outcomes than luminal A tumors is notable; however, the mechanism(s) that drive the progression of these tumors is largely unknown. Our data suggest that RASAL2 loss/suppression may play a causal role in the progression of this subtype, although these observations do not preclude its potential involvement in other subtypes.

Finally, whereas *RASAL2* is mutated in breast cancer and in other human tumors, it appears to be more commonly inactivated via nonmutational mechanisms. Notably, the other Ras-GAP tumor suppressors, *NF1* and *DAB2IP*, are also inactivated by both genetic and several nongenetic mechanisms (McGillicuddy et al., 2009; Min et al., 2010). Similarly, *PTEN* and *INPP4B*, two other tumor suppressors that negatively regulate an overlapping set of signals, are also suppressed by multiple mechanisms in cancer, some of which have not yet been elucidated (Gewinner et al., 2009; Song et al., 2012). As such, loss of PTEN protein expression, rather than mutational status or copy number, is often evaluated in clinical samples during clinical trials and for pathological staging (Thomas et al., 2004). The observation that *RASAL2* loss plays a causal role in breast cancer progression and metastasis in animal models and that *RASAL2* expression is lowest in primary human tumors that ultimately progress or recur, suggests that *RASAL2* could be useful as a prognostic biomarker, in at least a subset of breast cancers, such as luminal B tumors. Regardless, these studies have identified an important tumor suppressor involved in breast cancer progression and have revealed an alternative mechanism by which Ras becomes activated in this disease.

EXPERIMENTAL PROCEDURES

Cell Culture and DNA Constructs

MEFs were immortalized as described previously (Johannessen et al., 2005). MCF7, MCF10A, and MDA-MB-361 cells were purchased from American Type Culture Collection. BT549, HS578T, MDA-MB-231, MDA-MB-453, MDA-MB-468, SKBR3, T47D, and ZR-75-1 cells were obtained from Dr. William Hahn (Dana-Farber Cancer Institute). SUM149PT, SUM159PT, SUM1315MO, and BT474 cells were obtained from Dr. Frank McCormick (University of California, San Francisco). CAMA1 cells were obtained from Dr. Marcia Haigis (Harvard Medical School). MCF10ADCIS were provided by Dr. Fred Miller (Karmanos Cancer Institute) and the Polyak laboratory.

shRNAs from the RNAi Consortium (Broad Institute, MIT) with the following sequences were utilized: *NF1* shRNA (5′-TTATAAATAGCCTGGAAAAGG-3′), *RASAL2* shRNA1 (5′-CCCTCGTGTTCTTGCTGATAT-3′), *RASAL2* shRNA2 (5′-GCCTTCCACCTCTTCATAGTA-3′), *KRAS* shRNA (5′- CAGTTGAGACCT TCTAATTGG-3′), and *HRAS* shRNA (5′- GACGTGCCTGTTGGACATCCT-3′). A scrambled shRNA was purchased from Addgene (5′-CCTAAGGTTAA GTCGCCCTCG-3′). A *RASAL2*-targeting shRNA was cloned into the pLKO vector (shRNA3) (5′-ATGGAGTGCAATAGGACATTG-3′). The Mammalian Gene Collection fully sequenced human *RASAL2* complementary DNA (cDNA) was purchased from Open Biosystems (cat. number MHS4426-99623118) and was cloned into the pHAGE-N-Flag-HA lentiviral expression vector (Dr. J. Wade Harper, Harvard Medical School) for expression in cell lines. Infections and transfections were performed as described in the Supplemental Experimental Procedures.

Proliferation, soft agar, migration, and in vitro invasion assays are described in the Supplemental Experimental Procedures.

Xenograft Assays

Female nude and NOD/SCID mice were purchased from Charles River Laboratories (cat. numbers 088 and 394, respectively) for subcutaneous xenograft experiments. Cells were injected with Matrigel (BD Biosciences, cat. number 354234) as follows: MCF10ADCIS (1×10^5 cells, 50% matrigel, nude mice), MDA-MB-231 (1×10^6 cells, 50% matrigel, nude mice), and CAMA1 (2×10^6 cells, 50% matrigel, NOD/SCID mice). For mammary fat pad orthotopic xenograft experiments, 1×10^6 MDA-MB-361 cells were injected in 50% matrigel bilaterally into the fourth mammary glands of female NOD/SCID mice (Jackson Laboratories). Tumor size was measured by caliper, and tumor volume was calculated using the formula of volume = (length × width^2) × $\pi/6$.

MCF10ADCIS Invasion Assay

RASAL2 expression was ablated in MCF10ADCIS cells using two distinct shRNAs, and loss of RASAL2 expression was confirmed by immunoblot. Female nude (nu/nu) mice were injected subcutaneously with 100,000 sh*RASAL2* or shScramble control cells. Five or six tumors of each genotype (Scramble shRNA, *RASAL2* shRNA1, or *RASAL2* shRNA2) were harvested after 3 weeks, fixed, and stained with hematoxylin and eosin (H&E) to assess tumor morphology. A pathologist scored a tumor as an invasive carcinoma if it was

representative section of lungs for each tumor-bearing female ($p = 0.04$). Average metastasis burden per animal: average total area of metastasis in a representative section of lung for each tumor-bearing female (arbitrary units; $p = 0.04$). See also Figure S2.

(F) H&E images of metastases to brain (a), gut (b), ovary (c), and kidney (d) in compound tumor-bearing females. M indicates regions of metastasis.

(G) Western blot analysis of phospho-ERK (pERK) and phospho-AKT (pAKT) levels in primary mammary tumors from *MMTVneu*; *Rasal2*$^{+/+}$ animals (numbers 1–9) and *MMTVneu*; *Rasal2*$^{-/-}$ animals (numbers 10–18).

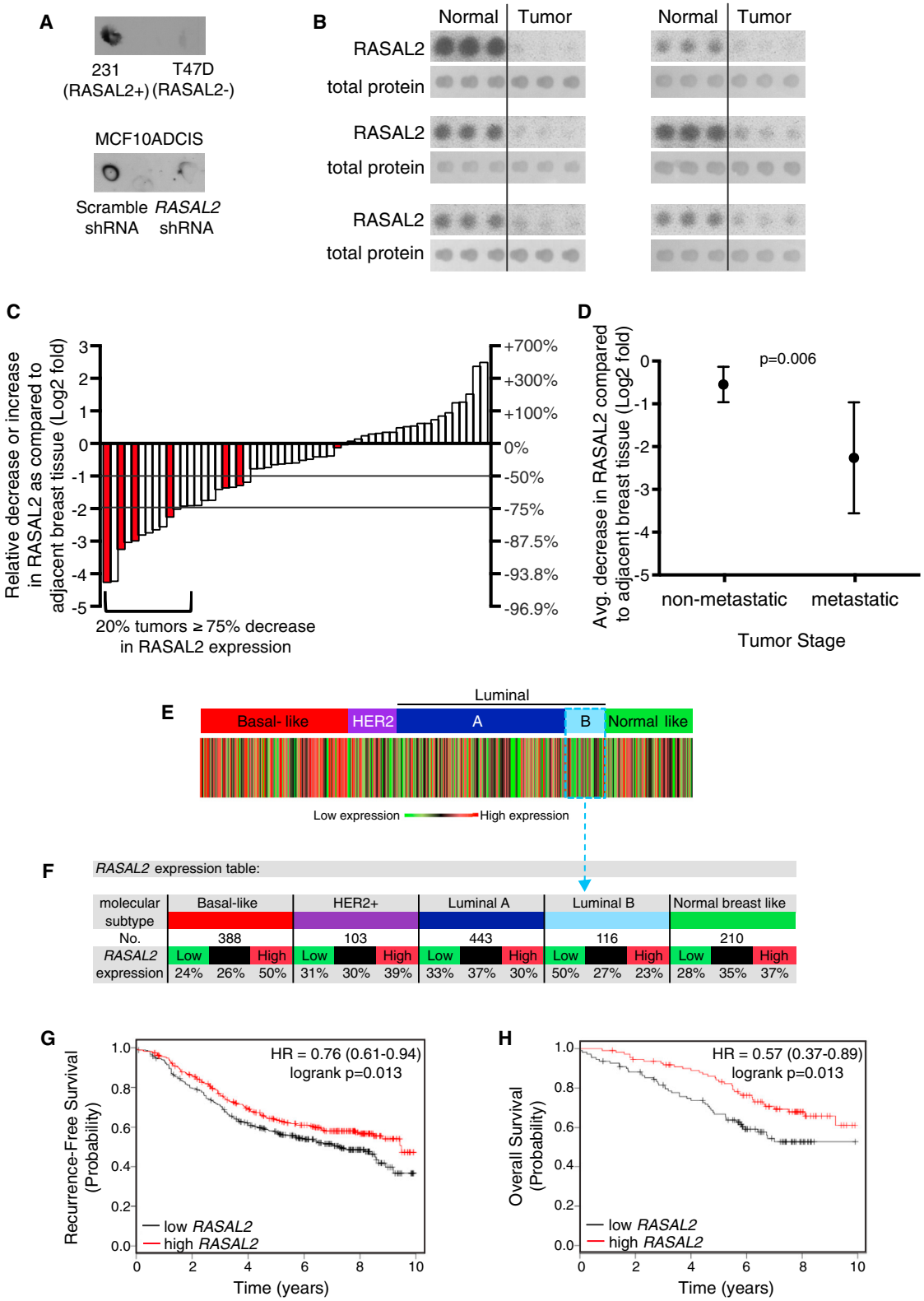

Figure 6. RASAL2 Expression Is Lost/Low in Primary Human Breast Cancers, and Low Levels Are Associated with Metastasis and Recurrence

(A) RASAL2 dot blot of whole-cell RIPA extracts from human breast cancer cell lines with high or low RASAL2 expression (MDA-MB-231 "231" and T47D, respectively) (top) or MCF10ADCIS cells infected with control or *RASAL2*-targeting shRNAs (bottom).

(legend continued on next page)

accompanied by an obvious loss in its well-circumscribed appearance and a disruption of the myoepithelium and basement membrane.

Rasal2 Mutant Mice

All animal procedures were approved by the Center for Animal and Comparative Medicine at Harvard Medical School in accordance with the National Institutes of Health Guildelines for the Care and Use of Laboratory Animals and the Animal Welfare Act.

A mouse embryonic stem cell line in which the pNMDi4 genetrap cassette targets *Rasal2* was purchased from the Toronto Centre for Phenogenomics/Canadian Mouse Mutant Repository (clone CMHD 463C12). The pNMDi4 genetrap cassette contains the following elements as depicted in Figure 4A: HA 3/5 SA (splice acceptor), FL (flexible linker), Venus (enhanced yellow fluorescent gene) with stop codon, loxP sites, pA (polyadenylation signal), PGK (promoter), neo (neomycin resistance gene) with stop codon, and HPRT SD (splice donor). The neomycin resistance gene stop codon prevents translation of 3′ exons. The presence of the genetrap cassette within the third intron of *Rasal2* was confirmed using cDNA PCR. Chimeric mice were generated and crossed to C57BL/6-E animals (Charles River Laboratories), and pups were tested for presence of the genetrap. Two additional copies of the genetrap cassette elsewhere in the genome were discovered in the mouse ES cell line and genetrap mice. Genetrap-positive mice were crossed to wild-type animals, and Southern blotting was used to identify pups that had the genetrap cassette only within the *Rasal2* locus (data not shown). These animals were used as founders for all cohorts and subsequent crosses.

Rasal2 Genotyping

Primers for PCR of the genetrap cassette were NMD.F (5′-CATGGTCCTGCTGGAGTTC-3′) and NMD.R (5′-TGCCTTTAGACCTTTTTGTGG-3′). Total RNA was extracted from homogenized tails using QiaShredder and RNeasy kits (QIAGEN), and cDNA was synthesized using qScript cDNA Synthesis Kit (Quanta). PCR was performed on cDNA with primers NeoL (5′-GCTATCAGGACATAGCGTTGGCTAC-3′), GT463C12_F3 (5′-TCGGATCCTTCTGGAGTCAG-3′), and GT463C12_R1 (5′-CTCTCTCGGAGGCAGAGCTA-3′) to detect wild-type (F3/R1) and mutant (NeoL/R1) transcripts.

Compound Mutant Mice

Rasal2 genetrap mice were crossed to FVB/N-Tg(MMTVneu)202Mul/J mice (Jackson Laboratories, cat. number 002376) (Guy et al., 1992) or to B6.129S2-*Trp53*^{Tm1Tyj}/J mice (Jackson Laboratories, cat. number 002101) (Jacks et al., 1994). Cohorts of *Rasal2* mutant mice and controls were on a 129-enriched background (75% 129SvImJ, 25% C57BL6). Cohorts of *Trp53; Rasal2* compound mice and controls were on a mixed 129/B6 background (62.5% C57BL6, 37.5% 129SvImJ). Cohorts of *MMTVneu*; *Rasal2* compound mice and controls were on a background of 56% 129SvImJ, 25% FVB, and 19% C57BL6.

Protein Lysates and Western Blot Analyses

Protein extracts were isolated from cells or homogenized tissue in 1% SDS boiling lysis buffer. Ras-GTP levels were determined using a Ras Activation Assay Kit (EMD Millipore). The following antibodies were used for immunoblots: actin (Sigma, cat. number A2066), phospho-AKT (Ser473, Cell Signaling, cat. number 4060), AKT (Cell Signaling, cat. number 9272), ER (Thermo, cat. number R9101-SO), phospho-ERK (Thr202/Thr204, Cell Signaling, cat. number 4370), ERK (Cell Signaling, cat. number 9102), GAPDH (Cell Signaling, cat. number 2118), HA (Covance, cat. number MMS-101P), HER2 (Cell Signaling, cat. number 2242), NF1 (UP69 C-terminal polyclonal antibody) (McGillicuddy et al., 2009), p120RasGAP (BD Transduction Laboratories, cat. number 610040), HRas (Santa Cruz, cat. number SC-520), KRas (Santa Cruz, cat. number SC-30), panRas (Upstate, cat. number 05-516), α-tubulin (Sigma, cat. number T5168), β-tubulin (Sigma, cat. number T4026), and Vinculin (Cell Signaling, cat. number 4650). A peptide antigen (NP_773793 amino acids 1111–1130) was used to generate and affinity purify an anti-RASAL2 rabbit polyclonal antibody (Covance ImmunoTechnologies). For RASAL2, reconstitution studies cells were typically plated in 5% serum overnight 36 hr posttransfection. pERK and ERK levels were assessed by western blot and quantified using ImageJ software.

Immunohistochemistry was performed as described in the Supplemental Experimental Procedures.

Mouse Tumor and Tissue Analysis

Tumors and tissues were fixed in buffered formalin, stored in 70% ethanol, paraffin embedded, and sectioned. Sections were stained with hematoxylin and eosin.

Human Tumor Lysate Array Analysis

Qualitative breast cancer tumor lysate arrays were purchased from Protein Biotechnologies (cat. number PMA2-001-L). Samples were deidentified and are not considered human subject research. Arrays were probed with the affinity purified RASAL2 antibody. The RASAL2 antibody was validated for this assay using tumor lysate arrays by probing nitrocellulose membranes spotted with 1 μg/μl RIPA lysates from human breast cancer cell lines with or without RASAL2. Developed film was scanned and quantified using ImageJ software. Arrays were stained with Colloidal Gold and scanned, and total protein was quantified using ImageJ. RASAL2 levels in each spot were normalized to the Colloidal Gold level in the same spot. Triplicate spots were averaged, and the ratio between the tumor normalized triplicate and normal normalized triplicate was calculated and reported as a Log2 fold change value.

Molecular Subtype Association and Survival Analysis

Gene expression correlations targeted analysis was applied on published genomic data on patients classified in the same molecular subtype with the six molecular subtype predictors (Sørlie et al., 2001; Hu et al., 2006), using GenExMiner as previously described (Jézéquel et al., 2012). Samples were deidentified and are not considered human subject research. A gene expression map was determined by molecular subtype predictors (single sample predictors [SSPs] and/or subtype clustering models [SCMs]). A gene expression table was also provided for robust classifications, indicating for each subtype the proportion of patient with low, intermediate, and high gene expression; gene expression values were split in order to form three equal groups.

Gene expression data and relapse-free and overall survival information were analyzed as previously described (Győrffy et al., 2010). Data were downloaded from GEO (Affymetrix HGU133A and HGU133+2 microarrays), EGA, and TCGA. The background database integrates gene expression and clinical data simultaneously. To analyze the prognostic value of RASAL2, the patient samples are split into two groups according to median expression of RASAL2.

(B) Dot blot images from human breast tumor lysate array. Six sets of RASAL2 and total protein stains are shown. Each set contains triplicate spots of tumor lysate (right) and triplicate spots of paired normal tissue lysate (left).
(C) Quantification of RASAL2 expression in tumor lysate arrays. Each bar depicts the change in RASAL2 expression in one sample as compared to the sample's matched normal control as described in the Experimental Procedures. Red bars indicate metastatic samples.
(D) RASAL2 protein expression in tumor versus normal in nonmetastatic (stages I, II, and III) versus metastatic (stage IV) tumors. Graph shows the Log2 fold change in RASAL2 protein expression in tumor versus normal. Data are reported as average ± 95% CI. p = 0.006.
(E) Heatmap of *RASAL2* gene expression as a function of robust molecular subtype predictor classification, which is based on patients classified in the same tumor subtype. Percentages of tumors with high, intermediate, and low *RASAL2* expression per molecular subtype are given in the gene expression table.
(F) *RASAL2* expression table. For each breast cancer subtype, the number of samples and percentage of samples with low, intermediate, or high *RASAL2* mRNA expression are indicated.
(G) Kaplan-Meier curve showing recurrence-free survival of luminal B tumors with high or low *RASAL2* expression (log rank p = 0.013).
(H) Kaplan-Meier curve showing overall survival of luminal B tumors with high or low *RASAL2* expression (log rank p = 0.013).

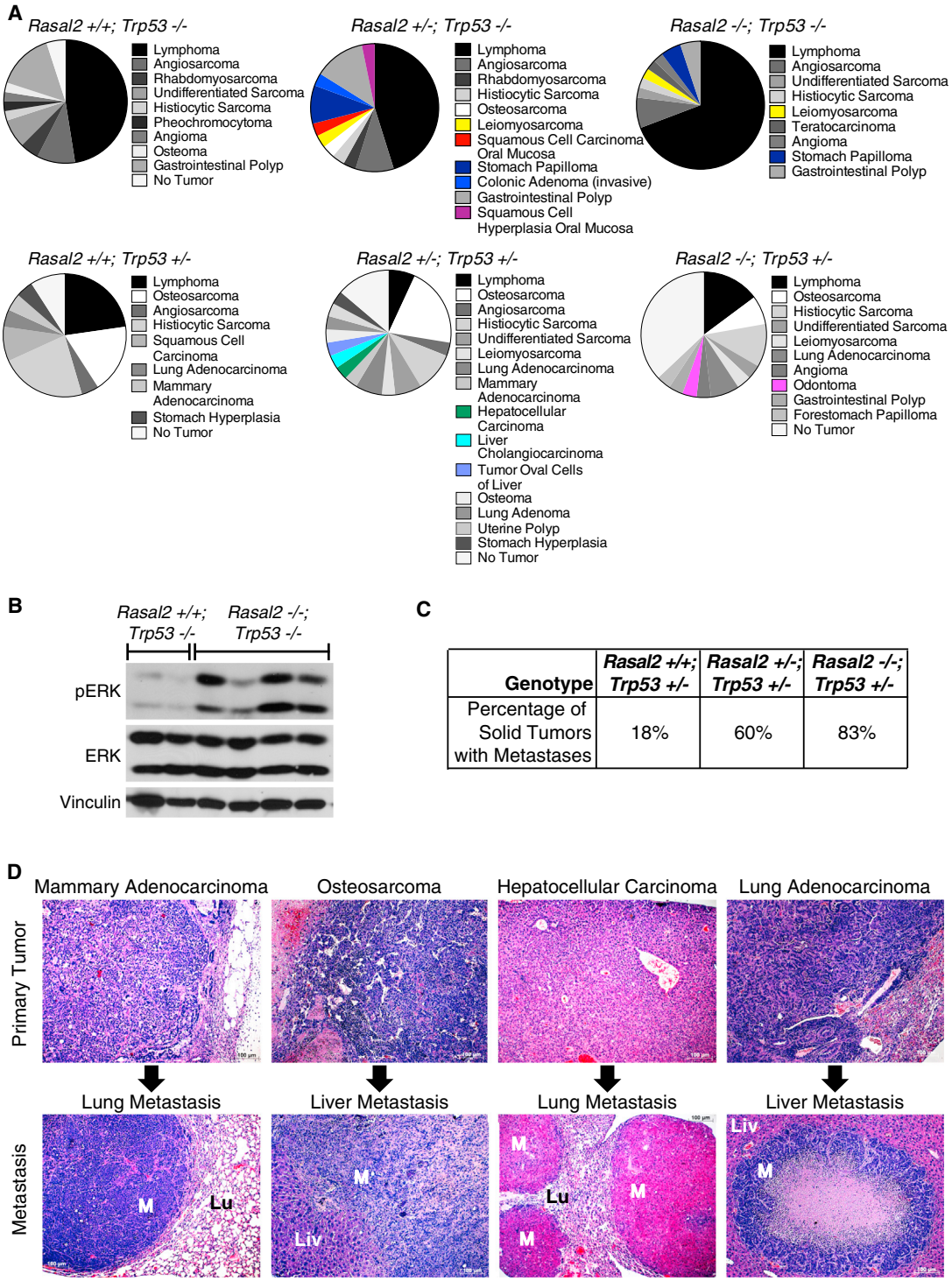

Genotype	*Rasal2 +/+; Trp53 +/-*	*Rasal2 +/-; Trp53 +/-*	*Rasal2 -/-; Trp53 +/-*
Percentage of Solid Tumors with Metastases	18%	60%	83%

Figure 7. *Rasal2*, *Trp53* Compound Mutant Mice Develop Highly Metastatic Tumors

(A) Phenotypes in *Rasal2*/*Trp53* compound mutant mice. Pie charts display the array of phenotypes in each genotype. Phenotypes observed in *Rasal2* mutant compound mice, but not observed in control cohorts, are shown in color. n = 21 $Rasal2^{+/+}; Trp53^{-/-}$, 18 $Rasal2^{+/-}; Trp53^{-/-}$, 31 $Rasal2^{-/-}; Trp53^{-/-}$ 16 $Rasal2^{+/+}; Trp53^{+/-}$, 21 $Rasal2^{+/-}; Trp53^{+/-}$, 21 $Rasal2^{-/-}; Trp53^{+/-}$.

(B) Western blot analysis of phospho-ERK (pERK) levels in primary tumors from $Rasal2^{+/+;}$ $Trp53^{-/-}$ and $Rasal2^{-/-}; Trp53^{-/-}$ compound mice.

(C) Percentage of metastatic solid tumors in $Rasal2^{+/+}$, $^{+/-}$, and $^{-/-}; Trp53^{+/-}$ compound mice. Increased metastasis in compound animals is statistically significant ($p = 0.003$). The paucity of metastatic solid tumors in $Trp53^{+/-}$ mice is supported by historical data.

(D) Images of metastatic lesions (bottom) and the corresponding primary tumors (top). From left to right: Mammary adenocarcinoma and lung metastasis, osteosarcoma and liver metastasis, hepatocellular carcinoma and lung metastasis, and lung adenocarcinoma and liver metastasis. M, metastasis; Lu, lung; Liv, liver.

SUPPLEMENTAL INFORMATION

Supplemental Information includes Supplemental Experimental Procedures, two figures, and three tables and can be found with this article online at http://dx.doi.org/10.1016/j.ccr.2013.08.004.

ACKNOWLEDGMENTS

This work was supported by grants from the Ludwig Center at Dana-Farber/Harvard Cancer Center (to K.C.), the National Cancer Institute (R01 CA111754 to K.C.), the Department of Defense (W81XWH-11-1-0140 to S.K.M.), and the National Institutes of Health National Heart, Lung, and Blood Institute (T32-HL07623 to S.K.M.).

Received: March 8, 2013
Revised: July 7, 2013
Accepted: August 6, 2013
Published: September 9, 2013

REFERENCES

Bamford, S., Dawson, E., Forbes, S., Clements, J., Pettett, R., Dogan, A., Flanagan, A., Teague, J., Futreal, P.A., Stratton, M.R., and Wooster, R. (2004). The COSMIC (Catalogue of Somatic Mutations in Cancer) database and website. Br. J. Cancer *91*, 355–358.

Bernards, A. (2003). GAPs galore! A survey of putative Ras superfamily GTPase activating proteins in man and Drosophila. Biochim. Biophys. Acta *1603*, 47–82.

Cancer Genome Atlas Network. (2012). Comprehensive molecular portraits of human breast tumours. Nature *490*, 61–70.

Cancer Genome Atlas Research Network. (2008). Comprehensive genomic characterization defines human glioblastoma genes and core pathways. Nature *455*, 1061–1068.

Cawthon, R.M., Weiss, R., Xu, G.F., Viskochil, D., Culver, M., Stevens, J., Robertson, M., Dunn, D., Gesteland, R., O'Connell, P., et al. (1990). A major segment of the neurofibromatosis type 1 gene: cDNA sequence, genomic structure, and point mutations. Cell *62*, 193–201.

Ding, L., Getz, G., Wheeler, D.A., Mardis, E.R., McLellan, M.D., Cibulskis, K., Sougnez, C., Greulich, H., Muzny, D.M., Morgan, M.B., et al. (2008). Somatic mutations affect key pathways in lung adenocarcinoma. Nature *455*, 1069–1075.

Donehower, L.A., Harvey, M., Slagle, B.L., McArthur, M.J., Montgomery, C.A., Jr., Butel, J.S., and Bradley, A. (1992). Mice deficient for p53 are developmentally normal but susceptible to spontaneous tumours. Nature *356*, 215–221.

Dote, H., Toyooka, S., Tsukuda, K., Yano, M., Ouchida, M., Doihara, H., Suzuki, M., Chen, H., Hsieh, J.-T., Gazdar, A.F., and Shimizu, N. (2004). Aberrant promoter methylation in human DAB2 interactive protein (hDAB2IP) gene in breast cancer. Clin. Cancer Res. *10*, 2082–2089.

Downward, J. (2003). Targeting RAS signalling pathways in cancer therapy. Nat. Rev. Cancer *3*, 11–22.

Gewinner, C., Wang, Z.C., Richardson, A., Teruya-Feldstein, J., Etemadmoghadam, D., Bowtell, D., Barretina, J., Lin, W.M., Rameh, L., Salmena, L., et al. (2009). Evidence that inositol polyphosphate 4-phosphatase type II is a tumor suppressor that inhibits PI3K signaling. Cancer Cell *16*, 115–125.

Győrffy, B., Lanczky, A., Eklund, A.C., Denkert, C., Budczies, J., Li, Q., and Szallasi, Z. (2010). An online survival analysis tool to rapidly assess the effect of 22,277 genes on breast cancer prognosis using microarray data of 1,809 patients. Breast Cancer Res. Treat. *123*, 725–731.

Guy, C.T., Webster, M.A., Schaller, M., Parsons, T.J., Cardiff, R.D., and Muller, W.J. (1992). Expression of the neu protooncogene in the mammary epithelium of transgenic mice induces metastatic disease. Proc. Natl. Acad. Sci. USA *89*, 10578–10582.

Herschkowitz, J.I., Simin, K., Weigman, V.J., Mikaelian, I., Usary, J., Hu, Z., Rasmussen, K.E., Jones, L.P., Assefnia, S., Chandrasekharan, S., et al. (2007). Identification of conserved gene expression features between murine mammary carcinoma models and human breast tumors. Genome Biol. *8*, R76.

Hollestelle, A., Elstrodt, F., Nagel, J.H.A., Kallemeijn, W.W., and Schutte, M. (2007). Phosphatidylinositol-3-OH kinase or RAS pathway mutations in human breast cancer cell lines. Mol. Cancer Res. *5*, 195–201.

Hölzel, M., Huang, S., Koster, J., Ora, I., Lakeman, A., Caron, H., Nijkamp, W., Xie, J., Callens, T., Asgharzadeh, S., et al. (2010). NF1 is a tumor suppressor in neuroblastoma that determines retinoic acid response and disease outcome. Cell *142*, 218–229.

Hu, Z., Fan, C., Oh, D.S., Marron, J.S., He, X., Qaqish, B.F., Livasy, C., Carey, L.A., Reynolds, E., Dressler, L., et al. (2006). The molecular portraits of breast tumors are conserved across microarray platforms. BMC Genomics *7*, 96.

Hu, M., Yao, J., Carroll, D.K., Weremowicz, S., Chen, H., Carrasco, D., Richardson, A., Violette, S., Nikolskaya, T., Nikolsky, Y., et al. (2008). Regulation of in situ to invasive breast carcinoma transition. Cancer Cell *13*, 394–406.

Jacks, T., Remington, L., Williams, B.O., Schmitt, E.M., Halachmi, S., Bronson, R.T., and Weinberg, R.A. (1994). Tumor spectrum analysis in p53-mutant mice. Curr. Biol. *4*, 1–7.

Jézéquel, P., Campone, M., Gouraud, W., Guérin-Charbonnel, C., Leux, C., Ricolleau, G., and Campion, L. (2012). bc-GenExMiner: an easy-to-use online platform for gene prognostic analyses in breast cancer. Breast Cancer Res. Treat. *131*, 765–775.

Johannessen, C.M., Reczek, E.E., James, M.F., Brems, H., Legius, E., and Cichowski, K. (2005). The NF1 tumor suppressor critically regulates TSC2 and mTOR. Proc. Natl. Acad. Sci. USA *102*, 8573–8578.

Kamangar, F., Dores, G.M., and Anderson, W.F. (2006). Patterns of cancer incidence, mortality, and prevalence across five continents: defining priorities to reduce cancer disparities in different geographic regions of the world. J. Clin. Oncol. *24*, 2137–2150.

Karnoub, A.E., and Weinberg, R.A. (2008). Ras oncogenes: split personalities. Nat. Rev. Mol. Cell Biol. *9*, 517–531.

Kim, I.S., and Baek, S.H. (2010). Mouse models for breast cancer metastasis. Biochem. Biophys. Res. Commun. *394*, 443–447.

Krauthammer, M., Kong, Y., Ha, B.H., Evans, P., Bacchiocchi, A., McCusker, J.P., Cheng, E., Davis, M.J., Goh, G., Choi, M., et al. (2012). Exome sequencing identifies recurrent somatic RAC1 mutations in melanoma. Nat. Genet. *44*, 1006–1014.

Lim, E., Vaillant, F., Wu, D., Forrest, N.C., Pal, B., Hart, A.H., Asselin-Labat, M.-L., Gyorki, D.E., Ward, T., Partanen, A., et al.; kConFab. (2009). Aberrant luminal progenitors as the candidate target population for basal tumor development in BRCA1 mutation carriers. Nat. Med. *15*, 907–913.

Maertens, O., Johnson, B., Hollstein, P., Frederick, D.T., Cooper, Z.A., Messaien, L., Bronson, R.T., McMahon, M., Granter, S., Flaherty, K.T., et al. (2012). Elucidating distinct roles for NF1 in melanomagenesis. Cancer Discov. *3*, 338–349.

McGillicuddy, L.T., Fromm, J.A., Hollstein, P.E., Kubek, S., Beroukhim, R., De Raedt, T., Johnson, B.W., Williams, S.M.G., Nghiemphu, P., Liau, L.M., et al. (2009). Proteasomal and genetic inactivation of the NF1 tumor suppressor in gliomagenesis. Cancer Cell *16*, 44–54.

Miller, F.R., Santner, S.J., Tait, L., and Dawson, P.J. (2000). MCF10DCIS.com xenograft model of human comedo ductal carcinoma in situ. J. Natl. Cancer Inst. *92*, 1185–1186.

Min, J., Zaslavsky, A., Fedele, G., McLaughlin, S.K., Reczek, E.E., De Raedt, T., Guney, I., Strochlic, D.E., Macconaill, L.E., Beroukhim, R., et al. (2010). An oncogene-tumor suppressor cascade drives metastatic prostate cancer by coordinately activating Ras and nuclear factor-kappaB. Nat. Med. *16*, 286–294.

Mueller, H., Flury, N., Eppenberger-Castori, S., Kueng, W., David, F., and Eppenberger, U. (2000). Potential prognostic value of mitogen-activated protein kinase activity for disease-free survival of primary breast cancer patients. Int. J. Cancer *89*, 384–388.

Mueller, C., Liotta, L.A., and Espina, V. (2010). Reverse phase protein microarrays advance to use in clinical trials. Mol. Oncol. *4*, 461–481.

Parsons, D.W., Jones, S., Zhang, X., Lin, J.C.-H., Leary, R.J., Angenendt, P., Mankoo, P., Carter, H., Siu, I.-M., Gallia, G.L., et al. (2008). An integrated genomic analysis of human glioblastoma multiforme. Science *321*, 1807–1812.

Perou, C.M., Sørlie, T., Eisen, M.B., van de Rijn, M., Jeffrey, S.S., Rees, C.A., Pollack, J.R., Ross, D.T., Johnsen, H., Akslen, L.A., et al. (2000). Molecular portraits of human breast tumours. Nature *406*, 747–752.

Pylayeva-Gupta, Y., Grabocka, E., and Bar-Sagi, D. (2011). RAS oncogenes: weaving a tumorigenic web. Nat. Rev. Cancer *11*, 761–774.

Shah, S.P., Roth, A., Goya, R., Oloumi, A., Ha, G., Zhao, Y., Turashvili, G., Ding, J., Tse, K., Haffari, G., et al. (2012). The clonal and mutational evolution spectrum of primary triple-negative breast cancers. Nature *486*, 395–399.

Sivaraman, V.S., Wang, H., Nuovo, G.J., and Malbon, C.C. (1997). Hyperexpression of mitogen-activated protein kinase in human breast cancer. J. Clin. Invest. *99*, 1478–1483.

Sjöblom, T., Jones, S., Wood, L.D., Parsons, D.W., Lin, J., Barber, T.D., Mandelker, D., Leary, R.J., Ptak, J., Silliman, N., et al. (2006). The consensus coding sequences of human breast and colorectal cancers. Science *314*, 268–274.

Song, M.S., Salmena, L., and Pandolfi, P.P. (2012). The functions and regulation of the PTEN tumour suppressor. Nat. Rev. Mol. Cell Biol. *13*, 283–296.

Sørlie, T., Perou, C.M., Tibshirani, R., Aas, T., Geisler, S., Johnsen, H., Hastie, T., Eisen, M.B., van de Rijn, M., Jeffrey, S.S., et al. (2001). Gene expression patterns of breast carcinomas distinguish tumor subclasses with clinical implications. Proc. Natl. Acad. Sci. USA *98*, 10869–10874.

Thomas, G.V., Horvath, S., Smith, B.L., Crosby, K., Lebel, L.A., Schrage, M., Said, J., De Kernion, J., Reiter, R.E., and Sawyers, C.L. (2004). Antibody-based profiling of the phosphoinositide 3-kinase pathway in clinical prostate cancer. Clin. Cancer Res. *10*, 8351–8356.

von Lintig, F.C., Dreilinger, A.D., Varki, N.M., Wallace, A.M., Casteel, D.E., and Boss, G.R. (2000). Ras activation in human breast cancer. Breast Cancer Res. Treat. *62*, 51–62.

Vousden, K.H., and Lane, D.P. (2007). p53 in health and disease. Nat. Rev. Mol. Cell Biol. *8*, 275–283.

Weigelt, B., Peterse, J.L., and van 't Veer, L.J. (2005). Breast cancer metastasis: markers and models. Nat. Rev. Cancer *5*, 591–602.

Cancer Cell
Article

Transformation-Associated Changes in Sphingolipid Metabolism Sensitize Cells to Lysosomal Cell Death Induced by Inhibitors of Acid Sphingomyelinase

Nikolaj H.T. Petersen,[1,5] Ole D. Olsen,[1,5] Line Groth-Pedersen,[1,6] Anne-Marie Ellegaard,[1] Mesut Bilgin,[2,7] Susanne Redmer,[3] Marie S. Ostenfeld,[1,8] Danielle Ulanet,[4] Tobias H. Dovmark,[1] Andreas Lønborg,[1] Signe D. Vindeløv,[1] Douglas Hanahan,[4,9] Christoph Arenz,[3] Christer S. Ejsing,[2] Thomas Kirkegaard,[1,5] Mikkel Rohde,[1] Jesper Nylandsted,[1] and Marja Jäättelä[1,*]

[1]Department of Cell Death and Metabolism, Danish Cancer Society Research Center (DCRC), DK-2100 Copenhagen, Denmark
[2]Department of Biochemistry and Molecular Biology, University of Southern Denmark, DK-5230 Odense, Denmark
[3]Department of Chemistry, Humboldt-Universität zu Berlin, D-10099 Berlin, Germany
[4]Department of Biochemistry and Biophysics, University of California, San Francisco, San Francisco, CA 94143, USA
[5]Present address: Orphazyme Aps, DK-2200 Copenhagen, Denmark
[6]Present address: Pediatric Clinic II, Rigshospitalet University Hospital, DK-2100 Copenhagen, Denmark
[7]Present address: Max-Planck-Institute of Molecular Cell Biology and Genetics, D-01307 Dresden, Germany
[8]Present address: Department of Molecular Medicine, Aarhus University Hospital, Skejby, DK-8200 Aarhus, Denmark
[9]Present address: Swiss Institute for Experimental Cancer Research (ISREC), Swiss Federal Institute of Technology Lausanne (EPFL), CH-1015 Lausanne, Switzerland
*Correspondence: mj@cancer.dk
http://dx.doi.org/10.1016/j.ccr.2013.08.003

SUMMARY

Lysosomal membrane permeabilization and subsequent cell death may prove useful in cancer treatment, provided that cancer cell lysosomes can be specifically targeted. Here, we identify acid sphingomyelinase (ASM) inhibition as a selective means to destabilize cancer cell lysosomes. Lysosome-destabilizing experimental anticancer agent siramesine inhibits ASM by interfering with the binding of ASM to its essential lysosomal cofactor, bis(monoacylglycero)phosphate. Like siramesine, several clinically relevant ASM inhibitors trigger cancer-specific lysosomal cell death, reduce tumor growth in vivo, and revert multidrug resistance. Their cancer selectivity is associated with transformation-associated reduction in ASM expression and subsequent failure to maintain sphingomyelin hydrolysis during drug exposure. Taken together, these data identify ASM as an attractive target for cancer therapy.

INTRODUCTION

Cancer cells frequently harbor genetic alterations that allow them to escape spontaneous and therapy-induced apoptosis. Resistance is often acquired already during an early phase of tumor development when genetic changes cause defects in caspase-dependent apoptosis pathways and provide transformed cells with higher growth and survival potential (Hanahan and Weinberg, 2011). Furthermore, cancers treated with chemotherapeutic drugs often acquire the ability to efflux drugs by increasing the expression of multidrug resistance (MDR) proteins, P-glycoproteins of the ATP-binding cassette transporter family (Gottesman et al., 2002). Thus, alternative cell death pathways capable of killing apoptosis- and therapy-resistant cancer cells have gained vast interest among cancer researchers, leading to the identification of lysosomal cell death programs as attractive means to circumvent therapy resistance (Česen et al., 2012; Groth-Pedersen and Jäättelä, 2013).

The concept of lysosomal cell death was originally presented by Christian de Duve, who was awarded the Nobel Prize in

Significance

Defective apoptosis signaling and multidrug resistance are prime obstacles for successful cancer treatment. Data presented here reveal acid sphingomyelinase (ASM) as a target for the treatment of therapy-resistant cancers. ASM activity is essential for lysosomal stability and survival of cancer cells, as well as for multidrug-resistant phenotype. Of note, several widely used cationic amphiphilic drugs, including tricyclic antidepressants, antihistamines and calcium channel blockers, inhibit ASM and trigger lysosomal cell death even in apoptosis- and multidrug-resistant cancer cells. ASM inhibitors should prove efficacious in tumors with low sphingomyelinase activity, or when combined with classic chemotherapy, even to treat tumors that have acquired therapy resistance.

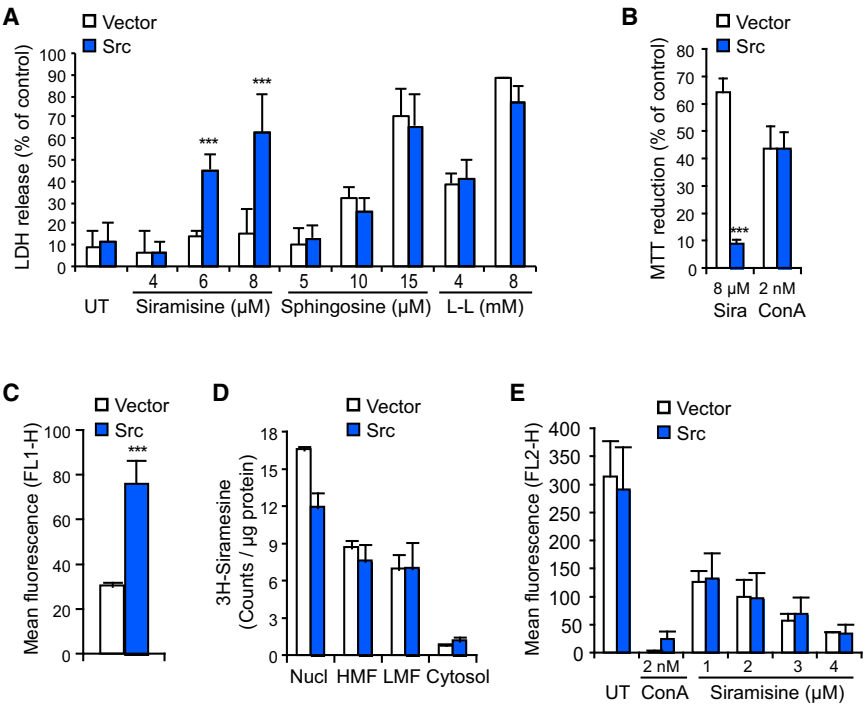

Figure 1. Transformation Does Not Alter Sensitivity to Detergents and Concanamycin A or Uptake of Siramesine

(A and B) The NIH 3T3-vector (Vector) and -*c-src*^{Y527F} (Src) cells were left untreated (UT) or treated as indicated for 26 hr. Cell death and viability were determined by LDH release (A) and MTT (B) assays, respectively. L-L, Leu-LeuOMe; Sira, siramesine; ConA, concanamycin A.

(C) Endocytic capacity of cells was analyzed by flow cytometry after treatment with 40 μg/mL dextran-488 for 2 hr.

(D) Subcellular distribution of ^{3}H-siramesine in cells treated with 0.1 μM ^{3}H-siramesine for 3 hr followed by a 1 hr chase period. The radioactivity in nuclei (Nucl), heavy membrane fractions (HMF), light membrane fractions (LMF), and cytosol were measured.

(E) The volume of the acidic compartment in cells treated as indicated for 1 hr with 25 nM LysotrackerRed present during the last 15 min was measured by flow cytometry.

Error bars indicate SD from two independent triplicate experiments in (B), three independent triplicate experiments in (A), (C), and (E), or a representative (n = 3) triplicate experiment in (D).

1974 for his discovery and characterization of lysosomes as cellular "recycling bins." Because of the potent hydrolytic capacity of lysosomal enzymes, he also defined lysosomes as "suicide bags" that can cause cell and tissue autolysis upon rupture (de Duve, 1983). This triggered an intensive search for compounds that destabilize lysosomal membranes for the treatment of cancer. As a result, amines with long hydrophobic chains and high pK values were identified as lysosomotropic detergents with potential applications in cancer therapy (Firestone et al., 1979). Interest in lysosomal cell death pathways waned, however, rapidly. This was largely due to the lack of proper assay systems that could differentiate lysosomal rupture that causes cell death from postmortal alterations in autolytic cells, as well as the assumption that lysosomotropic detergents would be equally toxic to normal and transformed cells (de Duve, 1983). Accordingly, novel assays to study lysosomal membrane permeabilization, as well as realization that cancer cell lysosomes are less stable than normal lysosomes, were needed to initiate a new wave of interest in lysosomal cell death pathways in the beginning of the 21st century (Fehrenbacher et al., 2004; Leist and Jäättelä, 2001). Subsequently, emerging genetic data have corroborated the role of cathepsins as evolutionarily conserved executors of cell death and the role of lysosomal leakage as a significant mediator of both physiological (e.g., mammary involution) and pathological (e.g., degenerative and infectious diseases) cell demise in diverse organisms from yeast, roundworm, and fruit fly to mammals (Canbay et al., 2003; Guicciardi et al., 2001; Halangk et al., 2000; Houseweart et al., 2003; Kinser and Dolph, 2012; Kreuzaler et al., 2011; Luke et al., 2007; Matsuda et al., 2012; Syntichaki et al., 2002).

We have recently identified siramesine (1′-[4-[1-(4-fluorophenyl)-1H-indol-3-yl]-1-butyl]spiro[iso- benzo furan-1(3H),4′-piperidine]) as a lysosomotropic detergent that kills transformed cells preferentially and shows potent antitumor activity in murine xenograft models without detectable adverse effects (Ostenfeld et al., 2005, 2008). Siramesine-induced nonapoptotic cell death is associated with oxidative stress and leakage of lysosomal proteases to the cytosol. The aim of this study was to reveal the molecular basis of siramesine's cancer-selective cytotoxicity and, thereby, to identify new targets for the treatment of therapy-resistant cancers.

RESULTS

Siramesine Inhibits Acid Sphingomyelinase Activity

Siramesine is a lysosomotropic detergent that shows cancer specific cytotoxicity both in vitro and in vivo. In order to enlighten the molecular basis underlying its cancer specificity, we compared *c-src*^{Y527F}- and vector-transduced NIH 3T3 murine embryonic fibroblasts that are siramesine sensitive and resistant, respectively (Ostenfeld et al., 2005). It is surprising that *c-src*^{Y527F}-driven malignant transformation failed to sensitize NIH 3T3 cells to compounds that induce similar lysosomal effects as siramesine, i.e., detergents that permeabilize lysosomal membranes (sphingosine and Leu-LeuOMe) and concanamycin A that neutralizes lysosomal pH (Figures 1A and 1B). In spite of the enhanced endocytic capacity in transformed cells, siramesine uptake and the subsequent neutralization of lysosomal pH were indistinguishable in *c-src*^{Y527F}- and vector-transduced cells (Figures 1C–1E). Thus, the cancer-selective toxicity of siramesine must be due to its activities not previously associated with the cytotoxic potential of lysosomotropic detergents.

Siramesine is an amphiphilic amine that induces phospholipidosis (Ostenfeld et al., 2008), a well-described "side effect" of many clinically relevant and widely used cationic amphiphilic drugs (CADs) (Halliwell, 1997). As basic substances, CADs

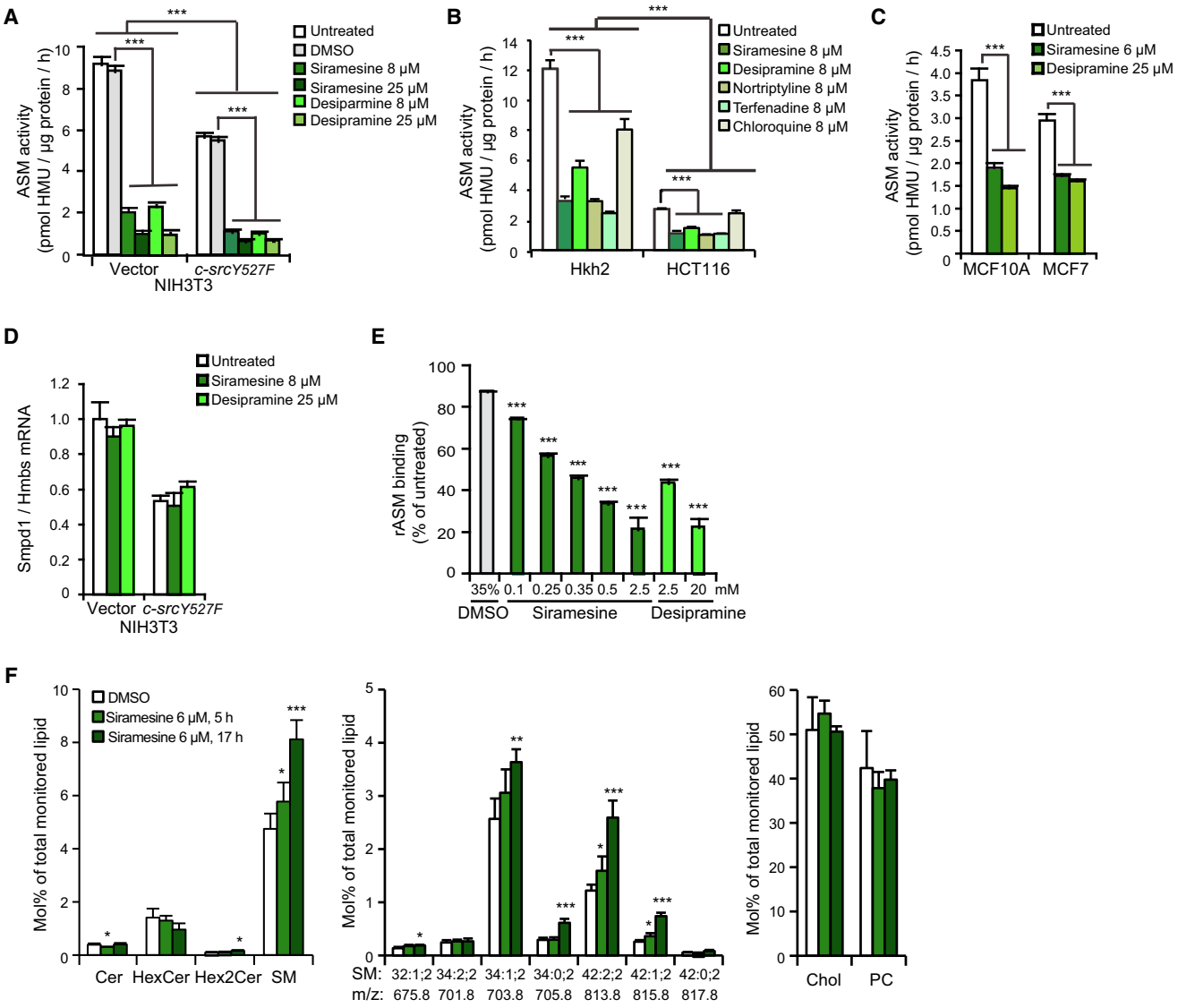

Figure 2. Siramesine Inhibits ASM Activity

(A–C) ASM activities in lysates of NIH 3T3-vector and -*c-src*^{Y527F} (A), Hkh2 and HCT116 (B), and MCF10A and MCF7 (C) cells that were treated as indicated for 1 hr.

(D) Quantitative PCR (qPCR) analysis of *Smpd1* mRNA levels in NIH 3T3-vector and -*c-src*^{Y527F} cells treated as indicated for 1 hr. Hydroxymethylbilane synthase (*Hmbs1*) served as an internal control. The expression is expressed relative to that in untreated NIH 3T3-vector cells.

(E) BIAcore analysis of the effect of indicated concentrations of siramesine and desipramine in 35% dimethyl sulfoxide (DMSO) on binding of prebound recombinant ASM to BMP-containing liposomes at pH 4.5. Drug concentrations used here reflect the reported up-to-1,000-fold accumulation of CADs in lysosomes (Anderson and Borlak, 2006).

(F) Quantitative lipid mass spectrometry analysis of lysosomes isolated from MCF7 cells treated as indicated. The monitored lipid species included ceramides (Cer), hexocylceramides (HexCer), diosylceramides (Hex2Cer), sphingomyelins (SM), cholesterol (Chol), and phosphatidylcholines (PC). Error bars indicate SD for a representative (n = 3) quadruplicate experiment in (A) through (C), duplicate experiment in (D) and (F), or triplicate experiment in (E).

*p < 0.05, **p < 0.01, and ***p < 0.001 as indicated or when comparing drug-treated samples to vehicle-treated ones in (E).

See also Figure S1.

accumulate in acidic lysosomes where they inhibit the activity of lipases, including acid sphingomyelinase (ASM) and acid ceramidase, which are responsible for the lysosomal hydrolysis of sphingomyelin to ceramide and ceramide to sphingosine, respectively (Kornhuber et al., 2010). Prompted by our recent data showing that ASM promotes lysosomal membrane integrity (Kirkegaard et al., 2010), we asked whether the lysosome-permeabilizing effect of siramesine could be due to the inactivation of ASM. Supporting this hypothesis, siramesine reduced the ASM activity in NIH 3T3-vector and NIH 3T3-*c-src*^{Y527F} cells as effectively as desipramine, a tricyclic antidepressant with a well-documented ASM inhibitory capacity (Kolter and Sandhoff, 2010) (Figure 2A; Figure S1A available online). ASM inhibitory effect of siramesine was observed in various human cell lines (Figures 2B and 2C) and was not associated with changes in *Smpd1* messenger RNA (mRNA) levels (Figure 2D).

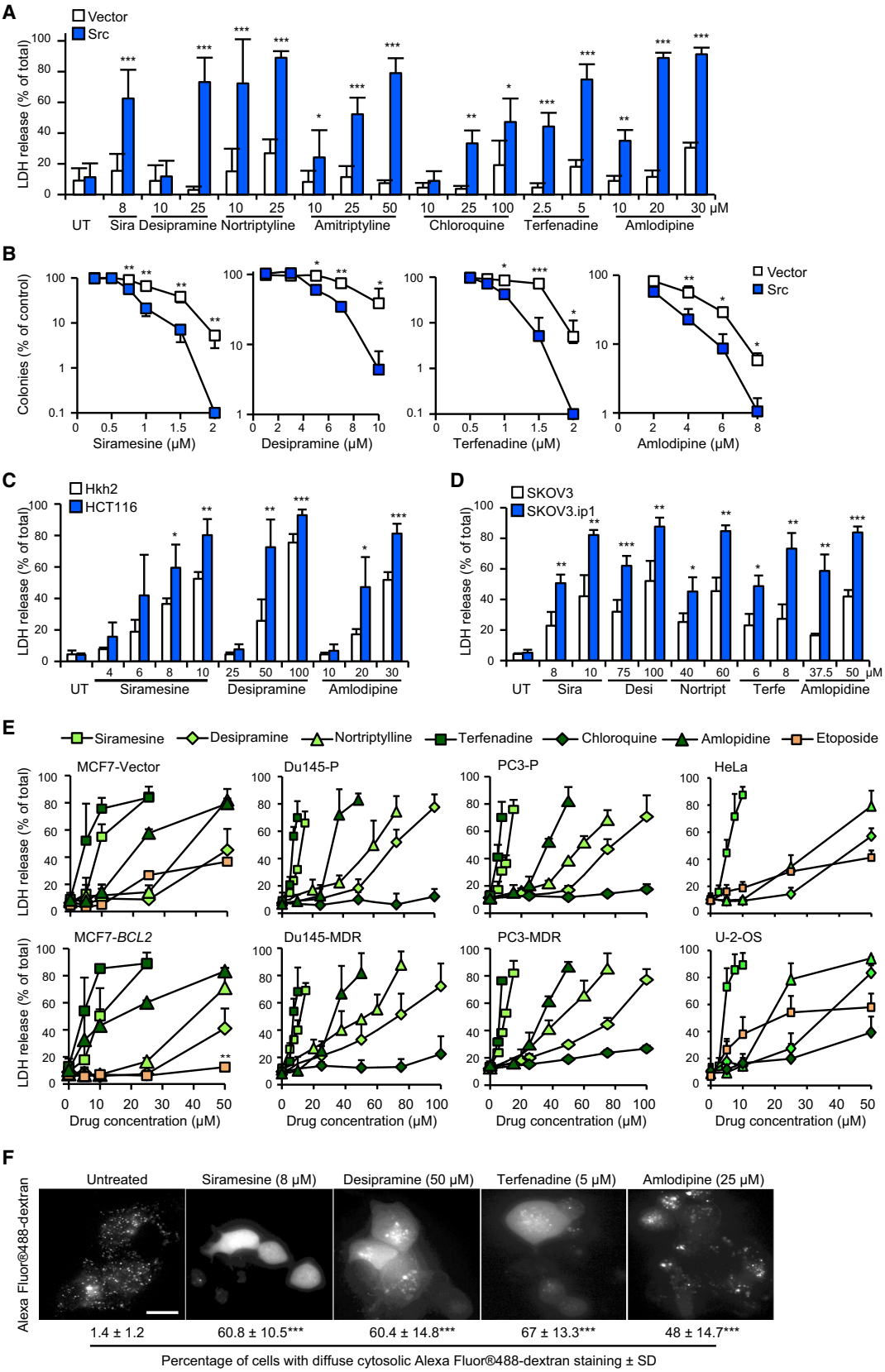

(legend on next page)

Bis(monoacylglycero)phosphate (BMP) is an endolysosomal phospholipid that serves as an essential docking lipid for ASM and other sphingolipid-hydrolyzing enzymes by tethering them to their substrates in BMP-rich intraluminal vesicles (Kolter and Sandhoff, 2010). Desipramine and other CADs inhibit ASM and, possibly, other sphingolipid-hydrolyzing enzymes by interfering with the electrostatic attraction between the negatively charged BMP and positively charged saposin domains found in ASM itself and in cofactors of many lysosomal lipases (Kolter and Sandhoff, 2010). BIAcore surface-plasmone resonance analysis revealed that siramesine inhibited the binding of ASM to BMP-containing liposomes even more effectively than desipramine (Figure 2E). Contrary to desipramine, cytotoxic concentrations of siramesine did not markedly reduce cellular levels of acid ceramidase, which, akin to ASM, is degraded by lysosomal cathepsins following desipramine-induced release from BMP-containing lysosomal membranes (Figure S1B).

To confirm that ASM was inhibited also in living cells, we used quantitative lipid mass spectrometry. The rapid siramesine-induced reduction in ASM activity in MCF7 cells (Figure 2C) was followed by a significant lysosomal accumulation of major sphingomyelin species and a corresponding decrease in ceramide levels (Figure 2F). A prolonged exposure to siramesine resulted in a further accumulation of lysosomal sphingomyelin, whereas lysosomal ceramide level returned to control levels (Figure 2F). Also, at this later time point, lysosomal diosylceramides accumulated significantly (Figure 2F). Notably, siramesine-induced increase in sphingomyelin was more rapid and greater in lysosomal membranes than in total cellular membranes, whereas the late effects of siramesine on glycosylated ceramides were more prominent in nonlysosomal membranes (Figures 2F and S1C). Siramesine treatment induced a similar sphingomyelin accumulation in NIH 3T3-*c-src*^{Y527F} cells without significant changes in ceramides or glycosylated ceramides (Figure S1D).

Taken together, these data support the hypothesis that the inhibition of the ASM activity inside the lysosomes is the primary sphingolipid-modifying effect of siramesine. Siramesine has two tertiary amine groups that can be protonated at acidic pH and an estimated log P (hydrophobicity) value of 5.7 (ChemDraw software, CambridgeSoft). Based on these two chemical facts and its ability to induce phospholipidosis, interact with BMP, and inhibit ASM activity, siramesine can be defined as a CAD and a functional inhibitor of ASM.

CADs Display Cancer-Specific Cytotoxicity In Vitro

Next, we asked whether clinically relevant CADs with reported ASM inhibitory activity display cancer-specific cytotoxicity similar to siramesine. Remarkably, micromolar concentrations of CADs used for the treatment of depression (desipramine, nortriptyline, and amitriptyline), malaria (chloroquine), allergies (terfenadine), or hypertension (amlodipine) killed *c-src*^{Y527F}-transduced cells at concentrations that did not compromise the survival of control cells (Figure 3A). The transformed cells were also significantly more sensitive to the long-term cytotoxicity of CADs as analyzed by the colony formation assay (Figure 3B). Similar *c-src*^{Y527F}-induced sensitization to CADs was observed in three independently transduced pairs of NIH 3T3-vector and NIH 3T3-*c-src*^{Y527F} cells (data not shown); siramesine, desipramine, and amlodipine also killed *K-Ras*-driven HCT116 colon carcinoma cells more effectively than their *K-Ras*-depleted "detransformed" Hkh2 variants (Figure 3C). Furthermore, all tested CADs, except for chloroquine, displayed profound cytotoxicity against cancer cell lines of various origins, including ovarian (SKOV3), breast (MCF7), prostate (PC3 and Du145), cervix (HeLa), and bone (U-2-OS) cancers (Figures 3D and 3E). CADs killed highly invasive SKOV3.ip1 variants of SKOV3 cells (Yu et al., 1993), apoptosis-resistant Bcl-2-transduced MCF7 cells (Høyer-Hansen et al., 2007), and multidrug-resistant PC3 and Du145 prostate cancer cells better or as effectively as their parental counterparts (Figures 3D and 3E).

Similar to siramesine (Ostenfeld et al., 2005), other cytotoxic CADs induced lysosomal membrane permeabilization in sensitive target cells prior to the permeabilization of the plasma membrane (Figure 3F; data not shown). The order of efficacy of the tested drugs was the same in all cell lines tested, terfenadine being the most potent with lethal dose 50 (LD_{50}) values between 3 and 5 μM, followed by siramesine ($LD_{50} \approx 4–9$ μM), amlopidine ($LD_{50} \approx 20–40$ μM), and nortriptylline ($LD_{50} \approx 20–60$ μM). Desipramine ($LD_{50} \approx 40–70$ μM) and chloroquine ($LD_{50} > 100$ μM) had the weakest cytotoxic activity, correlating with their lesser ability to inhibit ASM (Figure 2B).

CADs Display Cancer-Specific Cytotoxicity In Vivo

We have shown earlier that daily oral (p.o.) administration of siramesine at 30 and 100 mg/kg inhibits the growth of orthotopic MCF7 mammary cancer xenografts in immunodeficient mice and WEHI-R murine fibrosarcoma allografts in immunocompetent syngenic mice (Ostenfeld et al., 2005). Our attempts to

Figure 3. CADs Display Cancer-Specific Cytotoxicity In Vitro and In Vivo

(A) NIH 3T3-vector (Vector) and -*c-src*^{Y527F} (Src) cells were treated with indicated concentrations of siramesine (Sira) or indicated CADs for 28 hr, and the cell death was analyzed by the LDH release assay.

(B) Clonogenic survival of the same cells in (A) treated as indicated for 72 hr and analyzed by counting the colonies 5 days later.

(C) Hkh2 and HCT116 cells were treated with CADs as indicated for 40 hr, and the cell death was analyzed by the LDH release assay.

(D) Parental and highly invasive (.ip1) SKOV3 cells were treated with CADs as indicated for 44 hr, and the cell death was analyzed by the LDH release assay. Desi, desipramine; Nortript, nortryptyllin; Terfe, terfenadine;

(E) Vector- and *BCL2*-transduced MCF7 cells, parental (P) and MDR Du145 and PC3 cells, HeLa, and U-2-OS cells were treated as indicated for 48 hr, and the cell death was analyzed by the LDH release assay.

(F) Representative images of Alexa Fluor 488-dextran-loaded MCF7 cells treated as indicated for 20 hr. The percentage of cells with lysosomal membrane permeabilization (cytosolic Alexa Fluor 488-dextran staining) was obtained by counting ten randomly chosen areas, with a minimum of 50 cells for each condition. Scale bar, 20 μm.

Error bars indicate SD for a minimum of three independent triplicate experiments.

*$p < 0.05$, **$p < 0.01$, and ***$p < 0.001$ when comparing similarly treated NIH 3T3-vector and -*c-src*^{Y527F} in (A) and (B), Hkh2 and HCT116 in (C), SKOV3 and SKOV3.ip1 in (D), MCF7-Vector and -Bcl-2 in (E), or treated and untreated cells in (F).

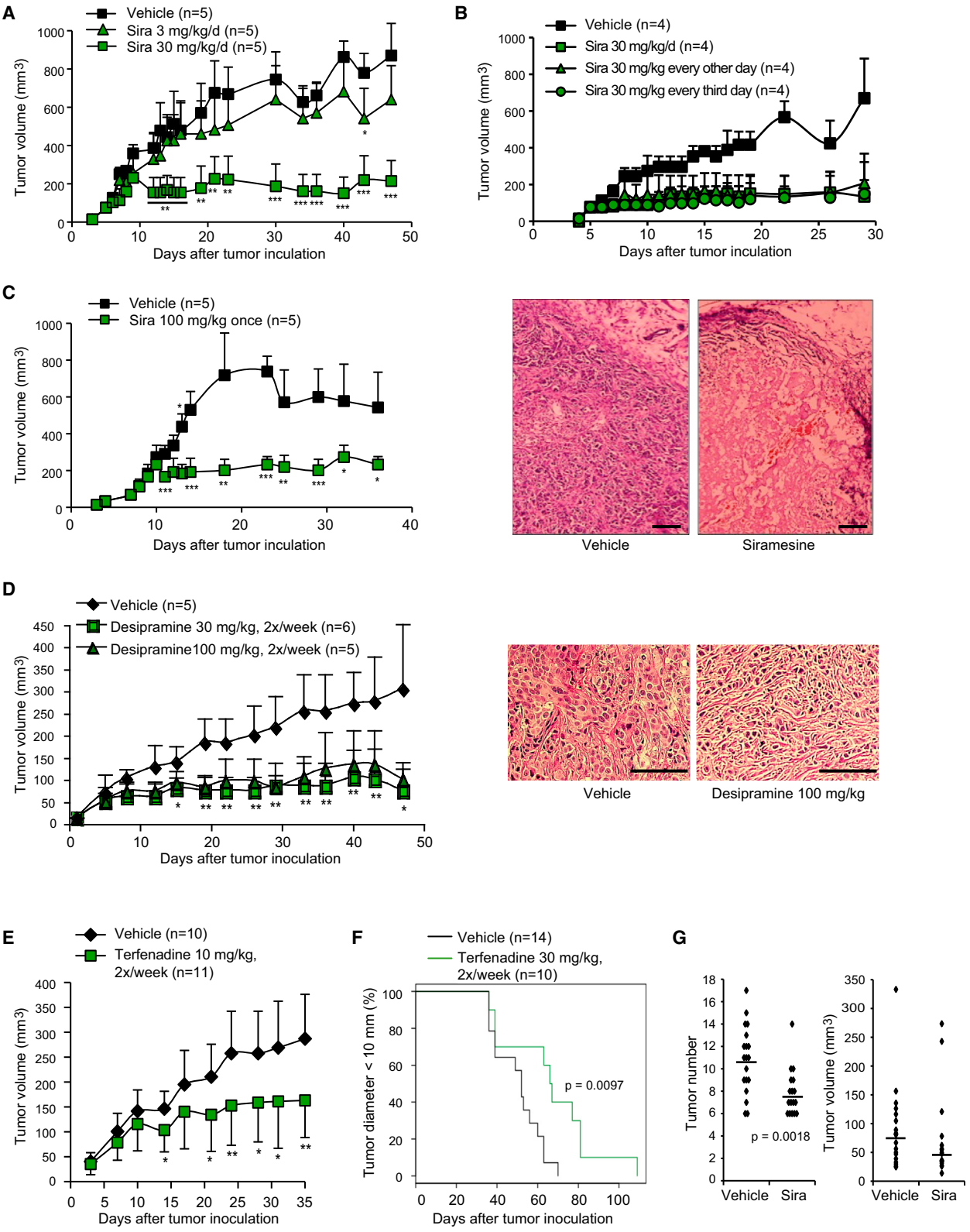

Figure 4. CADs Display Cancer-Specific Cytotoxicity In Vivo

(A–E) MCF7 cells (10×10^6 cells in 100 μl PBS) were inoculated into an axillary mammary fat pad of estrone-treated female SCID mice. After tumor manifestation, the mice were treated p.o. with 200 μl vehicle (0.5% methylcellulose 15 in 0.9% NaCl solution) alone or with indicated doses of siramesine (in A–C), desipramine (D), or terfenadine (E) at indicated intervals. Representative images of hematoxylin-eosin-stained tumors 4 days (C) or 6 weeks (D) after the first treatment are

(legend continued on next page)

find the minimal effective dose revealed that the anticancer effect of siramesine was largely lost at 3 mg/kg/day, whereas biweekly administration of 30 mg/kg was as effective as daily treatment, and even a single dose of 100 mg/kg induced massive necrosis (an expected consequence of lysosomal cell death) in tumors and attenuated their growth for several weeks (Figures 4A–4C). Notably, a biweekly treatment with 30 mg/kg desipramine inhibited the growth of MCF7 xenografts as effectively as the same dose of siramesine (Figure 4D). Even though desipramine-treated tumors did not shrink, the histological analysis of the remaining tumor masses 6 weeks after the start of the treatment revealed large areas of fibrotic tissue suggestive of a preceding therapy-induced necrosis corresponding to that observed in siramesine-treated tumors 4 days after the treatment (Figures 4C and 4D). The antihistamine terfenadine also delayed the growth of MCF7 and SKOV3.ip1 xenografts at biweekly doses of 10 and 30 mg/kg, respectively (Figures 4E and 4F). Finally, we tested the efficacy of siramesine in an aggressive *RIP1-Tag2* transgenic model of pancreatic β-cell cancer (Hanahan, 1985). As a consequence of simian virus large T antigen expression in pancreatic β cells, *RIP1-Tag2* mice develop multiple islet tumors by 12–14 weeks of age. Daily treatment with 100 mg/kg siramesine starting at the age of 11 weeks significantly reduced the number of tumors in *RIP1-Tag2* mice, and the tumor burden was reduced by 40% (Figure 4G). Of note, none of the treatment protocols induced weight loss or other noticeable adverse effects, indicating that siramesine and CADs display cancer specificity also in vivo.

Transformation Alters Sphingomyelin Metabolism

To enlighten the molecular basis of the cancer-selective cytotoxicity of CADs, we investigated whether transformation altered sphingomyelin metabolism. The data presented earlier already revealed significant transformation-associated reduction in ASM activity before and after CAD treatment (Figures 2A and 2B). The expression of ASM-encoding *Smpd1*/*SMPD1*, but not that of acid ceramidase-encoding *Asah1*/*ASAH1*, was also significantly reduced by transformation (Figures 5A and 5B). In accordance with the reported lysosome-stabilizing effect of ASM (Kirkegaard et al., 2010), the lysosomal membrane stability was dramatically reduced in *c-src*^{Y527F}-transformed cells with low ASM activity, as measured by the leakage of acridine orange from the lysosomes to the cytosol upon photo-oxidation (Figure 5C).

In accordance with decreased sphingomyelin levels in tumor tissues (colon, breast, esophagus, brain, and blood) and transformed cells (Barceló-Coblijn et al., 2011; Hendrich and Michalak, 2003), NIH 3T3-*c-src*^{Y527F} and HCT116 cells had significantly lower levels of sphingomyelin than their nontransformed control cells (Figures 5D and 5E). In search for the explanation for the transformation-associated fall in sphingomyelin levels, we sequenced the entire transcriptomes of three independently transduced pairs of NIH 3T3-vector and -*c-src*^{Y527F} cells and analyzed the expression of genes related to sphingomyelin synthesis and hydrolysis. The data obtained confirmed the significantly reduced expression of *Smpd1* and revealed an even stronger decrease in the expression of *Smpd3* and *Nsmaf*, which encode for neutral sphingomyelinase (NSM) 2 and NSM2 activation-associated factor, respectively (Figure 5F). Accordingly, *c-src*^{Y527F}-transduced cells had lower constitutive NSM activity than control cells (Figure 5G). The expression of sphingomyelin synthases was either increased (*Sgms2*) or not affected (*Sgms1*) (Figure 5F), and the levels of other genes encoding for enzymes involved in sphingolipid metabolism also failed to explain the transformation-associated reduction in sphingomyelin (Table S1). Instead, the decreased expression of *Smpd1* and *Smpd3*, as well as the increased expression of *Sgms2*, may be compensatory consequences of the low sphingomyelin levels in transformed cells. Of note, the transformation-associated decrease in the expression of *SMPD1* was not limited to the model systems used here. An analysis of a published gene expression microarray data set (Wolfer et al., 2010) revealed *ERBB2*- and epidermal-growth-factor-induced decrease in *SMPD1* mRNA levels in MCF10A breast epithelial cells (Figure 5H), and a database search demonstrated a highly significant cancer-associated reduction in *SMPD1* expression in numerous microarray studies comparing mRNA levels in tumors originating from gastrointestinal tract, liver, head and neck, kidney, pancreas, cervix, lung, brain, and lymphoid tissue with their appropriate control tissues (Figure S2). Also *SMPD3* mRNA levels were significantly reduced in gastrointestinal and lung carcinomas as well as in diffuse large B cell lymphomas (Figure S2).

Transformation-Associated Changes in Sphingomyelin Metabolism Sensitize Cells to Siramesine

Accumulation of sphingomyelin has a destabilizing effect on lysosomes (Kirkegaard et al., 2010), and the maintenance of low sphingomyelin levels may be especially important for cancer cell lysosomes, whose membrane stability is compromised by significantly increased proteolytic activity (Fehrenbacher et al., 2008). Thus, the lower constitutive ASM and NSM2 activities, as well as the lower residual ASM activity remaining after CAD treatment, may provide a molecular explanation for the cancer specific cytotoxicity of CADs. Fittingly, siramesine treatment increased sphingomyelin levels in sensitive NIH 3T3-*c-src*^{Y527F} cells, while no increase was detected in resistant NIH 3T3-vector cells (Figure 6A; Figure S1D). More important, pharmacological inhibition of NSM sensitized nontransformed cells to siramesine

shown. Note massive hemorrhagic necrosis in siramesine-treated tumors in (C) and large areas of fibrotic connective tissue in desipramine-treated tumors in (D). Error bars indicate SD for the indicated number of mice.

(F) SKOV3.ip1 cells (10×10^5 cells in 120 μl GelTrex) were inoculated into an axillary mammary fat pad of estrone-treated female SCID mice. After 6 days, the mice were treated p.o. with 200 μl vehicle (0.5% methylcellulose 15 in 0.9% NaCl solution) alone or with 30 mg/kg terfenadine twice a week. Percentages of mice with a tumor diameter under 10 mm are plotted.

(G) The *RIP-Tag2* mice were treated p.o. with vehicle (n = 19) or 100 mg/kg/day siramesine (n = 17) from week 11 of age. The mice were sacrificed at the age of 14 weeks and the tumors were counted and measured. Geometric means are indicated by horizontal lines.

*$p < 0.05$, **$p < 0.01$, and ***$p < 0.001$ when comparing drug-treated mice to vehicle-treated mice. In (B), $p < 0.05$ and $p < 0.01$ for all treated groups starting from days 10 and 18, respectively. The p values in (D) refer to mice treated with the 30 mg/kg siramesine. Scale bars, 100 μM.

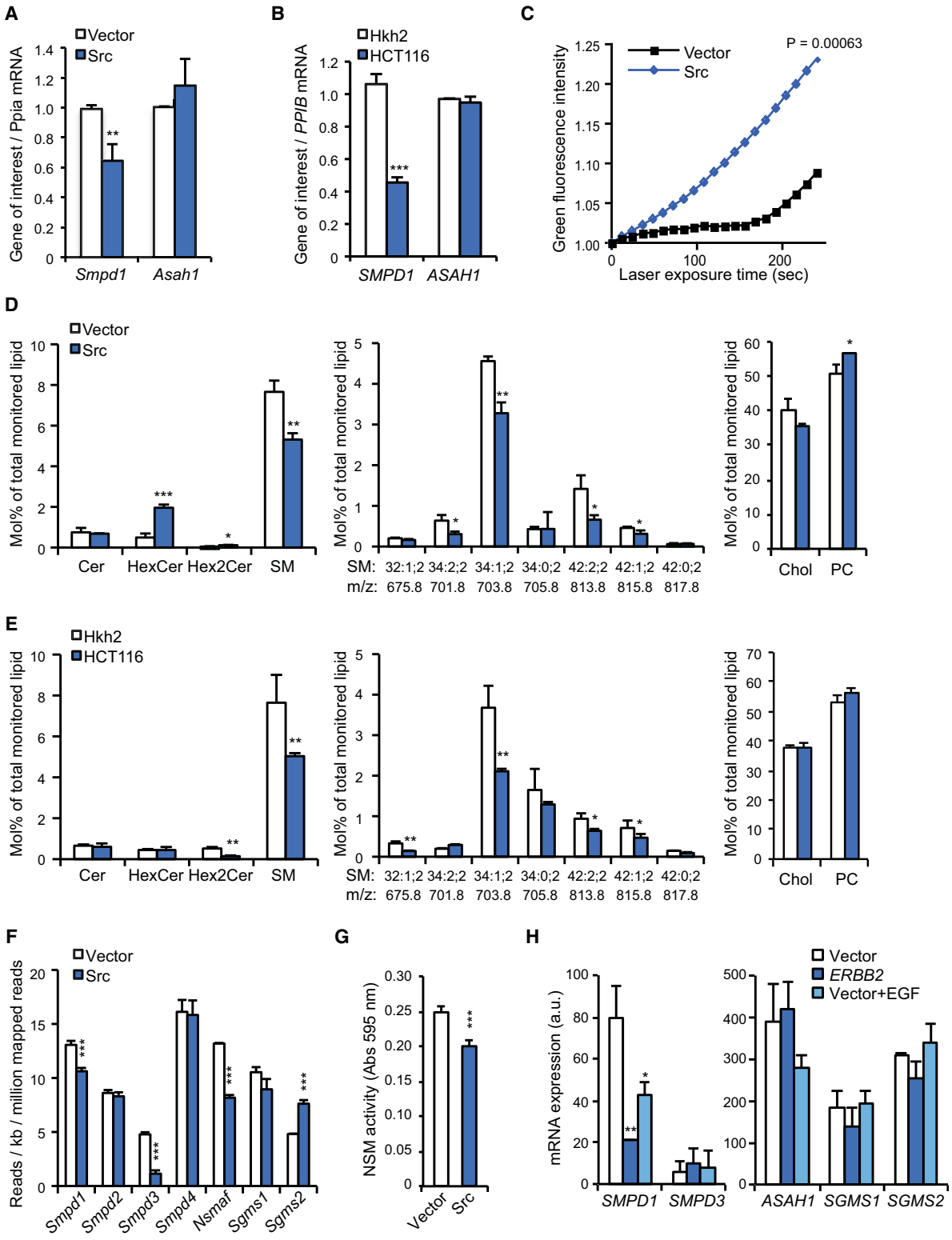

Figure 5. Transformation Alters Sphingolipid Metabolism and Destabilizes Lysosomes

(A and B) *Smpd1*/*SMPD1* (ASM) and *Asah1*/*ASAH1* (acid ceramidase) mRNA levels in NIH 3T3-vector (Vector) and -*c-src*^{Y527F} (Src) cells (A) and in Hkh2 and HCT116 cells (B) were determined by qPCR. The values are expressed relative to *Ppia* or *PPIB* (cyclophilin A or B) mRNA.

(C) Loss of lysosomal integrity was analyzed by live single-cell imaging of the increase in green fluorescence, which reflects the leakage of lysosomal acridine orange to the cytosol (see Supplemental Experimental Procedures), after laser treatment in acridine orange-labeled NIH 3T3-vector and -*c-src*^{Y527F} cells. Values represent means for 13 movies recorded in three independent experiments performed with three independent pools of NIH 3T3-vector and -*c-src*^{Y527F} cells.

(legend continued on next page)

(Figure 6B), whereas ectopic expression of *SMPD1*, as well as treatment with bacterial sphingomyelinase, protected transformed cells (Figures 6C and 6D). Thus, nonlysosomal sphingomyelinases can protect cells against cytotoxicity induced by ASM inhibitors. Furthermore, the sensitizing effect of 2-hydroxyoleic acid (2OHOA) (Figure 6E), a potent activator of sphingomyelin synthases (Barceló-Coblijn et al., 2011), suggested that the siramesine-induced increase in cellular sphingomyelin content is detrimental to cancer cells. The inability of ceramide, sphingosine, and sphingosine-1-phosphate to rescue cells from siramesine-induced cytotoxicity further endorsed the increase in sphingomyelin, rather than the decrease in sphingomyelin metabolites, as a mediator of lysosomal destabilization upon ASM inhibition (Figure 6F). Accordingly, depletion of ASM, but not that of acid ceramidase, sensitized cancer cell lysosomes to photo-oxidation-induced destabilization (Figure 6G).

Heat Shock Protein 70 and α-Tocopherol Protect Cells against CAD-Induced Cell Death

Transformation-associated destabilization of lysosomal membranes can be counteracted by lysosomal heat shock protein 70 (Hsp70), which binds with high affinity to lysosomal BMP, thereby stabilizing ASM-BMP interaction and enhancing ASM activity (Kirkegaard et al., 2010). Concentrations of CADs that effectively inhibited the binding of ASM to BMP-containing liposomes failed to affect the Hsp70-BMP interaction (Figure 2E; Figure 7A). Thus, we speculated that Hsp70 could protect ASM-BMP interaction from the CAD-induced interference. Accordingly, Hsp70-expressing immortalized embryonic fibroblasts and WEHI-S murine fibrosarcoma cells tolerated CADs better than control cells (Figures 7B–7D). Further connecting the ASM inhibitory activity of siramesine to its cytotoxic potential, α-tocopherol, which effectively inhibits siramesine-induced cytotoxicity (Ostenfeld et al., 2005), completely prevented siramesine-induced ASM inhibition (Figure 7E).

Inhibition of ASM Activity Reverts Multidrug-Resistant Phenotype

Numerous studies have demonstrated the ability of CADs to revert MDR, and already in 1995, Dr. Levade noticed that CAD-mediated ASM inhibition correlated well with their ability to revert MDR (Jaffrézou et al., 1995). In order to challenge this clinically attractive hypothesis, we created MDR variants of PC3 and Du145 prostate carcinoma cells by a long-term exposure to increasing concentrations of docetaxel. PC3-MDR (Figures S3A and S3B) and Du145-MDR (Ellegaard et al., 2013) cells overexpressed MDR1-encoding *ABCB1* gene and displayed significantly reduced sensitivity to microtubule-disturbing and DNA-damaging drugs while remaining highly sensitive to all tested CADs (Figure 3E). As expected, subtoxic concentrations of siramesine and desipramine fully resensitized MDR cells to docetaxel in vitro without affecting the level of MDR1 protein (Figures 8A and S3C). Siramesine also resensitized PC3-MDR xenograft tumors to docetaxel treatment in vivo (Figure 8B) and reverted the MDR phenotype in human CEM/A7 T-lymphoblasts in vitro (Figures S3D and S3E).

PC3-MDR and Du145-MDR cells had significantly higher *SMPD1* expression and slightly higher ASM activity than their parental cells (Figures 8C and 8D), and they displayed other variable signs of lysosomal activation (Figures S3B, S3F, and S3G). In order to test whether the inhibition of ASM contributed to the CAD-mediated reversal of MDR, we depleted the cells for ASM by three nonoverlapping *SMPD1* small interfering RNAs (siRNAs). ASM depletion reverted the MDR phenotype as effectively as that of MDR1, and ASM depletion alone was sufficient to trigger significant cell death, especially in PC3-MDR cells, in which the RNA interference was particularly efficient (Figures 8D and 8E).

DISCUSSION

The data presented above identify a subset of CADs as putative anticancer agents and open a feasible, safe, and economically sound possibility to test the clinical anticancer efficacy of antihistamines, calcium channel blockers, tricyclic antidepressants, and other widely used and relatively safe CADs with ASM inhibitory activity. In order to identify CADs with best anticancer efficacy for clinical trials, it is of utmost importance to understand the molecular basis of their cytotoxic mechanism and cancer selectivity. Here, we provide several lines of evidence that support ASM inhibition as a key to cancer selective cytotoxicity of CADs. Most convincing, ectopic expression of *SMPD1*, as well as pretreatment of cells with purified sphingomyelinase, protected cancer cells against siramesine, whereas pharmacological inhibition of NSM had a sensitizing effect. Moreover, Hsp70, which stabilizes BMP-ASM interaction and enhances ASM activity (Kirkegaard et al., 2010), conferred partial protection against siramesine- and desipramine-induced cytotoxicity, and α-tocopherol-induced protection from siramesine was associated with the loss of siramesine's ability to inhibit ASM. Finally, the cytotoxic potential of CADs tested here correlated well with their reported (Kornhuber et al., 2010) and measured ability to inhibit ASM. This correlation was further endorsed by our preliminary screen of clinically relevant CADs, which identified potent

(D and E) Lipid contents (mol%) of NIH 3T3-vector (Vector) and -*c-src*^{Y527F} (Src) cells (D) and in Hkh2 and HCT116 cells (E) as analyzed by quantitative mass spectrometry. All monitored lipid species are shown.

(F) Expression levels of indicated genes in three independent pairs of NIH 3T3-vector (Vector) and -*c-src*^{Y527F} (Src) cells were analyzed by whole transcriptome sequencing (RNA-Seq).

(G) NSM activity in lysates of NIH 3T3-vector (Vector) and -*c-src*^{Y527F} (Src) cells measured by an assay kit from Echelon.

(H) Expression of indicated genes (Affymetrix U133Plus2.0) in cells transduced with an empty retrovirus (Vector) or *pBabe* encoding for *ERBB2* and grown in medium supplemented with 2% horse serum for 26 hr (Wolfer et al., 2010). When indicated cells transduced with empty vector were treated with 50 ng/ml EGF for 2 hr before harvesting. a.u., arbitrary units.

Error bars indicate SD for a minimum of three independent duplicate experiments in (A) and (D) or triplicate experiments in (E), two quadruplicate experiments in (G), a representative (n = 3) duplicate experiment in (B), or three independently transduced samples in (F) and (H). *$p < 0.05$, **$p < 0.01$, and ***$p < 0.001$, when comparing transformed or treated cells with control cells.

See also Figure S2and Table S1.

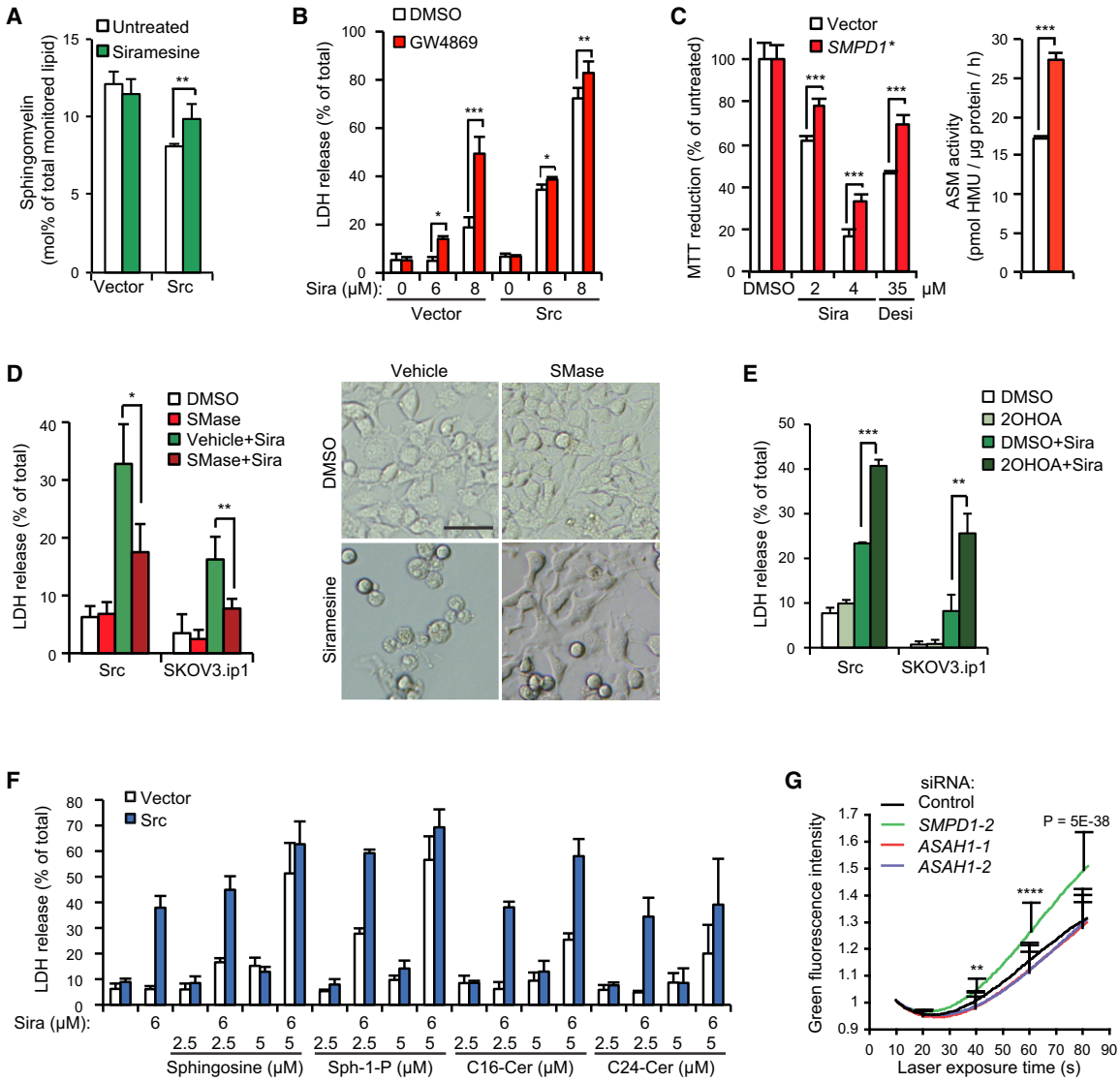

Figure 6. Failure to Compensate for ASM Inhibition Leads to Accumulation of Sphingomyelin and Sensitization to Cell Death

(A) Relative sphingomyelin contents of NIH 3T3-vector (Vector) and -*c-src*^{Y527F} (Src) cells left untreated or treated with 8 μM siramesine for 5 hr were analyzed by mass spectrometry. Values are expressed as mol% of total monitored lipid (Cer, HexCer, Hex2Cer, SM, and PC).

(B) NIH 3T3-vector (Vector) and -*c-src*^{Y527F} (Src) cells were pretreated with vehicle (DMSO) or 15 μM GW4869 for 1 hr before the treatment with indicated concentrations of siramesine for 26 hr. Cell death was analyzed by the LDH release assay.

(C) Viability (MTT reduction, left) and ASM activity (right) of HeLa cells transfected with a plasmid encoding for *SMPD1** or the corresponding empty vector 96 hr earlier and treated as indicated for the last 48 hr.

(D) Cell death (LDH release) of NIH 3T3-*c-src*^{Y527F} and SKOV3.ip1 cells treated with vehicle (DMSO) or 75 μM sphingomyelinase from Bacillus cereus (SMase) 72, 48, and 24 hr before 46 hr treatment with 6 μM (NIH 3T3-*c-src*^{Y527F}) or 8 μM (SKOV3.ip1) siramesine, respectively. Representative images of NIH 3T3-*c-src*^{Y527F} cells are shown on right. Scale bar, 50 μm.

(E) NIH 3T3-*c-src*^{Y527F} (Src) and SKOV3.ip1 cells were treated with vehicle (DMSO) or 400 μM 2-hydroxyoleic acid (2OHOA) for 45 hr and when indicated with 6 μM (Src) or 8 μM (SKOV3.ip1) siramesine for the last 28 hr. Cell death was analyzed by the LDH release assay.

(F) NIH 3T3-vector and -*c-src*^{Y527F} cells were treated with indicated combinations of D-sphingosine (Sph), sphingosine-1-phposphate (Sph-1-P), C16-ceramide (C16-Cer), C24-ceramide (C24-Cer) and siramesine (Sira) for 28 hr. Cell death was analyzed by the LDH release assay. The solvents used for Sph and C16-Cer (DMSO), Sph-1-P (MeOH), or C24-Cer (EtOH/Dod) had no significant effect alone or with siramesine.

(G) Loss of lysosomal integrity was analyzed by live single-cell imaging of the increase in green fluorescence after laser treatment in acridine orange-labeled U-2-OS cells pretreated for 72 hr with a nontargeting control siRNA or qPCR-validated siRNAs targeting *SMPD1* (85% reduction in mRNA) or *ASAH1* (82% and 85% reduction in mRNA).

Error bars indicate SD for a minimum of three independent duplicate experiments in (A) or triplicate experiments in (B), (D), (E), and (F), one representative (n = 3) quadruplicate experiment in (C), or four experiments with 20 movies each in (G).

*p < 0.05, **p < 0.01, and ***p < 0.001, as indicated or when comparing *SMPD1* siRNA to control siRNA in (G).

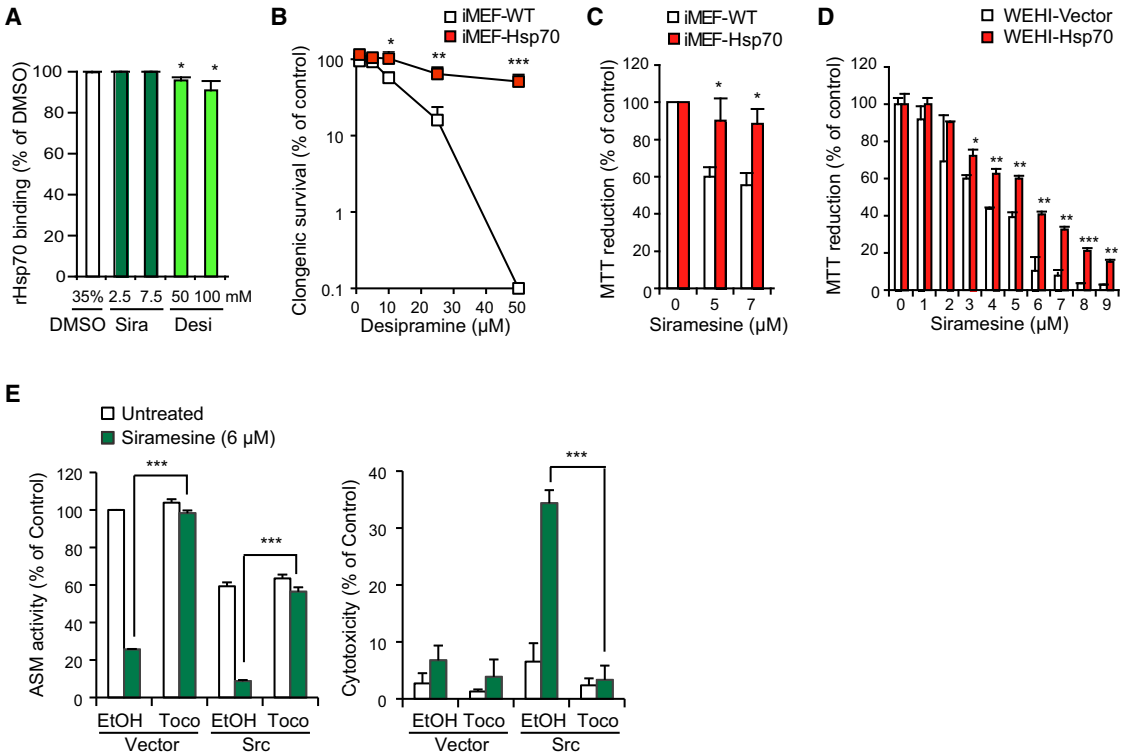

Figure 7. Hsp70 and α-Tocopherol Protect Cells against CAD-Induced Cell Death

(A) BIAcore measurement of the effect of indicated concentrations of siramesine and desipramine in 35% DMSO on binding of prebound rHsp70 to BMP-containing liposomes at pH 4.5. Drugs were added 10 min after Hsp70 immobilization.

(B) Clonogenic survival of wild-type (WT) and *Hspa1*-transgenic (Hsp70) iMEFs treated as indicated for 24 hr was analyzed by counting colonies 7 days after the treatment.

(C and D) Viability (MTT reduction) of wild-type (WT) and *Hspa1*-transgenic (Hsp70) iMEFs (C) and vector- and *HSPA1*-transduced (Hsp70) WEHI cells (D) treated as indicated for 24 hr.

(E) NIH 3T3-vector (Vector) and NIH 3T3-*c-srcY527F* (Src) cells were left untreated or treated with 8 μM siramesine for 24 hr before the analysis of the ASM activity (left, cleavage of HMU-PC) or cytotoxicity (right, LDH release assay). When indicated, 200 μg/ml α-tocopherol or vehicle (EtOH) was added 1 hr before the drug. Error bars indicate SD for a minimum of three independent experiments in (B), (C), (D), and (E) or a representative triplicate experiments out of three in (A).

*$p < 0.05$, **$p < 0.01$, ***$p < 0.001$, as indicated in (E) or when compared to vehicle-treated samples in (A), similarly treated iMEF-WT cells in (B) and (C), or WEHI-Vector cells in (D).

ASM inhibitors with varying structures and medical uses (e.g., perhexilline, sertraline, clomiphene, astemizole, maproteline, and tamoxifen) as effective inducers of cancer cell death, whereas CADs with only marginal ASM inhibitory activity (e.g., diphenhydramine, haloperidol, mirtazapine, fexofenadine, and mifepristone) were only weakly cytotoxic at concentrations up to 100 μM (A.-M.E., unpublished data).

The cytoprotective role of ASM in cancer cells was corroborated by the ability of *SMPD1* siRNAs to induce cell death in PC3-MDR cells. The degree of cell death was, however, clearly smaller than that induced by CADs, indicating that ASM inhibition is not the sole cytotoxic mechanism of CADs. As discussed earlier, CADs also induce the proteolysis of other lysosomal lipases, including acid ceramidase (Kolter and Sandhoff, 2010), which has been considered as a putative anticancer target due to the proapoptotic effects of ceramide (Zeidan et al., 2008). Contrary to desipramine, which triggered a rapid degradation of acid ceramidase in all tested cells, siramesine had either no effect or increased acid ceramidase levels. Accordingly, lysosomes of siramesine-treated cells accumulated sphingomyelin rather than ceramide prior to lysosomal leakage and cell death. Thus, ASM inhibition and subsequent sphingomyelin accumulation are likely to be the key changes in sphingolipid metabolism that underlie the cytotoxic effect of CADs. This conclusion appears to be in contrast to the reported ability of ASM to promote death-receptor-induced or radiation-induced apoptosis in endothelial cells (Jenkins et al., 2009). It should, however, be noted that the proapoptotic function of ASM depends on the translocation of ASM to the outer leaflet of plasma membrane, where ceramide-containing lipid microdomains enhance the activation of signaling molecules involved in apoptotic signaling (Smith and Schuchman, 2008). Thus, ASM may have opposing effects on cell survival, depending on its localization to either lysosomal or plasma membranes. Optimally, the inhibition of ASM might inhibit therapy-induced apoptosis in apoptosis-competent normal cells and sensitize apoptosis-defective cancer cells to a nonapoptotic lysosomal cell death pathway. The direct detergent activity of CADs, as well as their ability to enhance the production of reactive oxygen species, may be among the additional cytotoxic mechanisms that, together with ASM inhibition, lead to

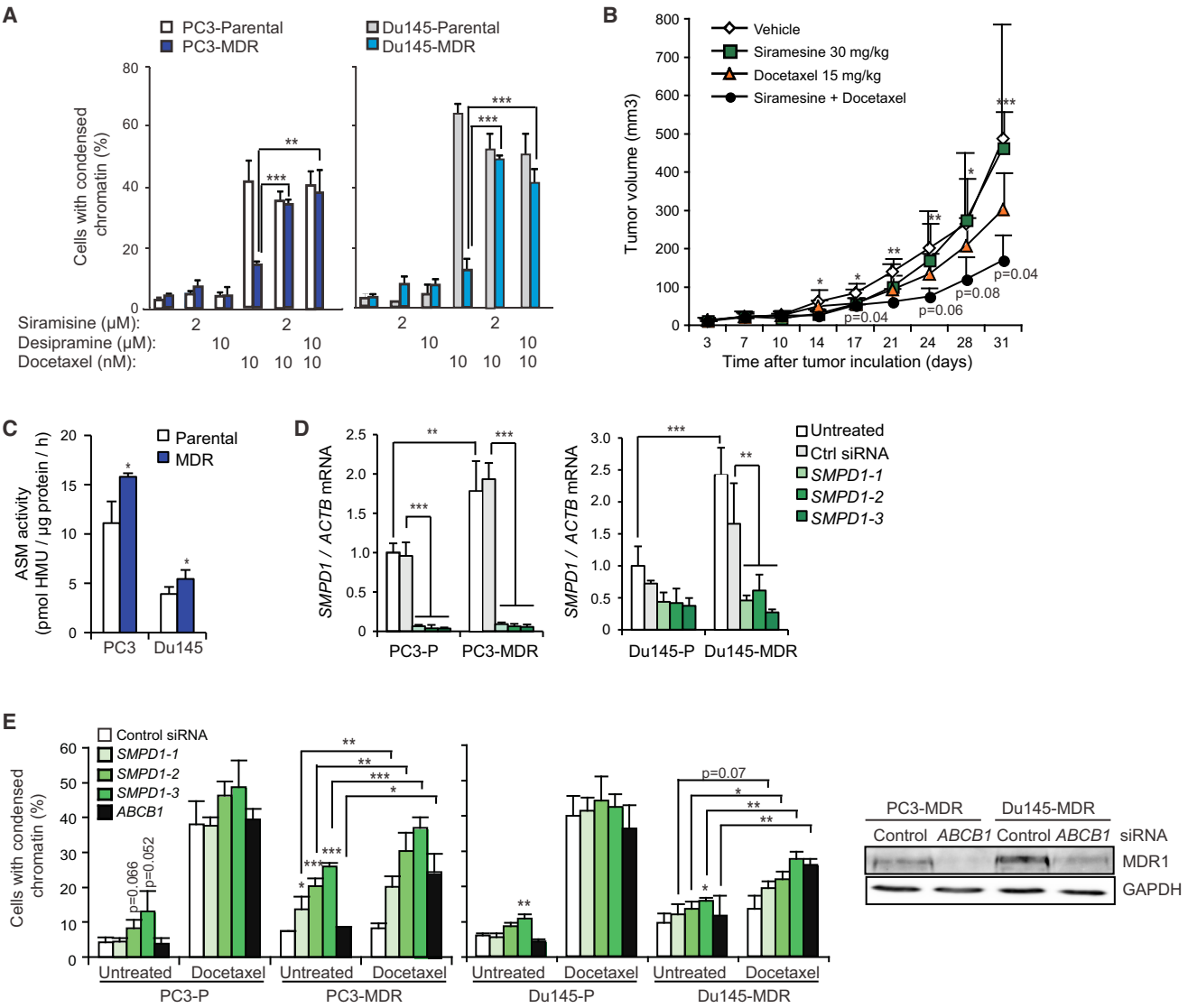

Figure 8. Inhibition of ASM Reverts Multidrug Resistance

(A) Apoptotic phenotype of parental (P) and MDR PC3 prostate carcinoma cells treated as indicated for 48 hr was determined by counting Hoechst-stained cells with condensed nuclei. Over 100 randomly chosen cells were counted for each condition.

(B) PC3-MDR cells (5×10^6 in 100 μl PBS) were inoculated subcutaneously into the flank of male SCID mice. After tumor manifestation (day 3), the mice were treated p.o. with 200 μl vehicle (0.5% methylcellulose 15 in 0.9% NaCl solution) alone or with siramesine (30 mg/kg). A weekly intraperitoneal treatment with 0.9% NaCl with or without docetaxel (15 mg/kg) was initiated on day 7. Each treatment group contained five mice. One vehicle-treated mouse and one docetaxel-treated mouse were sacrificed at days 29 and 10, respectively. The effect of neither drug alone was significant. Similar results were obtained in an independent experiment in which treatment was initiated when tumor diameter reached 5 mm (data not shown). The asterisks and p values refer to comparisons of combination treatment with vehicle and docetaxel, respectively.

(C) ASM activity in indicated cell lysates was determined by measuring the cleavage of HMU-PC.

(D) *SMPD1* mRNA levels relative to *ACTB* mRNA were analyzed by qPCR 72 hr after transfection with indicated siRNAs.

(E) Cells transfected with the indicated siRNAs were 24 hr later left untreated or treated with 20 nM docetaxel for 48 hr. Apoptotic cell death (left) was analyzed as in (A). The efficacy of *SMPD1* siRNAs is demonstrated in (D) and that of *ABCB1* siRNA is demonstrated in a representative immunoblot (right).

Error bars indicate SD for a minimum of three independent experiments—(A), (C), and (E),—a representative triplicate experiment (D), or 4 to 5 mice (B). *$p < 0.05$, **$p < 0.01$, and ***$p < 0.001$ when compared as indicated, or with similarly treated control siRNA-transfected cells in (C).

See also Figure S3.

lysosomal permeabilization. Supporting the role of reactive oxygen species in this process, depletion of ASM but not of acid ceramidase, sensitized cancer cell lysosomes to photo-oxidation-induced permeabilization.

Cancer selectivity and minimal toxicity are highly desired but rarely achieved properties of anticancer agents. In this respect, it is encouraging that siramesine and other tested CADs displayed selective cytotoxicity toward transformed cells and

showed no detectable adverse effects in mouse models. Moreover, long-term use of CADs by millions of people has proven them to be relatively safe, especially when compared with existing chemotherapeutics. Phase 1 studies of siramesine have also proven it safe at doses that result in plasma concentrations around 0.5 μM (single dose of 320 mg or 80 mg/day for 14 days p.o.; C. Volbracht, H. Lundbeck A/S, Valby, Denmark, personal communication). Our data suggest that the cancer selectivity of CADs is at least partially due to the significantly altered sphingolipid metabolism in transformed cells. As a result, transformed cells have lower residual ASM activity after CAD treatment and accumulate sphingomyelin, whose increased levels have been reported to be selectively toxic to transformed cells (Barceló-Coblijn et al., 2011). An increase in the sphingomyelin/ceramide ratio modifies the steric conformation of lysosomal membranes and hinders their fusion with other intracellular vesicles and plasma membrane (Utermöhlen et al., 2008). Thus, the additional changes in the lysosomal membrane composition and volume as a result of the sphingomyelin-induced reduction in lysosomal fusion capacity may contribute to the CAD-induced destabilization of lysosomal membranes.

Because of its ability to inhibit autophagy, chloroquine is currently tested as an anticancer agent in several clinical trials. Thus, it should be noted that siramesine and clomipramine are also effective inhibitors of autophagic flux (Ostenfeld et al., 2008; Rossi et al., 2009), and based on their basic nature, all clinically relevant CADs are likely to neutralize the lysosomal pH effectively and thereby inhibit autophagic degradation. Because the tumor environment is frequently characterized by low nutrient and oxygen content, the clinical efficacy of CADs may be further improved by their ability to prevent cytoprotective autophagy in metabolically stressed cancer cells.

Taken together, our data introduce ASM as an utmost attractive target for the treatment of therapy-resistant cancers and encourage extensive preclinical testing and subsequent clinical cancer trials for siramesine and clinically well-characterized and relatively safe CADs.

EXPERIMENTAL PROCEDURES

Cell Lines and Treatments

All cell lines are described in the Supplemental Experimental Procedures. Siramesine was kindly provided by C. Volbracht (H. Lundbeck A/S), C16-ceramide (N-palmitoyl-D-*erythro*-sphingosine) and C24 ceramide (N-lignoceroyl-D-*erythro*-sphingosine) were from Avanti Polar Lipids, and GW4869 was from Cayman Chemical. Other chemicals were from Sigma-Aldrich, if not otherwise stated.

Cell Survival and Lysosomal Stability

The cell density was assessed by the 3-(4,5-dimethylthiazol-2-yl)-2,5-diphenyltetrazolium bromide (MTT) reduction assay and the cell death was assessed by lactate dehydrogenase (LDH) release assay (Roche), as described previously (Foghsgaard et al., 2001). Cells with condensed chromatin were determined using an OLYMPUS IX microscope with the UV channel by counting condensed nuclei in cells stained with Hoeschst 33342 for 10 min. In order to assess clonogenic survival, the cells were seeded in six-well plates at a low density (1,000–3,000 cells per well) and treated as indicated. Five to 7 days after the treatment, the cells were washed with PBS and incubated with crystal violet/methanol for 15 min, washed twice in water, and dried. Colonies were counted manually. In all assays, great care was taken to ensure equal density of the cell lines to be compared when the drugs were added.

Lysosomal stability upon photo-oxidation was analyzed essentially as described previously (Kirkegaard et al., 2010) and in the Supplemental Experimental Procedures.

In order to visualize lysosomal membrane permeabilization, cells were loaded with 200 μg/ml Alexa Fluor 488-dextran (10 kDa) and chased for 1 hr in fresh medium before the indicated treatments. Pictures were taken with a Zeiss Axiovert 200M fluorescence time-lapse microscope equipped with a Colibri LED light source at 37°C.

Enzyme Activity Assays

Cellular ASM and NSM activities were measured by the cleavage of HMU-PC and by the Neutral Sphingomyelinase Assay Service kit from Echelon (T-1800), respectively, as described in the Supplemental Experimental Procedures.

BIAcore

Large unilamellar vesicles (10 mol% sphingomyelin, 50 mol% phosphatidylcholine, 20 mol% cholesterol, and 20 mol% BMP) were prepared, and surface plasmon resonance measurements using a BIAcore 3000 system were performed essentially as described elsewhere (Kirkegaard et al., 2010) and in the Supplemental Experimental Procedures. Recombinant proteins (1 μM, 60 μl in running buffer) were injected directly on the liposome surface. Recombinant ASM was kindly provided by K. Sandhoff (University of Bonn, Bonn, Germany), and rHsp70 was generated using the pET-16b vector system and Ni^{21}-affinity-purification (Novagen).

Lipid Mass Spectrometry

Sample aliquots corresponding to 2×10^5 cells or lysosomes from 3×10^6 cells (purified by Fe^{2+}-dextran fractionation as described in the Supplemental Experimental Procedures) per 200 μl were spiked with 10 μl internal standard mixture containing 85 pmol phosphatidylcholine 18:3/18:3, 60 pmol sphingomyelin 18:1;2/17:0;0, 45 pmol ceramide 18:1;2/17:0;0, 65 pmol galactosylceramide 18:1;2/12:0;0 and 65 pmol lactosylceramide 18:1;2/12:0;0. The samples were subsequently extracted with 990 μl chloroform/methanol (10:1, v/v) for 90 min as described elsewhere (Sampaio et al., 2011). The lower organic phase was collected and evaporated. The lipid extract was dissolved in 100 μl chloroform/methanol (1:2, v/v). Lipid extracts were analyzed in positive ion mode on a QSTAR Pulsar-i instrument (AB Sciex) equipped with a TriVersa NanoMate (Advion Biosciences) as described elsewhere (Ejsing et al., 2006; Zech et al., 2009) and in the Supplemental Experimental Procedures. The lipid species were identified and quantified using LipidView software (AB Sciex).

Tumor Xenografts

All animal studies were approved by Dyreforsøgstilsynet (Denmark) or the University of California, San Francisco, Institutional Animal Care and Use Committee (USA) and carried out in accordance with the National Institutes of Health guidelines. MCF7 and SKOV3.ip1 cells were inoculated into an axillary mammary fat pad of female FOX CHASE severe combined immunodeficient (SCID) mice pretreated with 0.67 mg/ml estrone in drinking water for a week. PC3-MDR cells were inoculated subcutaneously into the flank of male SCID mice. Tumor diameters were measured using a caliper, and volumes were estimated according to the formula: volume = $4/3 \cdot \pi \cdot r^3$. RIP1-Tag2 transgenic mice (Hanahan, 1985) were treated as indicated from the age of 11 weeks. At the age of 14 weeks, the pancreases were dissected, and macroscopic tumors (>0.5 mm^3) were counted and measured. Tumor volume was calculated by using the formula for a spheroid: volume = $0.52 \cdot (\text{width})^2 \cdot \text{length}$. RIP1-Tag2 mice received 50% sugar food (Harlan) to relieve hypoglycemia induced by the insulin-secreting tumors.

Transfections and Analyses of RNA and Proteins

Plasmids and siRNAs (20 nM) were transfected using Fugene HD transfection reagent (Promega) and Oligofectamine or RNAi Max (Invitrogen) according to the manufacturer's instructions. pEF6-V5/His vector encoding for S508A mutant of *SMPD1* (*SMPD1**), which has normal lysosomal activity but fails to translocate to plasma membrane upon stress stimuli (Zeidan and Hannun, 2007), was kindly provided by Y. Hannun (University of South Carolina, Charleston, SC, USA). Primer and siRNA sequences are listed in the Supplemental Experimental Procedures.

For the RNA sequencing (RNA-seq), total RNA was isolated from exponentially growing cells using the Nucleospin RNA II kit (Macherey-Nagel). Single-read 100 base pair libraries were constructed using the mRNA-Seq 8-Sample Prep Kit (Illumina). Deep sequencing was performed at the National High-Throughput DNA Sequencing Centre (University of Copenhagen, Copenhagen, Denmark) using Illumina Hiseq2000 instruments. Reads were aligned to the mouse genomic sequence and quantified using the CLC genomic workbench software (CLC bio). Reads were mapped with a minimum of 50 bases of consecutive matches allowing for up to three mismatches.

Protein separation and western blotting were performed using standard procedures and antibodies listed in Supplemental Experimental Procedures.

Statistical Analyses

Statistical analysis was performed using a two-tailed, paired Student's t test in order to evaluate the null hypothesis. The cutoff level for statistical significance was set to 5%, and all groups of data were tested for the comparability of their variances using an F test.

ACCESSION NUMBERS

The GEO accession number for RNA-seq data is GSE46340.

SUPPLEMENTAL INFORMATION

Supplemental Information includes Supplemental Experimental Procedures, three figures, and one table and can be found in this article online at http://dx.doi.org/10.1016/j.ccr.2013.08.003.

ACKNOWLEDGMENTS

We thank L. Cederkvist Kristiansen for assistance in statistical analyses; K. Grøn Henriksen, L. Jørgensen, and L. Bregnholt Larsen for technical assistance; and C. Volbracht, K. Sandhoff, S. Courtneidge, and S. Shirasawa for valuable cells and reagents. This work was supported by grants from the Danish Cancer Society (to M.J. and N.H.T.P.), the Danish National Research Foundation, the Danish Council for Independent Research in Medical Sciences, the Association for International Cancer Research, the European Commission FP7 (APO-SYS), the M.L. Jørgensen & G. Hansen Foundation, the Meyer Foundation, the Vilhelm Pedersen Foundation and the Novo Nordisk Foundation (to M.J.), the Lundbeck Foundation and the Danish Council for Independent Research in Natural Sciences (to C.S.E.), and Volkswagen Stiftung (to C.A. and S.R.).

Received: August 2, 2011
Revised: April 10, 2013
Accepted: August 6, 2013
Published: September 9, 2013

REFERENCES

Anderson, N., and Borlak, J. (2006). Drug-induced phospholipidosis. FEBS Lett. *580*, 5533–5540.

Barceló-Coblijn, G., Martin, M.L., de Almeida, R.F., Noguera-Salvà, M.A., Marcilla-Etxenike, A., Guardiola-Serrano, F., Lüth, A., Kleuser, B., Halver, J.E., and Escribá, P.V. (2011). Sphingomyelin and sphingomyelin synthase (SMS) in the malignant transformation of glioma cells and in 2-hydroxyoleic acid therapy. Proc. Natl. Acad. Sci. USA *108*, 19569–19574.

Canbay, A., Guicciardi, M.E., Higuchi, H., Feldstein, A., Bronk, S.F., Rydzewski, R., Taniai, M., and Gores, G.J. (2003). Cathepsin B inactivation attenuates hepatic injury and fibrosis during cholestasis. J. Clin. Invest. *112*, 152–159.

Česen, M.H., Pegan, K., Spes, A., and Turk, B. (2012). Lysosomal pathways to cell death and their therapeutic applications. Exp. Cell Res. *318*, 1245–1251.

de Duve, C. (1983). Lysosomes revisited. Eur. J. Biochem. *137*, 391–397.

Ejsing, C.S., Duchoslav, E., Sampaio, J., Simons, K., Bonner, R., Thiele, C., Ekroos, K., and Shevchenko, A. (2006). Automated identification and quantification of glycerophospholipid molecular species by multiple precursor ion scanning. Anal. Chem. *78*, 6202–6214.

Ellegaard, A.M., Groth-Pedersen, L., Oorschot, V., Klumperman, J., Kirkegaard, T., Nylandsted, J., and Jäättelä, M. (2013). Sunitinib and SU11652 inhibit acid sphingomyelinase, destabilize lysosomes and inhibit multidrug resistance. Mol. Cancer Ther. http://dx.doi.org/10.1158/1535-7163.MCT13-0084.

Fehrenbacher, N., Gyrd-Hansen, M., Poulsen, B., Felbor, U., Kallunki, T., Boes, M., Weber, E., Leist, M., and Jäättelä, M. (2004). Sensitization to the lysosomal cell death pathway upon immortalization and transformation. Cancer Res. *64*, 5301–5310.

Fehrenbacher, N., Bastholm, L., Kirkegaard-Sørensen, T., Rafn, B., Bøttzauw, T., Nielsen, C., Weber, E., Shirasawa, S., Kallunki, T., and Jäättelä, M. (2008). Sensitization to the lysosomal cell death pathway by oncogene-induced down-regulation of lysosome-associated membrane proteins 1 and 2. Cancer Res. *68*, 6623–6633.

Firestone, R.A., Pisano, J.M., and Bonney, R.J. (1979). Lysosomotropic agents. 1. Synthesis and cytotoxic action of lysosomotropic detergents. J. Med. Chem. *22*, 1130–1133.

Foghsgaard, L., Wissing, D., Mauch, D., Lademann, U., Bastholm, L., Boes, M., Elling, F., Leist, M., and Jäättelä, M. (2001). Cathepsin B acts as a dominant execution protease in tumor cell apoptosis induced by tumor necrosis factor. J. Cell Biol. *153*, 999–1010.

Gottesman, M.M., Fojo, T., and Bates, S.E. (2002). Multidrug resistance in cancer: role of ATP-dependent transporters. Nat. Rev. Cancer *2*, 48–58.

Groth-Pedersen, L., and Jäättelä, M. (2013). Combating apoptosis and multidrug resistant cancers by targeting lysosomes. Cancer Lett. *332*, 265–274.

Guicciardi, M.E., Miyoshi, H., Bronk, S.F., and Gores, G.J. (2001). Cathepsin B knockout mice are resistant to tumor necrosis factor-alpha-mediated hepatocyte apoptosis and liver injury: implications for therapeutic applications. Am. J. Pathol. *159*, 2045–2054.

Halangk, W., Lerch, M.M., Brandt-Nedelev, B., Roth, W., Ruthenbuerger, M., Reinheckel, T., Domschke, W., Lippert, H., Peters, C., and Deussing, J. (2000). Role of cathepsin B in intracellular trypsinogen activation and the onset of acute pancreatitis. J. Clin. Invest. *106*, 773–781.

Halliwell, W.H. (1997). Cationic amphiphilic drug-induced phospholipidosis. Toxicol. Pathol. *25*, 53–60.

Hanahan, D. (1985). Heritable formation of pancreatic beta-cell tumours in transgenic mice expressing recombinant insulin/simian virus 40 oncogenes. Nature *315*, 115–122.

Hanahan, D., and Weinberg, R.A. (2011). Hallmarks of cancer: the next generation. Cell *144*, 646–674.

Hendrich, A.B., and Michalak, K. (2003). Lipids as a target for drugs modulating multidrug resistance of cancer cells. Curr. Drug Targets *4*, 23–30.

Houseweart, M.K., Pennacchio, L.A., Vilaythong, A., Peters, C., Noebels, J.L., and Myers, R.M. (2003). Cathepsin B but not cathepsins L or S contributes to the pathogenesis of Unverricht-Lundborg progressive myoclonus epilepsy (EPM1). J. Neurobiol. *56*, 315–327.

Høyer-Hansen, M., Bastholm, L., Szyniarowski, P., Campanella, M., Szabadkai, G., Farkas, T., Bianchi, K., Fehrenbacher, N., Elling, F., Rizzuto, R., et al. (2007). Control of macroautophagy by calcium, calmodulin-dependent kinase kinase-β, and Bcl-2. Mol. Cell *25*, 193–205.

Jaffrézou, J.P., Chen, G., Durán, G.E., Muller, C., Bordier, C., Laurent, G., Sikic, B.I., and Levade, T. (1995). Inhibition of lysosomal acid sphingomyelinase by agents which reverse multidrug resistance. Biochim. Biophys. Acta *1266*, 1–8.

Jenkins, R.W., Canals, D., and Hannun, Y.A. (2009). Roles and regulation of secretory and lysosomal acid sphingomyelinase. Cell. Signal. *21*, 836–846.

Kinser, R.D., and Dolph, P.J. (2012). Cathepsin proteases mediate photoreceptor cell degeneration in Drosophila. Neurobiol. Dis. *46*, 655–662.

Kirkegaard, T., Roth, A.G., Petersen, N.H., Mahalka, A.K., Olsen, O.D., Moilanen, I., Zylicz, A., Knudsen, J., Sandhoff, K., Arenz, C., et al. (2010).

Hsp70 stabilizes lysosomes and reverts Niemann-Pick disease-associated lysosomal pathology. Nature *463*, 549–553.

Kolter, T., and Sandhoff, K. (2010). Lysosomal degradation of membrane lipids. FEBS Lett. *584*, 1700–1712. Published online October 16, 2009. http://dx.doi.org/10.1016/j.febslet.2009.10.021.

Kornhuber, J., Tripal, P., Reichel, M., Mühle, C., Rhein, C., Muehlbacher, M., Groemer, T.W., and Gulbins, E. (2010). Functional Inhibitors of Acid Sphingomyelinase (FIASMAs): a novel pharmacological group of drugs with broad clinical applications. Cell. Physiol. Biochem. *26*, 9–20.

Kreuzaler, P.A., Staniszewska, A.D., Li, W., Omidvar, N., Kedjouar, B., Turkson, J., Poli, V., Flavell, R.A., Clarkson, R.W., and Watson, C.J. (2011). Stat3 controls lysosomal-mediated cell death in vivo. Nat. Cell Biol. *13*, 303–309.

Leist, M., and Jäättelä, M. (2001). Four deaths and a funeral: from caspases to alternative mechanisms. Nat. Rev. Mol. Cell Biol. *2*, 589–598.

Luke, C.J., Pak, S.C., Askew, Y.S., Naviglia, T.L., Askew, D.J., Nobar, S.M., Vetica, A.C., Long, O.S., Watkins, S.C., Stolz, D.B., et al. (2007). An intracellular serpin regulates necrosis by inhibiting the induction and sequelae of lysosomal injury. Cell *130*, 1108–1119.

Matsuda, S., Okada, N., Kodama, T., Honda, T., and Iida, T. (2012). A cytotoxic type III secretion effector of Vibrio parahaemolyticus targets vacuolar H+-ATPase subunit c and ruptures host cell lysosomes. PLoS Pathog. *8*, e1002803.

Ostenfeld, M.S., Fehrenbacher, N., Høyer-Hansen, M., Thomsen, C., Farkas, T., and Jäättelä, M. (2005). Effective tumor cell death by sigma-2 receptor ligand siramesine involves lysosomal leakage and oxidative stress. Cancer Res. *65*, 8975–8983.

Ostenfeld, M.S., Høyer-Hansen, M., Bastholm, L., Fehrenbacher, N., Olsen, O.D., Groth-Pedersen, L., Puustinen, P., Kirkegaard-Sørensen, T., Nylandsted, J., Farkas, T., and Jäättelä, M. (2008). Anti-cancer agent siramesine is a lysosomotropic detergent that induces cytoprotective autophagosome accumulation. Autophagy *4*, 487–499.

Rossi, M., Munarriz, E.R., Bartesaghi, S., Milanese, M., Dinsdale, D., Guerra-Martin, M.A., Bampton, E.T., Glynn, P., Bonanno, G., Knight, R.A., et al. (2009). Desmethylclomipramine induces the accumulation of autophagy markers by blocking autophagic flux. J. Cell Sci. *122*, 3330–3339.

Sampaio, J.L., Gerl, M.J., Klose, C., Ejsing, C.S., Beug, H., Simons, K., and Shevchenko, A. (2011). Membrane lipidome of an epithelial cell line. Proc. Natl. Acad. Sci. USA *108*, 1903–1907.

Smith, E.L., and Schuchman, E.H. (2008). The unexpected role of acid sphingomyelinase in cell death and the pathophysiology of common diseases. FASEB J. *22*, 3419–3431.

Syntichaki, P., Xu, K., Driscoll, M., and Tavernarakis, N. (2002). Specific aspartyl and calpain proteases are required for neurodegeneration in C. elegans. Nature *419*, 939–944.

Utermöhlen, O., Herz, J., Schramm, M., and Krönke, M. (2008). Fusogenicity of membranes: the impact of acid sphingomyelinase on innate immune responses. Immunobiology *213*, 307–314.

Wolfer, A., Wittner, B.S., Irimia, D., Flavin, R.J., Lupien, M., Gunawardane, R.N., Meyer, C.A., Lightcap, E.S., Tamayo, P., Mesirov, J.P., et al. (2010). MYC regulation of a "poor-prognosis" metastatic cancer cell state. Proc. Natl. Acad. Sci. USA *107*, 3698–3703.

Yu, D., Wolf, J.K., Scanlon, M., Price, J.E., and Hung, M.C. (1993). Enhanced c-erbB-2/neu expression in human ovarian cancer cells correlates with more severe malignancy that can be suppressed by E1A. Cancer Res. *53*, 891–898.

Zech, T., Ejsing, C.S., Gaus, K., de Wet, B., Shevchenko, A., Simons, K., and Harder, T. (2009). Accumulation of raft lipids in T-cell plasma membrane domains engaged in TCR signalling. EMBO J. *28*, 466–476.

Zeidan, Y.H., and Hannun, Y.A. (2007). Activation of acid sphingomyelinase by protein kinase Cdelta-mediated phosphorylation. J. Biol. Chem. *282*, 11549–11561.

Zeidan, Y.H., Jenkins, R.W., Korman, J.B., Liu, X., Obeid, L.M., Norris, J.S., and Hannun, Y.A. (2008). Molecular targeting of acid ceramidase: implications to cancer therapy. Curr. Drug Targets *9*, 653–661.

Cancer Cell
Errata

Species- and Cell Type-Specific Requirements for Cellular Transformation

Annapoorni Rangarajan, Sue J. Hong, Annie Gifford, and Robert A. Weinberg*
*Correspondence: weinberg@wit.mit.edu
http://dx.doi.org/10.1016/j.ccr.2013.08.028

(Cancer Cell *6*, 171–183; August 2004)
We were apprised recently of errors made in the assembly of Figures 2B, 3A, 4A, 4B, and 5G, resulting in the incorporation of incorrect representative images in these figures. These errors occurred during the electronic assembly and have no bearing on the conclusions of the study. The corrected figures are shown below. The authors apologize for any possible confusion this might have caused.

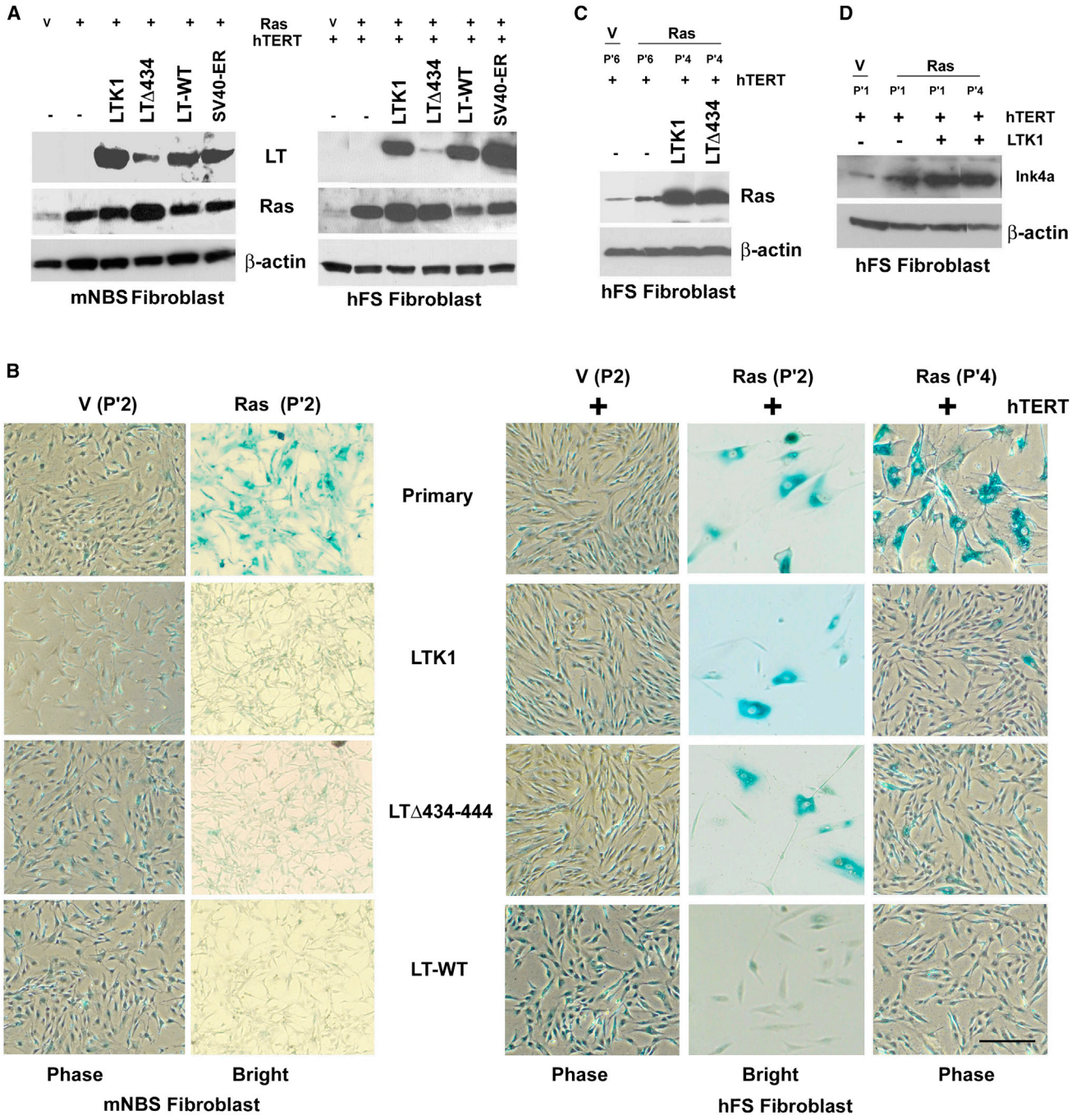

Figure 2. Effects of Different LT Mutants on Ras-Induced Senescence

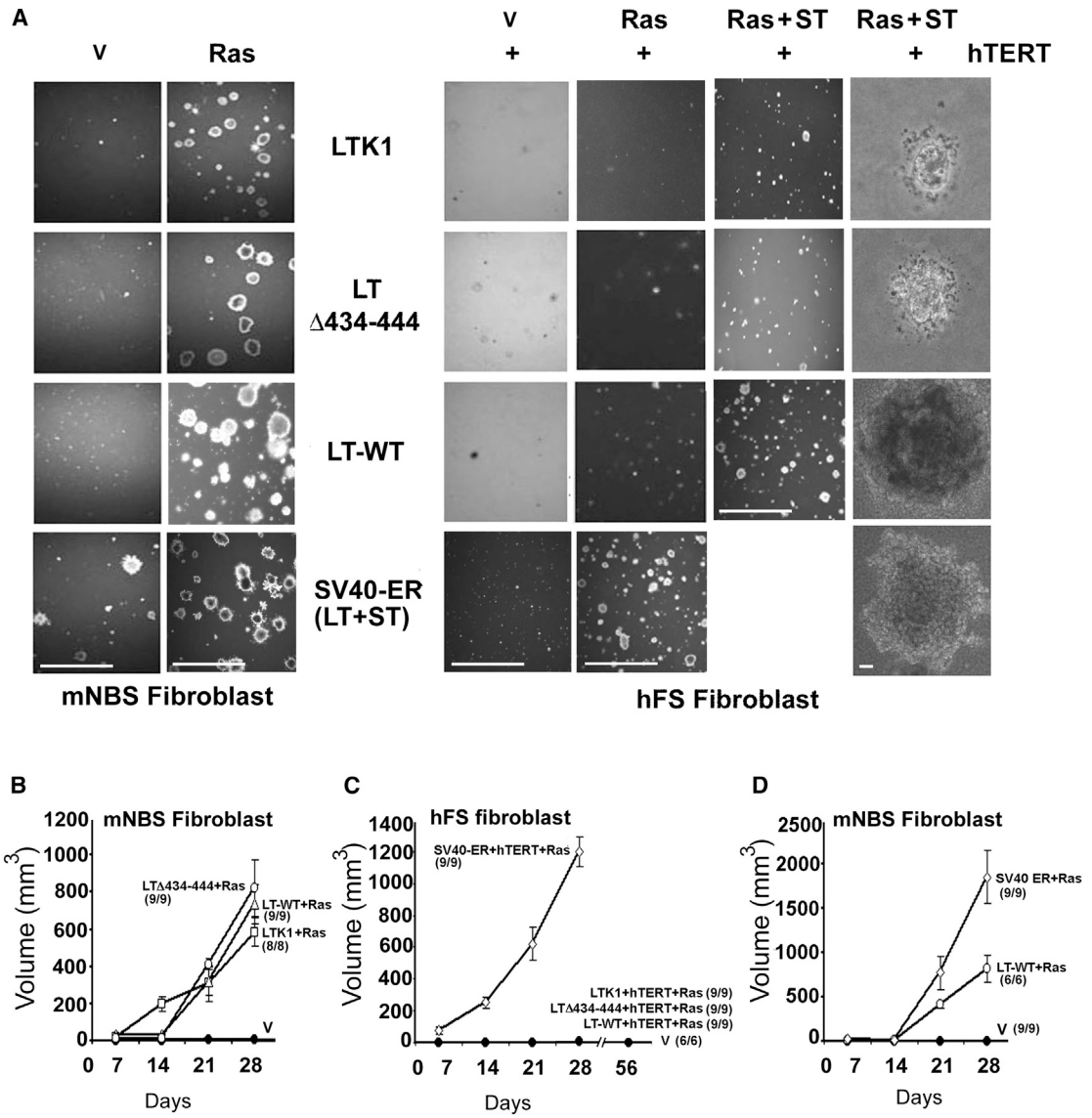

Figure 3. Anchorage-Independent Growth and Tumorigenicity of Ras-Expressing mNBS and hFS Fibroblasts

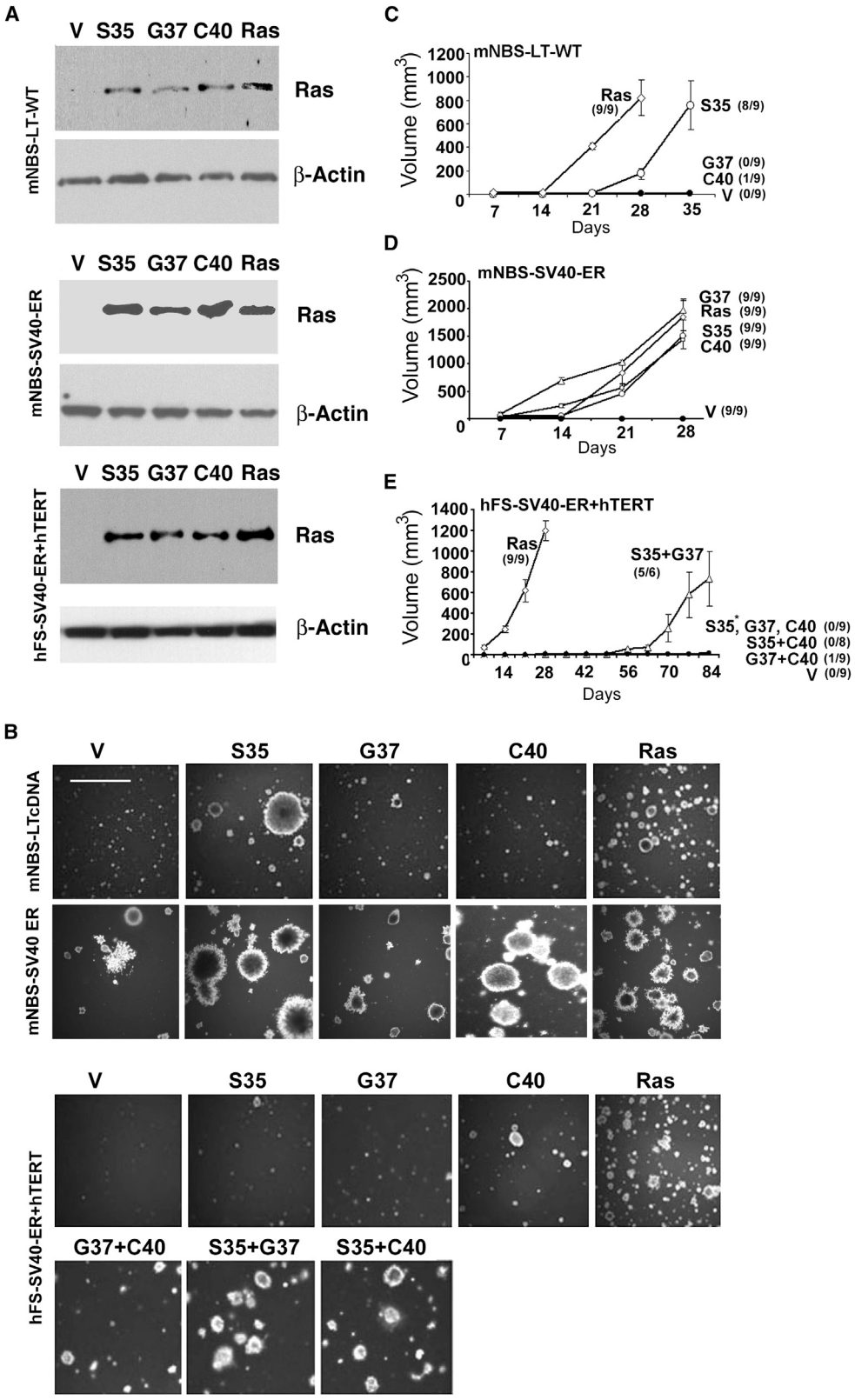

Figure 4. Requirements of Ras Pathways for Transforming mNBS and hFS Fibroblasts

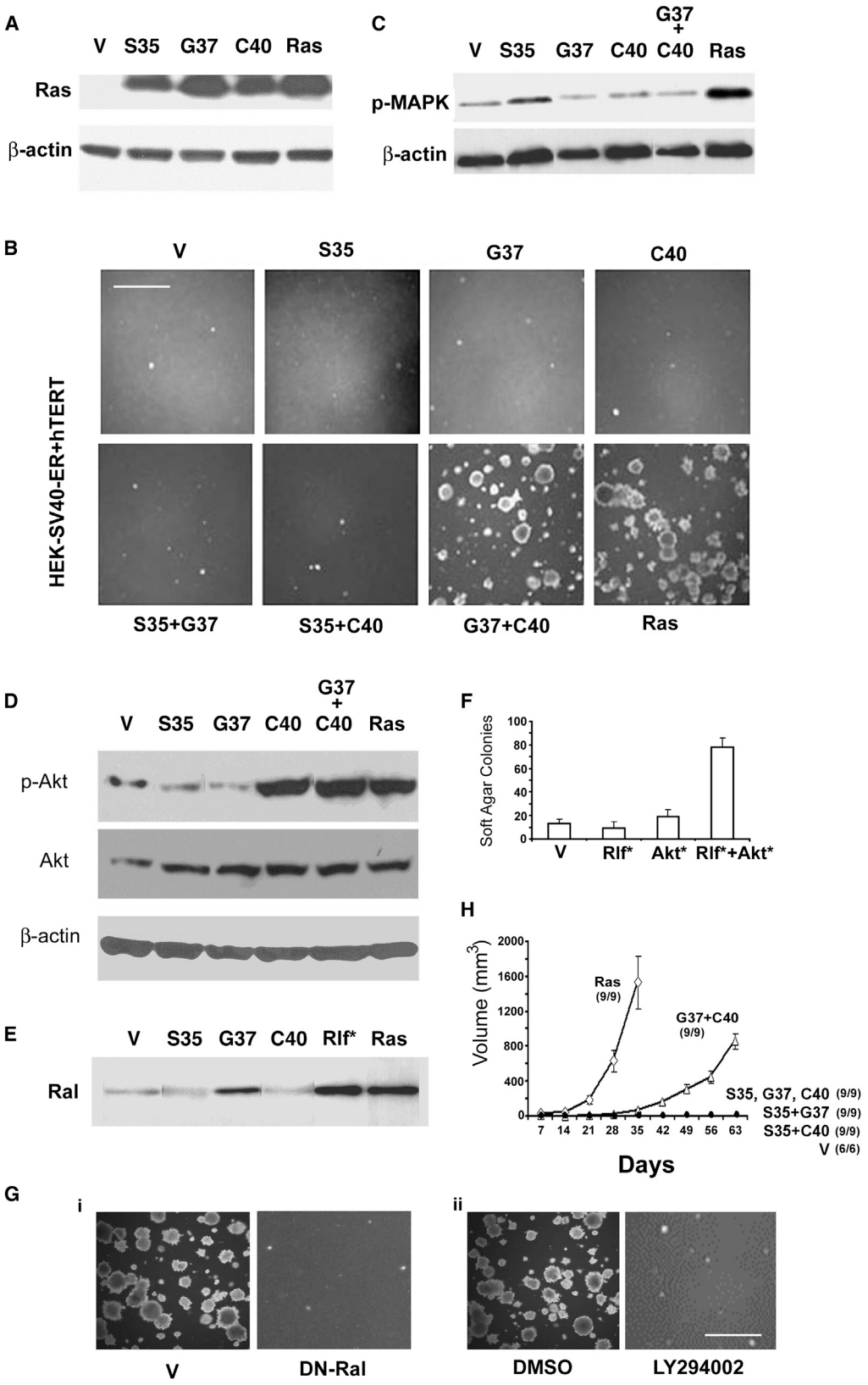

Figure 5. Requirements of Ras Pathways for Transforming Immortalized Human Embryonic Kidney (HEK) Cells

Cancer Cell
Errata

Hexokinase 2 Is Required for Tumor Initiation and Maintenance and Its Systemic Deletion Is Therapeutic in Mouse Models of Cancer

Krushna C. Patra, Qi Wang, Prashanth T. Bhaskar, Luke Miller, Zebin Wang, Will Wheaton, Navdeep Chandel, Markku Laakso, William J. Muller, Eric L. Allen, Abhishek K. Jha, Gromoslaw A. Smolen, Michelle F. Clasquin, R. Brooks Robey, and Nissim Hay*
*Correspondence: nhay@uic.edu
http://dx.doi.org/10.1016/j.ccr.2013.08.029

(Cancer Cell *24*, 213–228; August 12, 2013)
Following the publication of this paper, the authors noticed that Figures S2A–S2D in the online Supplemental Information document were inadvertently replaced by Figure S1 and contained a few typographical errors. The online Supplemental Information has now been replaced with a corrected document.

SnapShot: Prostate Cancer

LaMont J. Barlow and Michael M. Shen
Herbert Irving Comprehensive Cancer Center, Columbia University Medical Center, New York, NY 10032, USA

Cancer Cell

Clinical Progression of Prostate Cancer

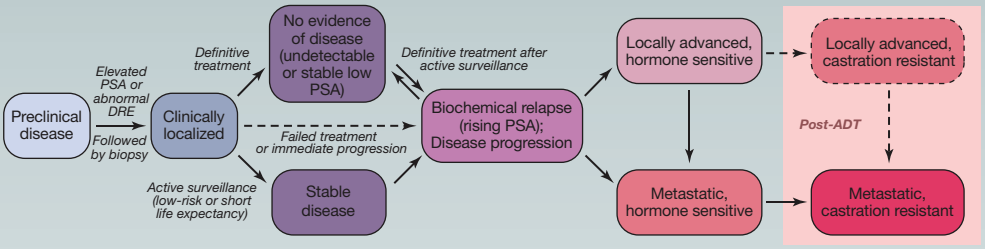

PSA: prostate-specific antigen
DRE: digital rectal exam
ADT: androgen-deprivation therapy
Definitive treatment: surgery or radiation, before or after ADT

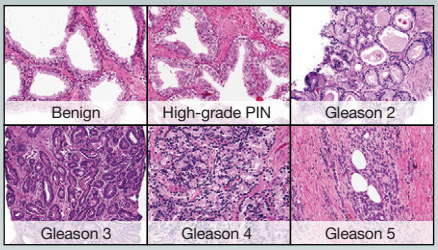

Reproduced with permission from Epstein et al., 2005 and R. Cardiff, unpublished

Risk Stratification for Recurrence after Prostatectomy for Local Disease, D'Amico Criteria

Risk group	PSA	Gleason score	Clinical stage	10-year recurrence rate
Low risk	<10	≤6	**T1-T2a** (nonpalpable tumor or palpable, confined to less than half of one lobe)	17%
Intermediate risk	10-20	7	**T2b** (palpable, involving more than half of one lobe)	54%
High risk	>20	≥8	**T2c or highter** (palpable, involving both lobes and/or beyond prostate)	71%

Patients are assigned to the highest catorgory of three variables

Chromosomal Rearrangements and Molecular Subtypes

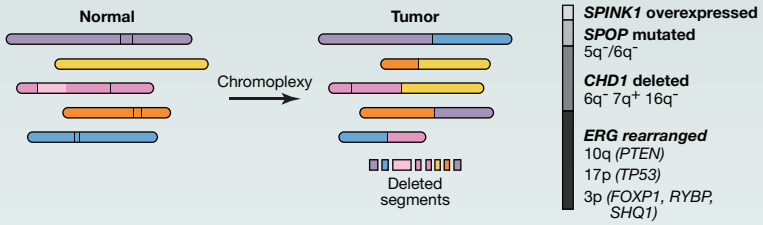

Androgen Biosynthesis Pathways and Inhibitors

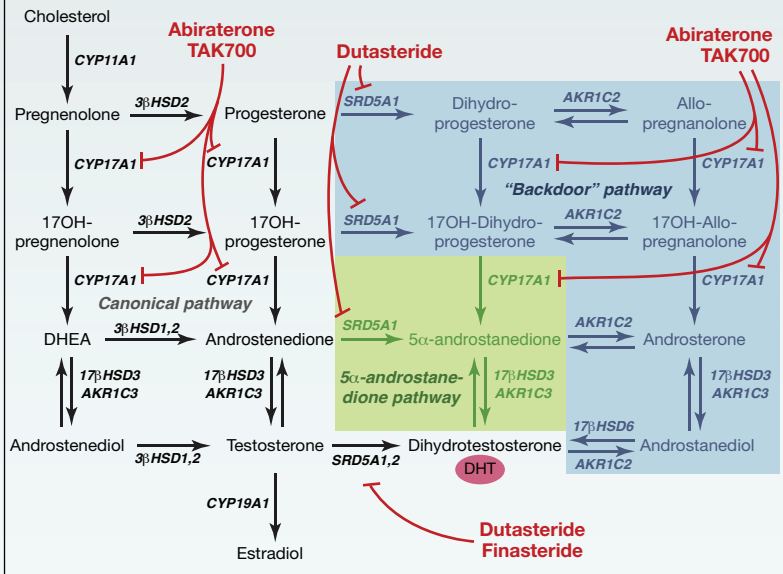

Treatment Options for Castration-Resistant Prostate Cancer (CRPC)

Treatment	Indication		
	M	S	Other
Observation	+/–	–	
Secondary hormone therapy	+/–	+/–	Mild symptoms
Docetaxel	+	+	Combine with other palliative measures
Abiratirone	+	+/–	Pre- or postdocetaxel treatment
Enzalutamide	+	+/–	Postdocetaxel (studies ongoing for predocetaxel use)
Sipuleucel-T	+	–/(+)	Asymptomatic or minimally symptomatic
Cabazitaxel	+	+	Postdocetaxel
Radium-223	+	+	Bone metastases only
Palliative radiation therapy	+	+	To symptomatic sites

M: metastatic S: symptomatic

Cross-talk between AR, PI3K, and MAPK Pathways

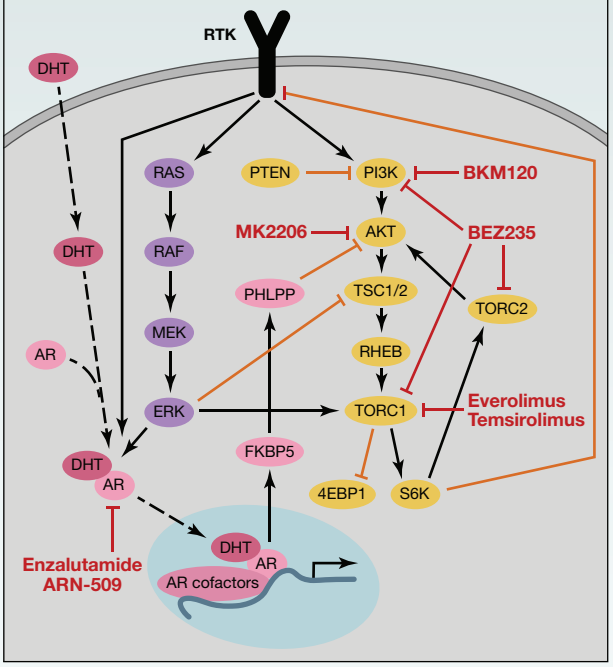

Selected Genetically Engineered Mouse Models

Name	Phenotype
TRAMP	Rapid progression to metastatic and castration resistant disease with neuroendocrine phenotype
Hi-Myc	Progression from PIN to invasive adenocarcinoma and metastasis
Nkx3.1$^{-/-}$	Develops PIN but not cancer
Pb-Cre4;Pten$^{flox/flox}$	Progression from PIN to adenocarcinoma
Pb-Cre4;Pten$^{flox/flox}$*; p53*$^{flox/flox}$	Rapid progression from PIN to invasive adenocarcinoma
Pb-Cre4;Pten$^{flox/flox}$*; Rosa26*$^{LSL-ERG/LSL-ERG}$	Rapid progression from PIN to invasive adenocarcinoma with patches of neuroendocrine differentiation
Nkx3.1$^{CreERT2/+}$*; Pten*$^{flox/flox}$*;Kras*$^{LSL-G12D/+}$	Rapid progression from PIN to invasive adenocarcinoma and castration-resistant disease with high frequency of metastasis

Cell Types of Origin for Prostate Cancer

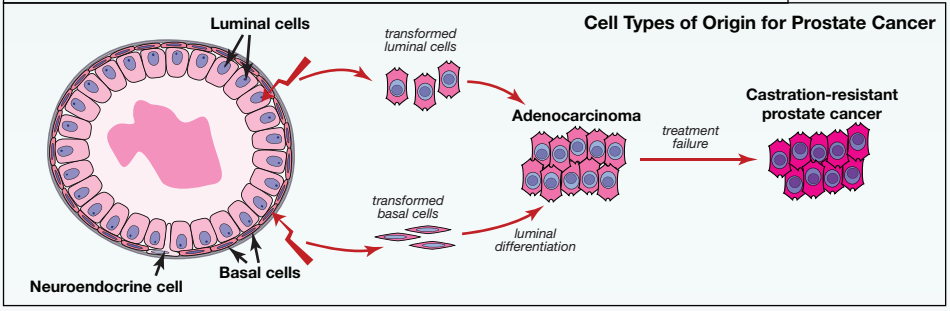

See online version for legend and references.

SnapShot: Prostate Cancer

LaMont J. Barlow and Michael M. Shen
Herbert Irving Comprehensive Cancer Center, Columbia University Medical Center, New York, NY 10032, USA

Cancer Cell

Prostate cancer (PCa) is the most commonly diagnosed cancer in men, with an estimated 238,000 new cases in the United States this year. It is the second highest cause of cancer-related death; nearly 30,000 men in the U.S. die from PCa each year. The discovery of prostate-specific antigen (PSA) as a biomarker for PCa has made it possible to detect the disease in early stages. It is estimated that there is often a lag-time of 15 years or more from initially detectable PSA elevation to clinically manifested PCa. In recent years, there has been considerable debate about the benefits versus risks of PSA screening, as there is a potential to over-treat indolent disease that may never have caused symptoms during a patient's lifetime. However, novel tumor markers and new mechanistic insights into disease progression may improve prognostic abilities.

Clinical Progression of Prostate Cancer and Histopathology

Most patients are diagnosed after presenting with elevated PSA or abnormal digital rectal exam, followed by a biopsy. Definitive treatments for clinically localized disease are surgery and radiation, but patients with low-risk disease or a shorter life expectancy can be managed with active surveillance, which consists of PSA assays and repeat biopsies at regular intervals until there is evidence of disease progression. Patients who progress may develop locally advanced or metastatic disease, which is initially treated primarily with androgen-deprivation therapy (ADT). However, almost all advanced prostate cancer progresses to castration-resistant disease after a period of ADT.

Histologic grading is based on the Gleason system, which ranges from grade 1 (most differentiated) to 5 (least differentiated). Each specimen is assigned a Gleason score based on their most prevalent and second-most prevalent histologic grades. The combination of the two grades gives the total score (ranging from 2 to 10, with most cancers falling between 6 and 8). When malignant cells are confined to the prostate acini and the basal cell layer remains at least partially intact, it is defined as prostatic intraepithelial neoplasia (PIN). High-grade PIN is an established precursor to adenocarcinoma, which is distinguished by an absence of the basal epithelial layer.

Cell Types of Origin, Genetic Alterations, and Molecular Subtypes

Prostate adenocarcinoma can derive from luminal or basal epithelial cells of the prostatic acini. While malignancies may arise from a single mutation followed by clonal propagation, many prostate cancers contain multiple foci with varying genetic alterations. Tumor heterogeneity at the molecular, cellular, and architectural levels makes it difficult to distinguish between synchronous tumors developing from independent oncogenic events versus clonally derived tumors whose cells become highly divergent.

Unlike most cancers that are commonly associated with specific point mutations, PCa involves large-scale genomic rearrangements and extensive copy number alterations involving multiple chromosomes. This phenomenon of chromoplexy often leads to loss of one or both copies of critical tumor suppressor genes such as *PTEN*, *NKX3.1*, *TP53*, and *CDKN1B* as well as oncogenic fusions such as *TMPRSS2-ERG*, which is observed in ~50% of prostate tumors. Exome and whole-genome sequencing studies have provided evidence for distinct molecular subtypes of PCa categorized by specific alterations such as *CHD1* deletions, *ERG* rearrangements, and *SPOP* mutations.

Chemoprevention

Because of the high prevalence and prolonged latency period of prostate cancer, chemoprevention approaches have been of particular interest. The most promising agents are the 5-alpha reductase inhibitors finasteride and dutasteride, which inhibit the conversion of testosterone to dihydrotestosterone, the most active prostatic androgen. Although data suggest that finasteride and dutasteride may reduce PCa risk overall, concerns of a potential increased risk of high-grade cancer have hindered their use in chemoprevention.

Mechanisms of Castration Resistance and Advances in Treatment of Castration-Resistant Prostate Cancer

Virtually every patient treated with ADT will eventually develop resistance with subsequent rise in PSA or clinical progression. Although the pathways that lead to castration resistance are not fully understood, potential mechanisms include (1) intratumoral androgen biosynthesis, (2) androgen receptor (AR) pathway hypersensitivity via AR gene amplification, (3) AR activation by noncognate ligands such as corticosteroids (often mediated by AR mutations), (4) growth factor-mediated increase in AR transcription activity, (5) expression of variant AR isoforms that are ligand independent, (6) activation of alternative survival pathways that bypass the AR pathway, and (7) selection of pre-existing castration-resistant epithelial stem cells. Castration resistance may involve several of these processes simultaneously as well as undiscovered mechanisms.

The available treatments for castration-resistant prostate cancer (CRPC) have traditionally been limited to cytotoxic chemotherapeutics and palliative measures. However, recent novel therapies with proven survival benefits have broadened the armamentarium for this disease state. In particular, Abiraterone is an oral agent that blocks androgen production in tumors as well as testis and adrenal gland through irreversible inhibition of products of the *CYP17A1* gene. Abiraterone prolongs overall survival in men with CRPC previously treated with docetaxel as well as in chemotherapy naive patients. Enzalutamide, another oral agent, blocks AR function by inhibition of androgen binding to AR, nuclear translocation of AR, and AR association with nuclear DNA, and also prolongs survival in men with metastatic CRPC after docetaxel treatment.

Activation of the PI3K-AKT-mTOR pathway is likely to play a key role in castration resistance, particularly through its complex regulation involving cross-talk with the AR and MAPK pathways. Agents that block various steps in the PI3K-AKT-mTOR pathway are currently being investigated as novel therapeutics for advanced PCa. Such agents may be used in the context of combinatorial treatments with agents that target the AR and/or MAPK pathways to counteract positive feedback loops that are activated when only a single pathway is targeted.

Mouse Models of Prostate Cancer

Genetically engineered autochthonous mouse models of prostate cancer have played important roles in the elucidation of molecular mechanisms for cancer initiation and progression. Newer models that display castration-resistant phenotypes are now being used for analyses of drug response and resistance mechanisms.

ACKNOWLEDGMENTS

We thank R. Cardiff for images, and N. Sharifi, K. Kelly, B. Carver, E. Gelmann, and C. Abate-Shen for comments. This work was supported by the NIH and the Urology Care Foundation.

REFERENCES

Baca, S.C., Prandi, D., Lawrence, M.S., Mosquera, J.M., Romanel, A., Drier, Y., Park, K., Kitabayashi, N., MacDonald, T.Y., Ghandi, M., et al. (2013). Punctuated evolution of prostate cancer genomes. Cell *153*, 666–677.

Bitting, R.L., and Armstrong, A.J. (2013). Targeting the PI3K/Akt/mTOR pathway in castration-resistant prostate cancer. Endocr. Relat. Cancer *20*, R83–R99.

Carver, B.S., Chapinski, C., Wongvipat, J., Hieronymus, H., Chen, Y., Chandarlapaty, S., Arora, V.K., Le, C., Koutcher, J., Scher, H., et al. (2011). Reciprocal feedback regulation of PI3K and androgen receptor signaling in PTEN-deficient prostate cancer. Cancer Cell *19*, 575–586.

D'Amico, A.V., Whittington, R., Malkowicz, S.B., Weinstein, M., Tomaszewski, J.E., Schultz, D., Rhude, M., Rocha, S., Wein, A., and Richie, J.P. (2001). Predicting prostate specific antigen outcome preoperatively in the prostate specific antigen era. J. Urol. *166*, 2185–2188.

Epstein, J.I., Allsbrook, W.C., Jr., Amin, M.B., and Egevad, L.L.; ISUP Grading Committee (2005). The 2005 International Society of Urological Pathology (ISUP) Consensus Conference on Gleason Grading of Prostatic Carcinoma. Am. J. Surg. Pathol. *29*, 1228–1242.

Irshad, S., and Abate-Shen, C. (2013). Modeling prostate cancer in mice: something old, something new, something premalignant, something metastatic. Cancer Metastasis Rev. *32*, 109–122.

Schoenborn, J.R., Nelson, P., and Fang, M. (2013). Genomic profiling defines subtypes of prostate cancer with the potential for therapeutic stratification. Clin. Cancer Res. *19*, 4058–4066.

Sharifi, N. (2013). Minireview: Androgen metabolism in castration-resistant prostate cancer. Mol. Endocrinol. *27*, 708–714.

Shen, M.M., and Abate-Shen, C. (2010). Molecular genetics of prostate cancer: new prospects for old challenges. Genes Dev. *24*, 1967–2000.

Wang, Z.A., Mitrofanova, A., Bergren, S.K., Abate-Shen, C., Cardiff, R.D., Califano, A., and Shen, M.M. (2013). Lineage analysis of basal epithelial cells reveals their unexpected plasticity and supports a cell-of-origin model for prostate cancer heterogeneity. Nat. Cell Biol. *15*, 274–283.

  DOI http://dx.doi.org/10.1016/j.ccr.2013.08.033